Analysis of Diffraction Anomalous Fine Structure

by

Julie Olmsted Cross

A dissertation submitted in partial fulfillment of the requirements for the degree of

Doctor of Philosophy

University of Washington

1996

Approved by ______________________________

(Chairperson of Supervisory Committee)

____

____

Program Authorized
to Offer Degree ______________________________

Date ______________________________

University of Washington

Abstract

Analysis of Diffraction Anomalous Fine Structure

by Julie Olmsted Cross

Chairperson of Supervisory Committee: *Professor Larry B. Sorensen*
Department of Physics

This thesis presents a systematic study of the application of DAFS to determine site-specific local structural and chemical information in complex materials, and the first application of state-of-the-art theoretical XAFS calculations using the computer program FEFF to model DAFS data. In addition, the iterative dispersion analysis method, first suggested by Pickering, *et al.*, has been generalized to accommodate the off-resonance anomalous scattering from heavy atoms in the unit cell. The generalized algorithm KKFIT was applied to DAFS data from eight (00ℓ) reflections of the high-T_c superconductor $YBa_2Cu_3O_{6.8}$ to obtain the weighted complex resonant scattering amplitudes $\Delta f_{\mathrm{w}}(\mathbf{Q}, E)$. The fine-structure functions $\chi_{\mathrm{w}}(\mathbf{Q}, E)$ isolated from the $\Delta f_{\mathrm{w}}(\mathbf{Q}, E)$ are linear combinations of the individual site fine structure functions $\chi_{\mathrm{w}}(\mathbf{Q}, E) = \sum_i W_{i,\mathbf{Q}} \chi_i(E)$ from the two inequivalent Cu sites, added together according to the structure factor for the Cu sublattice. The $\chi_{\mathrm{w}}(\mathbf{Q}, E)$ were fit *en masse* using the XAFS analysis program FEFFIT under a set of constraints on the coefficients $W_{i,\mathbf{Q}}$ based on the structure factor for kinematic scattering. The $W_{i,\mathbf{Q}}$ determined by FEFFIT were used to obtain the fully separated complex resonant scattering amplitudes $\Delta f(E)$ for the two Cu sites.

The theoretical connection between DAFS and XAFS is used to justify the application of state-of-the-art theoretical XAFS calculations to DAFS analysis. The polarization dependence of DAFS is described in terms of individual virtual photoelectron scattering paths in the Rehr-Albers separable curved-wave formalism. Polarization is shown to be an important factor in all DAFS experiments. Three experimental constraints are found necessary for obtaining site-separated $\Delta f(E)$ from DAFS data by linear inversion of the $W_{i,\mathbf{Q}}$ matrix and KKFIT isolated $\Delta f_{\mathrm{w}}(\mathbf{Q}, E)$: 1) The diffrac-

tion must be confined to a plane perpendicular to the incident photon polarization axis; 2) The sublattice of resonant sites must have a center of symmetry parallel to the diffraction wavevector transfer; and 3) The projected density of the resonant sites onto the scattering plane must be separable. Analysis methods based on FEFF, rather than direct linear inversion, lift the first restriction; methods that do not rely on the iterative dispersion analysis lift the second restriction.

Special attention was paid to demonstrating the reliability of the analysis methods for determining the complex amplitude from measured intensity data. The KKFIT algorithm was tested extensively on mocked-up DAFS data calculated by FEFF. The reliability tests showed that KKFIT accurately reproduces the input function $\Delta f(E)$.

TABLE OF CONTENTS

LIST OF FIGURES

LIST OF TABLES

ACKNOWLEDGMENTS

First I would like to thank Larry Sorensen for his kindly encouragement of my work and for allowing me a tremendous amount of freedom in pursuing my scientific interests. I thank Hans Stragier for blazing the trail, so to speak, with his pioneering DAFS analysis software that laid the foundation for my own codes. I thank Yizhak Yacoby for committing to my reading committee during his precious time here at the University of Washington: I truly enjoyed our discussions about DAFS and I hope I will have the privilege again. I thank John Rehr first for enduring all of my naive questions with such good humor and, more importantly, for being an XAFS fanatic and for creating FEFF. I thank Kelin Kuhn for setting an excellent example and for giving me the extra bit of confidence I needed to make it over the top. I thank Edward Stern for welcoming my participation in his research group. I thank Matthew Newville for his enthusiastic collaboration on this project and for being so generous with his time—none of the fine-structure analysis in this dissertation would have been possible without his codes and his willingness to change them at a moment's notice to accommodate DAFS. Rick and Louis on the tarmac. I have been here so long that the list of people in the Physics Department and around the University who have contributed to my happy quotient is longer than I can reasonably include here, but I want to specially thank Cecilia Bitz and Bruce Ravel for Thursdays, Cindy Hartway for the hat, Heinz Guldenman for ten years worth of sweetness, and Daniel Haskel for cracking me up with remarkable precision. Thank you also to all of the students in my 133 and 119 lab sections—you are champs!

All of the experiments described in this work were performed at the National Synchrotron Light Source beamline X23A-2, which is maintained by the National Institute of Standards and Technology (NIST). The development of a new spectroscopy requires large amounts of precious synchrotron beam time and special thanks are owed to my collaborators at NIST, particularly Charles Bouldin and Joseph Woicik, for dedicating their facility to this project during several six-week runs, spread out over the course of three years. I thank the members of Professor Sorensen's research group for sharing many long shifts at the synchrotron collecting the data for this project: Douglas Tweet, Brian Swanson, Hans Stragier, Cecilia Bitz, Dennis Yee and Tianming Zhang.

From my heart I thank guitarists Brad Rapp and Ron Martinez who somehow always know when I need to hear a song and, even more amazing, which one. I thank my clan in Portland, in the words of our people: *sõnhau̇nd te bāl õn, pähtā.* I thank my grandmother Charlotte Olmsted Kursh for her relentless generosity, her incisive perception and her sly wit. I thank Felix and Janet for being the best sisters in the world. I thank the Kern-Gangier family, Mare, Drew and especially Amabel for drooling all over me with such carefree abandon. I thank my hausmates Tülay, Laurel, John, Liza, Leslie and Steve for allowing me to get out of my share of the chores for over a year—I owe you! I thank Thomas Gorman for seeing me through the beginning of this adventure with his inimitable optimism, wisdom and kindness. Finally I thank my friend Mitchell Cline whose quiet, steady support during this last year has made all the difference in the world.

Sie schlief die Welt

R.M. Rilke

Chapter 1

INTRODUCTION

Diffraction anomalous fine structure (DAFS) is the name given to the energy dependent modulation observed in Bragg peak intensities near an atomic resonance. This fine structure is closely related to x-ray absorption fine structure (XAFS) and may be used to obtain the same kind of information about the local environment of the resonant atoms as is routinely obtained from XAFS, *i.e.*, the distances, atomic species and coordination numbers of the neighboring atoms. Figure 1.1(a) shows the DAFS spectrum for the Cu(111) Bragg peak of a thin film of crystalline Cu and Figure 1.1(b) shows the fluorescence XAFS spectrum measured from the same sample for comparison. The physical effects that are used to measure XAFS, such as x-ray fluorescence, total electron yield and direct beam attenuation are incoherent processes. Thus, while XAFS is very sensitive to the local environment around the absorbing atoms at resonance, the final measurement is an incoherent sum of the absorption signal from all of the absorbing atoms. DAFS, on the other hand, is measured in the coherent elastic scattering channel. The most significant difference between DAFS and XAFS is the crystallographic structure factor which underlies the DAFS signal and permits selection for local structural information about some subset of the resonant atoms within the diffracting material based on their long-range order. This promises tremendous power for obtaining XAFS-like information from the resonant atoms in complex materials that would be intractable using XAFS.

Although the existence of fine structure in the diffraction intensities has been known for many years [1, 2] and the theoretical connection between DAFS and XAFS is well understood [3–11], quantitative analysis of DAFS has only recently been attempted [12–18]. Around 1990, an algorithm for refining DAFS data, based on the Kramers-Krönig dispersion relations, was presented by Pickering, *et. al.* [17], and further developed by Stragier [13]. This iterative fitting procedure isolates the real and imaginary parts of the complex scattering amplitude from the measured DAFS

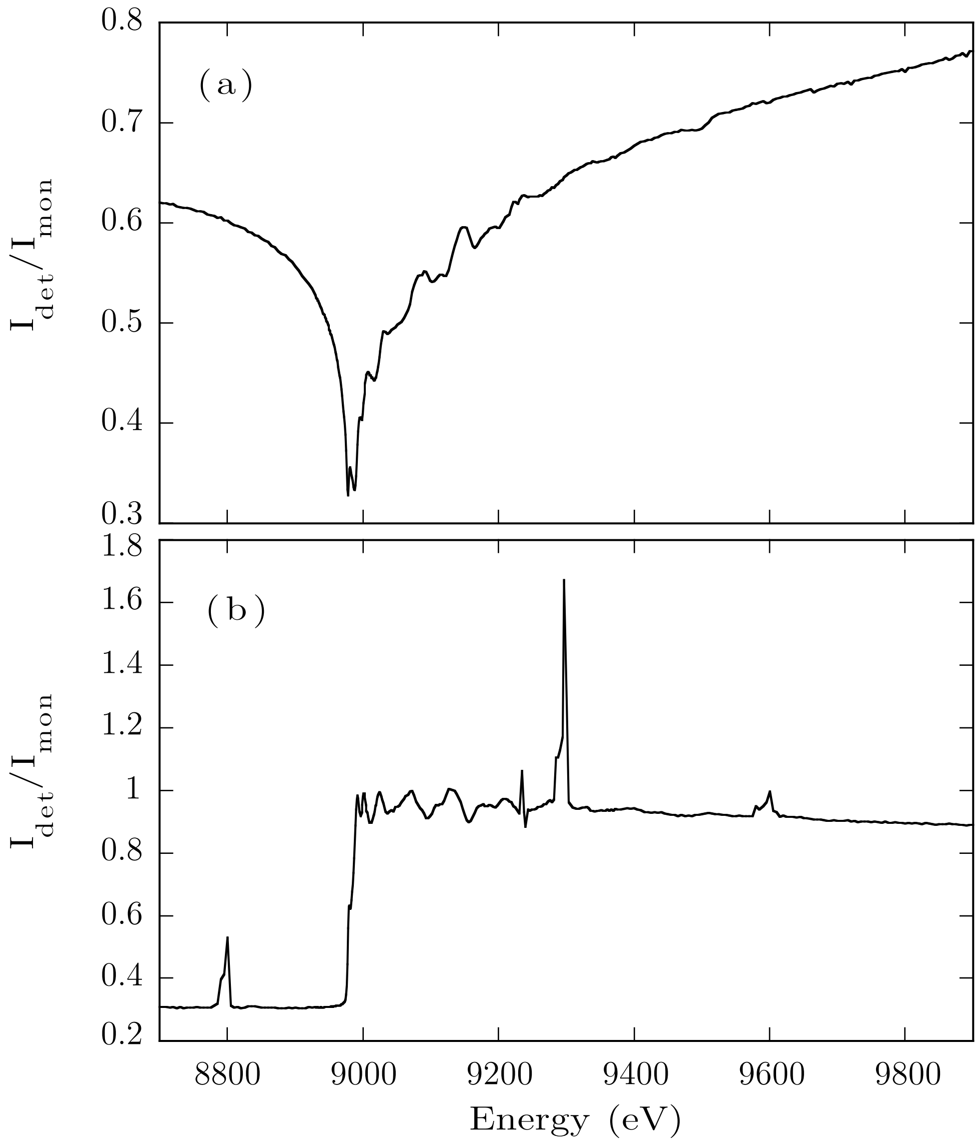

Figure 1.1: Simultaneously measured (a) DAFS and (b) fluorescence XAFS signals from a 2000 Å crystalline film of Cu metal on a mica substrate. The DAFS was measured for the Cu(111) reflection. Both of the signals are shown exactly as they were measured: DAFS and XAFS detector signals divided by the incident beam monitor signal. The XAFS detector was located at 90° from the (vertical) scattering plane in order to minimize diffraction into the fluorescence detector. The spurious *Bragg glitches* in the XAFS signal are typical of fluorescence XAFS measurements from single crystals.

intensity, which can then be analyzed using standard XAFS techniques.

This thesis presents the first attempt to consolidate XAFS and crystallography into a single structural analysis procedure by applying a self-consistent model to the crystallographically weighted fine structure signals from the (00ℓ) Bragg peaks in $YBa_2Cu_3O_{6.8}$. This is a significant advance in the development of DAFS analysis and care has been taken to provide a sufficiently explicit set of instructions so that other investigators can duplicate the methods presented here. In addition to these results, I address some lingering questions about the finer points of DAFS analysis, including the correct normalization procedure for the DAFS and the quality of structural parameters determined using DAFS as compared to XAFS. Previous work has demonstrated the potential utility of DAFS, but little has been done to quantify the reliability of the structural parameters obtained from DAFS analysis. These crucial details must be addressed before DAFS can attain its place within the ranks of well established structural analysis techniques.

1.1 Special properties of DAFS

When the resonant atoms in a material are situated in two or more inequivalent local environments, for example the iron atoms in the octahedral and tetrahedral sites of magnetite (ferrite spinel, Fe_3O_4), the XAFS signals from the different sites will always be mixed according to the number density of each of the sites. In the magnetite example, the piece of the total XAFS signal due to the octahedrally coordinated sites will always be twice as large as the piece due to the tetrahedrally coordinated sites because there are twice the number of octahedrally coordinated sites in the unit cell. Even when the unit cell structure is well known, it is a delicate operation to disentangle the fine structure from multiple sites in the XAFS signal, if it is possible at all. For a material with multiple resonant sites, analysis techniques that rely on *a priori* calculations of the EXAFS require a very good starting model, and even so will often miss characteristic features of the near-edge XAFS (XANES) from the unique sites. Polarization of the incident x-ray beam has been used successfully on single crystals of $YBa_2Cu_3O_7$ [76], but this only works for low symmetry materials.

In DAFS, on the other hand, the fine structure from inequivalent sites is mixed according to the crystallographic structure factor which can differ dramatically between Bragg reflections. This differential crystallographic mixing of the fine structure in the coherent diffraction channel opens up the possibility of separating the fine structure

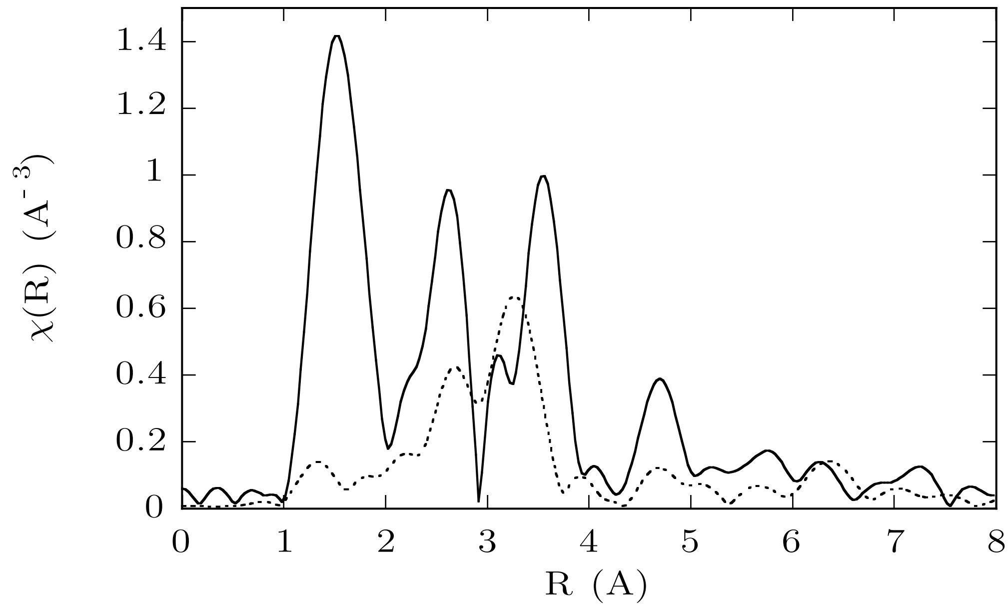

Figure 1.2: Fourier transform magnitudes of the DAFS fine structure from the (001), solid line, and (002), dashed line, reflections of $YBa_2Cu_3O_{6.8}$. Different combinations of the fine structure from inequivalent sites cause dramatic changes in the spectral content of the DAFS.

signals from the multiple sites directly. In the special case of magnetite, the fine structure contribution to the Bragg intensity from the octahedral sites vanishes for the (206) reflection, while the contribution from the tetrahedral sites vanishes for the (226) reflection. This property of DAFS is called *site selectivity* because it provides a means for probing the local structure around a specific resonant site within the unit cell based on its long-range order. In general, the fine structure signals from inequivalent sites do not separate as neatly as they do in magnetite. However, the mixing ratio of the signals will change between reflections, allowing the individual signals to be separated by taking linear combinations of the total signal at a few different reflections. Figure 1.2 shows the spectral content of the DAFS for the (001) and (002) Bragg reflections from $YBa_2Cu_3O_{6.8}$. There are three Cu atoms in two inequivalent sites in the $YBa_2Cu_3O_{6.8}$ unit cell. The dramatic difference in the Fourier transforms of the fine structure is due to the crystallographic weighting of the fine structure signals from the two inequivalent sites at these reflections. The details of the analysis techniques for isolating the individual fine structure signals using DAFS

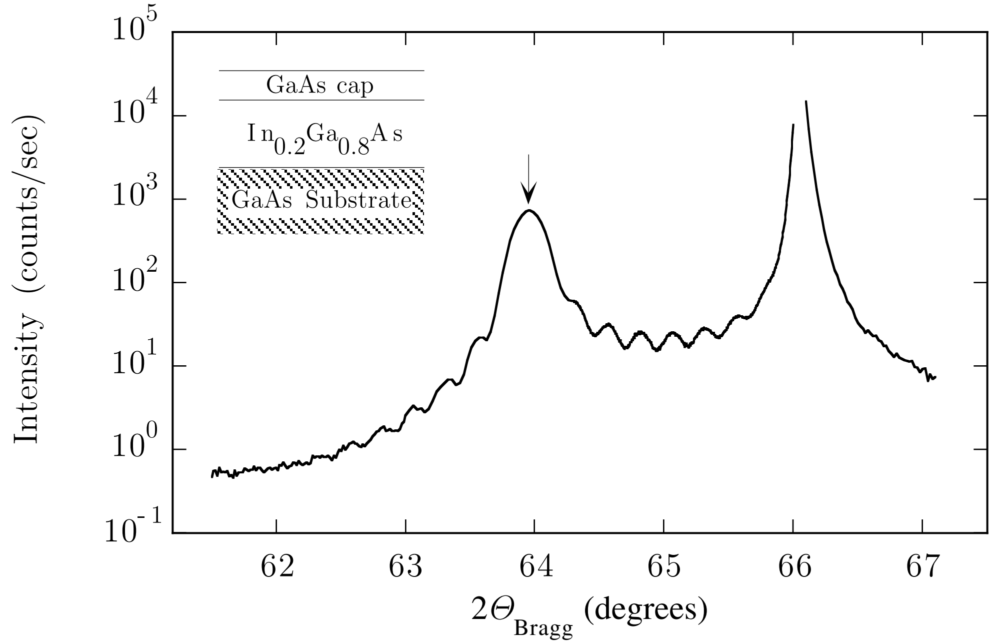

Figure 1.3: An example of DAFS lattice parameter selectivity. The measured specular reflectivity around the (004) reflection from an $In_xGa_{1-x}As$ multilayer structure. The sample was a 400 Å thick $In_{0.2}Ga_{0.8}As$ layer grown by molecular beam epitaxy on (001) GaAs with a 50 Å GaAs cap, as shown in the inset. DAFS measurements taken at the alloy layer peak at $2\theta \approx 64°$, indicated by the arrow, will contain information about the local structural parameters of absorbers in that layer only.

measured at several reflections are presented in Chapter 6.

DAFS can also be used to selectively probe the local structure around resonant atoms from regions of an inhomogeneous sample. The diffraction maxima from materials with different lattice parameters will satisfy the Bragg condition at different values of the photon momentum transfer. For example, the diffraction pattern from a mixed powder is the sum of the diffraction patterns from the individual constituents. Wherever the peaks do not accidentally overlap, the DAFS measured at a Bragg peak will yield information only about the subset of material that diffracted in that direction. This property of DAFS is called *spatial selectivity* because it selects for a spatial variation in the lattice parameter. DAFS spatial selectivity has recently been used to observe the fine structure from a buried Si/B($\sqrt{3} \times \sqrt{3}$)R30° reconstructed interface [16], to single out the fine structure signal from one buried layer in an $In_xGa_{1-x}As$ multilayer structure [13], and to separate the signals from the components of a mixed powder sample [17]. Figure 1.3 shows the specular reflectivity from the multilayer $In_xGa_{1-x}As$ structure. DAFS data collected by measuring the energy dependent intensity of the broad alloy peak (indicated by the arrow), corresponding to the $In_xGa_{1-x}As$ lattice parameter, contains information about the local structural parameters of absorbers in that layer only.

1.2 Analysis of diffraction fine structure

The most difficult aspect of DAFS analysis is reducing the fine structure signal from the Bragg intensity to a form that easily interpreted as a function of the material structure parameters. The reason diffraction fine structure is inherently more difficult to isolate than absorption fine structure is that the diffraction intensity mixes the real and imaginary parts of the scattering amplitude in a non-trivial way. This is also the great advantage of measuring the fine structure in the diffraction channel Since the coherent mixing can be used as a tool to separate signals that are not separable in the XAFS.

The integrated intensity of a Bragg reflection from a weakly scattering crystal is proportional to the square of the crystallographic structure factor

$$I(\mathbf{Q}) \propto \left| \sum_j f_j e^{-M_j} e^{i\mathbf{Q}\cdot\mathbf{R}_j} \right|^2, \tag{1.1}$$

which accounts for scattering at the photon wavevector transfer $\mathbf{Q} \equiv \mathbf{k}' - \mathbf{k}$ from each of the j atoms in the unit cell according to their positions $\mathbf{R}_j$ and their scattering amplitudes, f_j. Attenuation of the Bragg peak intensities is accounted for by the Debye-Waller factors[1], M_j.

When the incident photon energy is near the energy required to excite a bound atomic electron up into an unoccupied state, the scattering amplitude changes dramatically. The scattering amplitude f from a single atom may be written explicitly in terms of the Thomson scattering amplitude $f_0(\mathbf{Q})$, which is independent of the

[1] This expression for the structure factor treats the vibrating lattice as a lattice at rest composed of points having individual scattering power of fe^{-M} instead of f. Strictly speaking, the attenuation term is *outside* the square of the modulus since the thermal average is taken over the intensity and not over the amplitude. However, Equation (1.1) is formally equivalent to the exact treatment under the assumption of harmonic vibrations, and is more convenient for working with individual sublattices of the crystal. Chapter V, §1(q) of James [38] gives a justification for this formalism.

incident photon energy, and an energy-dependent resonant scattering correction Δf, which can also depend on the directions of the incident and outgoing photons

$$\begin{aligned} f(\mathbf{k},\mathbf{k}',E) &= f_0(\mathbf{Q}) + \Delta f(\mathbf{k},\mathbf{k}',E) \\ &= f_0(\mathbf{Q}) + f'(\mathbf{k},\mathbf{k}',E) + if''(\mathbf{k},\mathbf{k}',E). \end{aligned} \tag{1.2}$$

The terms f' and f'' are the real and imaginary parts of Δf, the *anomalous* correction to the Thomson scattering amplitude. These terms are near the size of f_0 when the incident x-rays are at the resonance energy. The fine structure part of the resonant scattering amplitude appears only with the presence of neighboring atoms in close proximity to the resonant atom. In the absence of neighbors, Δf is a rapidly changing but smooth function of energy. In the presence of neighbors, the resonance response develops structure due both to changes in the ground-state wavefunctions (embedded atom effects) and to interference effects caused by backscattering of the excited photoelectron off of the neighbors (fine-structure). The embedded atom effects are more slowly varying functions of energy than the fine structure, and may be combined with the smooth part. Then the smooth part and the fine structure part of Δf are separable [14, 31], and it is useful to write them as

$$\Delta f = f'_a + if''_a + f''_0(\chi' + i\chi'') \tag{1.3}$$

where the subscript a indicates the smooth *atomic* part of the response function and $\chi = \chi' + i\chi''$ is the complex fine structure with dependence on $\mathbf{k}$, $\mathbf{k}'$ and E understood. The coefficient f''_0 of χ is the matrix element for the resonant electrons only[2]. This amounts to a step from zero to some finite value at the absorption edge and has the effect of turning off the fine structure below the Fermi energy as well as setting the scale of the fine structure.

In the forward scattering limit, the imaginary part of the scattering amplitude is related to the total absorption cross-section, and consequently to the XAFS, by the optical theorem:

$$\mathrm{Im}\,[f(\mathbf{k}=\mathbf{k}',E)] = f''(E) = \frac{E}{4\pi\hbar c}\sigma_{tot}(E). \tag{1.4}$$

[2] I have chosen this notation to emphasize the relationship between XAFS embedded-atom $\mu_0(E)$, which is the absorption function due to the isolated deep core state in the absence of backscattering from the neighbors but embedded in the solid.

This suggests that if the dependence of f'' on $\mathbf{k}$ and $\mathbf{k}'$ is small, and if we can isolate f'' from the diffraction intensity, then analysis of the diffraction fine structure becomes identical to analysis of XAFS—a problem already solved through many years of hard work.

1.2.1 Dispersion relations in x-ray scattering

The problem of unfolding the DAFS signal may at first seem intractable, however it is possible because the real and imaginary parts of the scattering amplitude are not independent functions of energy. A mathematical consequence of the physical limitation that electromagnetic signals cannot travel faster than the speed of light is that the scattering amplitude is an analytic function in the upper half of the complex frequency plane [19], and therefore satisfies the Cauchy-Reiman conditions. The familiar differential relations between the real and imaginary parts of an analytic function written in their integral form are called Hilbert transforms. For $\mathbf{k} = \mathbf{k}'$ we have

$$\mathrm{Re}\,[f(E)] \;=\; f'(E) = \frac{1}{\pi}\mathrm{P}\int_{-\infty}^{+\infty} \frac{f''(E')dE'}{E' - E} \tag{1.5}$$

and

$$\mathrm{Im}\,[f(E)] \;=\; f''(E) = -\frac{1}{\pi}\mathrm{P}\int_{-\infty}^{+\infty} \frac{f'(E')dE'}{E' - E}. \tag{1.6}$$

If the $\mathbf{k}$ and $\mathbf{k}'$ dependence of f is small [39], then this integral relation holds at all values of $\mathbf{Q}$, and therefore the measured DAFS intensity may be modelled as a functional of a single real-valued response function: either f' or f''.

What physical meaning can be assigned to Equations (1.5) and (1.6) , since we cannot measure negative energies in the laboratory? If we insist that the incident and scattered waves are real, then $f''(-E) = -f''(E)$ and $f'(-E) = f'(E)$. With this crossing symmetry, only the positive frequencies need to be considered in Equation (1.6). The Hilbert transforms can be folded across $E = 0$ to obtain the more familiar Kramers-Krönig dispersion relations

$$f'(E) \;=\; \frac{2}{\pi}\mathrm{P}\int_{0}^{\infty} \frac{E' f''(E')}{E'^2 - E^2} dE' \tag{1.7}$$

and

$$f''(E) \;=\; -\frac{2E}{\pi}\mathrm{P}\int_{0}^{\infty} \frac{f'(E')}{E'^2 - E^2} dE'. \tag{1.8}$$

The dispersion relations reduce the DAFS problem to that of solving for one function and its Kramers-Krönig transform, provided we can actually calculate one of the integrals in Equations (1.7) and (1.8).

Clearly it is not possible to measure the scattering amplitude over the whole infinite range of the integral. In a controlled synchrotron experiment, it is usually impractical to measure over a range larger than about 2000 eV. Fortunately, the problem can be separated into two separate calculations: one for the smooth part of the resonant scattering amplitude, and one for the part that contains the fine structure [20]. Using Equation (1.3) and separating the smooth and fine structure terms, we find that

$$f'(E) = \frac{2}{\pi}\mathrm{P}\left(\int_0^\infty \frac{E' f''_a(E')}{E'^2 - E^2} dE' + \int_{\Delta E} \frac{E' f''_0(E')\chi''(E')}{E'^2 - E^2} dE'\right) \tag{1.9}$$

and

$$f''(E) = -\frac{2E}{\pi}\mathrm{P}\left(\int_0^\infty \frac{f'_a(E')}{E'^2 - E^2} dE' + \int_{\Delta E} \frac{f''_0(E')\chi'(E')}{E'^2 - E^2} dE'\right). \tag{1.10}$$

Here $f_a(E)$ is the smooth or bare atom part of the resonant scattering amplitude and is defined by $f_a(E) = f(E) - f''_0(E)\chi(E)$. The subscript ΔE indicates that the integral is calculated only over the energy range of the fine structure, which is band limited by several physical effects: bond length disorder between the neighboring atoms, photoelectron mean free path, instrument broadening and statistical noise in the real intensity measurements. The typical size of ΔE is on the order of 1000 eV, although this varies depending on the experimental conditions. For example data taken at very low temperatures will have fine structure evident over a larger range of energies than data taken at very high temperatures.

The first term in each of the integrals Equations (1.9) and (1.10) is just the transform of the smooth part of the response function which can be determined from theoretical calculations. Only the second term needs to be determined experimentally. This separation reduces the infinite dispersion integral to a finite integral over the range of the fine structure data, and therefore to a problem that is both experimentally and computationally feasible. An iterative algorithm, based on Equations (1.9) and (1.10) for reducing DAFS intensity measurements using the Kramers-Krönig relations will be presented in some detail in Chapter 5

1.2.2 Self-absorption correction

Up to this point, there has been no reason to choose f' over f'' as a starting place for the DAFS analysis. The historical precedence of XAFS suggests that f'' is the natural choice, but Equation (1.1) seems to be equally inclined to either one or the other. This symmetry is broken in two ways: first because the real part of the amplitude is the sum $f_0 + f'$ so that for most cases the intensity is dominated by f'; and second by the energy dependent attenuation of the incident and scattered beams as they pass through a finite amount of material to scatter from atoms deep in the sample. This self-absorption by the sample is treated as a correction to Equation (1.1). The attenuation of a beam passing through a slab of material is described by

$$dI(E) = I_0 e^{-\mu(E)t} dt, \tag{1.11}$$

where t is the path length of the beam in the material and

$$\mu(E) = \sum_j \mu_j(E) \tag{1.12}$$

is the mass absorption coefficient due to all of the atoms in the crystallographic unit cell. Since $\mu(E)$ depends on the total absorption cross-section, given in Equation (1.4), it also contains f'' fine structure. This causes the Bragg intensities, as calculated from Equation (1.1), to be transcendental in f'' while remaining merely quadratic in f', making it much more convenient to solve the measured intensity for f' than for f''. If the absorption correction is not made correctly, interference from the fine structure in the argument of the attenuation term will introduce phase shifts in the Fourier components of the DAFS $\chi(E)$ function. The size of these phase shifts and their effects on the structural parameters obtained analyzing the Fourier components of the fine structure is explored in Chapter 7.

Once the function $\chi(E)$ has been distilled from the DAFS data, it can be analyzed using the same analysis tools and methods that are routinely used for XAFS $\chi(E)$ data. In Chapters 5, 7 and 6, the results obtained using the computer programs FEFF 6.10 [23] and FEFFIT [59] to analyze DAFS data are presented. Two features of FEFFIT make it well suited to solve problems unique to DAFS analysis. The first feature is constrained fitting of multiple data sets. This was first developed to determine the shape of the interatomic potential using a model based on the thermal expansion coefficient to model XAFS data taken at several different temperatures

[21]. The method was easily adapted to model DAFS data taken at several Bragg reflections subject to a set of constraints on the crystallographic weighting of the fine structure from multiple resonant sites with **Q** as the independent variable. The crystallographic weights for the fine structure from the two inequivalent copper sites in the unit cell of $YBa_2Cu_3O_x$, including the Debye-Waller factors for the resonant atoms, are determined in this manner in Chapter 6. The second feature is the ability to add an energy independent phase shift to a single XAFS scattering path. This can be used, for example, to add $\pi/2$ to all of the XAFS scattering paths and fit the real part of the fine structure instead of the imaginary part. The constant phase can also be allowed to have a different value for each path.

1.3 The marriage of diffraction and XAFS

The discussion above has largely concentrated on analyzing the DAFS fine structure, which is the energy dependence of the Bragg intensity, and the changes in this fine structure as a function of **Q**. It is also possible to use the **Q**-dependence of the integrated Bragg intensities at any single value of the incident photon energy to obtain crystallographic information. The resonance fine structure and the Bragg peak intensities both depend on the details of the arrangement of the atoms inside the diffracting medium. Although the physics that determines the final measured response is different for DAFS and crystallography, the structural parameters determined by either technique should agree with the true nature of the sample and ultimately with each other.

The one-dimensional R-space Fourier components of the resonance fine structure depend on the relative positions of the neighboring atoms and thus contain information about the bond lengths between the resonant atom and its neighbors. The three-dimensional **R**-space Fourier components of integrated Bragg peak intensities depend on the electron density autocorrelation function, and thus contain information about the positions of the atoms within the unit cell. Since the bond length is defined as $R = |\mathbf{R}_2 - \mathbf{R}_1|$, the information contained in the XAFS cannot be independent of the information contained in the diffraction intensities. The DAFS weighted fine structure contains information about both positions and bond lengths, therefore it should be possible to constrain the DAFS model parameters to account for both the fine structure and the integrated intensities of the Bragg peaks.

Building the analysis tools for co-refinement of every one of the structural parameters that are common to both XAFS and crystallography is beyond the scope of this thesis, but there are several interesting and useful things that can be done with existing XAFS analysis programs and a simple understanding of x-ray diffraction. If the sublattice of resonant atoms has a center of symmetry parallel to $\mathbf{Q}$, DAFS data can be solved as a simple quadratic for the contribution from the resonant atoms. The results are a pair of weighted response functions, denoted throughout this work as f'_{w} and f''_{w}, that depend on the long-range order of the resonant atoms as well as on their local environment. The response functions from atoms sitting in equivalent sites are identical. If there are n inequivalent sites within the unit cell then f'_{w} and f''_{w} are of the form

$$f'_{\mathrm{w}}(\mathbf{Q}, E) = \sum_{j=1}^{n} W_j(\mathbf{Q}) f'_j(E) \tag{1.13}$$

and

$$f''_{\mathrm{w}}(\mathbf{Q}, E) = \sum_{j=1}^{n} W_j(\mathbf{Q}) f''_j(E), \tag{1.14}$$

where the weighting coefficients W_j are

$$W_j(\mathbf{Q}) = \frac{\sum_{i_j} e^{i\mathbf{Q}\cdot\mathbf{R}_{i_j}} e^{-M_{i_j}}}{\sum_{i=1}^{m} e^{i\mathbf{Q}\cdot\mathbf{R}_i} e^{-M_i}} \tag{1.15}$$

summing in the numerator over all of the resonant atoms in the j^{th} site and in the denominator over all of the resonant atoms in the unit cell. Equations (1.13) and (1.14) contain crystallographic information about the sublattice of resonant atoms. When there is only one type of resonant site, the weighting coefficients are trivially unity for all Bragg reflections. In materials with resonant atoms at several inequivalent sites, the amount of fine structure from each site changes with $\mathbf{Q}$. The DAFS fine-structure functions are defined by

$$\chi'_{\mathrm{w}}(\mathbf{Q}, E) = \frac{f'_{\mathrm{w}}(\mathbf{Q}, E) - f'_a(E)}{\Delta f''_0(E_0)} \tag{1.16}$$

and

$$\chi''_{\mathrm{w}}(\mathbf{Q}, E) = \frac{f''_{\mathrm{w}}(\mathbf{Q}, E) - f''_a(E)}{\Delta f''_0(E_0)} \tag{1.17}$$

normalized to the step height in $f''_0(E)$ at the edge. These mixed fine-structure functions can be fit using the same analysis programs as the XAFS $\chi(E)$, subject to the constraint that the mixture of χ''_1, χ''_2, ..., from the individual sites (site$_1$, site$_2$, ...), depends on $\mathbf{Q}$. In this manner, the positions of the resonant atoms within the unit cell become fitting parameters and the W_j are determined from the *en masse* fit to the fine structure in the extended energy region. The inverse of the matrix of mixing coefficients, determined by standard linear techniques, is applied to the set of $f_{\mathrm{w}}(\mathbf{Q}, E)$ to obtain f'_j and f''_j for each resonant site separately, including the XANES region. This type of constrained fitting and data inversion is demonstrated in Chapter 6 and appendix D using the (00ℓ) DAFS from a thin film of $YBa_2Cu_3O_x$. The example there is worked out in detail so that the interested reader will be able to adapt the method to other similar problems.

1.4 When is DAFS the right experimental technique?

Considering all of the differences between crystallography, XAFS and DAFS, and the time and effort involved in making a DAFS experiment as compared to other well-established techniques, it is appropriate to address the question of when DAFS is applicable. Certainly in most cases of crystalline materials, normal diffraction and crystallography will provide all of the information about the structure that is needed. Indeed, all of the DAFS analysis presented in this thesis makes use of information obtained from crystallographic studies to generate the structure factor model and for the FEFF fine-structure calculations. If the material is amorphous[3], then XAFS is useful for studying the local environment of the resonant atoms, but there is no obvious advantage to using DAFS. In cases where the material is crystalline but the local order is different from the long-range order, then DAFS has the advantage over XAFS *only* when there are competing fine-structure signals, such as from the two Cu sites in $YBa_2Cu_3O_x$, or in the case of mixed powders or multilayers. In particular, DAFS can provide the site-specific near-edge spectrum which often exhibits features that are not calculated by *ab initio* theoretical XAFS codes.

---

[3] Note that I am not excluding the case of quasi-crystals here. These may be a very interesting subject for a DAFS experiment—one of the benefits of working with DAFS is that since the technique is new almost any experiment you might think of trying has not been tried before.

1.5 Organization

The chapters are arranged with the intent of leading a DAFS initiate through the conceptual and technical steps needed to understand and analyze DAFS data: from the Feynman diagrams for quantum electrodynamics to the details of the synchrotron experiments, and, finally, to the determination of real structural parameters. Chapter 2 develops the theoretical background for the origins of DAFS fine structure using results from non-relativistic quantum mechanics in order to clarify the relationship between DAFS and XAFS. The crystallographic aspects of DAFS are presented in Chapter 3. Out of the crystallographic structure factor and the Bragg condition come some of the most valuable applications of DAFS, the *site selectivity* and *spatial selectivity* mentioned earlier in this introduction. In Chapter 4, the experimental methods used to collect DAFS data are described. In Chapter 5, the DAFS analysis techniques, specific models, and computer algorithms are described in as much detail as possible without sending the gentle reader out the window screaming for a cocktail.

In Chapter 6, constrained fitting with the program FEFFIT is used to determining the DAFS weighting coefficients from the results of KKFIT on the DAFS from eight specular reflections of $YBa_2Cu_3O_{6.8}$. The matrix of coefficients found by FEFFIT is inverted and applied to separate the resonant scattering amplitudes $\Delta f(E)$ from the two inequivalent copper sites, including the XANES region. The iterative Kramers-Krönig algorithm used by KKFIT is carefully studied in Chapter 7. Using simulated DAFS data, calculated by FEFF and FEFFIT, the reliability of the algorithm is tested with special attention paid to the effects on the material structural parameters determined from the Fourier components of the fine structure. Finally, in Chapter 8, some ideas for other experiments are presented and general comments are made about the applicability and usefulness of DAFS as an experimental technique.

There are also four appendices to help the reader interested in trying some of the methods presented here. Appendix A gives the conversion factors for translating $f''(E)$ into $\mu(E)$. Appendix B describes the application of FEFF and FEFFIT to calculate DAFS data. Appendix C and Appendix D give the FEFFIT input files used for fitting the DAFS fine-structure in Chapters 6 and 7, respectively. The Pascal source codes for KKFIT are freely available upon request from the author [36].

Chapter 2

X-RAY RESONANCE FINE STRUCTURE

If you want to learn something quantitative about the physical properties of a material using DAFS—or any other experimental technique—you need to know, in a quantifiable way, how the signal you measure depends on the properties you want to determine. A DAFS experiment measures the diffraction peak intensity of elastically scattered x-rays as a function of the photon energy. The x-ray scattering intensity is proportional to the square of the scattering amplitude which is the probability amplitude that an incident photon from the source will evolve, via its interaction with the material, to the photon that is registered at the detector. While it is unlikely that many of my gentle readers will need to calculate the matrix elements for photoelectron backscattering themselves, they should still want to know how the theoretical models used to calculate resonant scattering amplitudes are constructed. They will also want to know what assumptions and approximations were made in order to perform the calculations, whether these were sensible assumptions, and finally how modifications to the exact theory affect the final output of their analysis efforts: the local structural parameters of some mysterious diffracting material.

The goal of this chapter is to convey a basic understanding of the theoretical aspects of resonant x-ray scattering and x-ray absorption which are prerequisite to developing a sensible approach to DAFS analysis. My strategy for analyzing the spectral content of DAFS is to use as many of the existing XAFS analysis tools as possible. With this in mind, it is important to understand completely the relationship between DAFS and XAFS. Once the common nature of the fine structure is understood, it is also necessary to understand the crystallographic aspect of DAFS. The ways in which the fine structure signals from a collection of resonantly scattering atoms are combined in the Bragg peak intensities is the topic of Chapter 3. This knowledge can then be applied to the problem of unraveling the fine structure signals from a subset of the resonant atoms in materials with multiple inequivalent resonant sites based on their long-range order and, at the same time, solving for the crystallographic parameters associated with the sublattice of the resonant atoms.

In order to understand the behavior of the elastic scattering intensity near an atomic resonance, it is necessary to consider both the individual signal from any one of the resonant atoms and the collective signal from all of the atoms in the material. This chapter develops the equations for the scattering amplitude from a bound atomic electron in the presence of neighboring atoms. Section 2.1.2 presents a summary of the results from non-relativistic quantum electrodynamics that are germane to DAFS. These results are used in Sections 2.1.3 and 2.1.4 to obtain the matrix elements for resonant x-ray scattering and x-ray absorption. The relationship between the fine structure in DAFS and XAFS is most easily understood by comparing the matrix elements for the x-ray elastic scattering amplitude with the matrix elements for x-ray absorption. The fine structure in the absorption cross section is shown to be equivalent to the imaginary part of the complex fine structure in the scattering amplitude in the forward direction, consistent with the optical theorem. Chapter 3 uses these results in combination with the intensity formulae for kinematic diffraction to develop a model that can be used for computer analysis of DAFS data.

2.1 The interaction of light and matter

Light is an electromagnetic phenomenon, whether we prefer to think of it as waves or particles or as some fuzzy combination of both. When a charged particle is placed in an electric field it feels a force that is proportional to both the magnitude of the charge and the magnitude and direction of the electric field $\mathbf{F} = q\mathbf{E}$, and accelerates accordingly. As the charged particle accelerates it must also radiate. This is the essence of classical light scattering from matter, and all of the incredible variety of observed optical effects have their origins in it.

This section covers the classical and quantum mechanical descriptions of the energy dependent atomic scattering amplitude. While I make no direct use of the classical Lorentz dispersion formula for anomalous scattering, it is the conceptual basis for the quantum mechanical description and is helpful for understanding the simple physics. In the discussion of the classical model I will denote the frequency dependent scatting amplitude by $f(\omega)$, rather than $f(E = \hbar\omega)$, in keeping with the standard development of these formulae. The atomic scattering amplitude is part of a general class of functions called *response functions* which describe the response of a physical system to some external stimulus. There are numerous response functions in electrodynamics, such as the index of refraction, the dielectric constant, the elec-

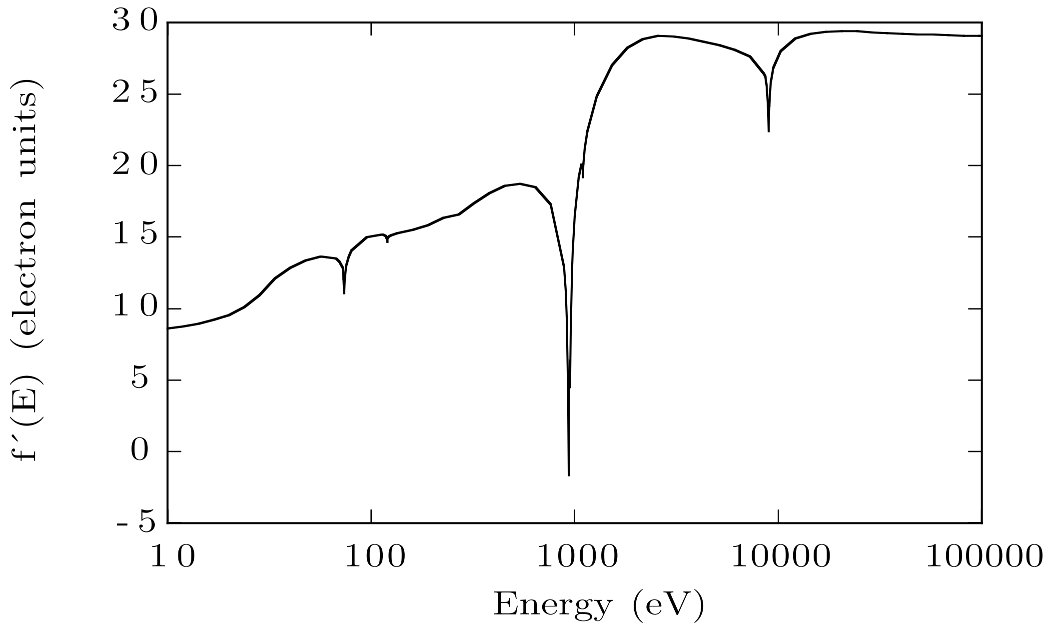

Figure 2.1: The real part of the light scattering amplitude from atomic copper as a function of energy over four decades. The regions where the energy derivative of the scattering amplitude is negative were historically labeled *anomalous*. This lineshape can be quantitatively explained by considering the bound atomic electrons to be classical damped, driven resonators responding to the electric field of the incident light.

tric susceptibility, and the polarizability, which are all interconnected by a chain of equations that is endlessly fascinating. For the discussion of the relationship between DAFS and XAFS I will only be working with the x-ray scattering amplitude and x-ray absorption cross-section.

2.1.1 Classical resonant scattering

With the exception of a few small regions, the amplitude for light scattering from any material is a monotonic increasing function of the frequency[1], levelling off to a constant value as $\omega \to \infty$, as shown in Figure 2.1. As is often the case, however, it

[1] A monotonic increase in the amplitude is in keeping with the almost universal convention that defines the Thomson scattering amplitude as positive and the real part of the anomalous correction to f_0 as a negative cusp. In quantum electrodynamics, however, the Thomson scattering amplitude is negative, and the correction is positive, and must be so in order to satisfy both the optical theorem and causality.

is exactly those small regions where the scattering amplitude misbehaves that have proven the most valuable in furthering our understanding of its nature. Almost all of the physics of dispersion, including the *anomalous* behavior near an electronic resonance, may be understood by considering the atomic electrons to be elastically bound to their nuclei by harmonic forces and acted on by the time dependent electric field of the incident radiation. This simple picture yields an equation of motion for each oscillator

$$m\left(\ddot{\mathbf{r}} + \gamma\dot{\mathbf{r}} + \omega_0^2\mathbf{r}\right) = -e\mathbf{E}(\mathbf{r}, t) \tag{2.1}$$

with γ accounting for a phenomenological damping force, and $\mathbf{r}$ taken to be the separation between the bound electron and the center of mass of the atom. To understand the behavior of the electron under the influence of the incident radiation, it is sufficient to consider the effects of a single Fourier component of the electric field, $\mathbf{E}_0(\mathbf{r})e^{-i\omega t}$. Then the standard ansatz for the steady-state position of the electron, $\mathbf{r}(t) = \mathbf{r}_0 e^{-i\omega t}$, in Equation (2.1) gives the frequency dependence of the electron's displacement as

$$\mathbf{r}(t) = \frac{-e}{m}\frac{\mathbf{E}_0(\mathbf{r})e^{-i\omega t}}{\omega_0^2 - \omega^2 - i\omega\gamma}, \tag{2.2}$$

as well as the time dependent dipole moment $\mathbf{P}(t) = -e\mathbf{r}(t)$ which is parallel to the incident electric field vector.

The atomic form factor[2] is defined as the ratio of the scattering amplitude from a single atom to the scattering amplitude A from a classical free electron under the same conditions. For a dipole oscillating with frequency ω, the outgoing amplitude at a distant observation point depends on the magnitude of the periodic moment at an earlier time $t_r = t - |\mathbf{R}|/c$, and on the angle θ between $\mathbf{R}$ and the dipole axis

$$A = \frac{\omega^2}{c^2}\frac{\mathbf{p}}{|\mathbf{R}|}\sin^2\theta = \frac{e^2}{mc^2}\frac{\omega^2\sin^2\theta}{\omega_0^2 - \omega^2 + i\omega\gamma}\frac{\mathbf{E}e^{-i\omega t}}{|\mathbf{R}|}. \tag{2.3}$$

The scattering amplitude from a single free electron A_e is obtained by letting the restoring force go to zero in the absence of damping

$$\lim_{\omega_0\to 0} A_e = -\frac{e^2}{mc^2}\frac{\mathbf{E}e^{-i\omega t}}{|\mathbf{R}|}\sin^2\theta. \tag{2.4}$$

[2] This quantity is also found in the literature as the *atomic scattering factor*. It differs from the atomic scattering amplitude only by a factor of e/mc^2 and outside of this short digression into classical electrodynamics I will use the same symbol $f(E)$ explicitly for the atomic scattering amplitude, including the factor of e/mc^2. I apologize for any confusion this may cause.

The classical atomic form factor for an atom with a single bound electron with characteristic frequency ω_0 is thus:

$$f(\omega) = \frac{A}{A_e} = \frac{-\omega^2}{\omega_0^2 - \omega^2 + i\omega\gamma}. \tag{2.5}$$

For scattering from an atom with n_j electrons having resonance frequency ω_j, the total form factor in the forward direction[3] is the sum

$$f(\omega) = \sum_j \frac{n_j \omega^2}{\omega^2 - \omega_j^2 - i\omega\gamma_j} \tag{2.6}$$

where the coefficients n_j satisfy the oscillator strength sum rule

$$\sum_j n_j = Z \tag{2.7}$$

for the total number of electrons in the atom. The scale of the response at resonance is set by n and γ, and can be quite dramatic, as in Figure 2.1.

This straightforward model describes an atom as a collection of damped harmonic oscillators driven by the electric field of the incident radiation. Equation (2.6), sometimes called the *Lorentz dispersion formula* [25, 97], is completely adequate for describing both the monotonic behavior of the scattering amplitude and its dramatic changes near a resonance frequency. However, it cannot account for the small, rapid oscillations that are observed in x-ray diffraction and x-ray absorption just above a core-state resonance. This energy-dependent fine structure is due to the wave nature of the electron that is excited by the incident radiation, and so it must be described and calculated in the language of quantum mechanics.

2.1.2 Nonrelativistic quantum electrodynamics

Before crossing the border into Hilbert space, it is helpful to have a picture of the physics we are trying to describe. Some of my readers may relate to the one in Figure 2.2, whose story goes as follows. When a photon is absorbed by an atom, the atom is left in an excited state. If the photon has sufficient energy, it may cause an electron to be ejected from the atom. As the ejected photoelectron travels

[3] I have left out the angular dependence of the scattering to keep the discussion simple. Away from the forward direction, scattering from each of the electrons will be slightly out of phase, causing f to decrease as the scattering angle increases at fixed wavelength [115].

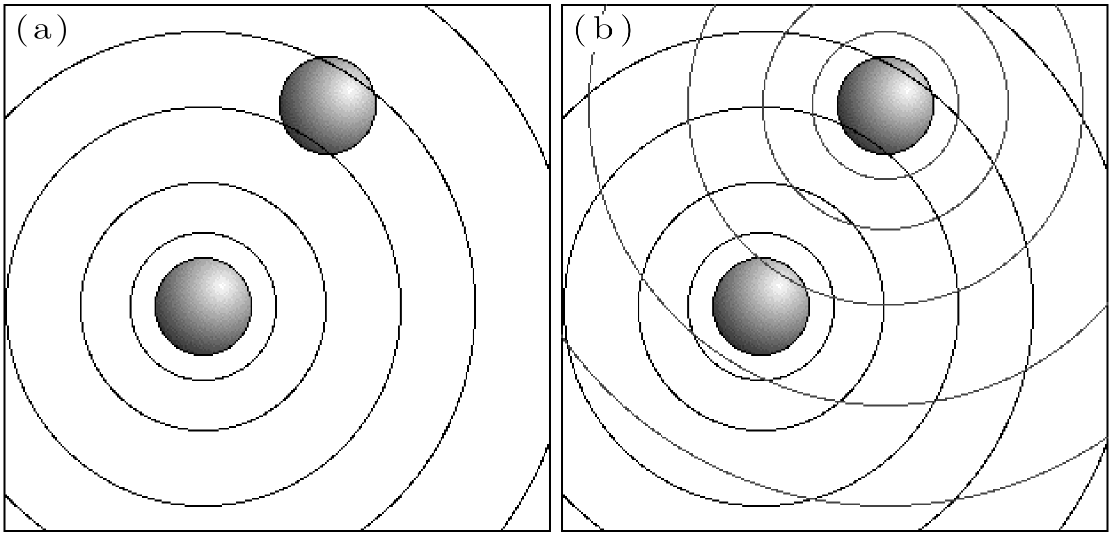

Figure 2.2: A simple picture illustrates the origin of the resonance fine structure. (a) An ejected photoelectron propagates outward as a spherical wavefront from the excited atom, the nodes of the waves are indicated by the circles. (b) Part of the wave backscatters from a neighboring atom and interferes with the original wave. Interference at the source modulates the interaction amplitude and this modulation is visible in the scattering and absorption cross sections.

outward, its probability amplitude is described by an outgoing spherical wave. As this outgoing wave expands, it can scatter off of other atoms in the vicinity of the original atom. The backscattered part of this wave that returns to the source of the original outgoing wave will interfere with the outgoing wave and thus modulate the absorption amplitude. This modulation is the fine structure we observe in x-ray absorption, and it is very sensitive to the distances between the resonant atom and its neighbors, as well as to the charge distribution of the resonant atom and the shape of the interatomic potential that it travels across.

For those among my readers who find the idea of a backscattered wave interfering with itself at the source unsettling, there is an alternate way to describe the physics. When an electron is promoted out of its ground state, it needs to go into a final state that satisfies conservation of energy, within the small uncertainty set by the lifetime of the hole that it leaves. The probability for absorption as a function of energy depends on the density of final states $\rho(E)$ available to the outgoing photoelectron at that particular energy. The function $\rho(E)$ is determined by the boundary conditions of the whole system. For an isolated atom, the energy dependence of $\rho(E)$ for $E > E_{Fermi}$ goes as E^2, which is featureless. For an absorber embedded in a solid, however, the boundary conditions change and $\rho(E)$ develops structure that depends on the numbers, distances and valence states of the neighboring atoms. Thus the probability of absorption is slightly higher when the energy of the outgoing photoelectron puts it into a final state that satisfies the additional boundary conditions imposed by the neighbors, and slightly smaller otherwise.

An x-ray scattering event described by quantum electrodynamics is a sum over all possible ways the process can occur, *i.e.*, of 1) the probability for absorption of the incident photon followed closely by emission of the outgoing photon and 2) the probability of emission of the outgoing photon followed closely by absorption of the incident photon—this second case being plausible only because in quantum electrodynamics there is some range of time ($t \approx \hbar/2E$) below which we can know nothing about the system without collapsing the wavefunction. During the small amount of time between the vanishing of the initial state and the appearance of the final state, the resonant atom exists in an excited intermediate state. When the energy of the incident photon is large enough to promote a bound electron up into an empty orbital, or into the continuum, the intermediate state of the atom is a *virtual* photoelectron, called virtual because it is not observed (detected) as physical electron, but by its interference signature. During its short lifetime, this virtual photoelectron can probe its local environment in the same manner as the real photoelectron does in absorption.

The following development of the matrix elements for x-ray absorption and for resonant elastic scattering is intended to demonstrate that the fine structure due to a real photoelectron and the fine structure due to a virtual photoelectron have exactly the same information content.

The nonrelativistic Hamiltonian

The interaction Hamiltonian between bound electrons and the quantized radiation field is obtained by replacing the usual particle momentum operator $\mathbf{p}$ by $\mathbf{p} - e\mathbf{A}/c$, where $\mathbf{A}$ is the quantized vector potential field operator acting at the space-time location $(\mathbf{r}, t)$. The quantized field is expressed in terms of creation and annihilation operators $a^{\dagger}_{\mathbf{k},\alpha}$ and $a_{\mathbf{k},\alpha}$, respectively, for photons with wavevector $\mathbf{k}$ and polarization

α:

$$\mathbf{A}(\mathbf{r},t) = \frac{1}{\sqrt{V}} \sum_{\mathbf{k}} \sum_{\alpha} c\sqrt{\frac{\hbar}{2\omega}} \left[a_{\mathbf{k},\alpha} \hat{\mathbf{e}}^{(\alpha)} e^{i\mathbf{k}\cdot\mathbf{r}-i\omega t} + a^{\dagger}_{\mathbf{k},\alpha} \hat{\mathbf{e}}^{(\alpha)} e^{-i\mathbf{k}\cdot\mathbf{r}+i\omega t} \right]. \tag{2.8}$$

The sums $\mathbf{k}$ and α are for all of the photons of the field, and the electromagnetic field is an ocean of photons blinking in and out of existence as they communicate the locations and activities of the charged particles. The normalization volume V comes from the assumption of periodic boundary conditions in the conversion from classical electrodynamics to quantum electrodynamics, and always goes away in the final calculation of real scattering cross sections by virtue of division by the incident flux density. This experimentalist prefers to eschew such abstractions without capable guidance from a high priest of quantum mechanics [27] or before cocktails.

The physical system is comprised of atoms and a radiation field, and the total Hamiltonian contains terms that operate only on the atoms, only on the field, and interaction terms that act on both

$$H = H_{\text{atom}} + H_{\text{int}} + H_{\text{rad}} = H_0 + H_{\text{int}}. \tag{2.9}$$

Since we are interested in photon-atom scattering, we need only consider the interaction Hamiltonian, which is given by [26]

$$H_{\text{int}} = \sum_j \left[-\frac{e}{2m_e c} \left(\mathbf{p}_j \cdot \mathbf{A}(\mathbf{r}_j,t) + \mathbf{A}(\mathbf{r}_j,t) \cdot \mathbf{p}_j \right) + \frac{e^2}{2m_e c^2} \mathbf{A}(\mathbf{r}_{\text{j}},t) \cdot \mathbf{A}(\mathbf{r}_j,t) \right]. \tag{2.10}$$

For simplicity, I have not included the two magnetic terms [28]. The operator $\mathbf{p}_j = -i\hbar\nabla_j$ acts on the coordinates $\mathbf{r}_j$ of the j^{th} atomic electron. In the radiation gauge, $\nabla \cdot \mathbf{A} = 0$ so that $\mathbf{p}_j$ commutes with $\mathbf{A}$, and Equation (2.10) can be simplified using $\mathbf{p}_j \cdot \mathbf{A} = \mathbf{A} \cdot \mathbf{p}_j$.

In the absence of the interaction terms, the eigenstates of H_0 are atoms and photons, and the resulting Hilbert space is a direct product space between the atomic state vectors and the radiation state vectors. In the presence of H_{int} the system will have a different set of eigenstates which, in general, cannot be determined exactly. The standard solution to this problem when the interaction is weak is to look only at the lowest order effects of H_{int} on the system, and to expand the eigenstates of H in terms the solutions of H_0 and powers of H_{int}. The question that we are ultimately interested in answering with these new wavefunctions is this: if I start initially with an atom in state $|\Psi_i\rangle$ and a photon in state $|\mathbf{k},\alpha\rangle$, what is the amplitude for ending up with an atom in state $|\Psi_{\mathrm{f}}\rangle$ and a photon in state $|\mathbf{k}', \alpha'\rangle$ due to the presence of H_{int}.

Time dependent perturbation theory

In the absence of an interaction term, the eigenstates $|\Psi_0; \mathbf{k}, \alpha\rangle$ of H_0 evolve in time according to the time dependent Schrödinger equation

$$i\hbar\partial/\partial t|\Psi_0; \mathbf{k}, \alpha\rangle = H_0|\Psi_0; \mathbf{k}, \alpha\rangle. \tag{2.11}$$

However, once H_{int} has been turned on, the system evolves according to

$$i\hbar\partial/\partial t|\Psi; \mathbf{k}, \alpha\rangle = (H_0 + H_{\mathrm{int}})|\Psi; \mathbf{k}, \alpha\rangle, \tag{2.12}$$

where $|\Psi\rangle \neq |\Psi_0\rangle$ is an eigenstate of the new Hamiltonian. It is usually not possible to solve Equation (2.12) in closed form, but if H_{int} is small, the changes in $|\Psi_0; \mathbf{k}, \alpha\rangle$ should also be small. Most of the time dependence of the state vectors is due to the effects of H_0 and this part of the time dependence can be taken out of the wavefunctions explicitly by defining a new set of state vectors

$$|\Psi(t); \mathbf{k}, \alpha\rangle = e^{-iH_0t/\hbar}|\Psi; \mathbf{k}, \alpha\rangle. \tag{2.13}$$

This causes H_0 to drop out of the right hand side of Equation (2.12), and the time dependence of the state vectors is determined by the differential equation

$$\begin{aligned} i\hbar\partial/\partial t|\Psi(t); \mathbf{k}, \alpha\rangle &= H_{\mathrm{int}}(t)|\Psi(t); \mathbf{k}, \alpha\rangle \\ &= e^{iH_0t/\hbar}H_{\mathrm{int}}e^{-iH_0t/\hbar}|\Psi(t); \mathbf{k}, \alpha\rangle. \end{aligned} \tag{2.14}$$

Integrating both sides of Equation (2.14) with respect to time from the time that H_{int} is turned on at $t' = 0$ until the observation time t gives a recursive expression for $|\Psi(t); \mathbf{k}, \alpha\rangle$

$$|\Psi(t); \mathbf{k}, \alpha\rangle = |\Psi(0); \mathbf{k}, \alpha\rangle + \frac{1}{i\hbar}\int_0^t dt' H_{\mathrm{int}}(t')|\Psi(t'); \mathbf{k}, \alpha\rangle. \tag{2.15}$$

The first order solution for $|\Psi(t); \mathbf{k}, \alpha\rangle$ is found by letting $|\Psi(t'); \mathbf{k}, \alpha\rangle = |\Psi(0); \mathbf{k}, \alpha\rangle$ inside the integral. The second order solution is found by substituting the first order solution, and so on for higher orders in the approximation. In most applications, only the first order term is considered. For resonant x-ray scattering it is necessary to consider both the first and second order terms in the perturbation series.

The time-dependent probability of a transition from the initial state to the final state is

$$\mathrm{P}_{i\to f} = |\langle \Psi_f(t); \mathbf{k}, \alpha | \Psi_i(t); \mathbf{k}, \alpha\rangle|^2, \tag{2.16}$$

which can be found to any order in H_{int} using Equation (2.15). Note that for the interaction Hamiltonian in electrodynamics, the time dependence of the quantized field operator is separable. In the case of absorption of a single incident photon, only the annihilation operator for that photon will couple the initial and final states. The time dependence of $\mathbf{A}$ is $e^{-i\hbar\omega t}$, and the first order transition amplitude is given by

$$\begin{aligned}\langle \Psi_f(t)|\Psi_i(t)\rangle &= \frac{1}{i\hbar}\int_0^t dt' \langle \Psi_f(t)|H_{\text{int}}(t')|\Psi_i(0)\rangle \\ &= \frac{1}{i\hbar}\int_0^t dt' \langle \Psi_f(0)|H'_{\text{int}}|\Psi_{\rm i}(0)\rangle e^{i(E_f - E_i)t'/\hbar} \\ &= \frac{1}{i\hbar}\langle \Psi_f|H'_{\text{int}}|\Psi_i\rangle \int_0^t dt' e^{i(E_f - E_i - \hbar\omega)t'/\hbar},\end{aligned} \tag{2.17}$$

with H'_{int} explicitly time independent. The time integral of the exponential gives a delta function as $t \to \infty$ since

$$\lim_{t\to\infty} \int_0^t \frac{dt'}{2\pi} e^{i\omega t'} = \delta(\omega) \tag{2.18}$$

and the first order transition probability per unit time to a specific final state $|\Psi_f(t)\rangle$ is given by

$$\frac{|\langle \Psi_f(t)|\Psi_i(t)\rangle|^2}{t} = \frac{2\pi}{\hbar}|\langle \Psi_f(0)|H'_{\text{int}}|\Psi_i(0)\rangle|^2 \delta(E_f - E_i \pm \hbar\omega) \tag{2.19}$$

with the minus sign corresponding to absorption and the plus sign corresponding to emission. The total probability for a transition into the collection of final states is the sum of Equation (2.19) over all of the allowed final states $|\Psi_f\rangle$.

2.1.3 Elastic x-ray scattering

Light scattering from an atom interacts with all of the charged particles, the electrons and the protons, in the atom. However, because the mass of the particle appears in the denominator of the oscillator strength, only the interaction with the electrons normally needs to be considered. In order to calculate the matrix elements for scattering, you need a set of eigenstates for the ground states of the atoms. Unfortunately, physics has yet to provide an exact solution even for the three body problem, let alone something as complicated as a copper atom. The methods for working around this deficiency have developed into a form of high art, and the reader interested in learning about *a priori* calculations of resonance fine structure is directed to papers by Rehr and co-workers [31] and references therein, or to the dissertations of various graduate students who have worked on the FEFF project [32–34].

For the discussion at hand, the most important simplification is to treat the scattering from each atomic electron separately. This assumes that any many body effects can be accounted for independently of the one-electron matrix element calculations. Single electron states are isolated using the method of Slater determinants, which properly accounts for the overall symmetry properties of the true multi-electron state under Fermi-Dirac statistics. The complicated electron cloud surrounding a real atom is thus approximated by a collection of properly symmetrized single electron states and the scattering from each one is treated independently. The n electron state $|\Psi\rangle \equiv |\Psi(1\ldots n)\rangle$ is replaced by the direct product of a single electron state $|\psi\rangle$ and the symmetrized $n-1$ electron state [37]

$$|\Psi(1\ldots n)\rangle = |\psi\rangle \otimes |\Psi(1\ldots n-1)\rangle. \tag{2.20}$$

The matrix elements for scattering from an atom then reduce to

$$\langle\Psi(1\ldots n)|H_{\text{int}}|\Psi(1\ldots n)\rangle = \langle\psi|H_{\text{int}}|\psi\rangle\langle\Psi(1\ldots n-1)|\Psi(1\ldots n-1)\rangle \tag{2.21}$$

which must be summed over the individual electron states. In the absence of many-body effects, $\langle\Psi(1\ldots n-1)|\Psi(1\ldots n-1)\rangle$ is unity. Calculation of the overlap for the non-interacting electrons is still a hot topic in the universe of XAFS theory.

Kramers-Heisenberg-Waller matrix elements

When light scatters from a bound atomic electron, the initial state of the system is an atom in some state $|\Psi_i\rangle$, and a photon in state $|\mathbf{k}, \alpha\rangle$. After the scattering, the final state of the system is an atom in a state $|\Psi_f\rangle$, and an outgoing photon in state $|\mathbf{k}', \alpha'\rangle$. We are interested in the case where is no net change in the total number of photons, therefore the only terms in the perturbation series which will give nonvanishing matrix elements of H_{int} are those that annihilate the incident photon and create the outgoing photon. To first order in the perturbation expansion, only $\mathbf{A} \cdot \mathbf{A}$ contributes to the transition probability because this term contains the combinations $aa^\dagger$ and $a^\dagger a$.

Notice however that $\mathbf{A}\cdot\mathbf{A}$ is on the same scale as $(\mathbf{p}\cdot\mathbf{A})^2$ in powers of e/mc, so that the second-order matrix elements of H_{int} can be as large as the $\mathbf{A}\cdot\mathbf{A}$, and they need to be considered as well.

Neglecting all many-body effects between the bound atomic electrons, the first order matrix element in the argument of Equation (2.17) for a single bound electron located at $\mathbf{r}$ is

$$\begin{aligned}
\mathrm{M}_{(1)} &= \frac{1}{i\hbar}\int_0^t dt' \langle\psi_f;\mathbf{k}',\alpha'|H_{\text{int}}|\psi_i;\mathbf{k},\alpha\rangle e^{i(E_f-E_i)t'/\hbar} \qquad (2.22)\\
&= \frac{1}{i\hbar}\int_0^t dt' \langle\psi_f;\mathbf{k}',\alpha'|\frac{e^2}{2m_ec^2}\mathbf{A}\cdot\mathbf{A}|\psi_i;\mathbf{k},\alpha\rangle e^{i(E_f-E_i)t'/\hbar}\\
&= \frac{1}{i\hbar}\frac{e^2}{2m_ec^2}\frac{c^2\hbar}{2V\sqrt{\omega\omega'}}\langle\psi_f|2\hat{\mathbf{e}}^{*(\alpha')}\cdot\hat{\mathbf{e}}^{(\alpha)}e^{i(\mathbf{k}-\mathbf{k}')\cdot\mathbf{r}}|\psi_i\rangle\int_0^t dt' e^{i(\hbar\omega'+E_f-\hbar\omega-E_i)t'/\hbar}
\end{aligned}$$

using Equation 2.8 for $\mathbf{A}(\mathbf{r},t)$. In second order scattering, we have to allow for the fact that the final state of the first interaction may evolve in the small amount of time before the second interaction occurs. Contributions from all intermediate states need to be considered, and the second-order matrix element must include a sum over the intermediate states of the excited electron. The second-order term in the perturbation series of Equation (2.17) is [26]

$$\begin{aligned}
\mathrm{M}_{(2)} &= \frac{1}{(i\hbar)^2}\left(\frac{-e}{m_ec}\right)^2\int_0^t dt'\int_0^{t'} dt''\sum_c\sum_{\mathbf{k}',\alpha''}\langle\psi_f;\mathbf{k}',\alpha'|\mathbf{p}\cdot\mathbf{A}|\psi_c;\mathbf{k}'',\alpha''\rangle e^{i(E_f-E_c)t'/\hbar}\times\\
&\qquad \langle\psi_c;\mathbf{k}'',\alpha''|\mathbf{p}\cdot\mathbf{A}|\psi_i;\mathbf{k},\alpha\rangle e^{i(E_c-E_i)t''/\hbar}\\
&= -\frac{1}{i\hbar}\frac{c^2\hbar}{2V\sqrt{\omega\omega'}}\left(\frac{e}{mc}\right)^2\sum_c\left[\frac{\langle\psi_f|\mathbf{p}\cdot\hat{\mathbf{e}}^{*(\alpha')}e^{-i\mathbf{k}'\cdot\mathbf{r}}|\psi_c\rangle\langle\psi_c|\mathbf{p}\cdot\hat{\mathbf{e}}^{(\alpha)}e^{i\mathbf{k}\cdot\mathbf{r}}|\psi_i\rangle}{E_c-E_i-\hbar\omega}\right.\\
&\qquad\left.+\frac{\langle\psi_f|\mathbf{p}\cdot\hat{\mathbf{e}}^{(\alpha)}e^{i\mathbf{k}\cdot\mathbf{r}}|\psi_c\rangle\langle\psi_c|\mathbf{p}\cdot\hat{\mathbf{e}}^{*(\alpha')}e^{-i\mathbf{k}'\cdot\mathbf{r}}|\psi_i\rangle}{E_c-E_i+\hbar\omega'}\right]\times \qquad (2.23)\\
&\qquad\int_0^t dt'' e^{i(E_f-E_i+\hbar\omega'-\hbar\omega)t''/\hbar}
\end{aligned}$$

For elastic scattering, the final state of the atom is the same as the initial state $|\Psi_f\rangle = |\Psi_i\rangle$. The outgoing photon has the same energy as the initial photon, but it can go out in any direction. $\omega' = \omega = |\mathbf{k}|c$. The total amplitude for scattering as a function of time is

$$M = \mathrm{M}_{(1)} + \mathrm{M}_{(2)}. \qquad (2.24)$$

The squared magnitude of M is formally integrated over all photon modes $\mathbf{k}'',\alpha''$, retaining only the initial and final state photons, to obtain the expression for the scattering probability. The time integral in Equation (2.17) brings down a factor of $\hbar/i$ along with the energy conserving delta function. The probability is normalized by the incident photon flux density, which eliminates the irksome volume term in the denominator and eliminates a factor of c, to produce the differential scattering cross section for elastic scattering:

$$\begin{aligned} \frac{d\sigma}{d\Omega} = & \Big| -r_0 \hat{\mathbf{e}}^{*(\alpha')} \cdot \hat{\mathbf{e}}^{(\alpha)} \sum_i \langle \psi_i | e^{i(\mathbf{k}-\mathbf{k}')\cdot\mathbf{r}} | \psi_i \rangle \\ & + \frac{r_0}{m} \sum_i \sum_c \left[\frac{\langle \psi_i | \mathbf{p} \cdot \hat{\mathbf{e}}^{*(\alpha')} e^{-i\mathbf{k}'\cdot\mathbf{r}} | \psi_c \rangle \langle \psi_c | \mathbf{p} \cdot \hat{\mathbf{e}}^{(\alpha)} e^{i\mathbf{k}\cdot\mathbf{r}} | \psi_i \rangle}{E_c - (E_i + \hbar\omega + \frac{1}{2} i \Gamma_c)} \right. \\ & \left. + \frac{\langle \psi_j | \mathbf{p} \cdot \hat{\mathbf{e}}^{(\alpha)} e^{i\mathbf{k}\cdot\mathbf{r}} | \psi_c \rangle \langle \psi_c | \mathbf{p} \cdot \hat{\mathbf{e}}^{*(\alpha')} e^{-i\mathbf{k}'\cdot\mathbf{r}} | \psi_i \rangle}{E_c - (E_i - \hbar\omega + \frac{1}{2} i \Gamma_c)} \right] \Big|^2 . \end{aligned} \tag{2.25}$$

Here the sum i is over all the electrons bound to the atom, and the sum c is over all possible intermediate states of the *virtual* photoelectron produces during the resonant scattering event. This form of the differential cross section should be compared to the classical formula Equation (2.6). The matrix elements in the numerator correspond to the scattering strengths $n_j\omega^2$ and energy denominator and damping terms are just the same as they are in the classical expression. Note that the energy denominator for the second term in Equation (2.25) is prevented from vanishing whenever the incident photon energy approaches a resonance energy of the bound electrons by the addition of $\frac{1}{2}i\Gamma_c$, in analogy with the classical equations. This term is included to account for the observed damping, and amounts to a small uncertainty in energy caused by the finite lifetime of the intermediate state. The damping effect is due to radiative and non-radiative processes. The radiative damping is due to resonance fluorescence from the elastic scattering process, Raman scattering, and characteristic fluorescence connected with inelastic scattering. The non-radiative part of the damping is due to autoionization and Auger decay [5].

Equation (2.25) is called the Kramers-Heisenberg formula [41], and the unsquared expression is called the Kramers-Heisenberg-Waller scattering amplitude [42]. The first part of the expression inside the absolute value signs is the Thomson scattering amplitude, which depends only on the change in the momentum transfer of the photon and not on the photon energy. Figure 2.3 shows the space-time Feynman diagrams that represent these three matrix elements. Figure 2.3(a) represents the first-order $\mathbf{A}\cdot\mathbf{A}$ matrix element and Figures 2.3(b) and 2.3(c) represent the two second-order $\mathbf{p}\cdot\mathbf{A}$ terms. In Figure 2.3(b), the incident photon is annihilated, leaving the atom

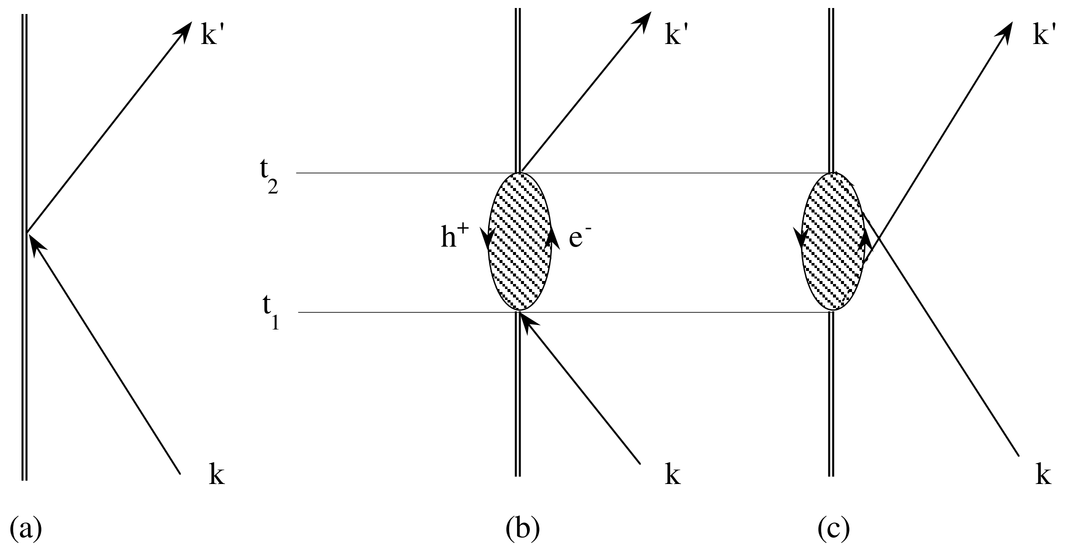

Figure 2.3: The Feynman diagrams for light scattering. A doubled line represents an atom, an arrow represents a photon. The hatching in (b) and (c) serves to represent the myriad intermediate states available to the short-lived excited state, between times t_1 and t_2.

in an excited state for a short period of time followed by creation of the outgoing photon. In Figure 2.3(c), the outgoing photon is created before the outgoing photon is annihilated. Note that at resonance, the energy denominator for the matrix element represented by Figure 2.3(b) is $-\frac{1}{2}i\Gamma_c$ compared to the denominator of the matrix element for Figure 2.3(c), which is $2\hbar\omega$. For the K-shell resonance, with $E_0 = 8980$ eV and $\Gamma_c = 2$ eV, the ratio of these two denominators is $\sim 6 \times 10^{-5}$

Resonant scattering amplitudes

The differential scattering cross section in Equation (2.25) may be written as the square of the scattering amplitude, and it is convenient to separate it explicitly into two terms, the Thomson scattering amplitude and the resonance correction to the Thomson scattering amplitude:

$$\begin{aligned} \frac{d\sigma}{d\Omega} &= |f(\mathbf{k}, \mathbf{k}', E)|^2 \\ &= |f_0(\mathbf{k} - \mathbf{k}') + \Delta f(\mathbf{k}, \mathbf{k}', E)|^2 \\ &= |f_0(\mathbf{k} - \mathbf{k}') + f'(\mathbf{k}, \mathbf{k}', E) + i f''(\mathbf{k}, \mathbf{k}', E)|^2. \end{aligned} \tag{2.26}$$

Here f' and f'' are the real and imaginary parts of the resonant scattering amplitude.

From Equation (2.25) and Equation (2.26), and using $\mathbf{k} - \mathbf{k}' = \mathbf{Q}$ for the momentum transfer, we obtain the following expressions. The Thomson scattering amplitude is

$$f_0(\mathbf{Q}) = -r_0 \hat{\mathbf{e}}^{*(\alpha')} \cdot \hat{\mathbf{e}}^{(\alpha)} \sum_i \langle \psi_i | e^{i(\mathbf{Q})\cdot\mathbf{r}} | \psi_i \rangle \tag{2.27}$$

and the resonant correction to the Thomson scatting is

$$\begin{aligned} \Delta f(\mathbf{k}, \mathbf{k}', E) &= f'(\mathbf{k}, \mathbf{k}', E) + i f''(\mathbf{k}, \mathbf{k}', E) \\ &= \left(\frac{e}{mc}\right)^2 \sum_i \sum_c \left[\frac{\langle \psi_i | \hat{\mathbf{e}}^{*(\alpha')} \cdot \mathbf{p} e^{-i\mathbf{k}'\cdot\mathbf{r}_i} | \psi_c \rangle \langle \psi_c | \hat{\mathbf{e}}^{(\alpha)} \cdot \mathbf{p} e^{i\mathbf{k}\cdot\mathbf{r}_i} | \psi_i \rangle}{E_c - (E_i + \hbar\omega + \frac{1}{2} i \Gamma_c)} \right. \\ &+ \left. \frac{\langle \psi_i | \hat{\mathbf{e}}^{(\alpha)} \cdot \mathbf{p} e^{i\mathbf{k}\cdot\mathbf{r}_i} | \psi_c \rangle \langle \psi_c | \hat{\mathbf{e}}^{*(\alpha')} \cdot \mathbf{p} e^{-i\mathbf{k}'\cdot\mathbf{r}_i} | \psi_i \rangle}{E_c - (E_i - \hbar\omega + \frac{1}{2} i \Gamma_c)} \right]. \end{aligned} \tag{2.28}$$

The sum i is over all of the electrons in the atom, and the sum c is over all of the states available to the virtual photoelectron in the intermediate excited state.

2.1.4 Comparison with X-ray absorption

Now consider the amplitude for a single photon to be absorbed by an atom. The initial state is an atom in its ground state $|\Psi_i\rangle$ and an incident photon in a state $|\mathbf{k}, \alpha\rangle$. The final state of the system is the atom in an excited state $|\Psi_f\rangle$ and no photon. The initial and final states can only be connected by the annihilation operator for the photon state $|\mathbf{k}, \alpha\rangle$, which appears to first order in the linear $\mathbf{p} \cdot \mathbf{A}$ term of the interaction Hamiltonian. In this case, the leading term in the perturbation expansion is of order e/mc larger than the second-order terms, so it is sufficient to consider only the first-order matrix element. Using again the independent particle approximation, the amplitude for absorption into a specific final state is given by

$$\begin{aligned} \mathrm{M}_{(1)} &= \frac{1}{i\hbar} \left(\frac{-e}{mc}\right) \int_0^t dt' \sum_i \langle \psi_f | H_{\mathrm{int}} | \psi_i; \mathbf{k}, \alpha \rangle e^{i(E_f - E_i)t'/\hbar} \\ &= \frac{1}{i\hbar} \left(\frac{-e}{mc}\right) \frac{1}{\sqrt{V}} c \sqrt{\frac{\hbar}{2\omega}} \sum_i \langle \psi_f | \hat{\mathbf{e}}^{(\alpha)} \cdot \mathbf{p}_i e^{i\mathbf{k}\cdot\mathbf{r}_i} | \psi_i \rangle \int_0^t dt' e^{i(E_f - E_i - \hbar\omega)t'/\hbar}. \end{aligned} \tag{2.29}$$

Figure 2.4 compares the Feynman diagram representation of the first order matrix element for absorption with the second order matrix element for resonant scattering for comparison. Following standard methods for evaluating the matrix elements, Equation (2.29) is simplified at this point in the discussion by assuming that only *one*

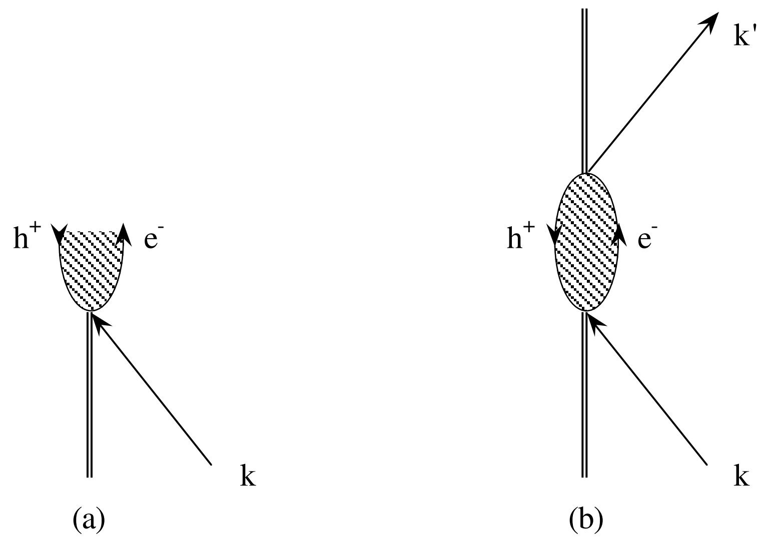

Figure 2.4: The Feynman diagrams for (a) photon absorption, and (b) the resonant part of Δf for comparison. A doubled line represents an atom, an arrow represents a photon. The hatching serves to represent (a) the final states available to the outgoing photoelectron and (b) the intermediate states available to the outgoing virtual photoelectron.

of the electrons participates in the absorption process. This disposes of the summand inside the squared matrix element of Equation (2.19), and gives the probability per unit time for transition from $|\psi_i\rangle$ to $|\psi_{\mathrm{f}}\rangle$ of

$$\frac{|\mathrm{M}_{(1)}|^2}{t} = \frac{2\pi}{\hbar}\left(\frac{e}{m}\right)^2 \frac{1}{V}\frac{\hbar}{2\omega}\left|\langle\psi_f|\hat{\mathbf{e}}^{(\alpha)} \cdot \mathbf{p}_i e^{i\mathbf{k}\cdot\mathbf{r}_i}|\psi_i\rangle\right|^2 \delta(E_f - E_i - \hbar\omega). \tag{2.30}$$

For elastic scattering, the final state of the atom was the same as the initial state. For absorption, however, there are many different possible final states for the outgoing photoelectron, and all of these need to be accounted for in calculating the total cross section for the absorption of a photon. Normalizing to the incident photon flux density and summing over all possible final states, the formal expression for the absorption cross-section [21, 26, 37] becomes

$$\sigma = \frac{4\pi^2 e^2}{\omega m^2 c}\sum_f \left|\langle\psi_f|\hat{\mathbf{e}}^{(\alpha)} \cdot \mathbf{p}_i e^{i\mathbf{k}\cdot\mathbf{r}_i}|\psi_i\rangle\right|^2 \delta(E_f - E_i - \hbar\omega). \tag{2.31}$$

The squared term can be written explicitly as the product of the matrix element and its complex conjugate

$$\sigma = \frac{4\pi^2 e^2}{\omega m^2 c} \sum_f \langle \psi_i | \hat{\mathbf{e}}^{*(\alpha)} \cdot \mathbf{p}_i^\dagger e^{-i\mathbf{k}\cdot\mathbf{r}_i^\dagger} | \psi_f \rangle \langle \psi_f | \hat{\mathbf{e}}^{(\alpha)} \cdot \mathbf{p}_i e^{i\mathbf{k}\cdot\mathbf{r}_i} | \psi_i \rangle \delta(E_f - E_i - \hbar\omega). \quad (2.32)$$

Notice now that the sum over the final states is a sum over the eigenstates of H_0, from the perturbation series, so that Equation (2.32) resembles a Fourier mode expansion. If H_0 is a well behaved self-adjoint linear operator with regular boundary conditions, then the eigenstates form a complete set and, in particular, the Green's function for the differential equation that results from operating with H on the ground state wavefunctions may be written as a sum over poles

$$G^+(E) = \sum_f \frac{|\psi_f\rangle\langle\psi_f|}{E - E_f + i\epsilon}. \quad (2.33)$$

With the choice of the negative sign for ϵ, this is the *retarded* Green's function. All of the poles of G^+ lie in the lower half of the complex energy plane (see Section 2.2.1 below). Using the identity

$$\frac{1}{E - E_f + i\epsilon} = P\left(\frac{1}{E - E_f}\right) - i\pi\delta(E - E_f) \quad (2.34)$$

where P means the principal part of the implied integral. Then

$$G^+(E) = \sum_f |\psi_f\rangle\langle\psi_f| P \frac{1}{E - E_f} - i\pi \sum_f |\psi_f\rangle\langle\psi_f| \delta(E - E_f) \quad (2.35)$$

and

$$\sigma = -\frac{4\pi e^2}{\omega m^2 c} \mathrm{Im}\left(\langle \psi_i | \hat{\mathbf{e}}^{*(\alpha)} \cdot \mathbf{p}_i e^{-i\mathbf{k}\cdot\mathbf{r}_i} G^+(E_i + \hbar\omega) \hat{\mathbf{e}}^{(\alpha)} \cdot \mathbf{p}_i e^{i\mathbf{k}\cdot\mathbf{r}_i} | \psi_i \rangle \right) \quad (2.36)$$

where I have used $\delta(x - x_0) = \delta(x_0 - x)$.

2.2 The relationship between DAFS and XAFS

To compare the matrix elements for DAFS and XAFS, apply the Green's function formalism of Equation (2.36) to the elastic scattering matrix elements in Equation (2.28). Using

$$G^+(E_i \pm \hbar\omega) = \sum_c \frac{|\psi_c\rangle\langle\psi_c|}{(E_i \pm \hbar\omega) - (E_c - \frac{1}{2}i\Gamma_c)} \quad (2.37)$$

Equation (2.28) becomes

$$\begin{aligned}\Delta f &= -\left(\frac{e}{mc}\right)^2 \sum_i \Big[\langle\psi_i|\hat{\mathbf{e}}^{*(\alpha')}\cdot\mathbf{p}e^{-i\mathbf{k}'\cdot\mathbf{r}_i}G^+(E_i+\hbar\omega)\hat{\mathbf{e}}^{(\alpha)}\cdot\mathbf{p}e^{i\mathbf{k}\cdot\mathbf{r}_i}|\psi_i\rangle \\ &\qquad + \langle\psi_i|\hat{\mathbf{e}}^{(\alpha)}\cdot\mathbf{p}e^{i\mathbf{k}'\cdot\mathbf{r}_i}G^+(E_i-\hbar\omega)\hat{\mathbf{e}}^{*(\alpha')}\cdot\mathbf{p}e^{-i\mathbf{k}\cdot\mathbf{r}_i}|\psi_i\rangle\Big] \qquad (2.38)\end{aligned}$$

Some small changes need to be made to Equation (2.38) before it can be equated directly with Equation (2.36). The first approximation is to treat Equation (2.38) as though only one electron participates in the resonance scattering event. This is the same approximation that was made to get from Equation (2.29) to Equation (2.30). Next, notice that the $G^+(E_i-\hbar\omega)$ matrix element in Equation (2.38) is small compared to the $G^+(E_i+\hbar\omega)$ matrix element. When E approaches a resonance energy, the denominator of the $G^+(E_i-\hbar\omega)$ matrix element goes to $2\hbar\omega+\frac{1}{2}i\Gamma$ while the denominator of the $G^+(E_i+\hbar\omega)$ matrix element goes to $\frac{1}{2}i\Gamma$. The width Γ is dominated by the short-lived core hole which, for K-shell resonances, is on the order of a few eV [81]. Compared to the resonance energies of the transition metals from Ti to Zn, the $G^+(E_i-\hbar\omega)$ matrix element is smaller by a factor of $\sim 10^{-4}$, using for example Cu with $\Gamma\sim 2.5$ eV and $\hbar\omega\sim 9000$ eV, so that it is reasonable to neglect this term. Finally, the meaning of the phase argument $\mathbf{k}'\cdot\mathbf{r}_i$ in Equations (2.38) and (2.36) is very different. Equation (2.38) comes from a second order term in the perturbation series, and the incident and outgoing photon directions are not necessarily the same. Equation (2.36), on the other hand, arises from expanding out the squared magnitude of the first order absorption matrix element so that the directions $\mathbf{k}$ and $\mathbf{k}'$ are the same. Provided that $\mathbf{k}=\mathbf{k}'$, we can equate the complete matrix elements from Equation (2.36) and the first term in Equation (2.38) to obtain

$$\begin{aligned}\sigma &= -\frac{4\pi e^2}{\omega m^2 c}\mathrm{Im}\left[-\left(\frac{mc}{e}\right)^2\Delta f\right] \\ &= \frac{4\pi c}{\omega}\mathrm{Im}\left[\Delta f\right] \qquad (2.39)\end{aligned}$$

which is the *optical theorem*[4]. This relationship strictly holds only in the forward scattering direction where $\mathbf{k}'$ of the final state photon is equal to $\mathbf{k}$ of the initial state. The optical theorem can be extended to non-forward scattering under the

[4] The optical theorem is usually written with the prefactor $\frac{4\pi c r_e}{\omega}$ when Δf is given in dimensionless *electron units*. In my derivation, Δf comes from the square-root of a scattering cross-section, and thus has dimensions of *length*. Tabulated values of Δf are generally provided in electron units.

dipole approximation. When the average radial size of the core electron ground state is small compared to the wavelength of the light, then the phase factor can be approximated by

$$e^{i\mathbf{k}\cdot\mathbf{r}} = 1 + i\mathbf{k}\cdot\mathbf{r} + \cdots \approx 1, \tag{2.40}$$

which removes the angular dependence of the resonant scattering[5]. The size of the core electron ground state for hydrogenic wavefunctions is related to the Bohr radius and to the charge on the nucleus by $\approx a_0/Z$ and the energy of the state goes as $E_{\mathrm{K}} \approx Z^2e^2/a_0$ so that the dipole approximation is expected to hold for $Z^2(e^2/\hbar c)^2 = Z^2\alpha^2 \ll 1$, where $\alpha \sim 137$ is the fine structure constant. For Cu, $Z^2\alpha^2 \approx 0.045$. The effects of the higher order terms have been considered both theoretically [39] and experimentally [7], and have been found to be small.

2.2.1 A note on sign conventions in x-ray scattering

Notice that the Thomson amplitude as it is defined in Equation (2.27) is explicitly negative. The scattering is π out of phase with the incident radiation and the intensity in the forward direction is never larger than incident beam. This is contrary to all of the standard sources of tabulated values of f_0 found in the literature [43, 44], in which the negative sign is supressed. Inconsistency in the sign conventions used in crystallography and in quantum mechanics has already been discussed in the context of comparing x-ray and neutron anomalous diffraction amplitudes [45], but it continues to be a problem even in more modern calculations of the matrix elements for x-ray scattering [46]. Until the introduction of multiple wavelength anomalous dispersion (MAD), crystallographic intensities were generally measured far from the atomic resonances, where there is only f_0 to consider. Since the intensity is measured, not the amplitude, a π phase shift for non-resonant diffraction calculations is moot, but it becomes very important in DAFS where interference terms are the dominant effect. Once the positive amplitude standard for f_0 was set, the choice for f' was forced because the Bragg peak intensities from monoatomic materials are *observed* to have a downward cusp near resonance, as shown in Figures 1.1(a) and 2.1. If the

[5] Note that this does not remove the polarization dependence of the fine structure, which can change with the directions of the incident and outgoing photons in the case of π-polarized scattering; Section 2.3.3.

scattering amplitude is causal, then $f(E)$ is analytic in the upper half of the complex frequency plane, and application of the integral Cauchy-Reiman conditions to the downward cusp in $\mathrm{Re}[f(E)]$ produces a *downward* step for $\mathrm{Im}[f(E)]$. This is in direct conflict with the optical theorem and the standard interpretation of the total absorption cross-section as strictly positive.

The positive standard for $f''(E)$, found in XAFS and elsewhere, comes from the sign convention for attenuation of radiation as it passes through an absorbing medium, defined by

$$I(E) = \int_0^t I_0(E) e^{-\mu(E)t'} dt' \qquad (2.41)$$

for an incident beam of intensity $I_0(E)$ passing through a slab of material with thickness t. If the intensity decreases as the incident beam penetrates the material, *i.e.*, excepting the special case of light amplification by stimulated emission, then $\mu(E) \propto f''(E)/E$ must be strictly positive. This clash of tradition has caused much confusion in sign conventions for optical dispersion relations throughout the literature on the subject, so I would like to take the time here to convince even my my most skeptical readers that the scattering amplitudes need to be: $f_0(\mathbf{Q})$ negative, $f'(E)$ an upward cusp and $f''(E)$ an upward step.

Dispersion relations and sign conventions

Suppose we have some function $f(\omega)$ that is analytic in the the upper half of the complex frequency plane and on the real axis, and that

$$\lim_{|\omega|\to\infty} f(\omega) = 0 \quad \text{for} \quad 0 \leq \arg(\omega) \leq \pi. \qquad (2.42)$$

The choice of analyticity in the upper half-plane may seem, from a purely mathematical standpoint, to be somewhat arbitrary. However, based on the conventions of positive frequency and time, it is consistent with the general observation that optical response functions are causal and that signals do not travel faster than the speed of light. Here and now I am only concerned with setting straight the sign conventions for the scattering amplitudes and the dispersion relations. Certainly no one will argue that the standard location for the poles of *all* optical response functions is the lower half of the complex frequency plane, consistent with causality [19], and so my argument begins from this convention.

The details of the steps for deriving the Hilbert transforms for a function that satisfies these conditions may be found in Arfken [95], Morse and Feshbach [96], or many textbooks on complex analysis. The derivation involves applying Cauchy's integral formula to calculate $f(\omega)$ in the analytic region with the contour taken to lie along the real axis and a semicircle enclosing the upper half-plane. As $\omega \to 0$, the integral on the semicircle vanishes and, as ω approaches the real axis from above, the contour integral becomes

$$\begin{aligned} f(\omega) &= \frac{1}{i\pi} P \int_{-\infty}^{\infty} \frac{f(\omega')}{\omega' - \omega} d\omega' \qquad (2.43) \\ &= \frac{1}{i\pi} P \int_{-\infty}^{\infty} \frac{(\mathrm{Re}[f(\omega')] + i\mathrm{Im}[f(\omega')])}{\omega' - \omega} d\omega' \\ &= \frac{1}{\pi} P \int_{-\infty}^{\infty} \frac{\mathrm{Im}[f(\omega')]}{\omega' - \omega} - i\frac{1}{\pi} P \int_{-\infty}^{\infty} \frac{\mathrm{Re}[f(\omega')]}{\omega' - \omega} d\omega'. \end{aligned}$$

Equating the real and imaginary parts gives

$$\mathrm{Re}[f(\omega)] = \frac{1}{\pi} P \int_{-\infty}^{\infty} \frac{\mathrm{Im}[f(\omega')]}{\omega' - \omega} d\omega' \qquad (2.44)$$

$$\mathrm{Im}[f(\omega)] = -i\frac{1}{\pi} P \int_{-\infty}^{\infty} \frac{\mathrm{Re}[f(\omega')]}{\omega' - \omega} d\omega'. \qquad (2.45)$$

$\mathrm{Re}[f]$ and $\mathrm{Im}[f]$ are thus *Hilbert transforms* of each other, with $f(\omega)$ assumed to be a complex function of the real variable ω. The integral relations in Equations (2.44) and (2.45) are referred to as *dispersion relations* because they relate the real and imaginary parts of the frequency-dependent optical response functions, which disperse and absorb the spectral components of light.

Crossing symmetry

We insist that the signals we measure in time are purely real. From the symmetry properties of the Fourier transform, this condition requires that the real and imaginary parts of the frequency-dependent response function satisfy *crossing symmetry*

$$\begin{aligned} \mathrm{Re}[f(-\omega)] &= \mathrm{Re}[f(\omega)] \qquad (2.46) \\ \mathrm{Im}[f(-\omega)] &= -\mathrm{Im}[f(\omega)], \end{aligned}$$

Applying Equation (2.46) to Equation (2.44) gives, for example,

$$\mathrm{Re}[f(\omega)] = \frac{1}{\pi} P \int_{-\infty}^{0} \frac{\mathrm{Im}[f(\omega')]}{\omega' - \omega} d\omega' + \frac{1}{\pi} P \int_{0}^{\infty} \frac{\mathrm{Im}[f(\omega')]}{\omega' - \omega} d\omega'$$

$$
\begin{aligned}
&= \frac{1}{\pi} P \int_0^{\infty} \mathrm{Im}[f(\omega')] \left(\frac{1}{\omega' + \omega} + \frac{1}{\omega' - \omega} \right) d\omega' \\
&= \frac{2}{\pi} P \int_0^{\infty} \frac{\omega' \mathrm{Im}[f(\omega')]}{\omega'^2 - \omega^2} d\omega' \qquad (2.47)
\end{aligned}
$$

and similarly for Equation (2.45)

$$
\mathrm{Im}[f(\omega)] = -\frac{2\omega}{\pi} P \int_0^{\infty} \frac{\mathrm{Re}[f(\omega')]}{\omega'^2 - \omega^2} d\omega'. \qquad (2.48)
$$

Equations (2.47) and (2.48) are the Kramers-Krönig dispersion relations. Care must be taken to subtract off the Thomson scattering amplitude from f to ensure that $\mathrm{Re}[f(\omega)] \to 0$ as $\omega \to \infty$. The situation is somewhat different for the relativistic treatment, and the interested reader is directed to the work of C. Chantler [64], and references therein.

The cusp and the step

Now that you are now convinced that Equation (2.47) and Equation (2.48) are the correct form for the Kramers-Krönig dispersion integrals, note carefully the order of the terms in the denominator. The literature is rife with examples where ω^2 and ω'^2 have been surreptitiously swapped in order to force agreement between the disparate sign conventions that I described above. One way to see that $\mathrm{Re}[f(\omega)]$ will be an upward cusp is to consider the sign of the integral in Equation (2.47) when $\mathrm{Im}[f(\omega)]$ is a positive step (see Figure 2.5) at ω_0 such that $\mathrm{Im}[f(\omega)] = 0$ for $\omega < \omega_0$. Approaching the pole from above and below,

$$
\mathrm{Re}[f(\omega)] = \lim_{\epsilon \to 0} \frac{2}{\pi} \left(\int_0^{\omega - \epsilon} \frac{\omega' \mathrm{Im}[f(\omega')]}{\omega'^2 - \omega^2} d\omega' + \int_{\omega + \epsilon}^{\infty} \frac{\omega' \mathrm{Im}[f(\omega')]}{\omega'^2 - \omega^2} d\omega' \right). \qquad (2.49)
$$

When $\omega < \omega_0$, the first integral in Equation (2.49) is zero and the second integral is positive-definite, increasing as $\omega \to \omega_0$ from below. This creates the rising edge of a positive cusp which reaches its peak value at $\omega = \omega_0$. Above ω_0, the first integral is negative-definite and competes with the second term, eventually bringing the sum back down to zero for $\omega \gg \omega_0$

The choice of overall phase is critical for modelling DAFS data. If tabulated is data used without correcting for the sign discrepency then the Kramers-Krönig dispersion integrals need to be changed to force agreement with the gross features of the data: the direction of the cusp and the step under transformation. Changing the sign on

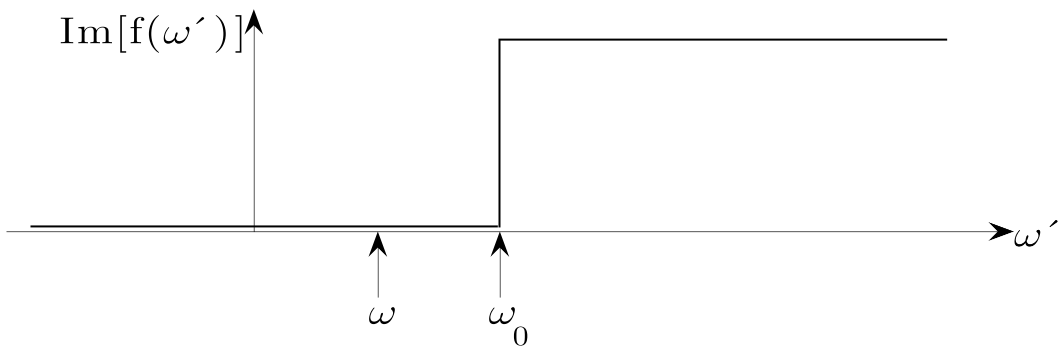

Figure 2.5: The result of applying the Kramers-Krönig dispersion integral to a positive step in the imaginary part of a response function is a positive upward cusp in the real part. If $f''(\omega')$ is a positive definite step, then $f'(\omega)$ is monotone increasing for $\omega < \omega_0$, as can be seen in Equation (2.47) and Equation (2.49). This figure illustrates the thought experiment suggested in Section 2.2.1.

the dispersion integrals will result in an overall phase shift of $-\pi/2$ in $\chi''(E)$ and the fine structure in $f''(E)$ will appear *upside-down* on the step compared to the measured fine structure in the absorption $\mu(E)$. The analysis can be forced to yield an $f''(E)$ that agrees with the XAFS $\mu(E)$ by multiplying the phase argument of Fourier components of the fine structure $sin(2kR + \delta)$ by -1 and then defining the DAFS fine structure as $-\mathrm{Re}[\chi(E)]$. These changes, which give the desired numerical result, are equivalent to choosing the acausal *advanced* Green's function. All of the analysis presented in this thesis uses the causal form of the response functions and consequently the figures of $f'(E)$ appear as positive upward cusps throughout.

2.3 Matrix element calculations

The equations in Sections 2.1.3 and 2.1.4 show the connection between absorption and resonance scattering, but they are only a starting place for useful data modelling and analysis. The steps for performing *a priori* theoretical calculation of the absorption matrix elements have been described in detail elsewhere [30–33]. For treatment of the computational gymnastics required to do the real calculations, I refer the interested reader to the following sources: Brian Hauser's dissertation [30] gives an exhaustive discussion of the Green's function formalism for calculating the absorption cross-section using the *separable spherical wave approximation.* The computational details, including the computer algorithms and the atomic wavefunctions, are discussed in the dissertations of José Mustre de Leon and Steven Zabinsky [32, 33]. For a more concise discussion, see the most recent published articles by John Rehr and collaborators [31], and the references therein.

2.3.1 Using FEFF *to calculate DAFS spectra*

The theoretical standards used in the DAFS analysis in Chapters 5 and 6 and the DAFS fine-structure simulations used for the reliability studies in Chapter 7 were calculated using the computer program FEFF, which was written by John Rehr and his collaborators for calculating XAFS spectra. Some aspects of the matrix element calculations need to be addressed in order to justify using an XAFS fine structure calculation code for DAFS.

FEFF calculates the embedded atom $\mu_0(E)$ to some extent[6], and therefore $f''_a(E)$, but FEFF does *not* calculate $f'_a(E)$. This lack of reciprocity arises from the computational difference between the real and imaginary parts of the individual terms in Green's function presented at the end of Section 2.1.4, that is

$$G^+(E) = \sum_f |\psi_f\rangle\langle\psi_f| P\frac{1}{E - E_f} - i\pi \sum_f |\psi_f\rangle\langle\psi_f|\delta(E - E_f). \tag{2.50}$$

The XAFS comes from the imaginary part of the Green's function which, according to Equation (2.50), is the energy conserving part of the kernel. An integral over a Dirac delta function is trivial, and so the calculation of the absorption coefficient in the dipole approximation reduces to calculating the overlap of the spatial wavefunctions. The real part of the Green's function, on the other hand, is the principle part of the integral, which must be evaluated from zero to infinite energy to determine $f'_a(E)$. This is computationally difficult and theoretical XAFS engines generally do not provide a direct calculation of $f'(E)$. The fine structure, which comes from backscattering off the neighboring atoms, is band-limited. The $\chi(E)$ function that FEFF calculates is the full complex fine structure function. Although XAFS analysis based on FEFF applications generally only makes use of the imaginary component of the fine-structure, the real part is already there for the taking.

[6] The full multiple scattering calculation in the XANES region is still in the developmental stage.

FEFF calculates the absorption coefficient, from reference [31], using

$$\mu(\hat{\mathbf{e}}, E) \sim -\frac{1}{\pi}\langle\psi_i|\hat{\mathbf{e}}^* \cdot \mathbf{r}G(\mathbf{r}, \mathbf{r}'; E)\hat{\mathbf{e}}^* \cdot \mathbf{r}'|\psi_i\rangle\Theta_c(E - E_F) \tag{2.51}$$

where G is the one particle Green's function and the sum is over unoccupied final states. The final states are calculated in the presence of a fully relaxed core hole, while the initial states are calculated with the initial-state Hamiltonian. The step function is approximated by an arctangent

$$\Theta_c(E - E_F) = \frac{1}{\pi}\tan^{-1}\left(\frac{\Gamma_c}{E - E_F}\right) \tag{2.52}$$

to account for the core-hole lifetime. The multiple-scattering expansion for the XAFS calculation is obtained by iterating $G = G^0 + G^0TG$ in terms of free propagators G^0 for the electron and scattering matrices T. Terms in the sum then represent single scattering, double scattering, etc..., representing all scattering paths. The T matrices contain the partial-wave phase shifts, the treatment is semi-relativistic, neglecting only the spin-orbit terms, expanded in the angular momentum and coordinate basis.

Separation of the atomic and fine structure terms

When the cross-sections in Equation (2.36) and Equation (2.38) are calculated using the Green's function formalism in the dipole approximation $\mu(E)$ and consequently $f(E)$, can be shown (*e.g.*, see Equation (2.37) of [21]) to separate into terms that depend only on the atomic physics and terms that depend on the backscattering from neighboring atoms. The atomic terms are slowly varying functions of the photon energy, the smooth cusp in the real channel and the smooth step in the imaginary channel that corresponds to $\mu_0(E)$ in the XAFS. The backscattering terms are rapidly varying functions of the photon energy, the complex $\chi(E)$ function. This can be formally written as

$$\begin{aligned} \Delta f(E) &= f'(E) + if''(E) \\ &= f_a'(E) + if_a(E) + f_0''(E)\left(\chi'(E) + i\chi''(E)\right) \\ &= \Delta f_a(E) + f_0''(E)\chi(E) \end{aligned} \tag{2.53}$$

The real and imaginary parts of $\Delta f_a(E)$ are the slowly varying atomic terms, $\mathrm{Re}f_a(E)$ is the upward pointing cusp and $\mathrm{Im}f_a(E)$ is the upward step at E_0. The imaginary part of the complex fine structure $\mathrm{Im}\chi(E) = \chi''(E)$ is the same as the XAFS fine structure in the absence of angular dependence in the resonant scattering amplitude.

2.3.2 Path formalism in the XAFS equation

A separable curved-wave formalism is used in FEFF to calculate an *effective* photoelectron backscattering amplitude t_{eff} for each possible scattering path. The total fine structure function is a sum over the contributions from all possible scattering paths

$$\chi(k) = \sum_{\text{path } j} \frac{S_0^2}{kR_j^2} |t_{\text{eff},j}(k)| e^{i(2kR_j+\delta_j)} e^{-2k^2\sigma_j^2} d^{-2R_j/\lambda(k)}. \tag{2.54}$$

The amplitude reduction factor S_0^2 is used to account for multi-electron effects, δ_j contains the combined phase shifts due to scattering and the final-state phase shift due to ionization of the central atom, and $2kR_j$ is the phase shift for a total path of length $R = r_{\text{tot}}/2$. FEFF uses degeneracies and amplitude filtering criteria to reduce the total number of calculations.

2.3.3 Polarization dependence of the fine structure

If the central atom coordinate is denoted $\mathbf{R} = \mathbf{0}$, then the path-by-path polarization dependence of the fine-structure on the polarization state of the incident photon in the XAFS equation comes from consideration of

$$\sum_m \langle l, m; \mathbf{0} | \hat{\mathbf{e}}^* \cdot \mathbf{r} | l_n, m_n; \mathbf{0} \rangle \langle l_0, m_0; \mathbf{0} | \hat{\mathbf{e}} \cdot \mathbf{r} | l, m; \mathbf{0} \rangle \tag{2.55}$$

Which includes contributions from all shells. The work in this thesis is for K-shell DAFS from Cu, with $l = 0$. The important thing to notice is that for more than single backscattering, the polarization dependence of the XAFS is on both the initial and final legs of the path, and that the direction of $\hat{\mathbf{e}}$ is the same for both. Figure 2.6 shows the geometry for a triangular path. In DAFS, the polarization directions of the incident and outgoing photons both appear in the matrix elements and, in general, $\hat{\mathbf{e}}$ can be different from $\hat{\mathbf{e}}'$. The coupling between $\hat{\mathbf{e}}$ and the bond direction is path dependent, as can be seen in Figure 2.7, so that the fine structure can in principle be very different for XAFS and DAFS. However, if the diffraction data is collected by rotating the crystal around an axis parallel to $\hat{\mathbf{e}}$, *i.e.*, when $\mathbf{Q}$ is confined to the plane perpendicular to $\hat{\mathbf{e}}$, then the polarization dependence of the DAFS is the same as that for the XAFS. The polarization dependence of the fine structure calculated by FEFF is included in the effective photoelectron backscattering amplitude for each path.

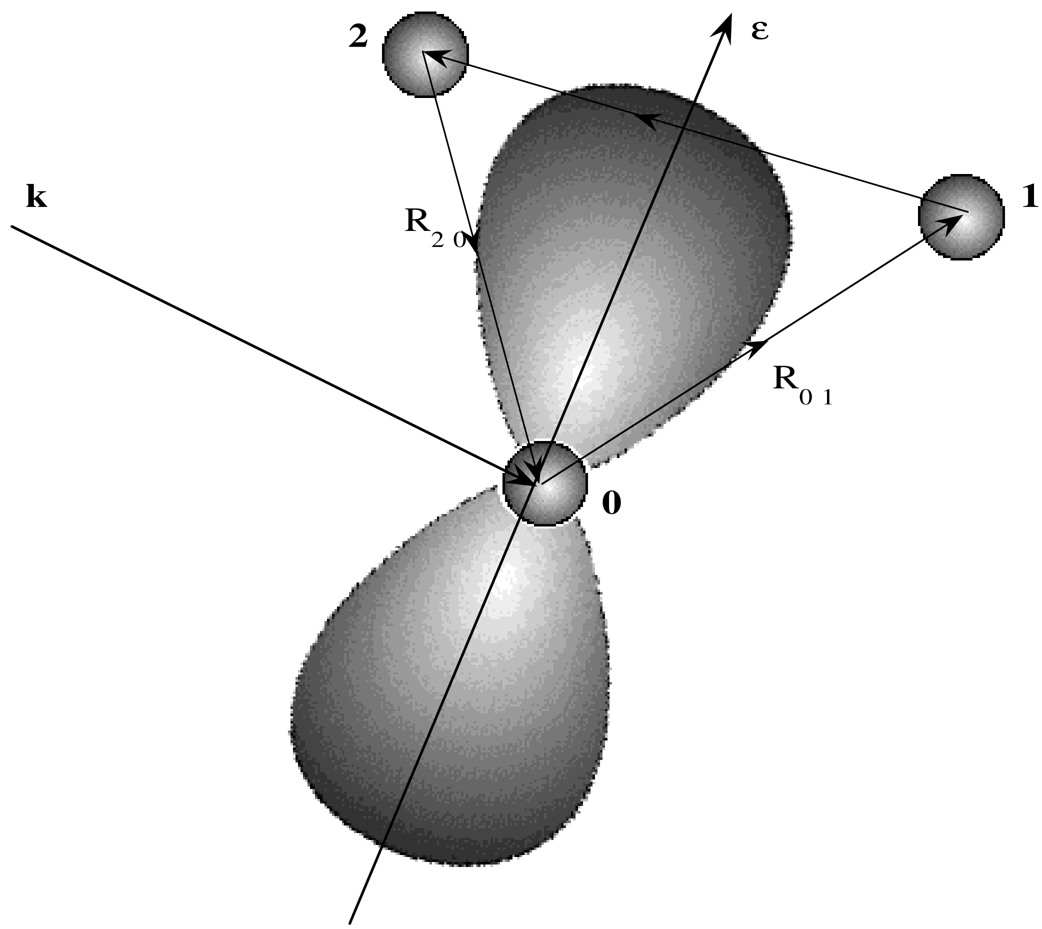

Figure 2.6: The polarization dependence of the contribution to the total XAFS $\chi(k)$ from a single triangular scattering path. For a K-shell resonance with $l = 0$, and if the incident photon is linearly polarized, the polarization dependence goes as $(\hat{\mathbf{e}} \cdot \hat{\mathbf{R}}_{01})(\hat{\mathbf{e}} \cdot \hat{\mathbf{R}}_{20})$: the polarization dependence comes from the first and last legs of the scattering path.

The Thomson scattering from Equation (2.27) is $\hat{\mathbf{e}}' \cdot \hat{\mathbf{e}}$ for linearly polarized light. Since synchrotron radiation is linearly polarized in the plane of the ring, diffraction experiments are mostly performed in the vertical scattering geometry to maximize intensity. This also keeps the polarization direction fixed and a happy harmony is achieved in which the fine-structure and the diffraction are simultaneously optimized.

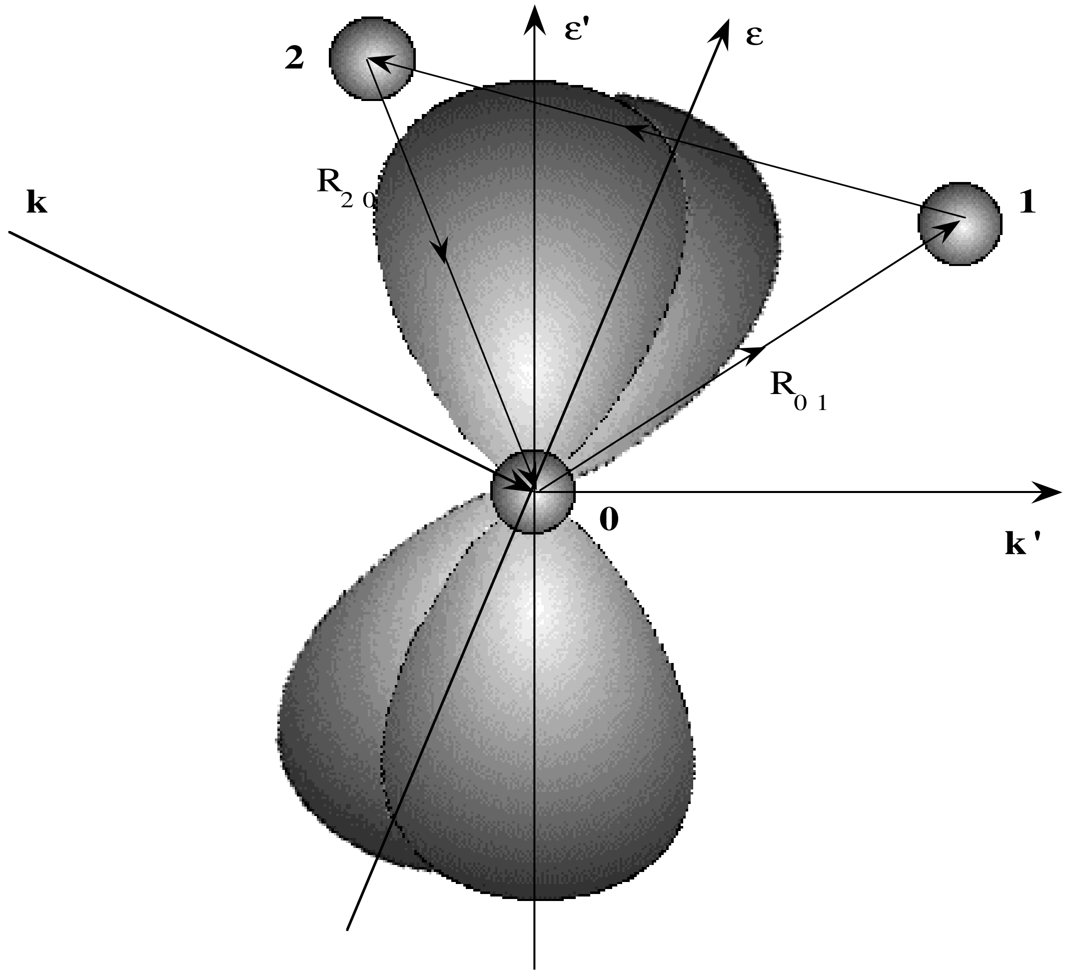

Figure 2.7: The polarization dependence of the contribution to the total DAFS $\chi(k)$ from a single triangular scattering path for the case $\hat{\mathbf{e}} \neq \hat{\mathbf{e}}'$ As before, the polarization dependence comes from the first and last legs of the scattering path. For linear polarized light, the path-by-path polarization dependence of $l = 0$ DAFS is $(\hat{\mathbf{e}} \cdot \hat{\mathbf{R}}_{01})(\hat{\mathbf{e}}' \cdot \hat{\mathbf{R}}_{20})$. The Green's function contains a term that corresponds to traversing this same path in the opposite direction. For some triangular paths, such as the one shown in this figure, the two directions will have strongly different amplitudes due to the difference in coupling between the two bonds and the two polarization directions. If the diffraction wavevector transfer is confined to the plane perpendicular to $\hat{\mathbf{e}}$, then $\hat{\mathbf{e}} = \hat{\mathbf{e}}'$ and DAFS and XAFS have the same polarization dependence for every path, which is independent of the direction the path is traversed.

Chapter 3

X-RAY DIFFRACTION IN THE KINEMATIC APPROXIMATION

The preceding chapter served to show the equivalence of the spectral content of XAFS and DAFS by relating the total absorption cross-section to the complex resonant scattering amplitude. The goal of this chapter is to understand how the fine structure measured in the Bragg peak intensities is related to the fine structure in the complex resonant scattering amplitude and to use this understanding to develop methods for analyzing DAFS data. Starting from the scattering amplitude for a single atom, this chapter develops the simple crystallographic aspects of DAFS that are required to solve for the real and imaginary parts of the resonant fine structure from the measured intensity. An excellent general reference for a more detailed development of non-resonant diffraction is *The Optical Principles of the Diffraction of X-Rays* by R.W. James [38].

3.1 X-ray diffraction

Consider a single atom in a beam of x-rays. If the amplitude of the incident beam is S_0, and the scattering strength of the atom is f, then the time independent amplitude for scattering at a distant observation point r is

$$S = \frac{S_0}{r} f(\mathbf{Q}, E) e^{ikr} \tag{3.1}$$

where $\hbar\mathbf{Q} = \hbar(\mathbf{k}_\mathrm{f} - \mathbf{k}_i)$ is the photon momentum transfer and $k = 2\pi/\lambda$. The scattering amplitude from a collection of atoms is the sum of the scattering amplitudes from each of the atoms added together according to their positions with respect to an origin of coordinates. Figure 3.1 shows the geometry for the simple case of two identical atoms separated by a distance r_{12}. The phase difference caused by the difference in path length for two scattered rays is $\Delta\phi = \hat{\mathbf{r}}_{12} \cdot \hat{\mathbf{k}}_\mathrm{f} - \hat{\mathbf{r}}_{12} \cdot \hat{\mathbf{k}}_i = \hat{\mathbf{r}}_{12} \cdot (\hat{\mathbf{k}}_\mathrm{f} - \hat{\mathbf{k}}_i)$. The total scattered amplitude from a collection of atoms is the sum of the scattering

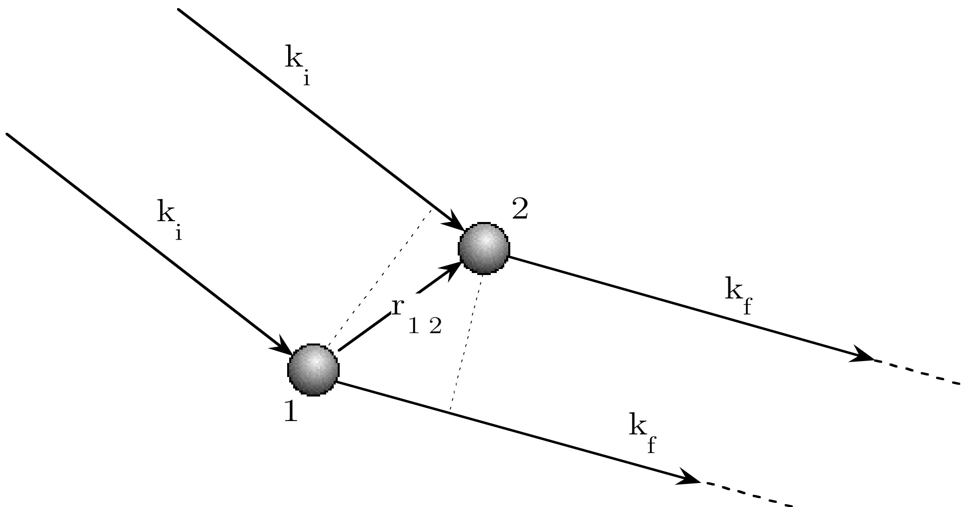

Figure 3.1: Scattering from two atoms. The detector is presumed to be at a distance that is large compared to the distance between the atoms. Then the incident and outgoing rays are parallel, and the phase difference between the rays scattered from the two atoms is $\mathbf{r}_{12} \cdot \hat{\mathbf{k}}_{\mathrm{f}} - \mathbf{r}_{12} \cdot \hat{\mathbf{k}}_i = \mathbf{r}_{12} \cdot (\hat{\mathbf{k}}_{\mathrm{f}} - \hat{\mathbf{k}}_i)$.

from all of the atoms

$$S = \frac{S_0}{r} \sum_j f_j e^{i\mathbf{Q}\cdot\mathbf{r}_j} \tag{3.2}$$

when r is large enough that the distance from the observation point to each of the atoms can be taken as a constant. This expression neglects multiple scattering of the x-rays. In general, there is the possibility that light scattered from one atom is re-scattered by another atom before reaching the observation point. However, this effect only contributes appreciably to the total coherent scattering amplitude when the spatial ordering of the atoms is nearly perfect and the domain size is large [52, 53]. When the diffracted intensity is weak, say 0.1% of the incident beam intensity, or when the size of the crystal is small the effects of multiple scattering is negligible. Diffraction under this approximation is called *kinematic diffraction*, as opposed to *dynamical diffraction* when the effects of multiple scattering are appreciable. I will only consider kinematical diffraction for describing the DAFS signal.

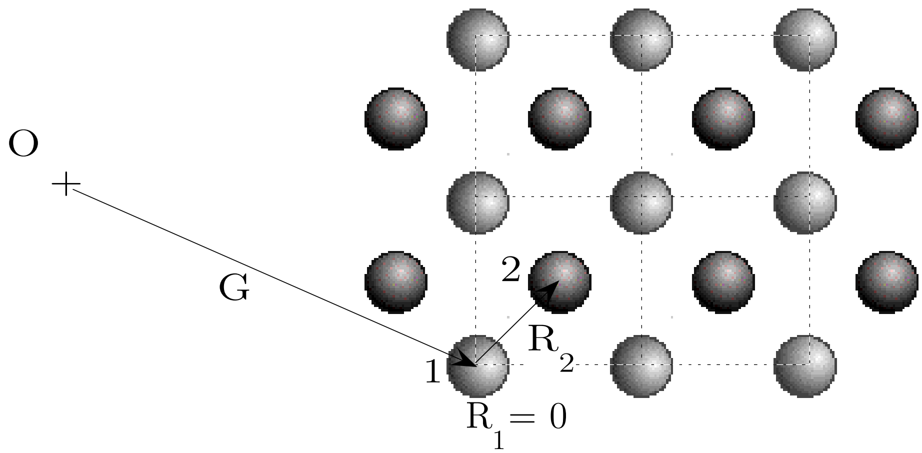

Figure 3.2: Scattering from a unit cell. The positions R_j of the atoms in the unit cell are defined with respect to a local origin of coordinates at each lattice site and the lattice sites are located by the lattice vectors $\mathbf{G}$ from a global origin of coordinates. In this figure the unit cell is comprised of two atoms at positions $\mathbf{R}_1 \equiv \mathbf{0}$ and $\mathbf{R}_2$ with respect to. the lattice vector.

When the scattering is from atoms arranged periodically in a crystal, Equation (3.2) can be rewritten as a double sum, first over the *lattice vectors* $\mathbf{G}$ and then over the *basis vectors* $\mathbf{R}$ from $\mathbf{G}$ to each of the atoms in the unit cell that decorates the lattice points. This is illustrated in Figure 3.2 for a two atom basis decorating a two dimensional square lattice. The location of the global origin of coordinates and the registry of the unit cell on the lattice are arbitrary, although they are usually chosen to make the best use the symmetry properties of the crystal. The important features that allow the sum Equation (3.2) to be simplified are the periodicity of the lattice and the invariance of the basis throughout the crystal. The position of each atom can then written

$$\mathbf{r}_j = \mathbf{G} + \mathbf{R}_j \tag{3.3}$$

and Equation (3.2) becomes

$$S = \frac{S_0}{r} \sum_i \sum_j f_j e^{i\mathbf{Q}\cdot\mathbf{G}_i} e^{i\mathbf{Q}\cdot\mathbf{R}_j}. \tag{3.4}$$

The sums are over all of the lattice sites in the crystal and all of the atoms in the basis. In Figure 3.2, there would be two terms in the sum over j, with the two atoms located at $\mathbf{R}_1 = \mathbf{0}$ and $\mathbf{R}_2$. When the lattice is periodic, $\mathbf{G}$ can be rewritten in terms of any set of translation vectors that generate the lattice. In three dimensions the translation vectors $\mathbf{a}$, $\mathbf{b}$, and $\mathbf{c}$ are often used to define the crystal axes. These vectors are not necessarily orthogonal, and their relationship to the Cartesian coordinates $\mathbf{x}$, $\mathbf{y}$, and $\mathbf{z}$ depends on the symmetry properties of the lattice. In three dimensions then,

$$\mathbf{G} = n_1\mathbf{a} + n_2\mathbf{b} + n_3\mathbf{c} \tag{3.5}$$

where n is an integer, and

$$\begin{aligned} S &= \frac{S_0}{r}\sum_{n_1}\sum_{n_2}\sum_{n_3}\sum_{j} f_j e^{i\mathbf{Q}\cdot(n_1\mathbf{a}+n_2\mathbf{b}+n_3\mathbf{c})} e^{i\mathbf{Q}\cdot\mathbf{R}_j} \\ &= \frac{S_0}{r}\sum_{n_1} e^{in_1\mathbf{Q}\cdot\mathbf{a}}\sum_{n_2} e^{in_2\mathbf{Q}\cdot\mathbf{b}}\sum_{n_3} e^{in_3\mathbf{Q}\cdot\mathbf{c}}\sum_{j} f_j e^{i\mathbf{Q}\cdot\mathbf{R}_j}. \end{aligned} \tag{3.6}$$

The three sums over the components of the crystal lattice vectors extend over the size of the crystal. The sum is a geometric series with the closed form expression

$$\sum_{n=0}^{N} e^{n\phi} = \frac{1-e^{iN\phi}}{1-e^{i\phi}}, \tag{3.7}$$

where the phase argument, for example in the sum for $\mathbf{a}$, is $\phi = \mathbf{a}\cdot\mathbf{Q}$. The intensity at the observation point is $I = SS^*$, turning the sum over each of the lattice vectors in Equation (3.6) into

$$|\sum_{n=0}^{N} e^{n\phi}|^2 = \frac{1-\cos(N\phi)}{1-\cos(\phi)} = \frac{\sin^2(\frac{N\phi}{2})}{\sin^2(\frac{\phi}{2})}. \tag{3.8}$$

The upper bound N on the sum is set by the size of the crystal, or crystallite in the case of a powdered or mosaic crystal. In the limiting case of $N \to \infty$, Equation (3.8) approaches a delta function of the argument. For real crystals with finite domains the scattered intensity is appreciably nonvanishing only when $\phi = m\pi$, for integer m. This is the diffraction condition. If the scattering is interpreted as a specular reflection from planes of atoms in the crystal, as illustrated in Figure 3.3, with spacing d perpendicular to $\mathbf{Q}$, and if θ is defined as the angle between $\mathbf{k}_i$ (and $\mathbf{k}_f$) and the planes as then the diffraction condition can be written

$$2d\sin\theta = m\lambda, \tag{3.9}$$

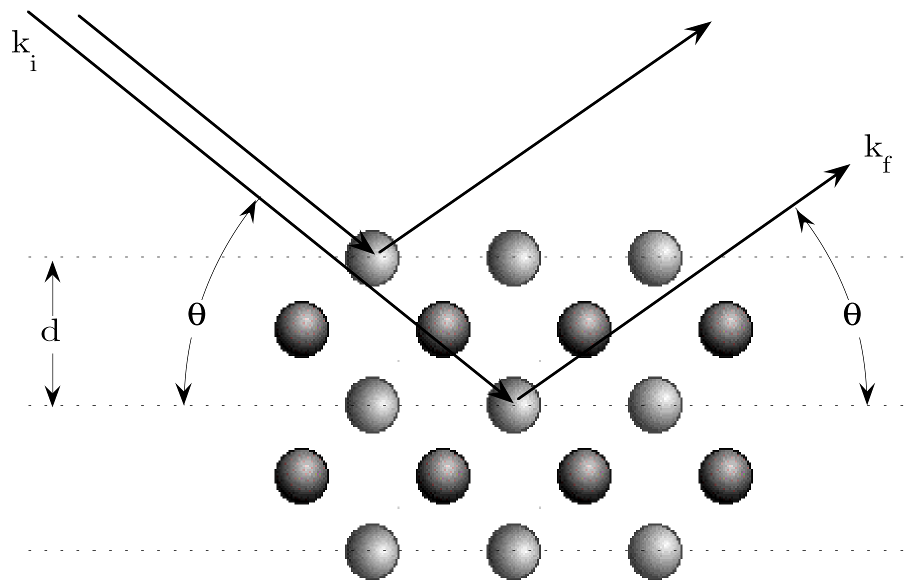

Figure 3.3: Bragg scattering from planes of atoms. The the incident $\mathbf{k}_i$ and outgoing $\mathbf{k}_f$ rays form equal angles θ with planes of atoms in the crystal. When the spacing between the planes is d, the diffraction condition can be written $d \sin\theta = n(2\pi/k) = n\lambda$, where $\lambda = 2\pi/k$ is the wavelength of the light.

which is the Bragg condition for diffraction of light with wavelength $\lambda = 2\pi/k$ from atomic planes of spacing d.

3.2 The crystallographic structure factor

The remaining sum in Equation (3.6) is the scattering amplitude from the atoms in the unit cell at each of the lattice sites

$$F(\mathbf{Q}, E) = \sum_j f_j(E) e^{i\mathbf{Q}\cdot\mathbf{R}_j}. \tag{3.10}$$

The basis vectors $\mathbf{R}_j$ in Equation (3.10) are the positions of the individual atoms in the unit cell with respect to a local origin of coordinates; the atomic scattering amplitude $f_j(\mathbf{Q}, E) = f_0(\mathbf{Q}) + \Delta f(E)$ was described in Section 2.1.3. The space filling unit cell in a three-dimensional periodic crystal is limited by geometry and symmetry to a countable number of possibilities. All of these are different decorations of fourteen basic space filling lattices called the Bravais lattices. The sum F is called the crystallographic structure factor, or structure factor, because it contains information about the structure of the material. The Bravais lattice and the point symmetry properties of the crystal determine where the diffraction peaks will be located, but intensities of the peaks are modulated by the structure factor.

3.2.1 The effects of thermal disorder on DAFS

Equation (3.10) assumes perfect long-range periodicity of the atoms. In a real crystal at finite temperatures the atoms may be displaced from their equilibrium positions. A complete treatment of the effects of disorder on DAFS would have to include the effects of both static disorder and thermal disorder. I will only consider thermal disorder in the following discussion, and only so far as to attempt to justify the simple expressions I have used for the DAFS Debye-Waller factors. To the best of my knowledge, the subject of disorder factors in the DAFS signal has not been addressed before now. The interested reader is encouraged to take pencil in hand and have a go at it. I found the treatment of the normal mode expansion for harmonic vibrations in a crystal in Chapter 5 of James [38], and the article on correlation functions in x-ray and neutron scattering by S. Dietrich [50] both to be very helpful.

The time scale for a non-resonant elastic scattering event goes as $t \sim \hbar/E_\gamma$, which is on the order of 5×10^{-19} seconds for 9000 eV photons. The time scale for resonant scattering, on the other hand, goes as the lifetime of the corehole, which is on the order of 2×10^{-15} seconds for the Cu K-shell resonance. Both of these times are small compared with the period of thermal motion for an atom, which is on the order of 10^{-12} seconds, so that the measured diffracted intensity at any time amounts to an instantaneous *snapshot* of the crystal. Since the diffracted intensity is measured over times that are long compared to the motion of the atoms, the observed signal amounts to an *ensemble average* of the squared magnitude of the structure factor over all of the allowed configurations of the crystal and is equivalent[1] to a time average taken over times that are long compared to the motion of the atoms. Starting from Equation (3.10), let the atoms take on small time-dependent displacements from their equilibrium positions $\mathbf{R} \rightarrow \mathbf{R} + \mathbf{u}(\mathbf{t})$.

$$\begin{aligned} \langle I(\mathbf{Q}) \rangle &\propto \langle F(\mathbf{Q}) F^*(\mathbf{Q}) \rangle \qquad (3.11) \\ &= \left\langle \sum_j f(\mathbf{Q}) e^{i\mathbf{Q}\cdot(\mathbf{R}_j + \mathbf{u}_j)} \sum_{j'} f^*(\mathbf{Q}) e^{-i\mathbf{Q}\cdot(\mathbf{R}_{j'} + \mathbf{u}_{j'})} \right\rangle \end{aligned}$$

[1] Ergodic theorem

The equilibrium positions of the atoms do not vary with time, so the time dependence separates term-by-term in the sum

$$\langle FF^* \rangle = \sum_j \sum_{j'} ff^* e^{i\mathbf{Q}\cdot(\mathbf{R}_j - \mathbf{R}_{j'})} \left\langle e^{i\mathbf{Q}\cdot(\mathbf{u}_j - \mathbf{u}_{j'})} \right\rangle . \tag{3.12}$$

The thermal average of the exponent in Equation (3.12) can be evaluated either in terms of the moments of the displacement $p_{jj'} = \mathbf{Q} \cdot (\mathbf{u}_j - \mathbf{u}_{j'}) = Q^\alpha u^\alpha_{jj'}$

$$\left\langle e^{ip_{jj'}} \right\rangle = \sum_{n=0}^{\infty} \frac{\langle (ip_{jj'})^n \rangle}{n!} \tag{3.13}$$

or in a cumulant expansion

$$\left\langle e^{ip_{jj'}} \right\rangle = e^{\left(\sum_{n=1}^{\infty} \frac{(i)^n}{n!} C_n\right)} \tag{3.14}$$

where the *cumulants* C_n are expressed in terms of the moments; the first three are

$$\begin{aligned}
C_1 &= \langle (p_{jj'}) \rangle &(3.15)\\
C_2 &= \left\langle (p_{jj'})^2 \right\rangle - \langle (p_{jj'}) \rangle^2 = \left\langle (p_{jj'})^2 \right\rangle - C_1^2 &(3.16)\\
C_3 &= \left\langle (p_{jj'})^3 \right\rangle - 3 \left\langle (p_{jj'})^2 \right\rangle \langle (p_{jj'}) \rangle + 2 \langle (p_{jj'}) \rangle^3 &\\
&= \left\langle (p_{jj'})^3 \right\rangle - 2C_1C_2 - C_1^3. &(3.17)
\end{aligned}$$

The moments are calculated by integrating over the probability distribution of the displacement

$$\langle u^n \rangle = \int_{-\infty}^{\infty} P(u) u^n du. \tag{3.18}$$

The probability distribution function $P(u)$ might be, for example, a Boltzman distribution, based on the energy of displacement for an atom in the lattice, or a harmonic distribution, based on the vibrational modes of the crystal. The moment expansion has been the conventional approach taken in neutron and x-ray diffraction but the cumulant expansion has the special advantage that for a Gaussian distribution of the displacements, only one term in the sum survives and the expansion is exact.

When the resonant scattering is taken into account, the scattering amplitude takes on a sum over the backscattering paths off of neighbors of the excited atoms. There are three types of terms that need to be taken into account for considering the effects of thermal disorder on the DAFS. The first terms are the sum over all of the atoms in the unit cell excluding the backscattering

$$\begin{aligned} \langle F_0 F_0^* \rangle &= \sum_j \sum_{j'} (f_0 + f'_a + i f''_a)_j (f_0 + f'_a - i f''_a)_{j'} \times \\ & \qquad e^{i\mathbf{Q}\cdot(\mathbf{R}_j - \mathbf{R}_{j'})} \left\langle e^{i\mathbf{Q}\cdot(\mathbf{u}_j - \mathbf{u}_{j'})} \right\rangle . \end{aligned} \tag{3.19}$$

The effects of disorder on this part of the sum follow exactly the arguments for x-ray diffraction. Debye-Waller factors $\exp(-M_j)$ for the individual atoms in Equation (3.19) are formally included in the structure factor sum. The argument of the exponent in the harmonic approximation corresponds to

$$\begin{aligned} M_j &= \frac{1}{2} \left\langle u_j^2 \right\rangle \mathbf{Q} \cdot \mathbf{Q} \\ &= B_j \left(\frac{Q^2}{4\pi} \right)^2 \end{aligned} \tag{3.20}$$

where B_j are the crystallographic Debye-Waller factors in the form most commonly found in the literature. The term $\left\langle u_j^2 \right\rangle$ is the time average displacement of the j^{th} atom in the direction of $\hat{\mathbf{Q}}$ and the correlation term in Equation (3.19) has been dropped[2].

In addition to the leading order Thomson sum there are two cross-terms between the resonant atoms and all of the atoms in the unit cell which I will discuss here, and one term that goes as $\chi(E)^2$ which I will neglect. Because $\chi(E)$ is zero for the off-resonance atoms, the formal double sum in Equation (3.19) is restricted in one index to the resonant subset of atoms in the cell. When there is only one resonant atom in the unit cell, this is only a single term. I will keep the expressions for the combined sums formally complete, but this is something to bear in mind. The two cross-terms are of the form, without loss of generality,

$$\begin{aligned} \langle F_0 \Delta F^* \rangle &= \sum_j \sum_{j'} (f_0 + f'_a + i f''_a)_j (f''_0)_{j'} e^{i\mathbf{Q}\cdot(\mathbf{R}_{jj'})} \sum_i \frac{t_i^*(\theta)}{k} e^{i\delta_i} \times \\ & \qquad \left\langle (\hat{\mathbf{e}} \cdot (\mathbf{R}_{ij'} + \mathbf{u}_{ij'}))^2 e^{i\mathbf{Q}\cdot\mathbf{u}_{jj'}} \frac{e^{-ik|\mathbf{R}_{ij'} + \mathbf{u}_{ij'}|}}{|\mathbf{R}_{ij'} + \mathbf{u}_{ij'}|^2} \right\rangle \end{aligned} \tag{3.21}$$

where $\chi(E)$ has been replaced with the sum over photoelectron backscattering paths from Equation (2.54). As a first approximation $\langle F_0 \Delta F^* \rangle$ is insensitive to the displace-

[2] The position correlations can be shown to contribute to the diffuse scattering in the harmonic approximation, but they do not contribute to the falloff in the Bragg peak intensities with $\mathbf{Q}$ [38].

ments $\mathbf{u}_{ij'}$ that appear in the denominator. The bond-length disorder is approximated by an expansion about the average bond length

$$|\mathbf{R}_{ij'} + \mathbf{u}_{ij'}| \quad \sim \quad |\mathbf{R}_{ij'}| + \hat{\mathbf{R}}_{ij'} \cdot \mathbf{u}_{ij'} \tag{3.22}$$

with the understanding that $\mathbf{R}_{ij'}$ and $\hat{\mathbf{R}}_{ij'}$ refer to the *average* bond between the resonant atom and the backscattering neighbor. This is equivalent to keeping only the leading terms and neglecting any change in direction of the bond with displacement of the atoms. Taking all of the time-independent terms outside the thermal average, the thermal disorder factors for each term in the sum are

$$\begin{aligned} \langle F_0 \Delta F^* \rangle \quad = \quad & \sum_j \sum_{j'} \sum_i (f_0 + f'_a + i f''_a)_j (f''_0)_{j'} e^{i\mathbf{Q}\cdot\mathbf{R}_{jj'}} \frac{f_i^*(\theta)}{kR_{ij'}^2} e^{i(kR_{ij'}+\delta_i)} \\ & (\hat{\mathbf{e}} \cdot \mathbf{R}_{ij'})^2 \left\langle e^{i\mathbf{Q}\cdot\mathbf{u}_{jj'}} e^{-ik\mathbf{R}_{ij'}\cdot\mathbf{u}_{ij'}} \right\rangle . \end{aligned} \tag{3.23}$$

Now we have only to consider the thermal average of the expression in the angled brackets in Equation (3.23). Figure 3.4 shows the geometry of this expression. The atoms j' are the resonant atoms and all of the disorder terms can be referenced to them. These are equivalent to the central atom in an XAFS calculation. The summation is restricted to $j \neq j'$ and $i \neq j'$, but it is possible to have $i = j$. For modelling DAFS fine structure with existing XAFS and crystallography analysis programs we would like to write the thermal average as

$$\left\langle e^{i\mathbf{Q}\cdot\mathbf{u}_{jj'} - ik\mathbf{R}_{ij'}\cdot\mathbf{u}_{ij'}} \right\rangle = \left\langle e^{i\mathbf{Q}\cdot\mathbf{u}_{jj'}} \right\rangle \left\langle e^{-ik\mathbf{R}_{ij'}\cdot\mathbf{u}_{ij'}} \right\rangle . \tag{3.24}$$

If the correlations are negligible then the crystallographic Debye-Waller factor for each type of atom can be formally included in the argument of the exponent of the structure factor, as in Equation (3.19), and the XAFS Debye-Waller factors would appear only in the argument of the path contributions to the fine-structure:

$$e^{-k^2\sigma^2} = e^{-\frac{1}{2}k^2\left\langle(\mathbf{R}_{ij'}\cdot\mathbf{u}_{ij'})^2\right\rangle} \tag{3.25}$$

following the standard formalism for XAFS calculations [51].

What terms have to be thrown out in order to achieve this desirable state of simple harmony? Drawing from work on correlations in disorder for neutron and x-ray scattering [49, 50] the cumulant expansion when there is more than one stochastic variable in the argument is given by

$$\left\langle e^{x_1+x_2} \right\rangle = \langle e^{x_1} \rangle \langle e^{x_2} \rangle \, e^{(\langle x_1 x_2 \rangle_c + \frac{1}{2}\left\langle x_1^2 x_2 x_1 x_2^2 \right\rangle_c + \frac{1}{4}\left\langle x_1^2 x_2^2 \right\rangle_c + \ldots)} \tag{3.26}$$

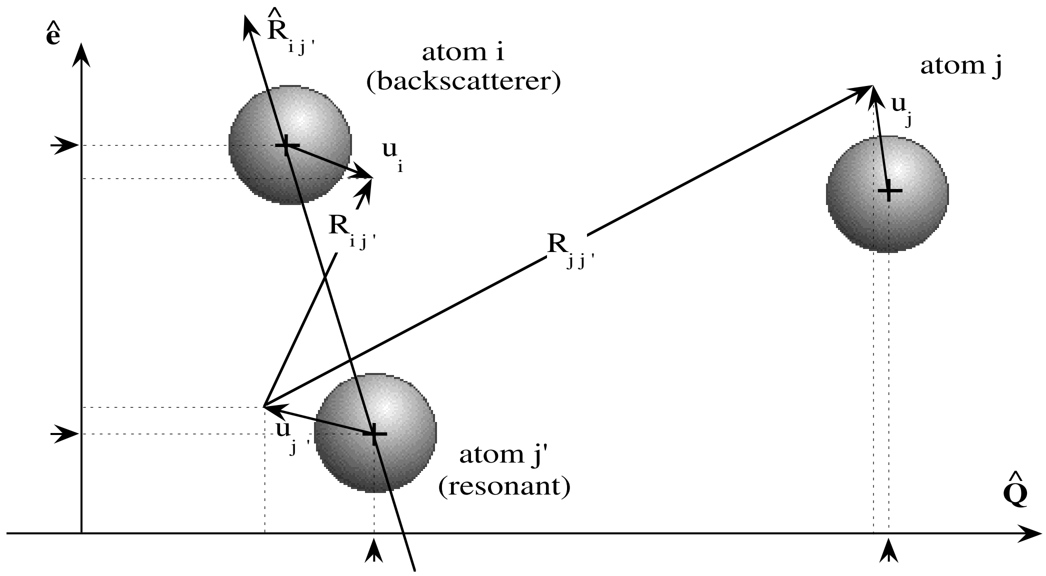

Figure 3.4: The Debye-Waller factors are determined by considering the effect of displacing the atoms from their equilibrium positions. In DAFS, there are cross-terms which include both positional disorder, from the structure factor sum, and bond-length disorder, from the sum over photoelectron backscattering paths around the resonant atoms. All of the displacements can be referenced to the resonant atoms j'. The bond-length disorder $\mathbf{u}_i$ and $\mathbf{u}_{j'}$ is projected onto the equilibrium bond direction $\hat{\mathbf{R}}_{ij'}$ for the XAFS-like Debye-Waller factors in the fine structure, making the approximation that the change in the bond direction with disorder is small. Path-by-path, the fine structure terms are further reduced by the polarization dependence of the resonance scattering cross-section $(\hat{\mathbf{e}} \cdot \mathbf{R}_{ij'})^2$. The positional disorder $\mathbf{u}_j$ and $\mathbf{u}_{j'}$ is projected onto $\hat{\mathbf{Q}}$ for the diffraction Debye-Waller factors.

where the $\langle\rangle_c$ in the argument of the exponent in terms of the moments are [50], for example

$$\begin{aligned} \langle x_1 x_2 \rangle_c &= \langle x_1 x_2 \rangle - \langle x_1 \rangle \langle x_2 \rangle \\ \langle x_1 x_2 x_3 \rangle_c &= \langle x_1 x_2 x_3 \rangle - \langle x_1 \rangle \langle x_2 x_3 \rangle - \langle x_2 \rangle \langle x_1 x_3 \rangle \\ &\quad - \langle x_3 \rangle \langle x_1 x_2 \rangle + 2 \langle x_1 \rangle \langle x_2 \rangle \langle x_3 \rangle . \end{aligned} \tag{3.27}$$

If $x_n = x$ Equation (3.26) reduces to the cumulant expansion Equations (3.15-3.17) for one stochastic variable. Considering only the leading order correlation between the diffraction and fine-structure disorder, in terms of the vector disorder of the atoms in the crystal

$$e^{\left\langle (i\mathbf{Q}\cdot\mathbf{u}_{jj'})(-ik\mathbf{R}_{ij'}\cdot\mathbf{u}_{ij'})\right\rangle_c} = e^{\left(\left\langle (\mathbf{Q}\cdot\mathbf{u}_{jj'})(k\mathbf{R}_{ij'}\cdot\mathbf{u}_{ij'})\right\rangle - \left\langle \mathbf{Q}\cdot\mathbf{u}_{jj'}\right\rangle \left\langle k\mathbf{R}_{ij'}\cdot\mathbf{u}_{ij'}\right\rangle\right)}. \qquad (3.28)$$

For harmonic displacement, the second terms in the argument of the exponent on the right of Equation 3.28 both vanish. The first term does not vanish, and allows the possibility that $i = j$. Notice, however, that the dot products in the argument pick out different parts of the displacements. The fine structure displacements have the largest effect when they are directed along the bond direction and, furthermore, the polarization dependence of the fine structure preferentially weights paths that are perpendicular to $\mathbf{Q}$. The diffraction displacements, on the other hand, have the largest effect when they are parallel to $\mathbf{Q}$. When the bond is aligned with $\hat{\mathbf{e}}$, these projection are anticorrelated, the one being sine-like and the other being cosine-like.

For all of the DAFS analysis in this dissertation, I have assumed that the effects of thermal disorder in the average positions of the atoms are calculationally separable from the effects of thermal disorder in the bond lengths. This facilitates modelling the smooth part of the DAFS with a simple expression for the structure factor and modelling the fine structure with existing XAFS analysis codes. In light of a possible unification of diffraction and XAFS, however, the theoretical problem begs to be carefully re-examined.

3.2.2 Structure factor model for DAFS

In order to analyze DAFS fine structure using XAFS analysis tools, $\Delta f(E)$ needs to be isolated from the measured intensity. It is convenient for modelling DAFS data to split the structure factor sum into resonant and non-resonant parts. Using the results from Section 2.3.1, Equation (2.26) can be rewritten as

$$\begin{aligned} F(\mathbf{Q}, E) &= \sum_j (f_{0,j} + \Delta f_{a,j})\, e^{i\mathbf{Q}\cdot\mathbf{R}_j} e^{-M_j} + \sum_{j'} f_{0,j'} e^{i\mathbf{Q}\cdot\mathbf{R}_{j'}} e^{-M_{j'}} \\ &\qquad + \sum_{j'} \left(\Delta f_{a,j'} + f''_{0,j'}\chi_{j'}\right) e^{i\mathbf{Q}\cdot\mathbf{R}_{j'}} e^{-M_{j'}} \\ &= F_0 + \Delta F \end{aligned} \qquad (3.29)$$

with the summation indices j over the non-resonant atoms, and j' over the resonant atoms. The Thomson scattering from the resonant atoms is part of the non-resonant

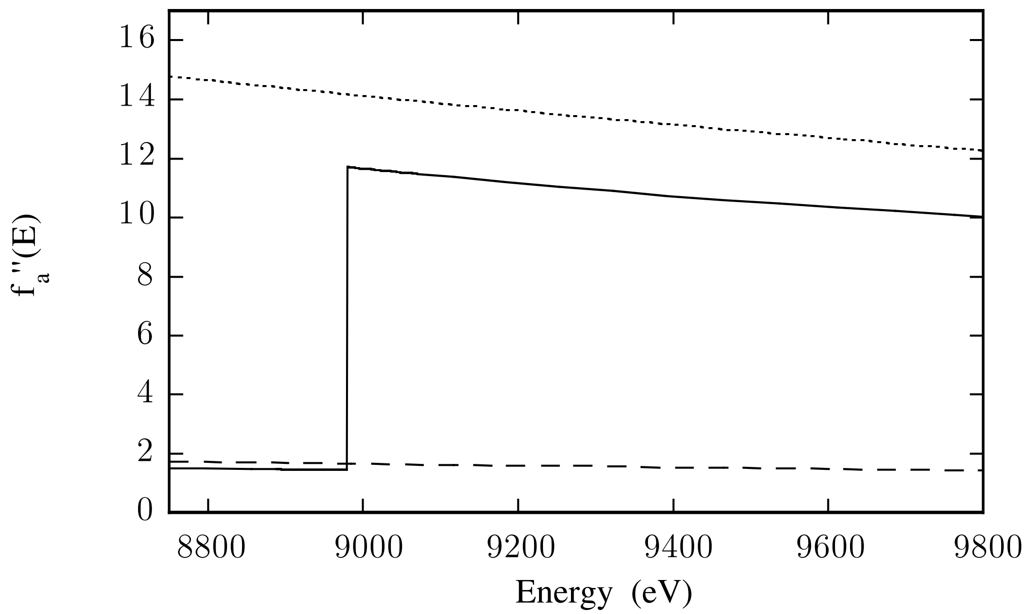

Figure 3.5: The $f''(E)$ contribution from the off-resonance atoms in $YBa_2Cu_3O_7$. The $f''_a(E)$ contribution to F_0 for $YBa_2Cu_3O_{6.8}$ in the forward direction the two Ba atoms (small dashes), and the single Y atom (large dashes) overplotted with the contribution from the three Cu atoms (solid line). The resonant scattering from the heavy atoms *off-resonance* determines the energy dependence of the non-resonant amplitude F_0. For monoatomic materials, there is no energy dependence to F_0. For multi-atom materials, such as $YBa_2Cu_3O_7$, the energy dependence of F_0 is small and approximately linear.

amplitude F_0. When the DAFS is from a monoatomic material, F_0 in Equation (3.29) is strictly energy independent. When there are several different types of atoms in the unit cell F_0 depends both on $\mathbf{Q}$ through f_0, and on E through corrections $\Delta f_a(E)$ from the *off-resonance* atoms, *e.g.*, the Ba atoms in $YBa_2Cu_3O_{7-\delta}$. Far from resonance $\Delta f_a(E)$ has only a weak energy dependence and, over the $\sim$ 1200 eV range of a DAFS scan, can be treated as roughly energy independent. Figure 3.5 compares the contribution to F_0 for $YBa_2Cu_3O_7$ from the two barium atoms and the one yttrium atom to the calculated $f''(E)$ from the three copper atoms. The Y contribution is nearly zero and the $2 \times$ Ba contribution, though larger than the step in $2 \times$ Cu $f''(E)$, has a only simple linear dependence on E over the energy range shown. For modelling the DAFS intensity, is convenient to write the non-resonant part of Equation (3.29) as a magnitude times a phase

$$F_0 = |F_0|\, e^{i\Phi_0} \tag{3.30}$$

with $|F_0|$ and Φ_0 treated as energy independent quantities. This simplification limits the amount of *a priori* information needed about the structure factor sum. If there is known to be a small linear energy dependence in F_0, such as when there are large Z off-resonance atoms, this can be accounted for by introducing a linear correction to a model for $|F_0|$. The resonant part of the structure factor is

$$\Delta F(\mathbf{Q}, E) = \sum_{j'} \left[\Delta f_a(E) + f_0''(E)\chi(E)\right]_{j'} e^{i\mathbf{Q}\cdot\mathbf{R}_{j'}} e^{-M_{j'}} \tag{3.31}$$

which depends on both E and on $\mathbf{Q}$. The integrated Bragg peak intensity $I(\mathbf{Q}, E)$ is proportional to the squared magnitude of the structure factor, that is

$$\begin{aligned} I(\mathbf{Q}, E) &\propto |F_0(\mathbf{Q}) + \Delta F|^2 \qquad (3.32)\\ &= |F_0|^2 \left(\left(\cos\Phi_0 + \frac{1}{|F_0|}\mathrm{Re}[\Delta F] \right)^2 + \left(\sin\Phi_0 + \frac{1}{|F_0|}\mathrm{Im}[\Delta F] \right)^2 \right). \end{aligned}$$

The complete expressions for the real and imaginary parts of ΔF in the most general case are

$$\begin{aligned} \mathrm{Re}[\Delta F] &= \Bigg(\sum_{j'} e^{-M_{j'}} \left[f_a' \cos(\mathbf{Q}\cdot\mathbf{R}_{j'}) - f_a'' \sin(\mathbf{Q}\cdot\mathbf{R}_{j'}) \right] \qquad (3.33)\\ &\quad + \sum_{j'} e^{-M_{j'}} \left[f_0''\chi' \cos(\mathbf{Q}\cdot\mathbf{R}_{j'}) - f_0''\chi'' \sin(\mathbf{Q}\cdot\mathbf{R}_{j'}) \right] \Bigg) \end{aligned}$$

and

$$\begin{aligned} \mathrm{Im}[\Delta F] &= \Bigg(\sum_{j'} e^{-M_{j'}} \left[f_a' \sin(\mathbf{Q}\cdot\mathbf{R}_{j'}) + f_a'' \cos(\mathbf{Q}\cdot\mathbf{R}_{j'}) \right] \qquad (3.34)\\ &\quad + \sum_{j'} e^{-M_{j'}} \left[f_0''\chi' \sin(\mathbf{Q}\cdot\mathbf{R}_{j'}) + f_0''\chi'' \cos(\mathbf{Q}\cdot\mathbf{R}_{j'}) \right] \Bigg). \end{aligned}$$

Because the intensity is proportional to the squared magnitude of the scattering amplitude, the real and imaginary parts of ΔF are mixed in such a way that there will generally be cross-terms with the product $f_a' f_a''$. The exception is when the sublattice of resonant atoms in the crystal has a center of symmetry parallel to $\mathbf{Q}$.

This causes the sum over the imaginary components of the resonant atom phase factors to vanish, that is

$$\sum_{j'} \sin(\mathbf{Q} \cdot \mathbf{R}_{j'}) e^{-M_{\mathbf{r}}} = 0. \tag{3.35}$$

In this case, the real and imaginary parts of ΔF are purely sums over the real and imaginary parts of Δf, respectively, and are therefore related by the Kramers-Krönig dispersion relations. Since the Kramers-Krönig integrals are based on the crossing symmetry of $f'(E)$ and $f''(E)$, cross-terms will not satisfy the same relations. They also complicate direct solution of the measured intensity and normalization of the fine-structure. I have not been able to derive closed-form algebraic solution that would allow application of the iterative dispersion algorithm to intensity data from a material with an asymmetric resonant sublattice, nor have I seen a solution elsewhere. I will limit my discussion to the case where the partial sum over the $\sin(\mathbf{Q} \cdot \mathbf{R})$ terms vanishes since that is most immediately applicable to the physical systems studied in this thesis. When this symmetry does not exist, a different approach to the analysis needs to be taken. The entire energy-dependent amplitude, including the fine-structure, can be forward modeled using FEFF and the average structure factor. A program for fitting the whole DAFS intensity signal in energy space is discussed briefly in Chapter 8.

The smooth part of the resonance response has approximately the same shape for all of the resonant atoms, with the exception of a possible shift in position due to differences in valence state for inequivalent resonant sites. In general, $f'_a(E)$ and $f''_a(E)$ can be brought outside of the sum[3] and the resonant part of Equation (3.29) becomes

$$\begin{aligned} \Delta F &= \sum_{j'} [\Delta f_a + f''_0 \chi]_{j'} e^{i\mathbf{Q}\cdot\mathbf{R}_{j'}} e^{-M_{j'}} \\ &= \Delta f_a \sum_{j'} e^{i\mathbf{Q}\cdot\mathbf{R}_{j'}} e^{-M_{j'}} + f''_0 \sum_{j'} \chi_{j'} e^{i\mathbf{Q}\cdot\mathbf{R}_{j'}} e^{-M_{j'}} \\ &= \Delta f_a \alpha + f''_0 \sum_{j'} \chi_{j'} e^{i\mathbf{Q}\cdot\mathbf{R}_{j'}} e^{-M_{j'}} \end{aligned} \tag{3.36}$$

where the coefficient $\alpha(\mathbf{Q})$ is defined by

$$\alpha(\mathbf{Q}) = \sum_{j'} \cos(\mathbf{Q} \cdot \mathbf{R}_{j'}) e^{-M_{j'}}. \tag{3.37}$$

[3] This step is completely justified when the differential form of the Kramers-Krönig integrals are used, so long as $\Delta f_a(E)$ is analytic and the remainder $\Delta f(E) - \Delta f_a(E)$ is strictly band-limited.

The resonant atom partial structure factor, ΔF, can now be rescaled to the signal from a single atom by dividing $\alpha(\mathbf{Q})$ out of ΔF to obtain the crystallographically *mixed* scattering amplitude Δf_{w}, given by

$$\begin{aligned}\Delta f_{\mathrm{w}} &= \frac{1}{\alpha}\Delta F \\ &= \Delta f_a + \frac{f_0''}{\alpha}\sum_{j'}\chi_r \cos(\mathbf{Q}\cdot\mathbf{R}_{j'})e^{-M_{j'}} \\ &= \Delta f_a + f_0''\chi_{\mathrm{w}}.\end{aligned} \tag{3.38}$$

Since $\alpha(\mathbf{Q})$ is purely real the real and imaginary parts of ΔF can be simplified and the intensity, Equation (3.33), can be written as

$$\begin{aligned}I(\mathbf{Q},E) &\propto |F_0+\Delta F|^2 \\ &= |F_0|^2\left|e^{i\Phi_0}+\frac{\alpha}{|F_0|}\Delta f_{\mathrm{w}}\right|^2 \\ &= |F_0|^2\left((\cos\Phi_0+\beta f_{\mathrm{w}}')^2+(\sin\Phi_0+\beta f_{\mathrm{w}}'')^2\right)\end{aligned} \tag{3.39}$$

where $\beta \equiv \beta\mathbf{Q} = \alpha/|F_0|$. The parameterization of the structure factor in Equation (3.40) is the starting place for a computer model of the DAFS intensity. I will begin from this equation in Chapters 5 and 6, for analyzing DAFS data from Cu metal and $YBa_2Cu_3O_{6.8}$, respectively.

3.3 The DAFS χ_{w} function

This is a good place to stop and examine the nature of the crystallographically mixed $\chi_{\mathrm{w}}(\mathbf{Q},E)$ that we have just distilled from the structure factor algebra. Note that the smooth part of mixed resonant scattering amplitude $\Delta f_{\mathrm{w}}(\mathbf{Q},E)$ in Equation (3.38) is just the single atom $\Delta f_a(E)$. The way that the structure factor sum is broken up in Equation (3.40), all of the dependence on atomic positions of the resonant atoms within the unit cell is contained in $\chi_{\mathrm{w}}(\mathbf{Q},E)$. For monoatomic materials, or materials in which all of the resonant atoms have the same local environment, the mixing coefficient for the i^{th} site α_i/α is unity and $\chi_{\mathrm{w}}(\mathbf{Q},E) \equiv \chi(E)$. However, when there are two or more inequivalent sites, α_i is generally not the same as α. This can cause $f_{\mathrm{w}}''(\mathbf{Q},E)$ and $\chi_{\mathrm{w}}''(\mathbf{Q},E)$ to behave very differently from the $\mu(E)$ and $\chi''(E)$ functions of XAFS, in ways that would be unphysical for a true absorbance function. For example, is that when α is small compared to α_i, the amplitude of the oscillations in χ_{w} can be *larger* than the step height of $f_a''(E)$.

The ratios α_i/α are the *mixing coefficients* for the individual site response functions, and χ_{w} can be rewritten

$$\chi_{\mathrm{w}}(\mathbf{Q}, E) = \sum_i W_{i,\mathbf{Q}} \chi_i(E). \tag{3.40}$$

Since the $W_{i,\mathbf{Q}}$ are energy independent, Equation (3.40) represents a system of linear equations of dimension $N_{\mathbf{Q}} \times N_i$, where $N_{\mathbf{Q}}$ is the number of Bragg peaks measured and N_i is the number of inequivalent sites in the unit cell, *e.g.*, for the two-site problem:

$$\begin{pmatrix} \chi_{\mathrm{w}}(\mathbf{Q}_1, E) \\ \ddots \\ \chi_{\mathrm{w}}(\mathbf{Q}_N, E) \end{pmatrix} = \begin{pmatrix} W_{1,\mathbf{Q}_1} W_{2,\mathbf{Q}_1} \\ \ddots \\ W_{1,\mathbf{Q}_N} W_{2,\mathbf{Q}_N} \end{pmatrix} \begin{pmatrix} \chi_1(E) \\ \chi_2(E) \end{pmatrix}. \tag{3.41}$$

If the matrix $W_{i,\mathbf{Q}}$ can be inverted, then the individual site response functions can be retrieved from DAFS data.

3.3.1 Site selectivity in DAFS

Isolating the fine structure signals from individual resonant sites within a complicated unit cell is the most powerful application of DAFS. I do not know any closed form for a limit on the number of sites that can be separated. In the simplest case of a two-site unit cell, which is demonstrated in Chapter 6 by DAFS analysis of $YBa_2Cu_3O_{6.8}$, the fine structure can nominally be isolated using only two Bragg peaks. Overdetermination of the problem only improves the quality of the fine structure functions. For a material with N_i inequivalent sites, it would be sufficient to measure the DAFS at $N_{\mathbf{Q}} = N_i$ non-degenerate reflections—non-degenerate in the sense that the matrix of mixing coefficients $W_{i,\mathbf{Q}}$ has an inverse.

In order to make linear combinations of the DAFS $\chi_{\mathrm{w}}(\mathbf{Q}, E)$, the individual site fine-structure functions $\chi_i(E)$ need to be the same at each value of $\mathbf{Q}$. Since the DAFS fine-structure depends on both the incident and outgoing photon polarization directions, the geometry of the experiment needs special consideration when site separation is the goal. If $\mathbf{Q}$ is confined to a plane perpendicular to $\hat{\mathbf{e}}$, then $\hat{\mathbf{e}} = \hat{\mathbf{e}}'$ and the DAFS polarization $(\hat{\mathbf{e}} \cdot \hat{\mathbf{R}})(\hat{\mathbf{e}}' \cdot \hat{\mathbf{R}})$ reduces to the XAFS polarization $(\hat{\mathbf{e}} \cdot \hat{\mathbf{R}})^2$. Polarization effects are unimportant when the material has high symmetry, such as for Cu metal, but for low symmetry materials, such as $YBa_2Cu_3O_7$, polarization effects will cause the $\chi_{\mathrm{site}}(k)$ functions to change with the reflection unless the direction in reciprocal space is confined to the plane perpendicular to $\hat{\mathbf{e}}$. The choice $\mathbf{Q} \perp \hat{\mathbf{e}}$ insures that there are *no more than* N different response functions[4] to consider. The resulting site-separated response functions are equivalent to the results that would be obtained from polarized XAFS in the absence of the other sites.

3.3.2 Spatial selectivity in DAFS

The fine structure measured in the diffraction channel contains local structural information solely about the resonant atoms contributing to the specific Bragg peak. When the diffraction condition is satisfied at a unique value of $\mathbf{Q}$ for some macroscopic domain in an inhomogeneous sample, the fine structure from that region of the sample can be isolated, even in the presence of other scatterers and absorbers of the same atomic species. For example, isolation of the fine structure from components of a mixed powder is possible by measuring the DAFS at a Bragg peak due to one of the materials in the mix. Isolation of the fine structure from an inhomogeneous alloy is a feature that cannot be matched by the incoherent XAFS processes. This effect has recently been used to measure the fine structure from a buried Si/B($\sqrt{3} \times \sqrt{3}$)R30° reconstructed interface [16]; from a single buried layer in a multilayer $In_xGa_{1-x}As$ alloy structure [13]; from the components of a mixed powder sample [17]; and from Ir(100)/Fe superlattices [104, 105]

3.4 Corrections to the diffraction intensity

There are several standard corrections to the integrated Bragg peak intensities that are used in crystallography and that take on slightly different forms when the intensity is measured as a continuous function of the energy. Since the development of these is covered very well in James [38] and Cullity [115] I will only mention here the special considerations that arise due to the energy dependence of the intensity, and give the specific forms of these corrections that I have used. The additional instrument-dependent correction for the total spectrometer response is discussed in Section 4.3.1.

---

[4] I am not considering the possibility of quadrupole transition effects, which have a different dependence on the photon wavevector directions and polarization. These effects are small when dipole transitions are present, and depend on both ratio of the matrix elements E1 to E2 and on the density of final states. As an example, the dramatic quadrupole effects due to the ($1s \rightarrow 3p$) transition in the pre-edge Fe K absorption of αFe_2O_3 [109, 68] are smaller than $\sim 1\%$ of the normal absorption due to the dipole transition ($1s \rightarrow 4p$).

3.4.1 Lorentz correction

The Lorentz correction is a geometric correction that comes from considering the integrated Bragg peak intensity from a finite sized crystallite. Since most diffraction and crystallography experiments are monoenergetic, the standard form for the Lorentz correction $1/\sin 2\theta$ does not take into account the energy of the incident beam. The energy-dependent Lorentz correction [47, 48], up to a constant scale factor, is given by

$$L(\mathbf{Q}, E) = \left(\frac{1}{E}\right)^3 \frac{1}{\sin 2\theta}. \tag{3.42}$$

This is the form that was used for correcting the data in this work. It is also common to see the polarization dependence of the intensity lumped together with the Lorentz correction as the Lorentz-polarization correction, but I treat the two separately.

3.4.2 Polarization dependence of DAFS

The discussion of site selectivity in Section 3.3.1 and the polarization dependence of the fine structure in Section 2.3.3 suggest that for most DAFS experiments the diffraction wavevector transfer should be confined to a plane perpendicular to the incident photon polarization direction. Under this restriction the polarization dependence of the Thomson scattering amplitude is unity, and the fine structure maintains the same path-by-path polarization dependence for all reflections. When $\hat{\mathbf{e}} \neq \hat{\mathbf{e}}'$ the Thomson scattering has the usual $\hat{\mathbf{e}} \cdot \hat{\mathbf{e}}'$ dependence, but the polarization correction to the fine structure is non-trivial since both the incident and outgoing photons couple to the local atomic bond directions. The polarization dependence of the fine structure in this case must be considered path-by-path at each $\mathbf{Q}$. While FEFF is fully capable of calculating the polarization dependence of each scattering path, the linear decomposition by direct inversion described in Section 3.3.1 is not applicable.

3.4.3 Polarization dependence in powder diffraction

Experiments on powder samples have their own special considerations. When the Bragg condition is satisfied, the incident and outgoing photon wavevectors have an orientational relationship with the diffracting planes of atoms. There is no equivalent of the XAFS powder average in synchrotron DAFS measurements; the DAFS fine-structure is always more sensitive to bonds that lie in the diffracting planes. In polarized XAFS measurements made on single crystals, the amplitude of the single scattering paths is proportional to $3(\hat{\mathbf{e}} \cdot \hat{\mathbf{R}})^2$, where $\hat{\mathbf{e}}$ is the polarization direction of the incident beam and $\hat{\mathbf{R}}$ is the direction from the central atom to the backscattering neighbor. Pickering, *et. al.* [17], have derived an *enhancement* factor for powder DAFS to account for the fact that the polarization vector prefers to lie in the diffraction plane. The amplitude of the single scattering paths is proportional to $(3\sin^2\zeta)/2$, where ζ is the angle between $\hat{\mathbf{e}}$ and the normal to the diffracting plane.

3.4.4 Absorption correction

X-rays diffracted from some small volume element deep in the sample will be attenuated by absorption along the entire length of the beam path, going into and coming out of the material. The magnitude of this *self-absorption* by the sample depends on the mass absorption coefficient $\mu(E)$, which is proportional to $f''(E)/E$ and thus contains fine structure. If the self-absorption is not correctly accounted for in the data, then the fine structure generated by the attenuation term will contribute to the fine structure of the diffraction. Since the Fourier components of the diffraction $\chi(E)$ are used to determine the local structural environment of the absorbing atoms, this can affect the analysis results. Therefore it is very important to make an accurate absorption correction to the data. All of the DAFS experiments described in this thesis used thin film samples where $t\mu \ll 1$. I will develop here the equation for the absorption correction I have used.

Geometry of the absorption correction

Consider a cross-section through the beam incident on the sample, and diffraction by a small volume element of the sample, Figure 3.6. Let the incident beam, with unit cross-sectional area and intensity I_0, be incident on the sample at angle α and scattering at angle β. Then the total linear path length traveled by the beam to scatter from the volume element $(1/\sin\alpha)dx$ at depth x is $x/\sin\alpha + x/\sin\beta$, and the attenuation is determined by integrating:

$$dI = I_0 f dV = \frac{I_0 f}{\sin\alpha} e^{-\mu x(\frac{1}{\sin\alpha}+\frac{1}{\sin\beta})} dx, \tag{3.43}$$

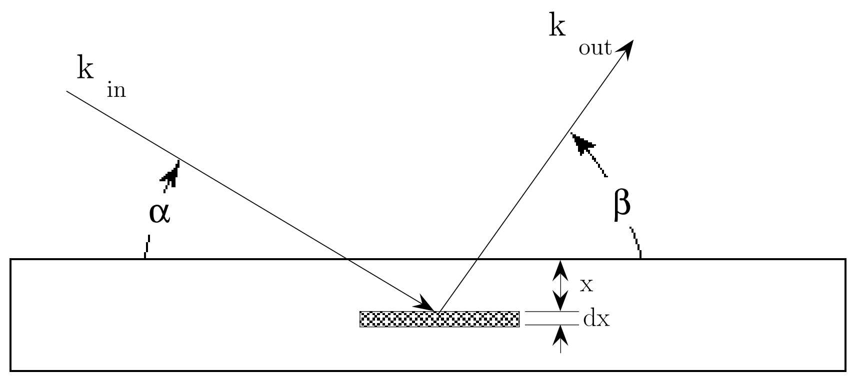

Figure 3.6: Absorption correction geometry. X-rays scattered from a small volume element at depth x within the sample are attenuated by absorption along a path of length $t' = x(\frac{1}{\sin\alpha} + \frac{1}{\sin\beta})$, which is the *effective thickness* of the film at for these angles.

where f is the fraction of the incident beam that is scattered by the volume element. If the scattering is from a film of thickness t, the integral is

$$\begin{aligned} I &= \frac{I_0 f}{\sin\alpha}\int_0^t dx e^{-\mu x\left(\frac{1}{\sin\alpha}+\frac{1}{\sin\beta}\right)} \\ &= \frac{I_0 f \sin\beta}{\sin\alpha + \sin\beta}\left(\frac{1 - e^{-\mu t\left(\frac{\sin\alpha+\sin\beta}{\sin\alpha\sin\beta}\right)}}{\mu}\right) \end{aligned} \tag{3.44}$$

The DAFS data used in this thesis was all collected at specular Bragg reflections, *i.e.*, $\alpha = \beta = \theta_B$. In this case, the absorption correction becomes

$$A(\mathbf{Q}, E, t) = \frac{I}{I_0 f} = \frac{1 - e^{-2\mu(E)t/\sin\theta_B}}{2\mu(E)}. \tag{3.45}$$

This form of $A(\mathbf{Q}, E, t)$ will be used throughout the discussion of the DAFS analysis in Chapters 5 through 6.

The effects of the absorption correction is to change the overall shape of the cusp in the intensity signal. Figure 3.7 shows the calculated effect of the smooth part of the absorption correction on the intensity without the fine structure

$$I(\mathbf{Q}, E, t) = |F(\mathbf{Q}, E)|^2 A(\mathbf{Q}, E, t) \tag{3.46}$$

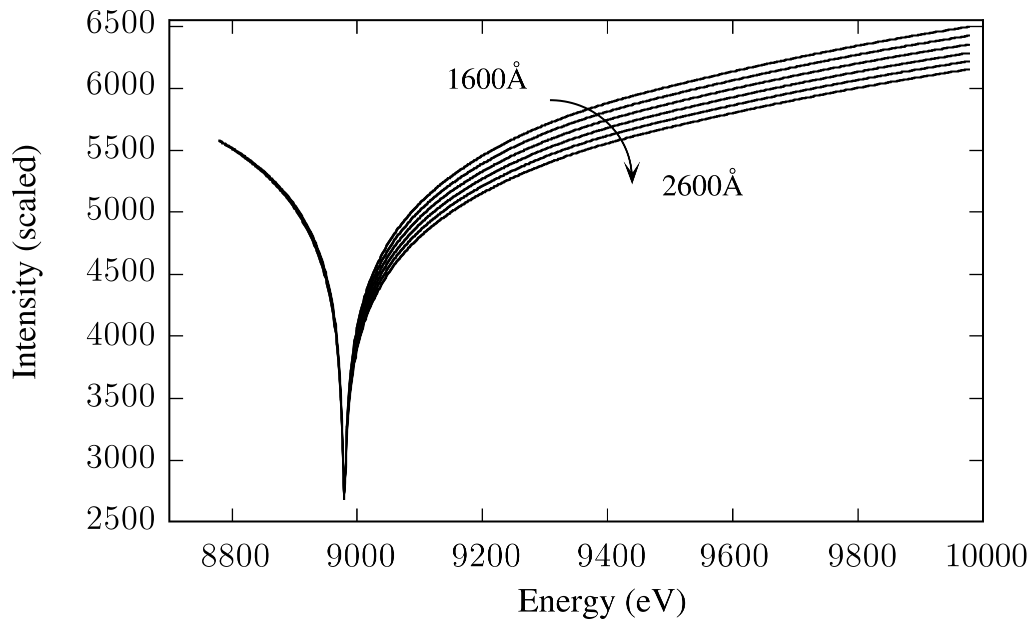

Figure 3.7: Calculated Bragg intensity for a thin film of Cu as a function of the film thickness showing the effect of the absorption correction on the shape of the cusp. Film thicknesses are t = 1600 Å through t = 2600 Å in 200 Å steps, with the direction of increasing t indicated by the arrow. The large step in the absorption correction above the K-shell energy in copper causes a drop in the diffracted intensity above the edge. Theoretical intensities were calculated for the (111) reflection from f.c.c. Cu and rescaled to the cusp depth for $E < E_0$.

for the (111) reflection from a thin film of Cu metal. Equation (3.46) was calculated for t = 1600 Å to t = 2600 Å in 200 Å steps in the argument of $A(\mathbf{Q}, E, t)$ and normalized to the cusp depth on the low energy $E < E_0$ side, before the step in the absorption correction, to highlight this effect. Changes of 10% in the film thickness are readily distinguished. The fine structure in the absorption correction will interfere with the fine structure in the structure factor. The effects of making an incorrect absorption correction are explored in Section 7.4.2.

Chapter 4

DAFS EXPERIMENTS

This chapter describes the instruments and methods used for performing the DAFS experiments in this thesis. Most of the components are common to either XAFS or diffraction spectrometers, but special considerations arise when they are combined for measuring DAFS. The experiments presented here were intended as *proof in principle* that DAFS is a viable technique for determining material structures, therefore the spectrometer was engineered to the minimum level required for collecting the necessary data. The reader is encouraged to imagine all of the improvements and degrees of sophistication that might be added. The material in this chapter applies to the general DAFS experiment[1], with examples taken from both the Cu and $YBa_2Cu_3O_{6.8}$ experiments. I have reserved the details of specific experiments for the chapters in which the analysis is presented, Cu in Chapter 5 and$YBa_2Cu_3O_{6.8}$ in Chapter 6.

4.1 Spectrometer

The basic DAFS spectrometer comprises a continuously tunable x-ray source, a goniometer for positioning the sample in the beam, and three detectors: one to monitor the incident beam, one to measure the diffracted beam, and one to measure the fluorescence. Figure 4.1 shows a block schematic for a DAFS spectrometer, and this section describes each of the main components. DAFS is a function of the incident photon energy near an atomic resonance so the source needs to provide a continuously spectrum of x-rays over the energy range that the fine structure is observed. In practice, this means that DAFS experiments require a synchrotron radiation.

Most existing synchrotron beamlines are optimized either for XAFS or for crys-

[1] All of these experiments were performed in the energy scanning mode, in which the incident monochromatic beam is scanned through the resonance, similar to the standard XAFS experiments. Recent experiments at the European Synchrotron Radiation Facility in the dispersive energy mode are briefly addressed in Chapter 8.

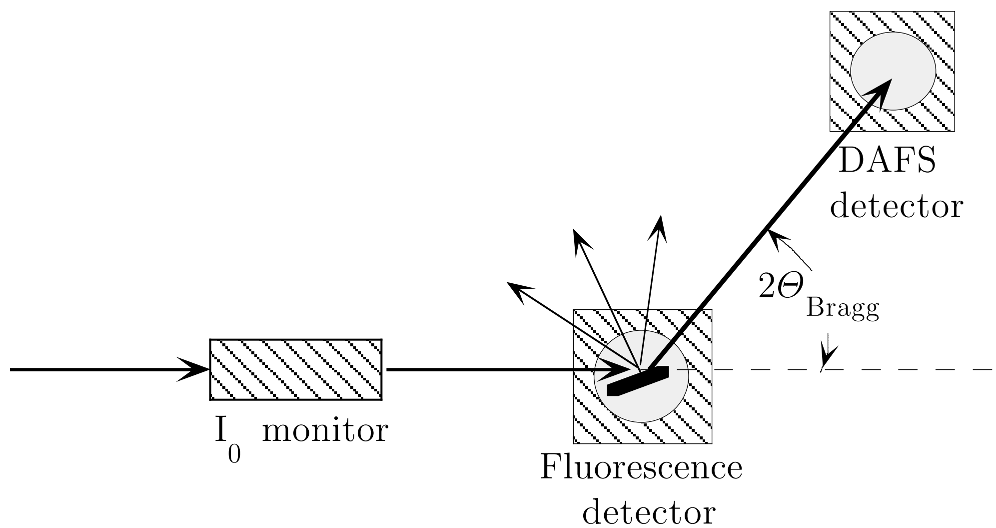

Figure 4.1: Tunable monochromatic x-rays pass through the incident beam monitor, in this case a gas ionization chamber, to the sample mounted on a scanning goniometer. As the beam interacts with the sample, two separate processes are measured: 1) The fluorescence XAFS is detected by an ion chamber located at 90° to the vertical scattering plane. This placement of the fluorescence detector uses the polarization of synchrotron radiation to minimize accidental Bragg scattering into the XAFS channel, such as the *glitches* seen in Fig. 1.1(b). 2) The intensity of the diffracted beam is measured by a detector positioned at the Bragg angle, $2\theta_{\mathrm{B}}$. The sample and the DAFS detector must move together as the incident energy is scanned in order to maintain the diffraction condition $\sin\theta_{\mathrm{B}} = hc/2dE$.

tallography. XAFS experiments require an incident energy resolution on the order of ~ 2 eV in order to resolve the smallest features in the resonance, but there is no need for controlled movement of the sample. Crystallography and diffraction, on the other hand, require precise control of the angular orientation of the sample with respect to the incident beam in order to resolve the smallest features in reciprocal space, but can tolerate energy resolutions on the order of 10's of eV. Diffraction beamlines are typically optimized for intensity and beam placement and the use of focusing optics degrades the natural collimation of the incident synchrotron radiation so that the beam striking the monochromator may diffract over a wider band of energies. A DAFS spectrometer must have high resolution in both photon energy and momentum transfer. We were unable to find a beamline that satisfied this condition ready-made. We chose to modify an existing XAFS beamline to meet the needs of the experiment because is easier to install a simple goniometer than to replace the primary optical system. All of the experiments for this work were performed at the National Synchrotron Light Source beamline X23A-2, which is maintained by the National Institute of Standards and Technology (NIST). With the exception of the sample holder and goniometer, the components described here are all part of the standard operating equipment at X23A-2.

4.1.1 Counting time

The samples used in this study scattered weakly, with diffracted intensities on the order of 10^{-3} of the incident beam intensity. Under these conditions, the statistical uncertainty in the measurements is assumed to obey Poisson statistics [54], where the noise goes roughly as the square root of the number of detected counts. The fine structure is a small modulation of the Bragg peak intensity, typically around 10^{-3} of the total diffracted intensity, so that to have a noise level of less than $\sim 0.1\%$ of the fine structure it is necessary to count better than 10^9 photons at each value of the energy.

At beamline X23A-2, the monochromatized incident intensity in the vicinity of the Cu K-shell resonance is $\sim 3 \times 10^9$ photons/second for a 2 mm $\times$ 10 mm incident beam area and Si (222) monochromator crystals. The diffracted count rates from our 2000 Å thick Cu film sample were on the order of $\sim 10^7$ photons/second. This translated into minimum data collection times of $\sim$ 2 minutes for each individual value of the incident photon energy. In order to measure the entire range of the fine structure, $\sim$ 1200 eV, a total scan time of $\sim$ 16 hours per Bragg reflection was required. We typically set up four scans of four hours each, to minimize the risk of a scan overlapping with a beam dump or an orbit correction.

4.2 Monochromator

The monochromator requirements for a DAFS experiment are very nearly the same as those for an XAFS experiment. The monochromator must be able to move quickly and reliably to a specified energy, it must have an energy resolution at least as fine as the smallest feature of interest in the DAFS spectrum (typically ~ 2 eV for XANES measurements and up to ~ 5 eV for EXAFS), and it needs to have some degree of harmonic rejection. In addition, the beam needs to maintain the same position and incidence angle with respect to the eucentric point of the scanning goniometer which holds the sample. Most XAFS beamlines are designed to keep the beam position stable on the sample as the energy is scanned, either by clever design of the monochromator or by tracking the beam with the sample holder. The monochromator at X23A-2 is the former type and one of its designers (P. Cowan) was always happy to explain its inner workings to curious neophytes over a pint at Fadley's.

The Heinzelman's eighth crystal boomerang

The X23A-2 monochromator is in the Golovchenko-Levesque-Cowan *boomerang* geometry[55]. This is a double crystal monochromator in which the second crystal slides along an axis parallel to the face of the first crystal in order to keep the position of the monochromatic exit beam at a fixed position on the sample. The first crystal sits on a pivot fixed at the position of the white-beam off the synchrotron. The second crystal is mounted on a sliding mechanism at the end of a rigid right angle. One end of the right angle is attached by a sliding mechanism under the pivot of the first crystal. The other end is a long bar which the second crystal is free to slide along. As the first crystal is turned to change the Bragg condition, the rigid right angle moves with it in such a way that its apex is held on a line that runs parallel to the white beam and exactly halfway between the white beam and the sample position. The second crystal slides along the bar to intercept the diffracted beam off the first crystal. Strict parallelism between the first and second crystals is maintained by a piezoelectrically controlled analog feedback circuit. The second crystal is mounted on a "corrector" stage that dithers its angle about some average position with respect to the first crystal. The dithering produces a small modulation in the monochromator output as the crystal is detuned from exact parallel. A gas ionization chamber placed upstream of the experiment I_0 monitor samples the intensity output of the monochromator and provides the feedback signal to a lock-in amplifier. The phase sensitive dc output of the lock-in amplifier is then sent back to the operational amplifier to adjust the average position. When the phase of the lock-in is set to the point of zero first derivative on the top of the double crystal rocking curve, the monochromator output is maximized. The monochromator can be *detuned* slightly by setting the phase to hold a position just off the side of the rocking curve. The width of the Bragg reflectivity from a perfect crystal varies inversely with energy, so that detuning the angles between the two crystals causes any diffracted harmonic off the first crystal to miss the Bragg condition at the second crystal.

Energy calibration

The energy of the monochromatic x-rays is determined by the scattering angle between the incident beam and the Bragg planes of the monochromator crystal according to the Bragg condition. It is not possible to measure the absolute angle directly, so the energy must be calibrated according to some known physical phenomena. We calibrated our monochromator by measuring the positions of the absorption edges for Cu, Fe, Ni, Zn, Ga, and As and then using monochromator control software [56] to correct for differences between the true value of the energy and nominal position set by the computer. Before every DAFS data set, several precautionary measures were taken to insure energy reproducibility and Bragg peak tracking. The monochromator was allowed to warm up under the incident white beam for $\sim$ 20 minutes. The position of the Bragg peak as a function of energy was checked at ten energy values spanning the data set by measuring the θ-rocking curve and making sure that the position of the peak was located at the central counting bin. Any small shifts were corrected for using a second software "fix" in the spectrometer program. Even with this care, the output was observed to shift by as much as 10 eV in 800 eV total range over the course of one day. The cause of the instabilities in the X23A2 monochromator are not known at this time.

4.2.1 Goniometer

For the experiments described here, two goniometers were built in-house at the University of Washington and installed temporarily at X23A-2. This is a side-station beamline, *i.e.*, the white beam output from the bending magnet is split between two nearly colinear experimental stations with A-2 on the upstream side of the neighboring A-3. The beam pipe for X23A-3 runs through the X23A-2 hutch parallel to the beam and very close to it. The center of the X23A-2 monochromator output is located 605 mm to the front of and 32 mm above the near corner of the X23A-3 bremsstrahlung exclusion zone. This puts severe constraints on the goniometer design

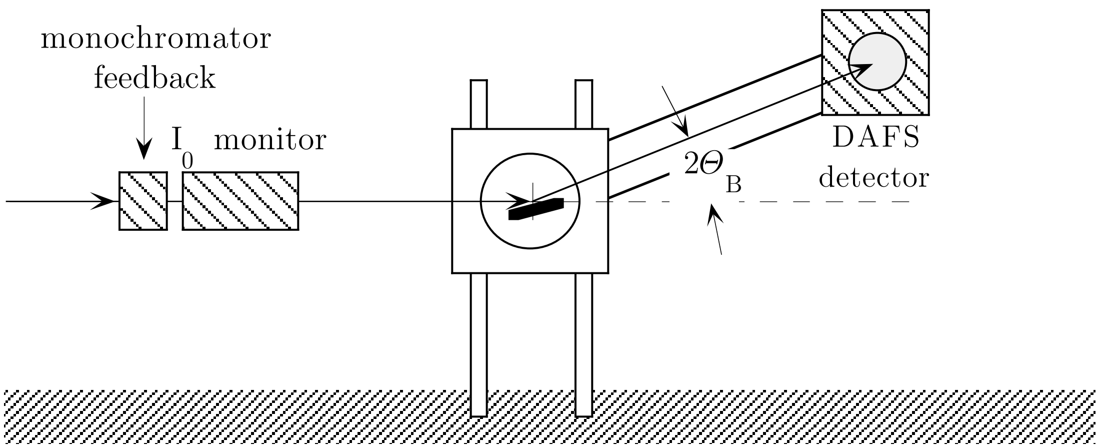

Figure 4.2: A sketch of the first generation DAFS spectrometer. The goniometer was built from two rotation stages mounted concentrically and attached to an x-y translation stage. The directions of the translational motion were perpendicular to the beam with x horizontal (normal to the page) and y vertical. The front surface of the sample was aligned to meet the concentric axis using an optical microscope with the goniometer off of the translator. The x-y stage was then used to align the crystal face with the center of the incident beam.

and is the main reason that synchrotron side-stations are more commonly used for XAFS than for x-ray diffraction.

First generation goniometer

The first two-circle spectrometer comprised a pair of microstepper rotation stages (Aerotech, model no. ART-100N) mounted concentrically on a plate bolted to an x-y translation stage. Figure 4.2 shows a sketch of the spectrometer geometry and Fig. 4.3 shows a schematic of the sample holder and goniometer, including the placement of the DAFS and XAFS detectors. The directions of the translational motion were perpendicular to the beam with x horizontal (normal to the page in Figure 4.2) and y vertical. A boom was attached to the 2θ stage to hold the DAFS detector and collimation slits for fluorescence background exclusion. The sample was

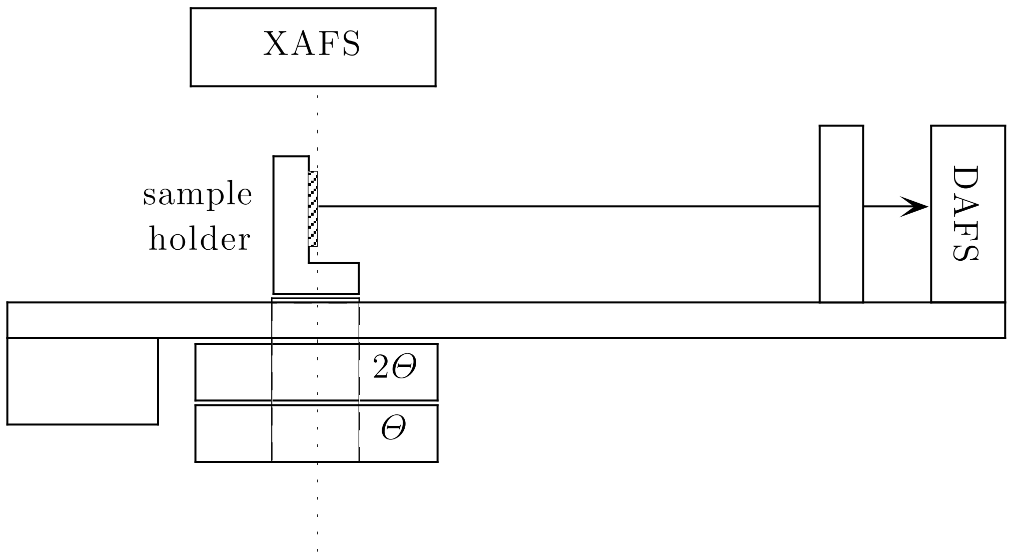

Figure 4.3: A sketch of the goniometer in Fig 4.2 showing the positions of the DAFS and XAFS detector with respect to the diffracting face of the sample. This is a view at $2\theta_B = 90°$ looking into the incident x-ray beam path. The goniometer was built from two concentric Aerotech ART-100N rotation stages controlled by a UNIDEX microstepper driver which interfaced to the spectrometer software via RS-232.

mounted on the θ stage via a post that was fed through the 2θ stage. The sample was aligned by hand, using a screwdriver to adjust the slotted base plate. The front surface was brought in line with the concentric axis of θ-2θ using an optical microscope positioned on the axis of the goniometer head off of the translator. The x-y stage was then used to align the crystal face with the center of the incident beam by splitting the I_0 intensity with the sample positioned at 0° and 180°. The rotational motion of the goniometer was controlled by a Unidex microstepper controller interfaced to the University of Washington x-ray scattering group's integrated spectrometer software FOCIS.

Second generation goniometer

The second generation goniometer was designed to access a larger volume of reciprocal space and to allow for more control in positioning the sample. The goniometer was

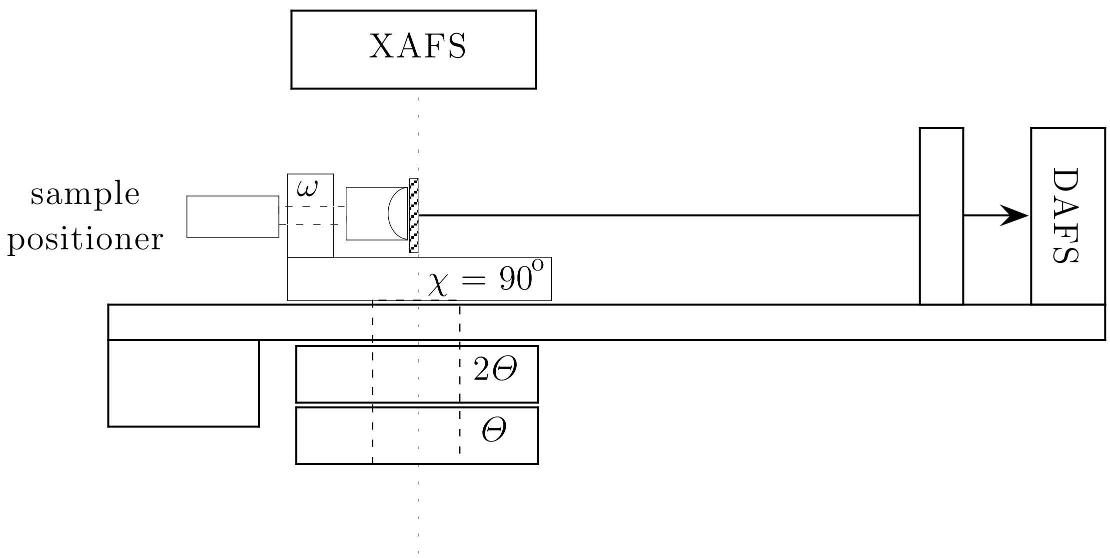

Figure 4.4: A sketch of the second generation DAFS goniometer looking into the incident beam. The goniometer comprises three rotation stages, with θ-2θ as before and a third ω circle mounted equivalent to the $\chi = 90°$ geometry in a four-circle Eulerian cradle. This allows any point in the half reciprocal space in front of the sample to be brought in line with the vertical scattering plane. Scans are measured in θ-2θ mode.

built from three rotation stages, with θ-2θ as before and a third ω circle mounted equivalent to the $\chi = 90°$ geometry in a four-circle Eulerian cradle. This geometry allows any point in the half reciprocal space in front of the sample (Bragg scattering geometry) to be brought in line with the vertical scattering plane. The scans are still measured in a θ-2θ mode. Figure 4.4 is a sketch of the rotation stages. The sample was positioned to the eucentric point of the goniometer using a micrometer that was press-mounted through the center of the ω stage.

Bragg peak tracking

The scanning DAFS spectrometer must be able to to accurately track the position of the Bragg peak as the incident energy is changed. The structure factor presented in Section 3.2 describes the integrated intensity of a Bragg reflection. If the mosaic distribution of crystallites within the sample is Gaussian, then it is sufficient to measure the peak intensity as a function of energy. This will only work if it is possible to accurately place the detector at the peak for every value of the energy. If this is not possible, the scanning times need to be increased by an order of magnitude so that a complete mosaic scan (θ rocking curve) can be measured at each energy. We made some of our earliest measurements this way, and then compared them to measurements made by software tracking of the peak and found the ratio of the peak intensity to the integrated intensity to differ (up to a constant scale factor) by less than 3% over 1200 eV when the sample mosaic was broad.

4.2.2 Detectors

In order to minimize the amount of time it takes to collect DAFS data, it is necessary to maximize the count rates into the diffraction channel. For incident count rates of $\sim 10^9$ photons/second, kinematic diffraction yields $\sim 10^6$ photons/second at the detector. The detectors must be able to reliably track small fluctuations in the intensity as a function of the photon energy. Since the beam is scattered elastically into the DAFS detector, the energy of the diffracted beam is the same as the incident beam and the detector response needs to be featureless over the entire scan range.

Figure 4.5(a) shows the instrument response function, defined as $I_{\text{det}}/I_{\text{mon}}$ at $\mathbf{Q} = 0$ with no sample, for the spectrometers with a photodiode in the detector position and a gas ionization chamber at the monitor. The envelope of the response is nearly linear over the entire range of interest for Cu K-shell resonance, but there are numerous catastrophic non-linearities. Figure 4.5(b) shows an expanded view of these glitches, demonstrating that they are reproducible. We suspect that these are due to the crystalline nature of the Si photodiode. Whatever their source, they make these detectors unsuitable for DAFS measurements.

4.3 Experimental corrections to DAFS data

The energy dependence of the spectrometer itself needs to be known in order to correctly interpret the measured intensity. The instrument response can be measured directly by placing the detector and I_0 monitor in line with the direct beam and stopping down the entrance slits. Since there may be some more subtle variations in the non-forward direction, it is also wise to measure the Bragg peak intensity from a non-resonant sample over the same ranger of energy as the DAFS. If the instrument

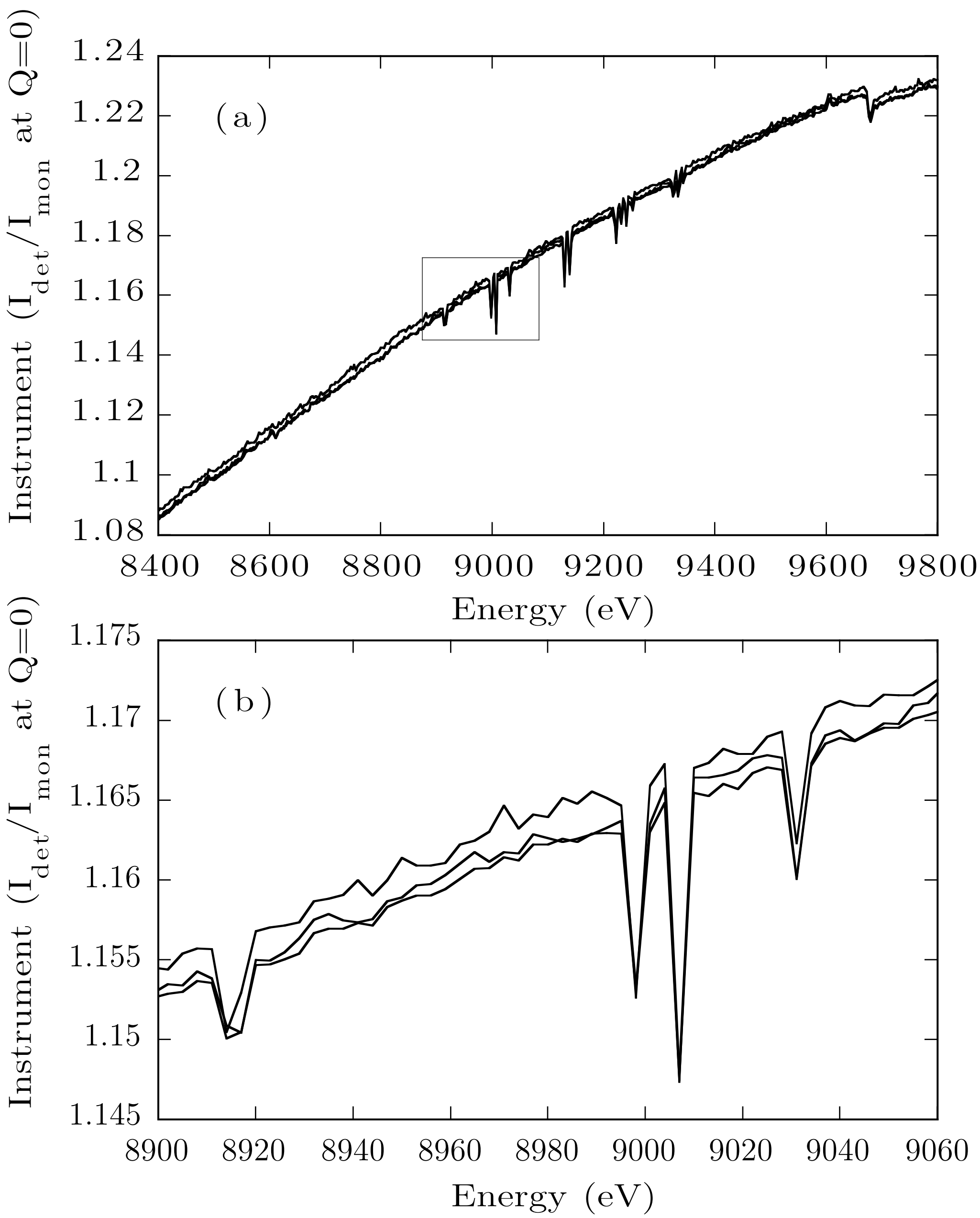

Figure 4.5: The energy dependent response of the DAFS spectrometer using photodiode detectors. The boxed region in (a) is expanded in (b) to illustrate the reproducibility of the *glitches* in the response as a function of energy. These detectors are not suitable for DAFS measurements.

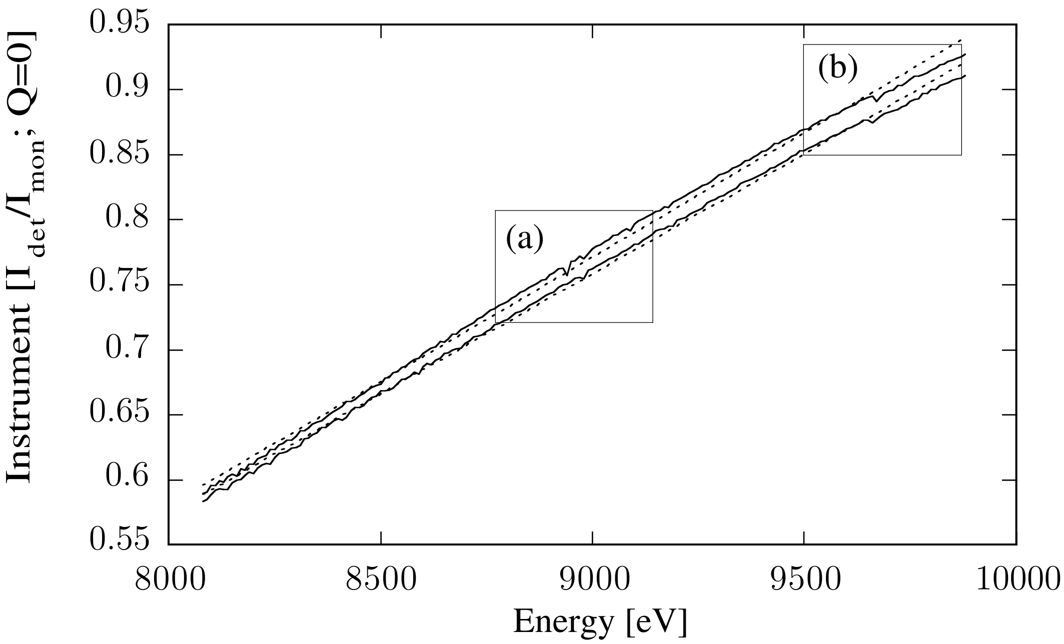

Figure 4.6: The energy dependent response of the DAFS spectrometer using gas ionization chamber detectors. The boxed regions in (a) and (b) are expanded in Figs. 4.7 and 4.8 to show the results of modeling the instrument response as linear or as a third-order polynomial of the energy, respectively. The drop in intensity around 9660 eV is due to the Zn K-edge; many beamline components are made of brass. The overplot of two scans taken $\sim$ 20 hours apart shows a 10 eV drift in the monochromator tracking.

response in non-linear as a function of the incident beam intensity, then any large fluctuations in the source will create problems in the data. You can prevent analysis headaches by examining the output from the I_0 monitor for each scan and throwing out any data set with obvious problems. The intensity of the diffracted beam in the DAFS detector is sensitive to the angle of beam incidence and orbit corrections during a scan can damage the data set beyond use. Since orbit corrections are a fairly common occurrence at a synchrotron, the best strategy is to keep the scan time as short as practicable.

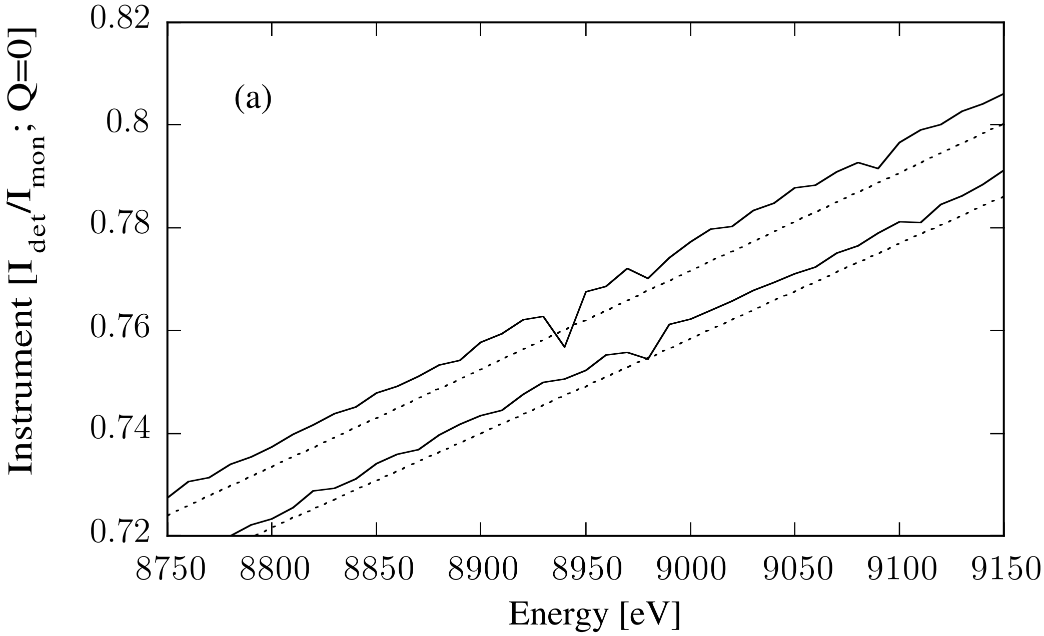

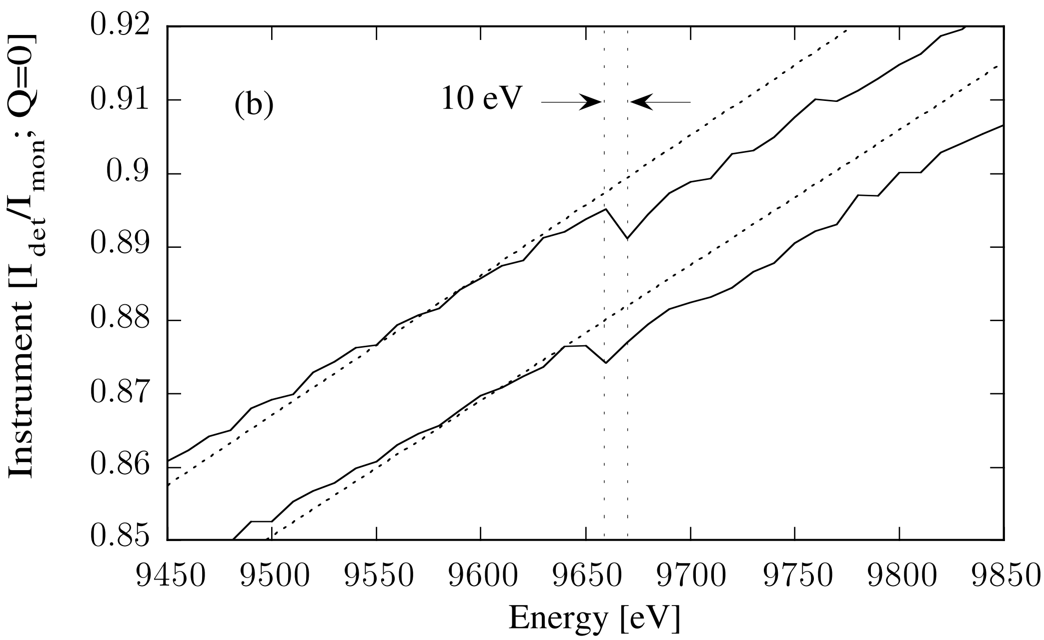

Figure 4.7: Expanded view of the insets (a) and (b) from Fig. 4.6 showing an unsatisfying linear fit to the total instrument response. Notice that the position of the Zn K-edge is shifted by approximately 10 eV between the two scans. The monochromator tracking must be recalibrated frequently, using known energy markers, to prevent drift.

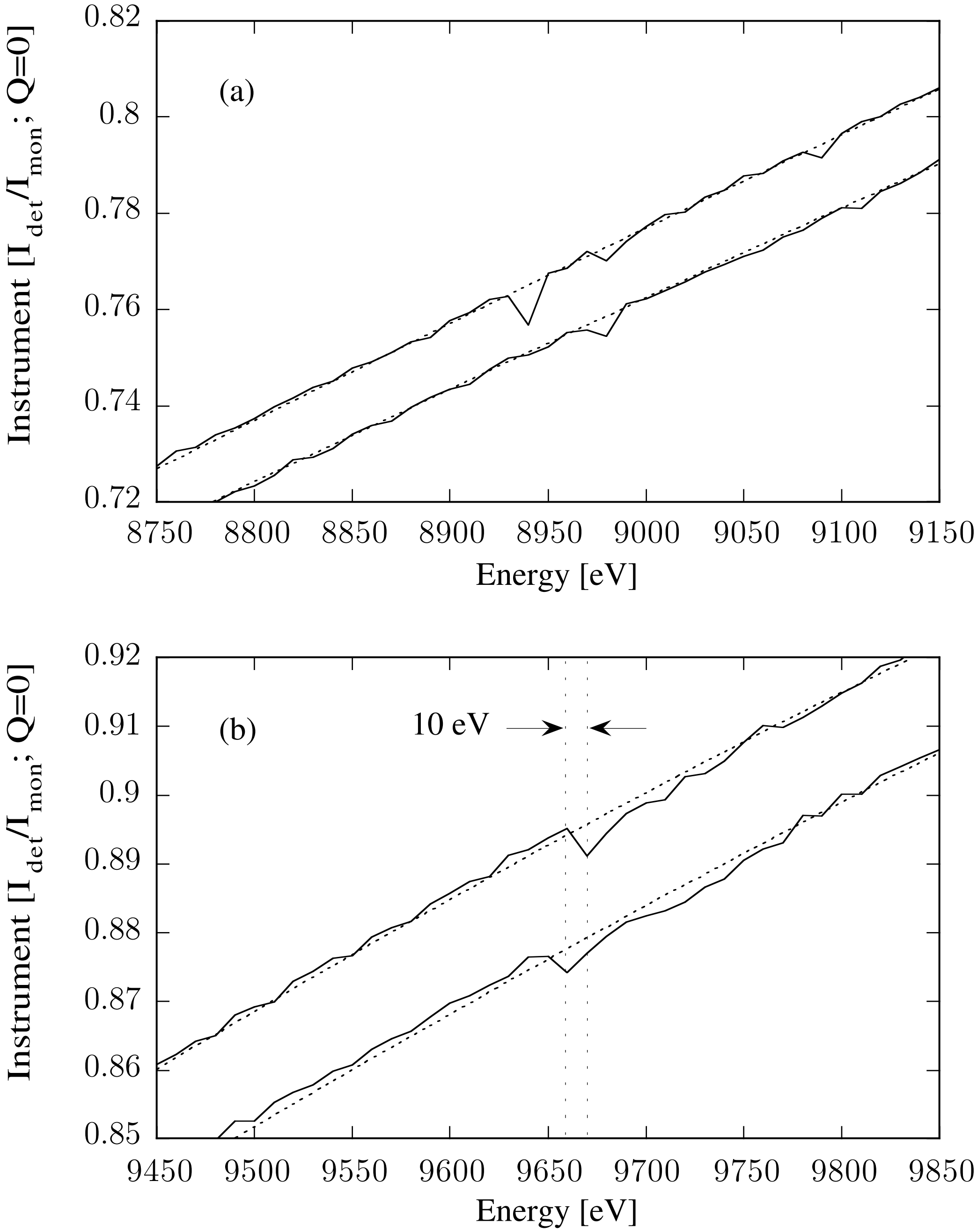

Figure 4.8: The instrument response from Fig 4.7 fit with a third order polynomial in energy. This still leaves a small error at the Zn K-edge, but is a better approximation over the whole range than the linear fit. The first choice for an instrument correction is to use the measured response, is this can be done while maintaining a reasonable signal-to-noise ratio.

4.3.1 Instrument correction

DAFS data is subject to the usual spectroscopic problem of separating the energy dependent response of the sample from the energy dependent response of the instrument. In an ideal experiment, the response of the spectrometer without the sample will be a flat or smooth, linear function of energy that can be easily divided out from the sample spectrum. In DAFS experiments, the Fourier transform of the fine structure piece of the intensity has a unique power spectral density that is sufficiently small at the low R that the instrument response is generally unimportant. However, because of coupling between fitting parameters, DAFS data is easier to model using the kinematical structure factor when the instrument correction has been made beforehand. Figure 4.5(a) shows the energy dependent response of a DAFS spectrometer with Si photodiodes for the I_0 monitor and DAFS detector. There are several non-linearities in the instrument response which are completely reproducible. It would not be appropriate to model this instrument response as a linear correction to the DAFS data. The instrument response for ion chamber I_0 monitor and DAFS detector, Fig. 4.6, is more nearly linear in energy though it is better modeled by a third order polynomial. Dividing a DAFS scan by the measured instrument response function will introduce additional noise into experiments where the signal to noise ratio is already small. One solution is to model the instrument response by a polynomial in energy and to divide the polynomial from the data. This works well to prevent extra noise but care must be taken that real instrument data, such as the inverted step at Zn K-edge, is not lost.

4.3.2 Background fluorescence correction

The background fluorescence can be in two ways. If the complete rocking-curve is measured at each energy, then the tails of the mosaic scan can be used for the fluorescence background. In the peak-tracking scan, the background fluorescence can be measured separately by offsetting θ outside the rocking curve and measuring a complete DAFS scan with this angle mis-set. We measured the background fluorescence in this manner with a mis-set angle in the θ-2θ scan of 5°.

4.3.3 Absorption correction

The absorption correction, Equation (3.45) has two important effects on DAFS data. First, because $\mu(E)$ contains fine structure the absorption correction interferes with the fine structure in the scattering intensity. The effects of small amounts of interference from the absorption correction fine structure on DAFS structural parameters is explored in Chapter 7. Second, the large step in the absorption coefficient near an absorption edge causes a drop in the diffracted data for $E > E_0$ that is proportional to the film thickness for diffraction from a thin film. Figure 3.7 shows the effect of film thickness on $I(\mathbf{Q}, E, t)$ for the Cu(111) reflection. This effect can be used to determine the film thickness directly from the DAFS intensity whenever an approximate unit cell structure is known.

Absorption correction using fluorescence XAFS

In materials with inequivalent resonant sites, in may be difficult to include the absorption correction fine structure in the fitting. The crystallographic coefficients α of Equation (3.37), which determine the amount of the resonance scattering signal from each site, will generally be different from the stoichiometric ratio of the sites. In addition, a non-zero Im[ΔF] appears as the coefficient of $f''_{\mathrm{w}}(\mathbf{Q}, E)$, and thus directly competes with the absorption correction in parameter space. The absorption correction can be determined independently of the DAFS by measuring the attenuation of the beam due to absorption [17], or by monitoring some characteristic decay process that is proportional to the absorption coefficient, such as the fluorescence intensity or the total electron yield. It is always a good idea to measure at least one of these quantities, regardless of whether it is necessary for the absorption correction, since it allows a convenient way to calibrate the position of the absorption edge in the DAFS. This section will describe the steps to transform a fluorescence XAFS measurement into a DAFS absorption correction. For a discussion of the total electron yield, see reference [61].

To construct the absorption correction to the scattering, we are looking for a way to determine the factor μ_{tot} in Equation (3.45). In order to get this from the measured fluorescence, we need to consider carefully the nature of the fluorescence signal from our sample. The number of fluorescence photons produced by the absorption process is proportional to the probability that that the incident photon has created a core hole, *i.e.*, the absorption coefficient, and to the probability that the core hole decays by a radiative transition at the fluorescence energy, ϵ_f, which is called the fluorescence yield. Radiation incident at angle θ_i penetrates to some finite depth in the sample where the core hole is created. After the core hole decays, the outgoing photon must pass back through the sample before reaching the detector. The outgoing radiation is emitted in all directions, so the measured intensity is also proportional to the fraction of 4π solid angle captured by the detector. To simplify the calculation, we assume that the solid angle Ω subtended by the detector is small and that we can characterize the outgoing radiation by a single exit angle θ_f, rather than performing the full solid angle integral. Under this simplification, the basic geometry is the same as that in Fig. 3.6. The attenuation of the incident and outgoing beams must be taken into consideration, and the formula for each leg are the same as those presented above, in section 3.4.4, except that now the outgoing radiation has energy E_f, which is smaller than the incident photon energy. For a detector with solid angle of Ω, the fluorescence intensity due to absorption from the n^{th}-shell of atoms located at depth x is related to the absorption coefficient for that shell, ${}^n\mu_j(E)$, by

$$dI_f = I_0 \left(\frac{\Omega}{4\pi}\right) e^{-\mu_{tot}(E)x/\sin\theta_\mathrm{i}} \frac{\epsilon_n \mu_n(E)dx}{\sin\theta_\mathrm{i}} e^{-\mu_{tot}(E_n)x/\sin\theta_\mathrm{f}} \tag{4.1}$$

with μ_{tot} the total absorption coefficient for the material (see appendix A). Integrating Equation (4.1) over the thickness t of the sample gives an expression for the contribution from a single fluorescence decay channel:

$$\frac{I_n(E)}{I_0} = \left(\frac{\Omega}{4\pi}\right) \frac{\epsilon_n \mu_n(E)}{\mu_{tot}(E) + \gamma\mu_{tot}(E_n)} \left(1 - e^{-(\mu_{tot}(E)+\gamma\mu_{tot}(E_n))t/\sin\theta_\mathrm{i}}\right), \tag{4.2}$$

with $\gamma = \sin\theta_\mathrm{i}/\sin\theta_\mathrm{f}$. The measured fluorescence XAFS is the sum of Equation (4.2) over all of the shells shells in each of the atomics species, but the values of ϵ_f and $\mu_{tot}(E_f)$ will generally cause the signal to be dominated by only a few terms. Furthermore, it is clear that the measured fluorescence is only indirectly related to the quantities we need for making the absorption correction to DAFS data.

Example: absorption correction for $YBa_2Cu_3O_{6.8}$

As an example, these are the steps taken for determining the self-absorption correction to the DAFS from the thin $YBa_2Cu_3O_{6.8}$ films studied in chapter 6. There is no contribution to the x-ray fluorescence signal from the oxygen atoms, leaving only Y, Ba and Cu to consider. Tabulated values of ϵ_f [57] for the only accessible absorption

Table 4.1: Tabulated values for the fluorescence yield from the contributing atomic species in $YBa_2Cu_3O_{6.8}$. There is no contribution from Oxygen, and the low energies of the L fluorescences from Cu and Y cause these contributions to be an insignificant part of the total fluorescence signal.

	ϵ_f (*fluorescence yield*)		
Process	Yttrium	Barium	Copper
L-Shell ϵ_f	0.0315	0.093	0.0056
Energies [eV]	1996, 1922	4828, 4467	933, 930
K-Shell ϵ_f	—	—	0.44
Energies [eV]	—	—	8904, 8047

processes in the energy range for Cu K edge DAFS are shown in Table 4.1, and $\mu_{tot}(E_f)$ for these same energies, using Equation (A.4), are shown in Table 4.1. The energies of the Y L shell fluorescence are very low, and very few these photons will ever reach the detector, as may be seen from the calculation of $\mu_{tot}(E)$ for those energies. This leaves only the Ba L and Cu K processes to consider in the measured fluorescence. The factors γ and $1/\sin\theta_{\mathrm{i}}$ will be different for different Bragg conditions. For the (00ℓ) reflections of $YBa_2Cu_3O_x$, $\sin\theta\mathrm{i} = hc/2dE \approx 0.059\ell$, for $c = 11.6916$ Å, and $E \approx 9000$ eV; $\gamma \approx 0.34\ell$, taking the average θf to be 10°. If we assume a 3000 Å film, and look at the the fluorescence signal that was collected simultaneously with the (001) DAFS, then $1/\sin\theta_{\mathrm{i}} \sim 17$ and $\gamma \sim 0.34$, and the difference in the size of the Ba contribution, which is attenuated by the Cu K shell absorption with its step, below and above the K edge is $\sim 6\%$. This difference is diminished as γ increases, so that approximating the Ba contribution to the fluorescence becomes a better approximation as ℓ increases. The Cu K-shell fluorescence signal, which is the only piece of the absorption correction that cannot be looked up in a table, is also attenuated by the step in $\mu(E)$. The factor $\mu_{CuK}(E)$ is zero for $E < E_{CuK} = E_0$, so the signal is normalized by determining the step height, but the fine structure in the absorption correction non-linearly attenuates the fine structure in the signal. For our ~ 3000 Å film at the (001) reflection, the argument of the exponent in Equation (4.2) is on the order of 0.5, so that $1-e^x$ in the numerator is only marginally approximated by the first term in the Taylor series expansion. The error introduced into the step height this way is $\sim 15\%$, but since the fine structure signal is $\sim 10\%$ of the step, normalizing in this manner introduces an error in the fine structure of $\sim 1.5\%$, which is

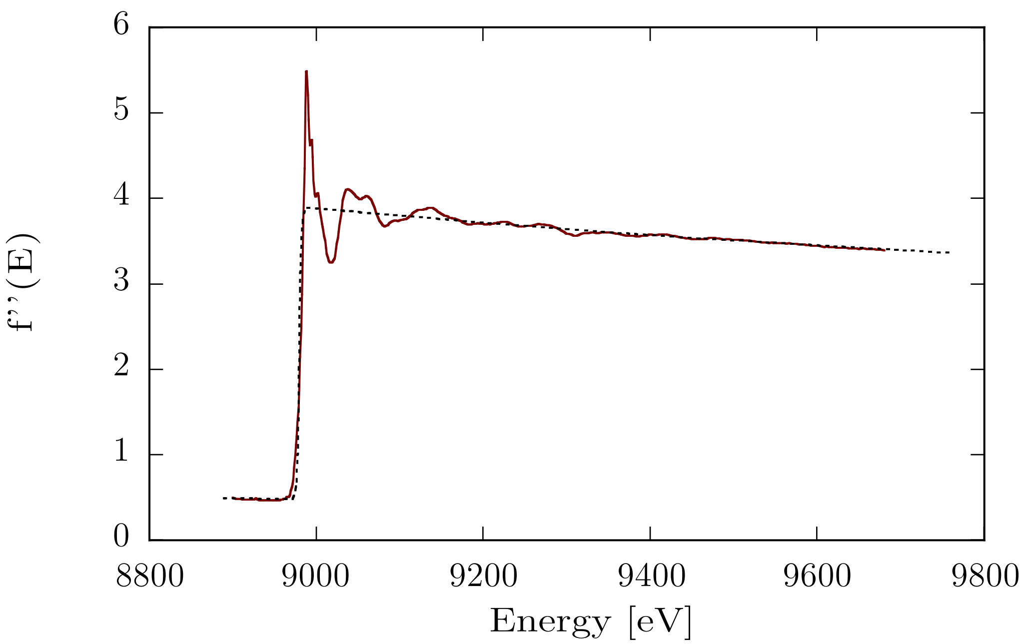

Figure 4.9: The combined $f''(E)$ due to the K-shell electrons of the Cu atoms in $YBa_2Cu_3O_x$ as determined by a fit to the fluorescence XAFS measured at the same time as the DAFS. The fluorescence signals collected at several of the (00ℓ) reflections were fit using Equation (4.3), and the average $f''(E)$ functions are plotted here. The dashed line is the theoretical $f''(E)$ that was used in the model.

small, especially considering that this will be used to make an already small correction to the DAFS data. The final point to consider is that the energy dependent response of the incident beam monitor and the fluorescence detector will be different since the incident beam is changing in energy but the fluorescence signal always has the characteristic energy of the transitions. The fluorescence data is fit to the following model function

$$I_f(\mathbf{Q}, E) \simeq a_1(1 + a_2\delta E)\frac{\mu_K(E)}{\mu_{\text{tot}}(E) + \mu_{\text{tot}}E_K}\left(1 - e^{-(\mu_{\text{tot}}(E)+\mu_{\text{tot}}(E_K)t/\sin\theta_i}\right) \tag{4.3}$$

with the μ_{tot} and μ_K for copper taken from tables of theoretical calculations [62, 63].

Chapter 5

ANALYSIS OF DAFS DATA

This chapter describes the methods used for isolating, normalizing and analyzing DAFS fine structure. The goal of DAFS analysis is to learn about the local environment and chemical state of a subset of the resonant atoms in a diffracting material based on their long-range order. This is accomplished by isolating the fine structure from the energy-dependent Bragg peak intensities and then by modeling and interpreting the spectral content of the fine structure in the same context as XAFS. In this chapter I will use DAFS and XAFS data from copper metal as the example to demonstrate the iterative dispersion integral method for isolating the real and imaginary parts of the complex DAFS $\Delta f(E)$ function and to compare the structural information content of the XAFS and DAFS directly. Chapter 7 addresses the reliability of the iterative Kramers-Krönig analysis method used to isolate the real and imaginary parts of the fine structure. In Chapter 6, the more complicated system of $YBa_2Cu_3O_{6.8}$ is analyzed to demonstrate methods for isolating the individual fine structure functions from inequivalent resonant sites within the unit cell.

Wherever possible, I have used the analysis methods developed by the University of Washington XAFS research group for determining material structural information from the resonance fine structure. However, this chapter is not intended as a primer for XAFS analysis and I have assumed that my readers are at least familiar with the terminology. For the XAFS background removal and fine structure analysis I have followed the procedures in Matthew Newville's dissertation [21] and the UWXAFS 3.0 documentation. The fluorescence background removal, the Fourier transforms and the fine structure fits in R-space were done using the computer programs AUTOBK and FEFFIT, written by Matthew Newville. Analysis of the fine structure by FEFFIT takes the *ab initio* theoretical spectra calculated by the computer program FEFF, written by John Rehr and his collaborators [31–34], and modifies the individual photoelectron scattering path contributions until a best fit to the data is found. The real and imaginary components of the DAFS fine structure were isolated from the measured intensity using the computer program KKFIT and its accompanying support programs and utilities, written by me with many helpful suggestions from Chuck Bouldin, Matthew Newville, Bruce Ravel, Larry Sorensen and Hans Stragier. The iterative Kramers-Krönig method is adapted from an algorithm first presented by Pickering, *et al* [17], that uses the optical dispersion relations to solve for a self-consistent pair of conjugate functions $f_0''\chi_{\mathrm{w}}'(E)$ and $f_0''\chi_{\mathrm{w}}''(E)$ that best fit the fine structure in the data. The details of each step of this process are described in Section 5.2.3 below. FEFFIT is part of the UWXAFS 3.0 analysis package, and a complete description of it can be found in the UWXAFS 3.0 documentation [58]. Information about FEFF is available through the FEFF project [35]. The KKFIT source codes are available upon request from the author [36].

5.1 Experiment: Cu metal film

In order to quantitatively compare the DAFS and XAFS structural parameters obtained by the analysis methods presented here, the fluorescence XAFS and the (111) DAFS from a single crystal of Cu metal were collected simultaneously. The experiment was performed at NSLS beamline X23A-2 using Si(222) crystals in the double crystal fixed-exit monochromator described in Section 4.2. The sample was a 2000 Å thick film of Cu deposited by electrochemical plating on a 2 cm diameter mica wafer. The mosaic spread of the crystal was 0.25° as determined from the θ rocking curves. The central peak intensity was measured rather than the integrated intensity over the rocking curve. The ratio of $I_{\mathrm{p}}(E)$ to $\int I(E,\theta)$ was checked at 100 eV intervals and found to be nearly constant over the 1200 eV energy range of the data. Some deviation from a constant, less than 0.8 % of the ratio, was observed.

The diffractometer response, which was shown in Figure 4.6, was determined by measuring the intensity as a function of energy with no sample in place as discussed in Section 4.3.1. The background fluorescence signal was measured by detuning θ by 5° in a θ-2θ scan. The DAFS data was collected at the (111) reflection over the range 8080 eV to 9955 eV. This gave a range of 975 eV above the absorption edge which is still smaller than the range of persistence of the fine structure, as evident from the background subtracted XAFS and DAFS $\chi(k)$ functions in Figures (5.2) and (5.6) respectively. Four peak-tracking scans were taken, measuring for 10 seconds or $\sim 3.3 \times 10^8$ diffracted photon counts at each energy value in 3 eV steps. Because of orbit corrections during two of the scans, only half of the DAFS data sets could be used. This serves as a small reminder that the time savings advantage of peak-tracking measurements may be lost due to heightened sensitivity to the beam position. Both of the good DAFS data sets were first corrected for the instrument response and background fluorescence, and then averaged for the DAFS analysis. The corrected data for the (111) reflection is shown in Figure 5.4(a). The fluorescence XAFS data was not susceptible to the orbit correction errors but it was prone to Bragg *glitches* when the diffraction condition was accidentally satisfied in the direction of the detector. One XAFS data set, complete with glitches, was shown in Chapter 1 Figure 1.1. The XAFS detector was placed at 90° to the vertical scattering plane in order to minimize this effect, and the energy positions of the glitches could be moved around by rotating the sample using the ω axis of the goniometer, but they could not be eliminated entirely. The flourescence XAFS data used for the analysis were hand corrected by excluding the data in the vicinity of the glitch from the average of these four scans. The deglitched, averaged XAFS data is shown in Figure 5.1. In the discussion of the analysis in this chapter, all of the examples are illustrated using these two averaged XAFS and DAFS data sets.

5.2 *Background removal*

Before analyzing the spectral content of DAFS or XAFS the oscillatory fine structure needs to be separated from the rest of the signal which is treated as background. I will begin with a discussion of XAFS background removal and analysis, both for context and for historical precedent, and then go on to discuss DAFS background removal. Since the XAFS fine structure function is equal to the imaginary part of the complex DAFS fine structure function in the dipole approximation, the fine structure analysis of the DAFS $\chi''(k)$ is exactly the same as the analysis of the XAFS $\chi(k)$ and I have used the symbol $\chi''(k)$ to denote both functions, reserving the symbol $\chi(k)$ to denote the full complex function, *i.e.*, $\chi(k) = \chi'(k) + i\chi''(k)$. This small change of notation is the only place where my treatment of the XAFS differs from the standard.

5.2.1 *In which $\chi''(k)$ is isolated from XAFS data*

XAFS is measured either by the attenuation of the direct beam on passing through the sample, or by monitoring one of the byproducts of the decay processes for the excited state, such as fluorescence photon yield or total electron yield, that are proportional to the total absorption cross-section. Starting with the measured absorption

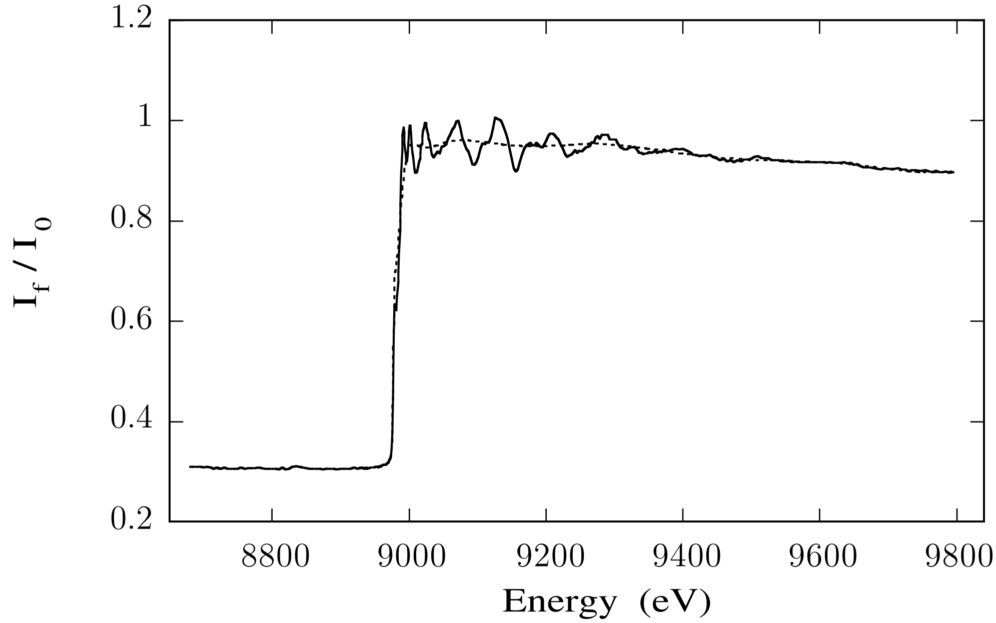

Figure 5.1: Cu fluorescence XAFS signal and background spline. Fluorescence XAFS from a 2000 Å film of Cu metal (solid line) and the background function calculated by AUTOBK (dashed line). The 11 knot spline was determined using a theoretical $\chi''(k)$ generated by FEFF in the minimization of the differential Fourier transform (see Section 5.2.1). The background region in R-space was taken to be $0 < R_{\rm bkg} < 1.2$ Å. The fluorescence data was measured simultaneously with the Cu(111) DAFS shown in Figure 5.4. All of the Bragg glitches were removed by hand, and the average of four data sets is shown.

cross-section $\mu_{\rm tot}(E)$, the absorption from the excited core level is first isolated by extrapolating a linear background from the fluorescence in the region $E < E_0$ below the step. For Cu, this separates the K-shell absorption from all of the other contributions to the total absorption cross-section. The resulting $\mu(E)$ is the absorption cross-section of the single core level, including effects due to the presence of neighbors. The fine-structure part of the signal $\chi''(E)$ is solved for by

$$\chi''(E) = \frac{\mu(E) - \mu_0(E)}{\mu_0(E)} \tag{5.1}$$

where the function $\mu_0(E)$ is the total core level absorption cross-section for the embedded atom without the fine structure due to backscattering. Since the resonance fine structure is periodic in the photoelectron momentum and not in the energy, the argument of $\chi''(E)$ needs to be converted using

$$\hbar k = \sqrt{2m(E - E_0)} \tag{5.2}$$

before calculating its Fourier transform. The structural parameters for the material are generally determined in the conjugate R-space.

The embedded atom absorption cross-section $\mu_0(E)$ is equivalent to f_0'' in Equation (2.54) up to a factor of $1/E$ and a constant scale (see Appendix A). The existence of overlap between the electron orbitals of the absorbing atom and the other atoms of the solid gives $\mu_0(E)$ a slowly varying energy dependence that differs from absorption of an isolated atom. In principle, the embedded atom lineshape can be calculated by FEFF, but application of these theoretical calculations to background removal from experimental data is still in early development. In practice, $\mu_0(E)$ in the numerator is replaced by a smooth spline through the fine structure and $\mu_0(E)$ in the denominator is replaced by $\Delta\mu_0(E_0)$, the height of the step in $\mu(E)$ above the signal at $E < E_0$. The game is to use a sensible algorithm for choosing the spline such that the slow energy-dependent variations in the absorption due to the embedded atom are removed from $\chi''(E)$ without affecting the more rapid energy-dependent variations due to the neighboring atoms.

AUTOBK

The method for determining the best-fit spline described in [21] uses results from information theory to determine the difference between data and "background". The details of the program can be found in the AUTOBK document [60]. AUTOBK models the background using a fourth order spline with knots evenly spaced in k. The values $\mathbf{y}(k)$ of the spline at each k chosen to minimize the functional

$$g(\mathbf{y}(k)) = \mathrm{FT}\left[\frac{\mu(k) - \mu_0(k, \mathbf{y}(k))}{\Delta\mu_0(k=0)} - \chi_{\mathrm{model}}(k)\right], \qquad R \leq R_{\mathrm{bkg}} \tag{5.3}$$

where R_{bkg} is some small distance, typically half the distance to the nearest neighbor, below which all of the information is assumed to be non-structural, and FT is the Fourier transform from k-space to R-space. This gives the spline shown in Figure 5.1 for Cu fluorescence XAFS. Note that the spline is not flat, but has some slowly varying energy dependence. Restricting the R-space minimization to the low R region insures that this variation does not affect the structural information contained in the

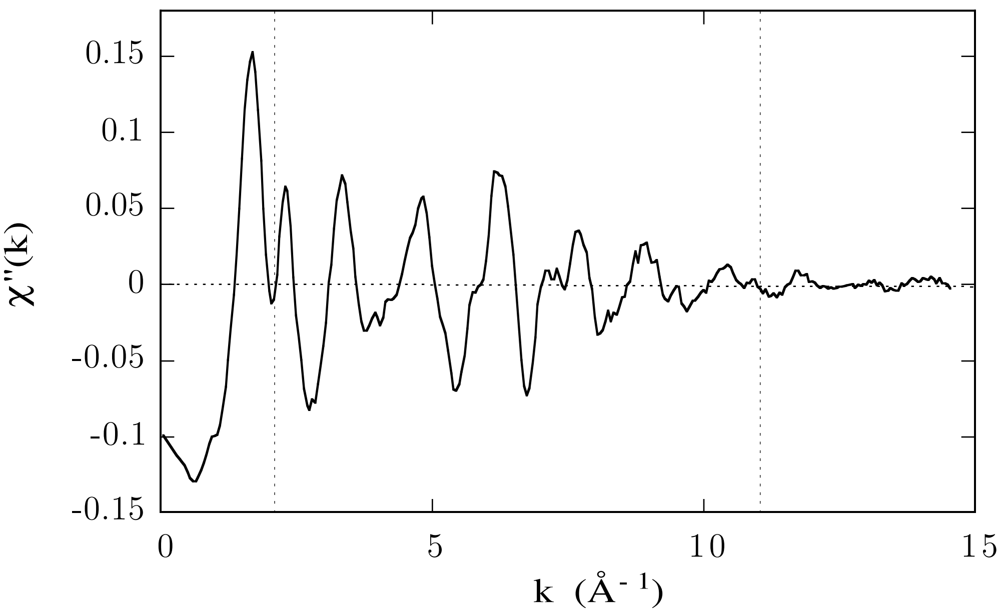

Figure 5.2: Fluorescence XAFS $\chi''(k)$ function from the $\mu(E)$ data and AUTOBK determined $\mu_0(E)$ shown in Figure 5.1. The vertical lines at $k = 2$ and $k = 11$ indicate the range used for the Fourier transform of this data shown in Figure 5.10.

extended fine structure. The resulting $\chi''(k)$, after removing the background spline $\mu_0(E)$ determined by AUTOBK from the original $\mu(E)$ data, is shown in Figure 5.2. The step height used to normalize the fine structure is found by fitting a quadratic polynomial to the best-fit spline over some energy range, typically E_0+100 to E_0+300, and extrapolating back to E_0.

5.2.2 In which $\chi'(k)$ and $\chi''(k)$ are isolated from DAFS data

DAFS is measured in the energy dependence of the Bragg peak intensities. The resonance fine structure is a small part of the total scattering amplitude from a crystal, and it is carried on the real and imaginary parts of the resonant correction to the Thomson scattering. The DAFS analog to Equation (5.1) can be taken from the real or the imaginary parts $\Delta f(E)$ in Equation (2.54), so that either

$$\chi'(E) = \frac{f'(E) - f'_a(E)}{f''_0(E)} \tag{5.4}$$

or

$$\chi''(E) = \frac{f''(E) - f''_a(E)}{f''_0(E)} \tag{5.5}$$

is a reasonable choice for structural analysis of the DAFS. Since $f''(E)$ is proportional to $\mu(E)/E$ in the dipole approximation, the imaginary part $\chi''(E)$ gives exactly the same result as Equation (5.1), Unfortunately, the functions $f'(E)$ and $f''(E)$ cannot be simply extracted from the measured intensities. The intensity is proportional to the squared magnitude of the scattering amplitude, and so DAFS data is quadratic in $\Delta f(E)$ and $\chi(E)$.

Two observations about the general nature of the fine structure buried in the diffraction signal are helpful for gaining insight into the analysis solution. First, the integral dispersion relations between $f'(E)$ and $f''(E)$ effectively reduce the amount of unknown information in Δf by half. Thus instead of solving a quadratic for two unknown, highly oscillatory, energy-dependent functions, the problem can be rewritten in terms of, without loss of generality, $f'(E)$ and $\mathrm{KT}(f'(E))$, where KT is the integral Kramers-Krönig transform. The second observation is that the scattering amplitude from each atom is generally dominated by the real part since $f_0(\mathbf{Q})$ is generally larger than either $f'(E)$ or $f''(E)$, even near resonance. When the symmetry of the crystal allows the antisymmetric imaginary terms in the structure factor sum to cancel, the intensity is dominated by the sum over the real parts of the scattering amplitudes. Using these ideas, Pickering, *et al.* [17], devised an iterative algorithm to solve for a self-consistent pair of functions from DAFS data by first treating the resonance fine structure in the intensity as purely real to obtain a first approximation to $\chi'(E)$, and then applying the dispersion integral to obtain a $\chi''(E)$ from this. The resulting pair of functions are an approximation to the true functions, but with some knowledge of $\chi''(E)$, a better next guess for $\chi'(E)$ is obtained from the data. This process can be iterated, solving for $\chi'(E)$, taking the Kramers-Krönig transform, *etc.*..., until a stable pair of functions settles out. Most of the rest of this section will present the steps of this algorithm with none of the details left to the readers imagination.

Spline-based methods for isolating DAFS fine structure, modeled after Equation (5.1), are also found in the literature [10, 11], but the resulting function is a mixture of $\chi'(k)$ and $\chi''(k)$. I will describe the form of the spline-based fine structure briefly at the end of this chapter in Section 5.4 for comparison with the Kramers-Krönig-based results. A direct spline may seem like the simplest way to isolate DAFS fine structure, but the resulting functions are not as easy to interpret as $\chi_{\mathrm{w}}(k)$ of Equation (3.38).

5.2.3 Iterative Kramers-Krönig analysis of DAFS

The iterative algorithm proceeds in two separate stages. The smooth part of the intensity is first modeled using a parameterization of the kinematic structure factor, omitting the fine structure by substituting the bare-atom $\Delta f_a(E)$ lineshape for $\Delta f(E)$. A few energy-independent parameters are adjusted in a Levenberg-Marquardt non-linear least squares fit. The resulting approximation to the data is a simple quadratic function of $\Delta f_a(E)$ that resembles the result of a spline fit. The intensity can be solved using the theoretical functions and the parameters determined from the smooth fit for either the real or imaginary parts of the fine structure. In the second stage of the fitting, the fine structure is approximated by the quadratic solution to the dominant part of $\Delta f(E)$ and its numerically calculated Kramers-Krönig transform. The dominant term can be distinguished either from some knowledge of the unit cell structure, or guessed from the overall shape of the intensity. When the real part of $\Delta f(E)$ dominates, the overall signal shows the clearly-defined cusp seen in Figure 5.4. When the imaginary part dominates, the intensity develops a more step-like lineshape, as evident in the $YBa_2Cu_3O_{6.8}$ (002) DAFS shown in Figure 5.3. The value of the phase argument of the non-resonant scattering $e^{i\Phi_0}$ weights the real and imaginary parts of $\Delta f(E)$. In monoatomic materials, where the imaginary part of F_0 is identically zero, the real part of $\Delta f(E)$ always dominates.

The structure factor model

The model for the intensity based on kinematic diffraction was developed in Section 3.2. The sublattice of resonant sites is assumed to have a center of symmetry parallel to $\mathbf{Q}$ and the structure factor sum is arranged so that the anomalous Δf contributions from the off-resonance atoms are grouped together with the energy independent Thomson scattering amplitudes from all the atoms into $F_0(\mathbf{Q} = |F_0|e^{i\Phi_0}$. The energy dependent Bragg peak intensities are proportional to the squared magnitude of the structure factor

$$\begin{aligned} I(\mathbf{Q}, E) &= |F_0(\mathbf{Q}) + \Delta F(\mathbf{Q}, E)|^2 A(\mathbf{Q}, E, t) L(\mathbf{Q}, E) \\ &= |\mathrm{F}_0|^2 \left[(\cos\Phi_0 + \beta f'_{\mathrm{w}})^2 + (\sin\Phi_0 + \beta f''_{\mathrm{w}})^2 \right] A(\mathbf{Q}, E, t) L(\mathbf{Q}, E). \end{aligned} \tag{5.6}$$

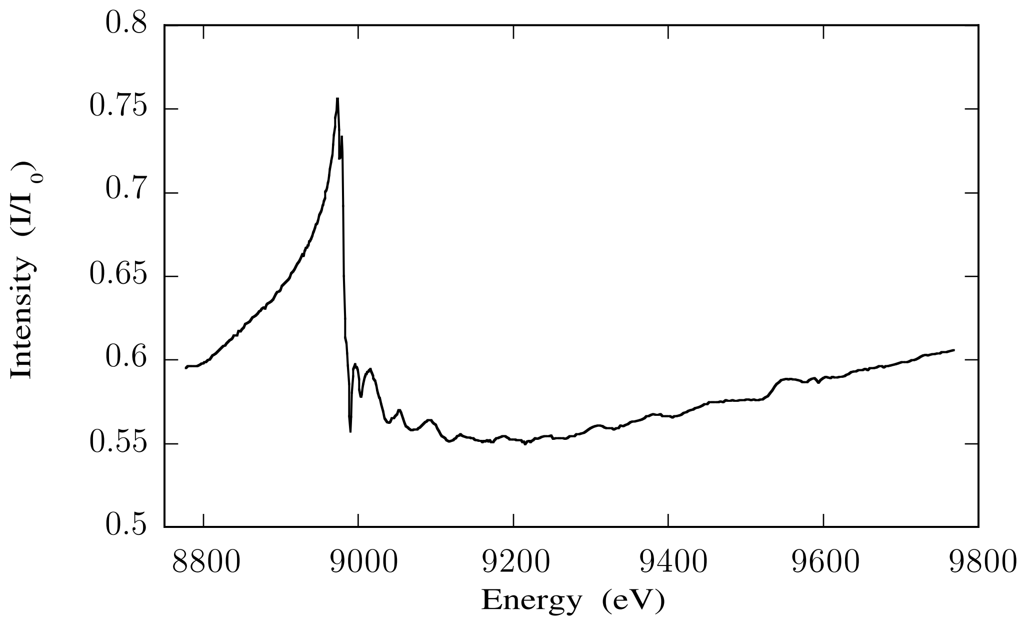

Figure 5.3: When the imaginary part of $\Delta f(E)$ dominates, then the measured intensity exhibits a step-like lineshape, as evident in this figure of the $YBa_2Cu_3O_{6.8}$ (002) DAFS. When the real part dominates, the measured intensity exhibits the cusp-like shape seen in Figure 5.4.

where $\beta = \alpha/|F_0|$; f'_{w} and f''_{w} are the real and imaginary parts, respectively, of the crystallographically mixed resonant scattering correction; $A(\mathbf{Q}, E, t)$ is the thin film absorption correction from Equation (3.45); and L($\mathbf{Q}$,E) is the energy dependent Lorentz correction $L(\mathbf{Q}, E) = 1/(E^3 \sin 2\theta)$ The overall shape of the energy dependent structure factor is due solely to the resonantly scattering atoms. The unique profiles of the cusp in $f'_a(E)$ and the step in $f''_a(E)$ are invariant and the model amounts to scaling and weighting these two functions until a best fit to the measured intensity is obtained.

In order to use Equation (5.6) as a computer model, the non-resonant phase Φ_0 and the magnitude of the non-resonant scattering $|F_0|$ are treated as energy independent over the entire range or the data. This strictly holds for monoatomic materials. In complex materials, it is a good approximation provided the resonance correction terms $\Delta f(E)$ in $|F_0|$ due to the off-resonance atoms are small. Occasionally there are small corrections to the intensity that are not accounted for by the measured instrument response and background. A small additive fitting parameter with no physical

Table 5.1: The adjustable fitting parameters used by KKFIT to model the overall lineshape of DAFS data. With the exception of $I_{\rm off}$, these are all energy-independent

I_0	The overall amplitude is proportional to the squared magnitude of the non-resonant structure factor $\|F_0\|^2$;
$I_{\rm off}$	An offset correction that allows the fit to correct for any background in the data not removed by the instrument corrections; $I_{\rm off}$ is of the form $a_1 + a_2E$. For the Cu fitting in Chapter 5, a_2 was set to zero making $I_{\rm off}$ energy independent.
Φ_0	The overall phase of the non-resonant scattering amplitude from $F_0 = \|F_0\|e^{i\Phi_0}$;
β	$\beta = \alpha/\|F_0\|^2$ is the ratio of amplitude of the resonant scatterers to the squared magnitude of the non-resonant structure factor;
t	The film thickness in the absorption correction which may be varied with the cautions noted in Section 3.4.4;
δE_0	The difference in the position of the step between $f''_{theory}(E)$ and $f''_{\rm w}(E)$.

interpretation is included in the model to give it sufficient freedom to adjust the theoretical structure factor to fit the data. The absolute intensity is not measured, so that $I(\mathbf{Q}, E)$ is known only up to an overall scale factor. This can be made to include $|\mathrm{F}_0|^2$ so that a model for the smooth part of the DAFS intensity is parameterized

$$\begin{aligned} I_{\rm model} \;&=\; I_0 \left[\left(\cos\Phi_0 + \beta f'_{\rm w}(E)\right)^2 + \left(\sin\Phi_0 + \beta f''_{\rm w}(E)\right)^2 \right] \times \\ &\quad\; A(\mathbf{Q}, E, t) L(\mathbf{Q}, E) + I_{\rm off}. \end{aligned} \tag{5.7}$$

This is the model I will be using throughout this work. Equation (5.7) is quadratic in $f'_{\rm w}(E)$ and $f'_{\rm w}(E)$. The choice of which part to solve for depends on the structure of the unit cell and on the particular reflection. For convergence of the iterative Kramers-Krönig method the dominant function should be chosen so that the initial pass through the iterative algorithm gives a good starting value for $\chi_{\rm w}(E)$. The model in Equation (5.7) has six possible energy-independent fitting parameters, enumerated in Table 5.1. The adjustable fitting parameters are energy independent and serve only to change the position and scale of the energy dependent theoretical functions $f'_a(E)$

and $f''_a(E)$ until the theoretical structure factor agrees with the data. The positions and x-ray Debye-Waller factors of the atoms are not needed in the fitting, however starting from the known structure factor will put the phase Φ_0 in the correct quadrant.

The film thickness is an unstable fitting parameter

The overall intensity I_0 and film thickness t are highly correlated fitting parameters, and in all of the fits described above t was held fixed at the value provided with the sample. Since the thin film absorption correction Equation abscorr depends on the total absorption cross-section, which is not generally zero for $E < E_0$, small changes in t will change I_0 over the whole energy range. This competition can be alleviated somewhat by renormalizing absorption correction to the non-resonant contribution below E_0. The absorption correction when t is varied is given by

$$A(\mathbf{Q}, E, t) = \begin{cases} 1, & E < E_0; \\ \frac{\mu_N}{\mu_N+\mu_f} \frac{1-e^{-2(\mu_N+\mu_f)t/\sin\theta}}{1-e^{-2\mu_N t/\sin\theta}}, & E \geq E_0 \end{cases} \tag{5.8}$$

where μ_N is the non-resonant contribution to the mass absorption coefficient which has been approximated by a constant for $E < E_0$. When t is not varied, the numerator goes back to the original expression in Equation abscorr and the constant term in the denominator is kept for scale. When I_0 and t were decoupled using Equation (5.8), KKFIT determined the correct value of the film thickness to within $\sim 5\%$ in trials on mocked-up DAFS data when t was the only parameter allowed to vary.

The best fit to the data is determined by minimizing the functional

$$g(E, \mathbf{p}) = f_w(E, \mathbf{p}) - f_a(E) \tag{5.9}$$

where $\mathbf{p}$ are the adjustable fitting parameters from Table 5.1 and $f'_w(E)$ is determined by solving the structure factor, using the measured data I, as a quadratic in $f'_a(E)$ or $f''_a(E)$

$$f'_{\mathrm{w}}(\mathbf{Q}, E) = \frac{1}{\beta}\left(\pm\sqrt{\frac{I(\mathbf{Q}, E) - I_{\mathrm{off}}}{I_0 A(\mathbf{Q}, E, t)} - [\sin\Phi_0 + \beta f''_{\mathrm{a}}(E)]^2} - \cos\Phi_0\right) \tag{5.10}$$

with the sign $\pm$ set equal to the sign of $\cos\Phi_0$ so that the resulting cusp points upward, as required, or

$$f''_{\mathrm{w}}(\mathbf{Q}, E) = \frac{1}{\beta}\left(\pm\sqrt{\frac{I(\mathbf{Q}, E) - I_{offset}}{I_0 A(\mathbf{Q}, E, t)} - [\cos\Phi_0 + \beta f'_{\mathrm{a}}(E)]^2} - \sin\Phi_0\right) \tag{5.11}$$

with the sign $\pm$ set equal to the sign of $\sin\Phi_0$ so that the step in $f''_a(E)$ is positive. For any monoatomic material, such as Cu metal, $\Phi_0 = \pi$. For non-forbidden reflections in high-symmetry materials Φ_0 lies close to the real axis and the antisymmetric part of the structure factor sum comes only from the imaginary contributions to $|F_0|$ from the off-resonance atoms. Throughout the remainder of this chapter I will simplify the discussion to the case where $f'(E)$ is dominant.

The results of the first stage of fitting is shown in Figure 5.4(a). Only three of the adjustable parameters were varied in the least squares fitting and the following values were obtained: $I_0 = 1.492$; $I_{\rm off} = -0.07279$; and $\beta = 0.04194$. The film thickness was held fixed at 2000 Å, as determined during film growth by the group that provided the sample [67]. The non-resonant phase was held at $\Phi_0 = \pi$, based on the structure factor for f.c.c. copper, and the edge shift was held at $\delta E_0 = 0$.

Solving for $f_{\rm w}(E)$ by the iterative Kramers-Krönig method

After the structure factor model has been applied to the DAFS data, and a best fit to the smooth background intensity has been determined, the data is solved one final time for $f'_{\rm w}(E)$ using the original smooth approximation for $f''_a(E)$. The result will become the first guess for the true $f'_{\rm w}(E)$ in the second round of fitting. This function for Cu(111) DAFS is shown in Figure 5.4(b), and $f'_{\rm w}(E)$ and $f''_{\rm w}(E)$ in near-edge region for Cu(111) and Cu(222) DAFS are overplotted in Figure 5.5.

The fine structure on this first solution for $f'_{\rm w}(E)$ is a mix of the true $\chi'(E)$ and $\chi''(E)$, but it is dominated by the real part. The first guess to $f''_{\rm w}(E)$ is calculated by numerically integrating $f'_{\rm w}(E)$ using the differential form of the Kramers-Krönig dispersion integrals presented in Section 1.2.1, *i.e.*

$$f''_{\rm w}(E) \quad = \quad f''_a(E) - \frac{2E}{\pi}\mathrm{P}\left(\int_{\Delta E} \frac{f''_0(E')\chi'_{\rm w}(E')}{E'^2 - E^2} dE'\right). \tag{5.12}$$

The resulting complex $\Delta f_{\rm w}$ is then put back into the structure factor model for another round of fitting and this process is iterated until the fine structure stabilizes. The resulting complex $f_{\rm w}(\mathbf{Q}, E)$ has a known relationship to the step in the background function $f_0(E)$, since it is built into the structure factor model, so the fine structure can be normalized to the step with great accuracy.

The differential form of the integral Equation (1.9) reduces the original infinite energy range of the Kramers-Krönig dispersion relations to the energy range of the fine-structure. The key to getting a good result is to have the fine structure strictly

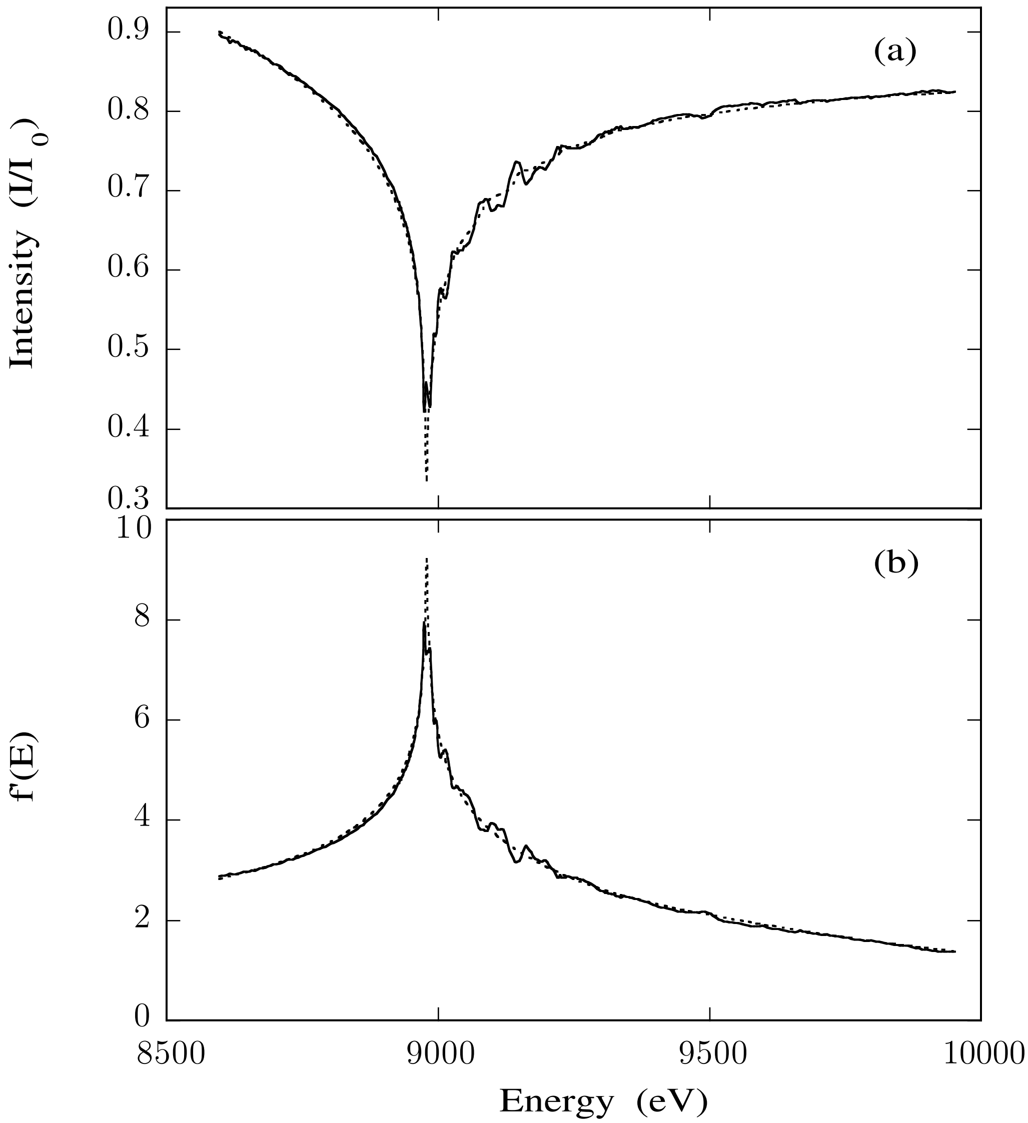

Figure 5.4: Cu (111) $f'(E)$ from DAFS data using KKFIT and solving the quadratic structure factor model. (a) Measured Cu(111) DAFS signal (solid line) and fit to theoretical structure factor model (dashed line). (b) The $f'(E)$ function obtained by solving the intensity data as a quadratic using the structure factor model (solid line) compared to theoretical $f'(E)$ (dashed line) from tables [63].

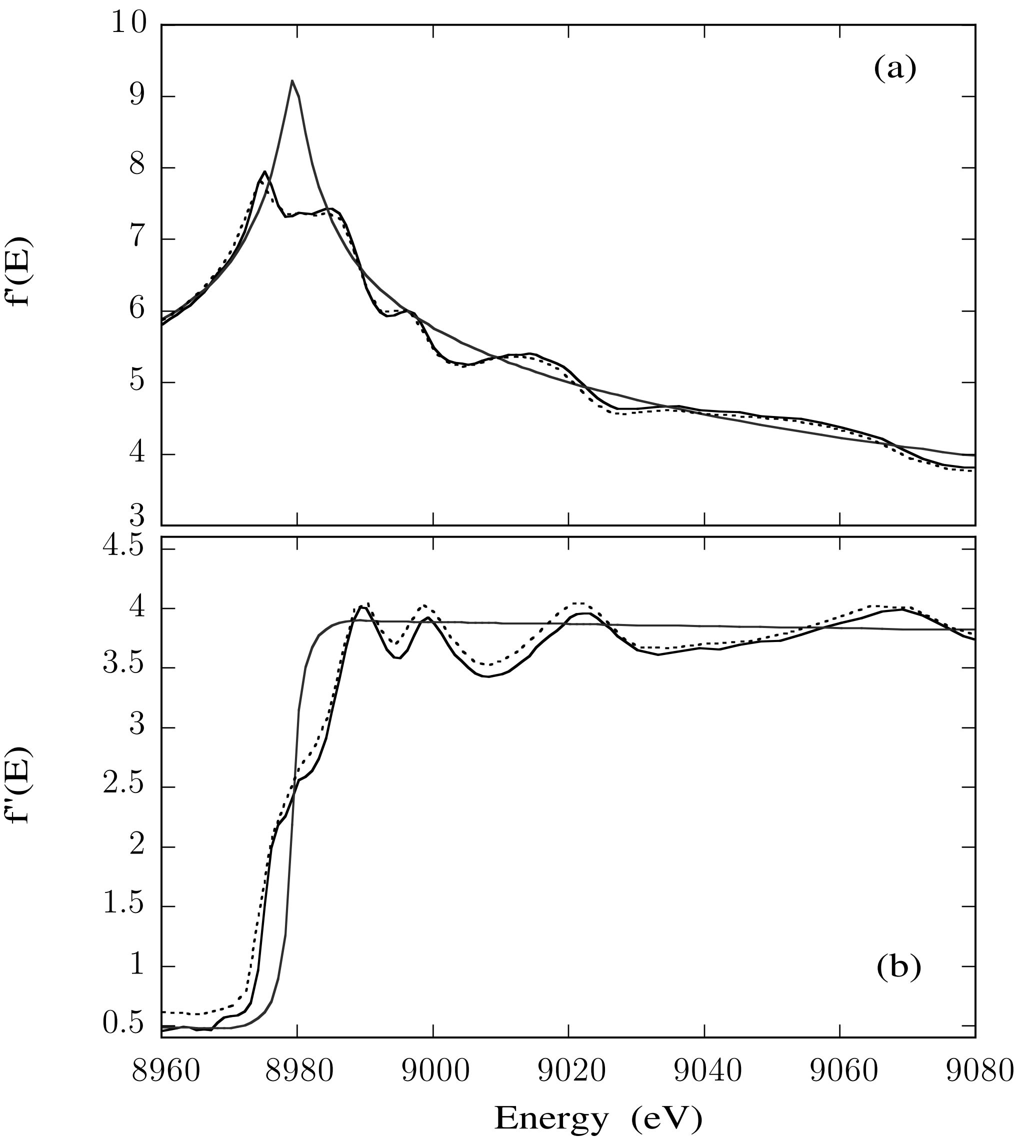

Figure 5.5: (a) $f'(E)$ and (b) $f''(E)$ from the Cu(111) (solid line) and Cu(222) (dashed line) DAFS using KKFIT, overplotted with Cromer-Liberman functions convolved with a 2 eV Lorentzian.

band-limited. The measurements need to be taken out to the end of the range of $\chi(E)$ oscillations, and the smooth part of the fit needs to match very closely to the tails of $f_{\mathrm{w}}(E)$. The exact functions used for $f_a(E)$ is not important as long as they can be made to agree with the overall shape of the measured intensity well enough to band-limit the argument of the integral in Equation (5.12), and as long as they are invariant under the infinite Kramers-Krönig transform. This means that *any* complex function satisfying these two criteria will work for the iterative analysis, but it is important to recognize that while $f'_{\mathrm{w}}(E)$ and $f''_{\mathrm{w}}(E)$ will be returned correctly, $\chi_{\mathrm{w}}(E)$ depends on the function that is subtracted off of $f_{\mathrm{w}}(E)$. There are many excellent versions of the atomic functions available, either in tables [63] or on the internet [65, 66]. Since none of the theoretical calculations presently available are as accurate in the immediate vicinity of E_0 as they are far from the edge, the near-edge structure of $\chi_{\mathrm{w}}(E)$ will not be accurate. This is the same as the usual situation for XAFS. However, the total function $f_{\mathrm{w}}(E)$ *will* be accurate since both the smooth part and the fine structure part are invariant under Kramers-Krönig and since the original Reimann sum is linear in the argument. I will explore the reliability of this iterative algorithm carefully in Chapter 7.

The $\chi'_{\mathrm{w}}(\mathbf{Q}, E)$ functions

Once $f_{\mathrm{w}}(E)$ has been determined, $\chi\mathrm{w}(k)$ is found by Equations (5.4) and (5.4), and by converting the argument from E to k. Normalization of $\chi_{\mathrm{w}}(k)$, analogous to Equation (5.1), is straightforward since the functions were fit using theoretical standards and the height of step with respect to the fine structure is known exactly. The results of the iterative Kramers-Krönig fit to the Cu (111) DAFS are shown in Figure 5.6 and again, over a more limited k-space range, in Figure 5.7. The symmetry condition causes the antisymmetric parts of the structure factor sum to cancel so that the real and imaginary parts of $\chi_{\mathrm{w}}(E)$ are separated into sums over the real and imaginary parts, respectively, of the individual site signals. These are:

$$\begin{aligned}
\chi'_{\mathrm{w}}(\mathbf{Q}, E) &= \frac{\sum_{\text{atom } r} \chi'_r(E) \cos(\mathbf{Q} \cdot \mathbf{R}_r) e^{-M_r}}{\sum_r \cos(\mathbf{Q} \cdot \mathbf{R}_r) e^{-M_r}} \\
&= \frac{1}{\alpha} \sum_{\text{site } j} \alpha_{j,\mathbf{Q}} \chi'_j(E) \\
&= \sum_{\text{site } j} W_{j,\mathbf{Q}} \chi'_j(E)
\end{aligned} \tag{5.13}$$

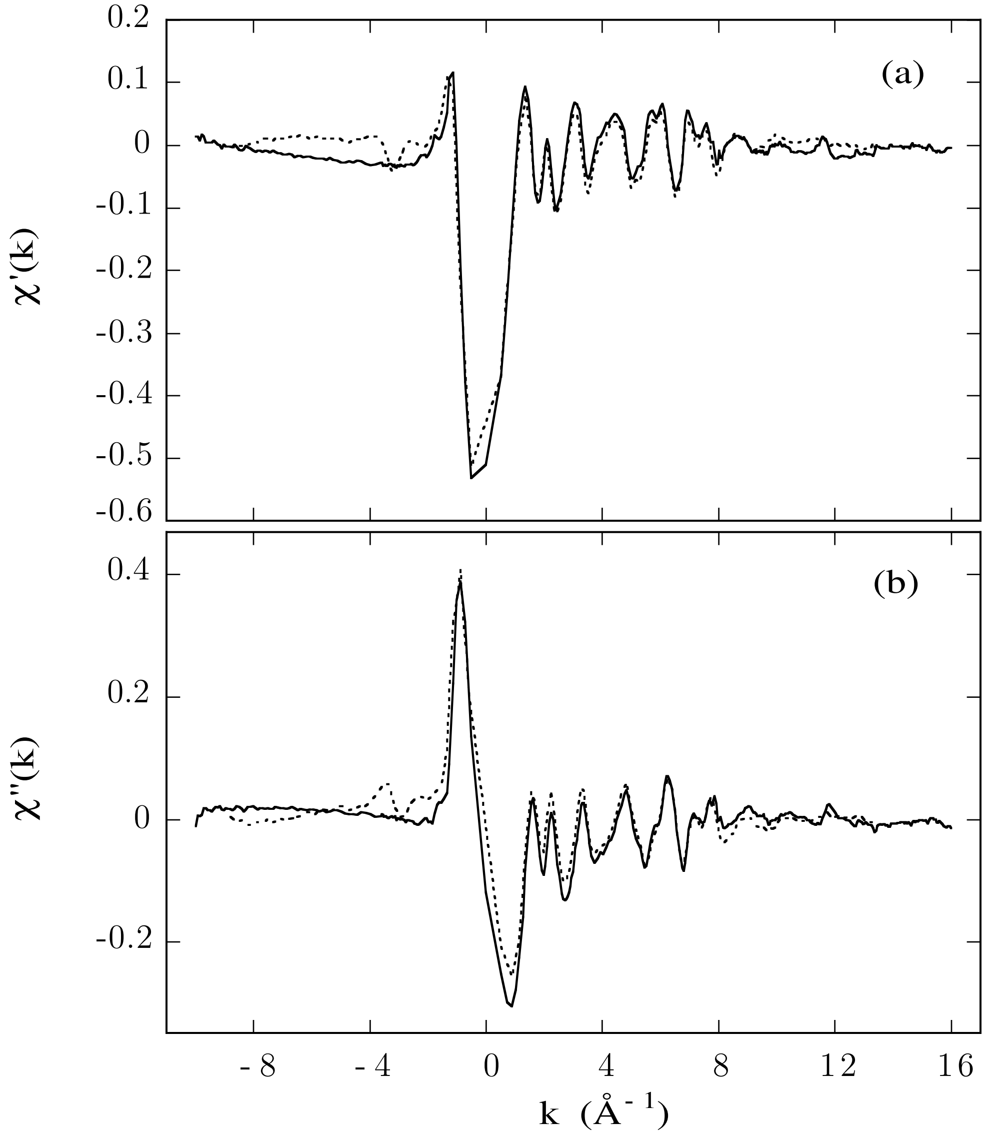

Figure 5.6: Cu (111) (solid lines) and Cu (222) (dashed lines $\chi'(k)$ and $\chi''(k)$ functions from DAFS using KKFIT. The iterative Kramers-Krönig method produces a pair of functions (a) $\chi'(k)$ and (b) $\chi''(k)$ that span the range of the original data. The low frequency drift is due to the inflexibility of the structure factor model. The structural parameters are not affected by this smooth background, and it can be corrected by FEFFIT in R-space.

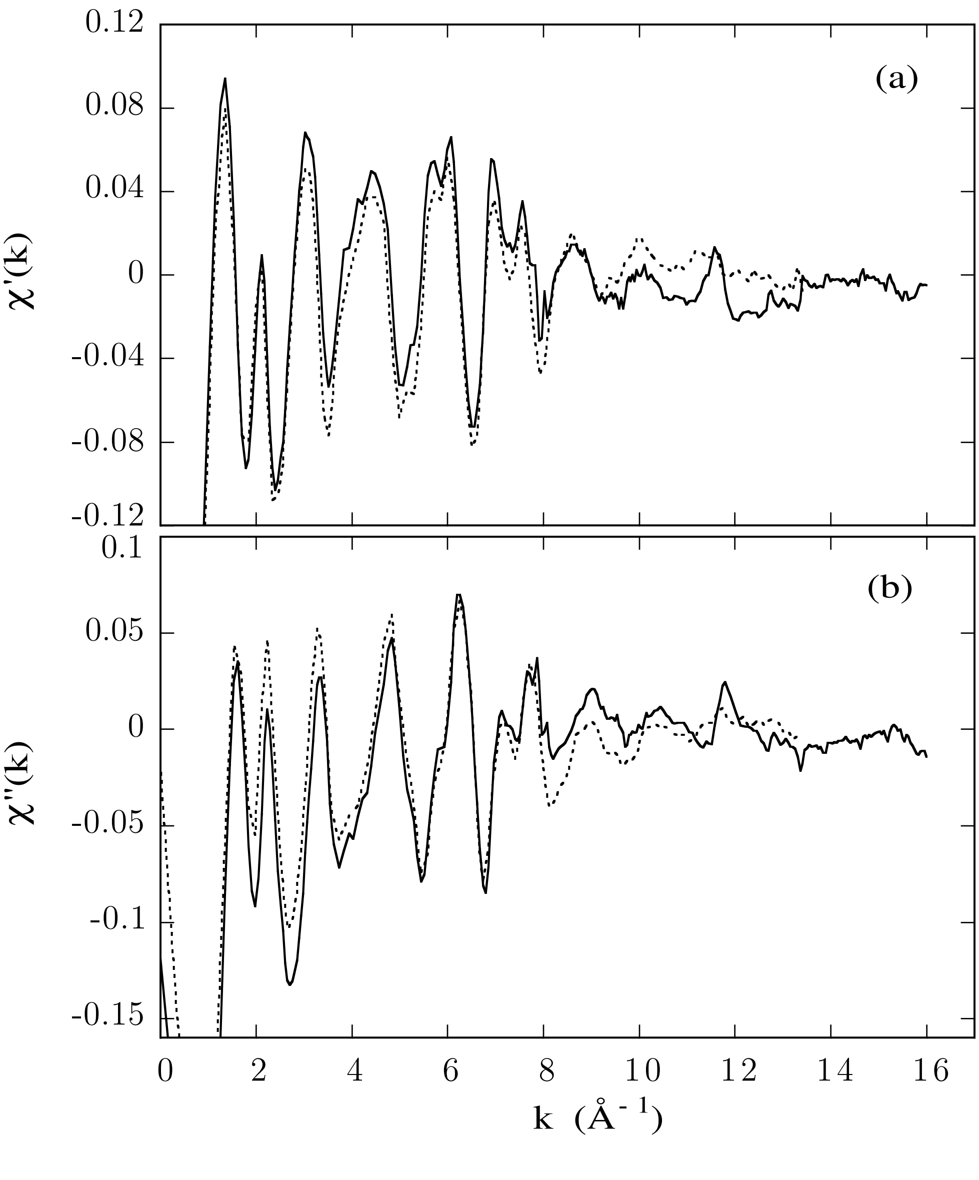

Figure 5.7: An expanded view of the functions from Figure 5.6 showing the range that is modeled using FEFFIT (a) $\chi'(k)$ and (b) $\chi''(k)$

and the conjugate function

$$\chi''_{\mathrm{w}}(\mathbf{Q},E) \;=\; \sum_{\text{site } j} W_{j,\mathbf{Q}}\chi''_j(E). \tag{5.14}$$

The sum is taken only over the resonant sites in the unit cell and the $\mathbf{Q}$ dependence of the diffraction Debye-Waller factors is given by $M = B\,(\mathrm{Q}/4\pi)^2$ [38]. The $\chi_{\mathrm{w}}(\mathbf{Q},E)$ functions contain information about the long-range order of the sublattice of resonant atoms through the mixing coefficients $W_{j,\mathbf{Q}}$ and about the local environment of the resonant atoms through the spectral content of the individual site fine structure functions $\chi_j(E)$. They are *linear* sums of the fine structure functions from the individual resonant sites, normalized to the sublattice structure sum α.

For materials with only a single type of resonant site contributing to the Bragg reflection, such as for a monoatomic material or for a spatially inhomogeneous alloy with well separated diffraction peaks, the isolated $\chi_{\mathrm{w}}(E)$ has a trivial coefficient $W_{j,\mathbf{Q}}$ of unity for all reflections. Cu metal is a good example for showing the general approach to the fine structure analysis, and to give a simple demonstration of the use of FEFF and FEFFIT to obtain structural parameters from the the fine structure. The high symmetry of f.c.c. copper metal eliminates the need to consider polarization effects in the DAFS of this material, and for the monoatomic problem the diffraction Debye-Waller factors are the same for all of the atoms so that they cancel out of the numerator and denominator of $W_{j,\mathbf{Q}}$. Polarization needs to be considered in materials with lower symmetry and the diffraction Debye-Waller factors will not necessarily cancel when there are resonant atoms in inequivalent sites in the unit cell. I will discuss both of these issues in Chapter 6 for $YBa_2Cu_3O_{6.8}$ DAFS, where they are relevant.

For pure dipole scattering and when the polarization direction does not change during the diffraction, the $\chi''(E)$ determined by KKFIT from the DAFS is the same as the $\chi''(E)$ function determined by AUTOBK from the XAFS with two small exceptions: First, the XAFS and DAFS functions are normalized to the step height, not to the step line shape, and since $f''(E)$ differs from $\mu(E)$ by a factor of $1/E$, the $\chi''(E)$ function in Equation (5.5) by a factor of E_0/E. I have analyzed the DAFS $\chi''(E)$ with and without this scale factor using standard XAFS analysis programs and have found no effect on the resulting structural parameters, but to err on the side of caution, KKFIT multiplies the final value of $\chi(k)$ by this factor; Second, the structure factor model to the DAFS background intensity in KKFIT is not as flexible as the spline in AUTOBK and cannot compensate for any low R noise in the resulting complex χ function. AUTOBK's more sophisticated background removal scheme uses the information content of the fine structure to minimize the low R region of $\tilde{\chi}(R)$. Background removal using Eqs. (5.4) and (5.5) isolates the fine structure and gets the normalization perfectly every time, but it typically leaves in a lot of low R noise in the Fourier transform.

Correcting KKFIT *background subtraction using* FEFFIT

The non-structural background left in $\chi(k)$ by KKFIT can be can be corrected for by using the background removal feature of FEFFIT. This gives a visually pleasing result, but does not change any of the structural information. To use this feature, FEFFIT needs to be run twice. The first call, with the background fitting feature turned on, will generate k-space and R-space background files consistent with low R minimization of $\tilde{\chi}(R)$. This generates the background curve shown in Figure 5.8(a). The second call, with the background feature turned off and the files generated on the first pass named as the background source files, will subtracted off the background signal generated by first call and fit to this new background-subtracted function. The background-subtracted DAFS $\chi''(k)$ function generated in this manner is overplotted with the XAFS $\chi''(k)$ determined by AUTOBK Figure 5.8(b). The FEFFIT command input files used for analyzing Cu DAFS with background removal are included in Appendix C.

5.3 *Fine structure analysis*

The fine structure functions shown in Figs. 5.2 and 5.7 were analyzed using FEFFIT and the input files in Appendix C. The real part $\chi'(k)$ of the DAFS fine structure differs from $\chi''(k)$ only by a uniform phase shift of $\pi/2$ on all photoelectron scattering paths. This was accommodated using the FEFFIT path parameter `dphase` in the input file for $\chi'(k)$. Otherwise the analysis procedure was identical for all three data sets. Following the the example in [21], the first shell was fit using the output from FEFF. The individual path files were calculated based on the f.c.c. structure of Cu metal and lattice parameter of 2.557 Å from reference [115]. The twelve backscattering paths shown in Table 5.2 were used in the fit and four variables in the model: the overall amplitude S_0^2; The Debye temperature Θ_D; an overall energy shift E_0; and

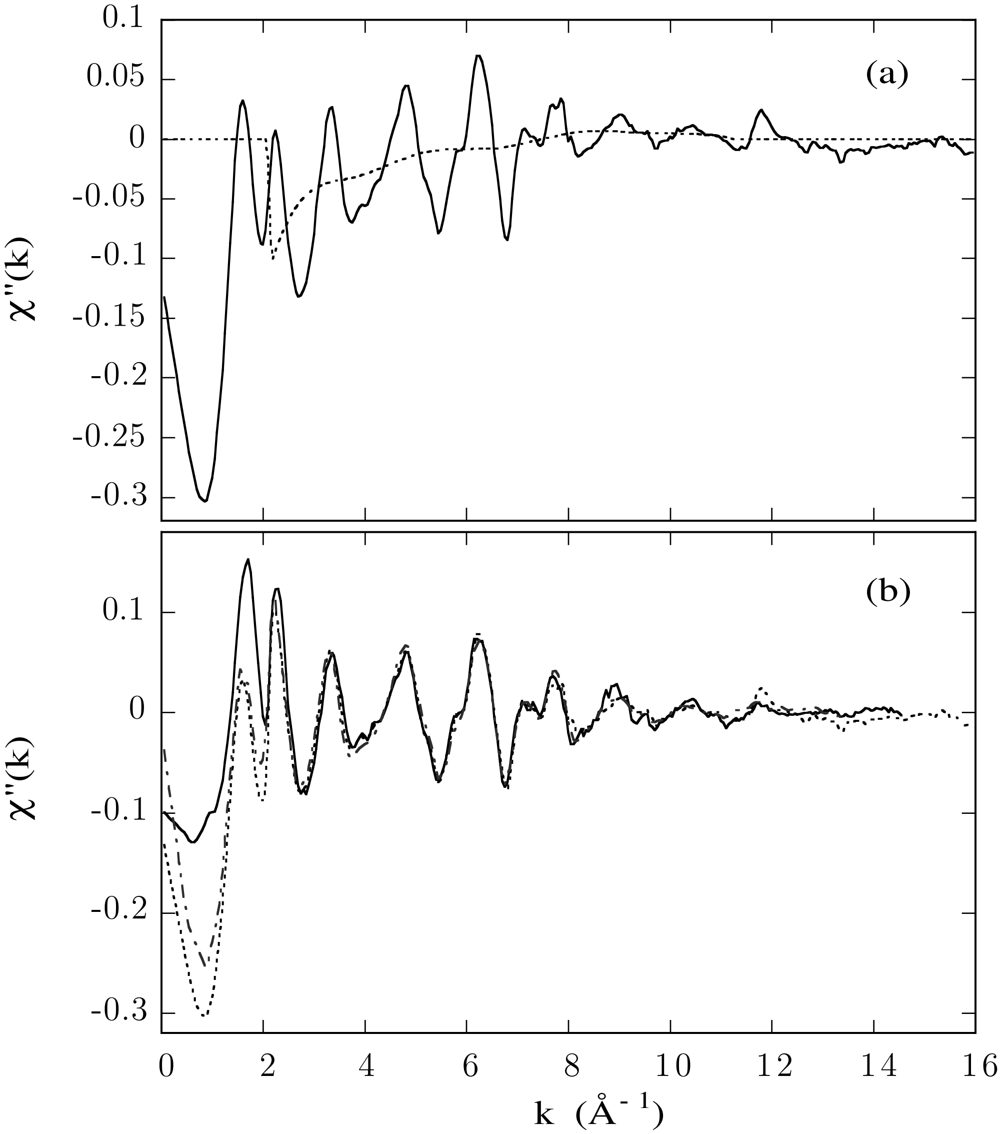

Figure 5.8: A background correction to the DAFS $\chi'(k)$ and $\chi''(k)$ from KKFIT can be made by using the FEFFIT `bkg` option to determine the non-structural background (a) The $\chi''(k)$ output from KKFIT (solid line) overplotted with the background file determined by FEFFIT (dashed line) on the $k_{min} = 2.2$ Å^{-1} to $k_{max} = 11$ Å^{-1} and $R_{bkg} = 1.5$ Å. (b) Overplot of the DAFS $\chi''(k)$ functions for the Cu (111) (dashed line) and Cu (222) (dot-dashed line), after subtracting the FEFFIT background, with the XAFS $\chi''(k)$ (solid line) from Figure 5.2.

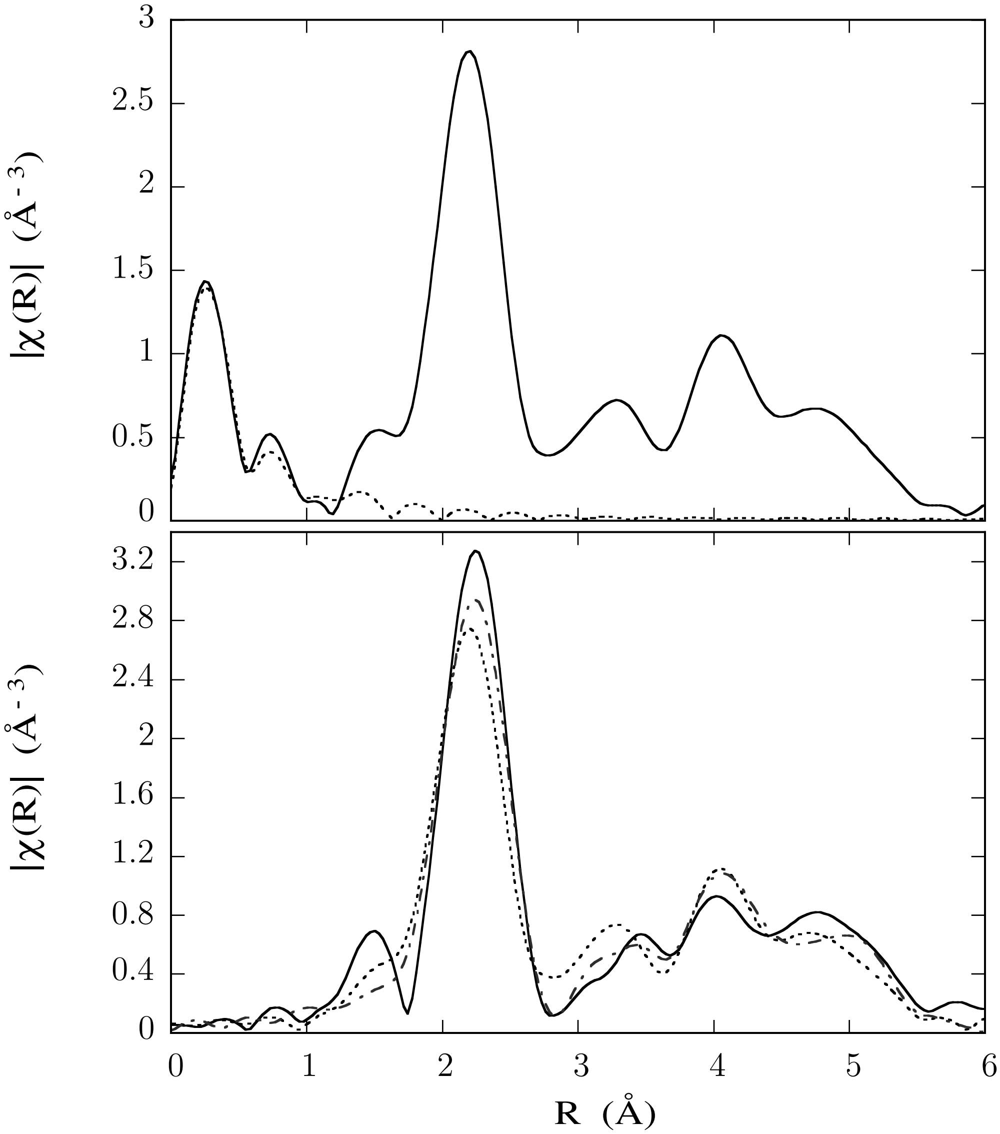

Figure 5.9: A background correction to the DAFS $\chi'(k)$ and $\chi''(k)$ from KKFIT using the FEFFIT `bkg` option to determine the non-structural background (a) The $\chi''(k)$ output from KKFIT (solid line) overplotted with the background file determined by FEFFIT (dashed line) on the $k_{min} = 0$ Å^{-1} to $k_{max} = 14$ Å^{-1} and $R_{bkg} = 1.5$ Å. (b) Overplot of the DAFS $\chi''(k)$ functions for the Cu (111) (dashed line) and Cu (222) (dot-dashed line), after subtracting the FEFFIT background, with the XAFS $\chi''(k)$ (solid line) from Figure 5.2.

Table 5.2: The first twelve important paths from FEFF 6.10 for Cu metal at 293K. Paths are ordered by increasing R. R_{eff} are the half-path distances, N_{degen} accounts for the number of scattering sites, and A_{cw} are the Zabinsky curved-wave importance factors, which are useful for eliminating scattering paths with negligible contributions to the fine structure.

Path Index	A_{cw}	N_{degen}	N_{scatt}	R_{eff}(Å)	Path
1	100.00	12	2	2.5560	SS, first shell
2	22.98	6	2	3.6148	SS, second shell
3	10.51	48	3	3.8341	triangular
4	8.62	48	3	4.3634	triangular
5	55.41	24	2	4.4272	SS, third shell
6	10.59	48	3	4.7697	triangular
7	21.88	96	3	4.7697	triangular
8	18.94	12	2	5.1121	SS, fourth shell
9	8.44	12	3	5.1121	linear
10	43.64	24	3	5.1121	focusing
11	8.22	12	4	5.1121	linear
13	32.72	12	4	5.1121	focusing

a linear expansion coefficient α which is related to the change in the effective path length by $\Delta R = \alpha R_{\text{eff}}$. The R-space transform $\tilde{\chi}''(R)$ of the XAFS data and the FEFFIT fit are shown in Figure 5.10. Similarly, results for the DAFS functions are shown in Figure 5.11 for the real part and Figure 5.12 for the imaginary part. The best-fit values for the adjustable path parameters found by FEFFIT are given in the top row of Table 5.3.

5.4 Spline-based fine structure isolation

I mentioned in Section 5.2.2 that it is also possible to subtract off the smooth part of the resonant scattering amplitude using a spline through the "background" intensity, similar to the standard treatment of XAFS data in Equation (5.1). Formally, this is equivalent to breaking up the expression for the intensity in a slightly different way than Equation (3.29). The spline follows the line of the cusp, so the $f_a(E)$ contribution to the structure factor is now considered as part of the smooth background. The meaning of the fine structure is different, as can be seen in the following equations.

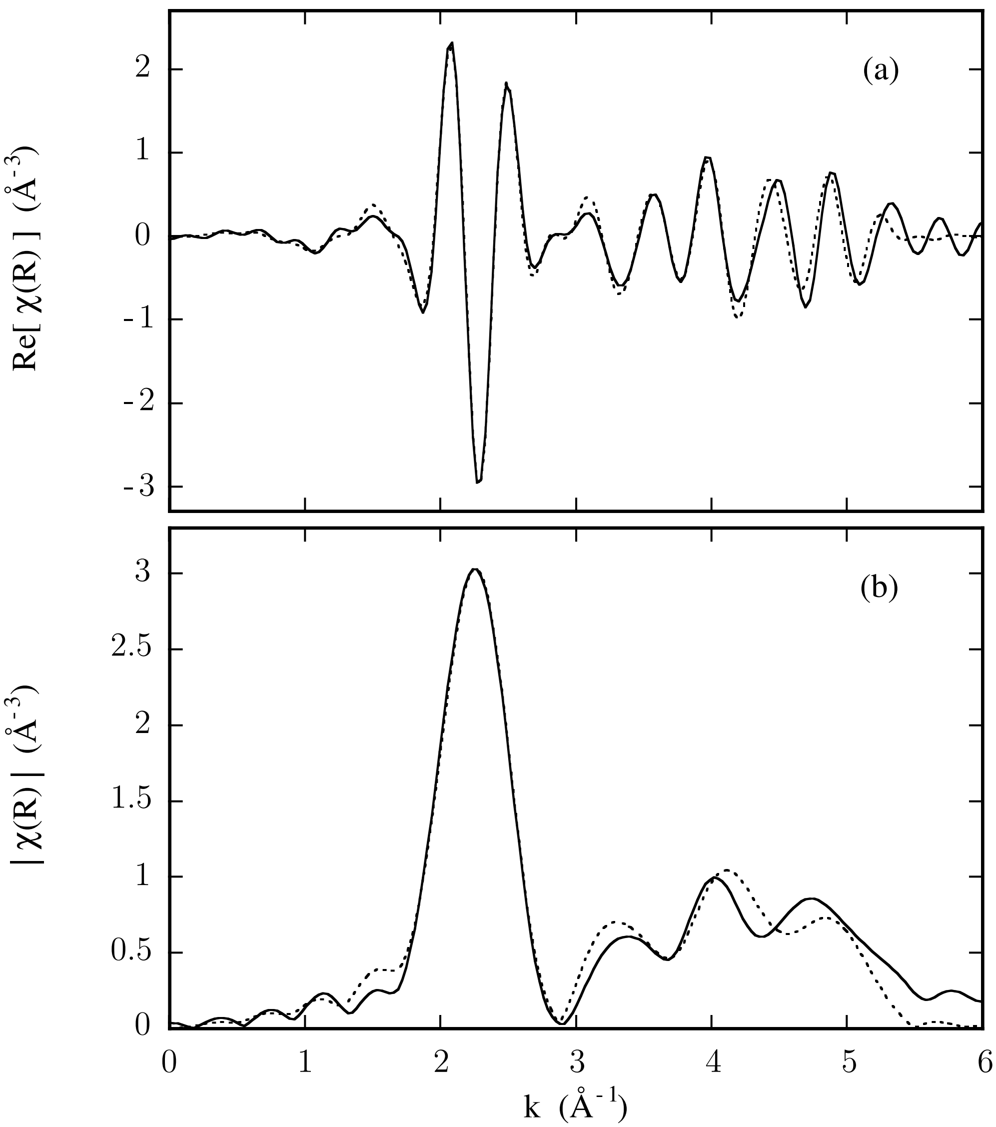

Figure 5.10: First shell fit (dashed line) to the R-space transform $\tilde{\chi}(R)$ (solid line) of the fluorescence Cu XAFS shown in Figure 5.1. The first shell fit used the twelve paths listed in Table 5.2. (a) The real part of the complex transform $\mathrm{Re}[\tilde{\chi}(R)]$ and (b) the magnitude of the R-space transform $\tilde{\chi}(R)$.

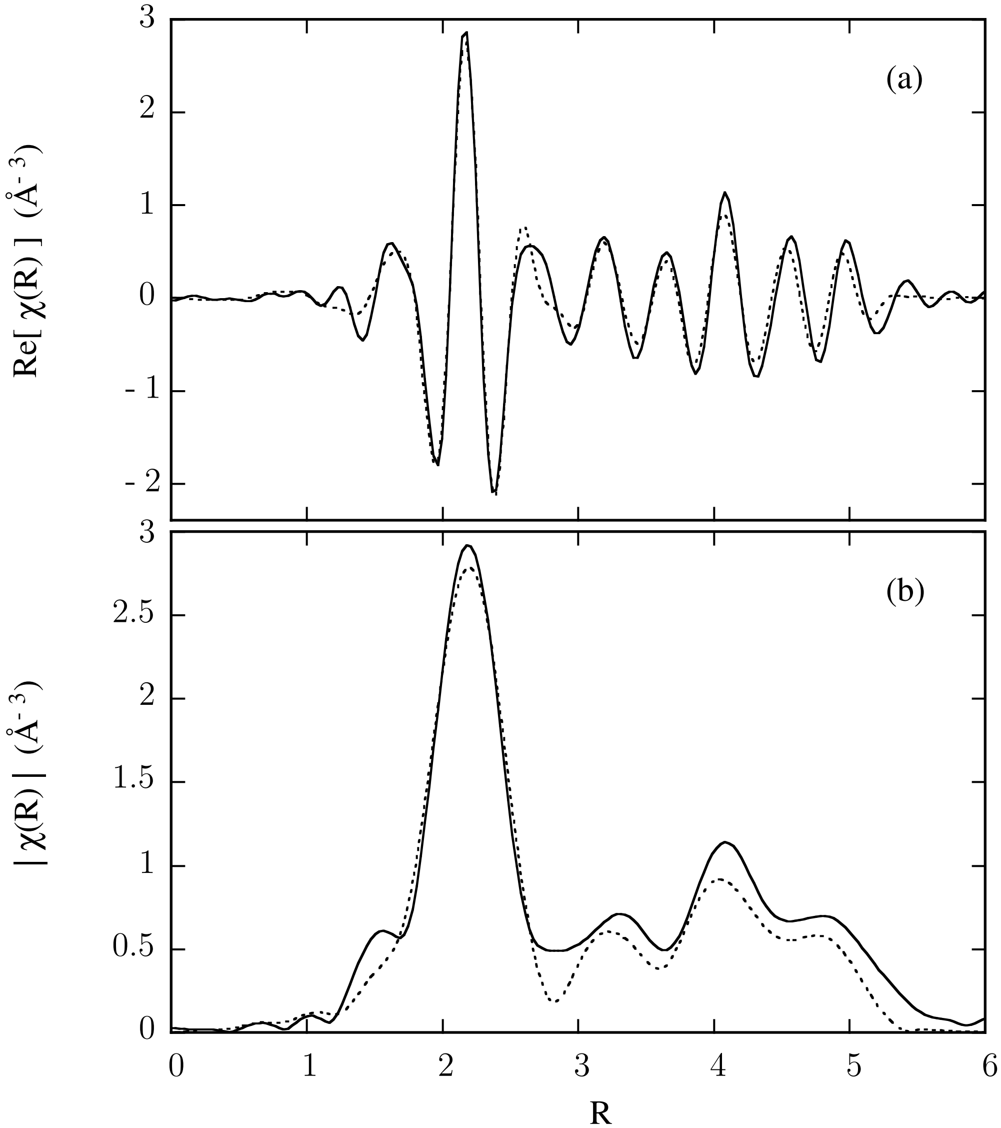

Figure 5.11: FEFFIT fit to Cu (111) DAFS $\tilde{\chi}'(R)$ after the smooth background has been removed by feffit. (a) Re$[\tilde{\chi}(R)]$ and (b) $|\tilde{\chi}(R)|$ data (solid lines) overplotted with the FEFFIT fits (dashed lines).

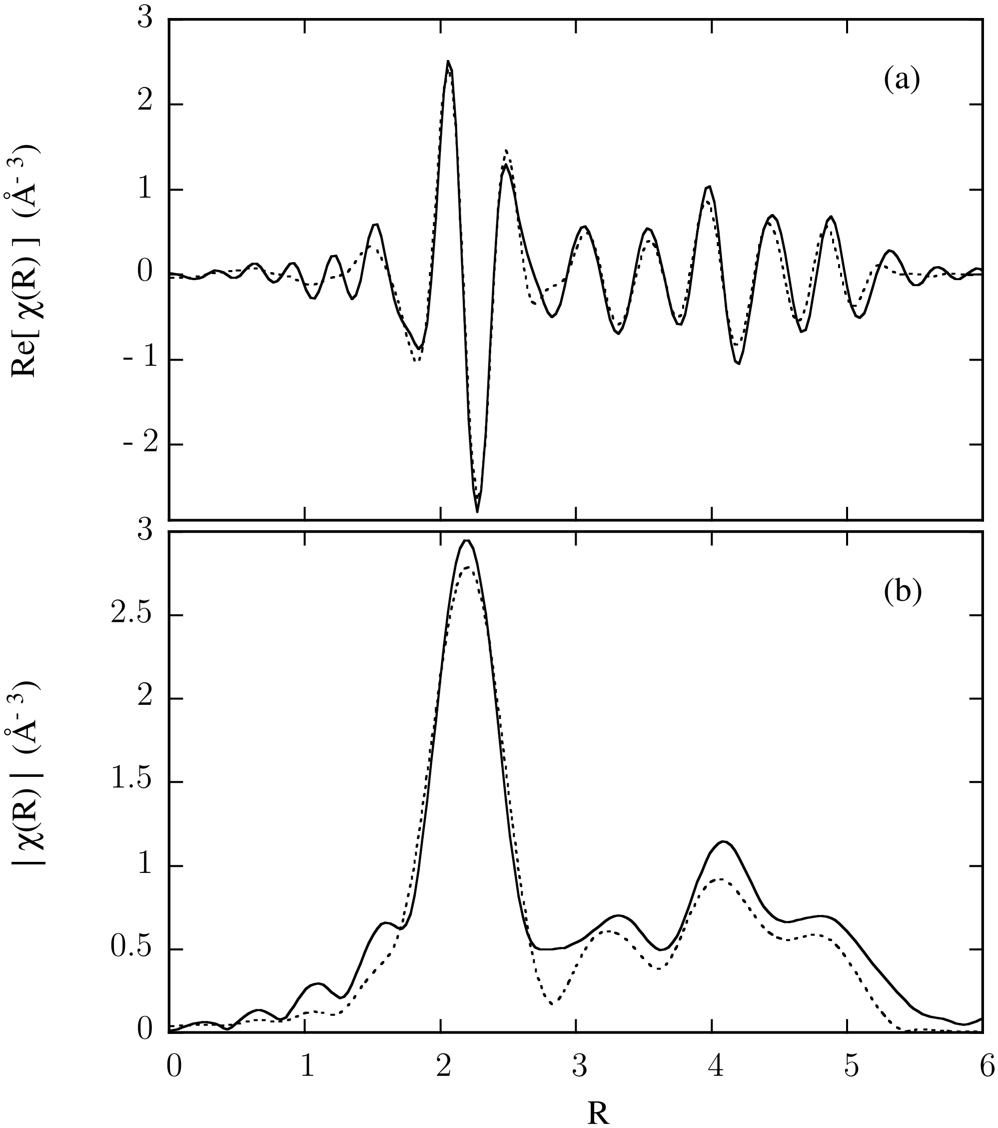

Figure 5.12: FEFFIT fit to Cu (111) DAFS $\tilde{\chi}''(R)$ after the smooth background has been removed by feffit. (a) Re$[\tilde{\chi}(R)]$ and (b) $|\tilde{\chi}(R)|$ data (solid lines) overplotted with the FEFFIT fits (dashed lines).

Table 5.3: Table of FEFFIT fitting results for Cu XAFS and Cu DAFS. Four adjustable fitting parameters were used in the Levenberg-Marquardt minimization: an overall amplitude S_0^2 that serves as the passive electron reduction factor; The Debye temperature Θ_D for the XAFS Debye-Waller factors; an overall energy shift E_0; and a linear expansion coefficient α which is related to the change in the effective path length by $\Delta R = \alpha R_{\text{eff}}$. The last column gives the value of the distance of closest approach, which can be compared to the value of 2.557 Å found in the literature [115].

data	S_0^2	Θ_D (K)	E_0 (eV)	α	d_0 (Å)
XAFS $\chi''(k)$	0.911±0.08	311±17	2.7 ±0.8	0.008006±0.002	2.5765±0.005
DAFS $\chi'(k)$	1.139±0.21	270±21	-0.47±1.9	-0.002553±0.005	2.5495±0.013
DAFS $\chi''(k)$	1.128±0.22	271±23	-0.16±1.9	-0.001674±0.005	2.5517±0.013

In a spline fit to DAFS, the *smooth* part of the structure factor F_s is defined by

$$\begin{aligned} I &= \left| \sum_j \left[f_0 + f'_a + i f''_a\right]_j e^{i\mathbf{Q}\cdot\mathbf{R}_j} e^{-M_j} + f''_0 \sum_r \left[\chi' + i\chi''\right]_r e^{i\mathbf{Q}\cdot\mathbf{R}_r} e^{-M_r} \right|^2 \qquad (5.15) \\ &= \left|F_\text{s} + f''_0 \alpha \chi_\text{w}\right|^2 , \end{aligned}$$

where I have assumed, as in Section 3.2, that f''_0 may be brought outside the sum, and α and χ_w have the same definitions as they did in Equation (3.37) and Equation (3.38), respectively. Squaring Equation (5.15) gives

$$I = |F_\text{s}|^2 + 2f''_0 \left(\text{Re}[F_\text{s}]\text{Re}[\alpha\chi_\text{w}] + \text{Im}[F_\text{s}]\text{Im}[\alpha\chi_\text{w}]\right) + (f''_0)^2 \left|\alpha\chi_\text{w}\right|^2 . \qquad (5.16)$$

Using Equation (5.16), in analogy to Equation (5.1), we can define a fine structure function

$$\begin{aligned} \overline{\chi}(E) &= \frac{I(E) - |F_\text{s}(E)|^2}{2\,|F_\text{s}(E)|\, f''_0(E)} \qquad (5.17) \\ &= \left(\cos\Phi_\text{s}\text{Re}[\alpha\chi_\text{w}] + \sin\Phi_\text{s}\text{Im}[\alpha\chi_\text{w}]\right) + \frac{f''_0}{|F_\text{s}|}\left|\alpha\chi_\text{w}\right|^2 \end{aligned}$$

where $\cos\Phi_\text{s} = \text{Re}[F_\text{s}]/|F_\text{s}|$ and $\sin\Phi_\text{s} = \text{Im}[F_\text{s}]/|F_\text{s}|$. A spline fit to DAFS data will closely approximate the function $|F_\text{s}(E)|$. AUTOBK can be used directly on DAFS data provided the step-height normalization feature is turned off. Since AUTOBK was designed to work with XAFS data, it expects a step function and will treat the spline as if there is one unless it is told explicitly to do otherwise. The normalization $2f''_0(E)$, based on Equation (5.17), can be forced by using the AUTOBK keyword `step`, but the structured part of the denominator $|F_s(E)|$ must be taken out by hand after the spline has been determined. Some care needs to be taken with the sign of the spline to avoid factors of π phase shifts in the resulting fine structure; fine structure determined by spline background fitting from a downward pointing cusp is multiplied by -1, from an upward pointing cusp is $+1$.

When the subset of resonant atoms has a center of symmetry at the reflection under consideration, the real and imaginary parts of $\alpha\chi_w$ reduce to expressions that involve only the real and imaginary parts of the response from each site

$$\begin{aligned} \mathrm{Re}[\alpha\chi_w] &= \alpha\chi'(E) \\ \mathrm{Im}[\alpha\chi_w] &= \alpha\chi''(E) \end{aligned} \tag{5.18}$$

where $\alpha = \sum_r \cos(\mathbf{Q}\cdot\mathbf{R})e^{-M_r}$ is purely real. Then Equation (5.17) becomes

$$\overline{\chi} = \alpha\left(\cos\Phi_s\chi'(E) + \sin\Phi_s\chi''(E)\right) + \frac{\alpha^2 f_0''}{|F_s|}.\,|\chi|^2 \tag{5.19}$$

Previous analysis of $\overline{\chi}$ [13] has neglected the second term in Equation (5.19), which is equivalent to assuming that the coefficient of $|\chi|^2$ is small compared to α, *i.e.*, that

$$\frac{|\alpha| f_0''}{|F_s|} \ll 1. \tag{5.20}$$

For a monoatomic material, this is true when the resonance correction is small compared to the magnitude of the Thomson scattering amplitude. At the Cu (111) reflection, for example, $f_0 \sim 20$, $f_0'' \sim 3.5$ near E_0, the maximum value of the real part of the resonance correction when $k > 3.5$ is $f' \approx 4$, and $\alpha = 4$ from the f.c.c. structure factor. Figure 5.13(a) is a plot of $|\chi(k)|^2$ for pure copper and Figure 5.13(b) shows an overplot of $\chi''(k)$ and $|\chi(k)|^2$ for visual comparison. The coefficient of $|\chi|^2$ for strong reflections is smaller than one, and for $k > 3.5$ the approximation of neglecting the $|\chi|^2$ term is good. When the scattering amplitude from the resonant atoms is small compared to the rest of the atoms, such as for strong reflections in materials with many non-resonant atoms, then the approximation is even better.

After making the approximation in Equation (5.20), the function $\overline{\chi}(k)$ can be interpreted as a sum over the harmonic components of χ with an additional phase shift for each path. Taking the complex expression for the fine structure in Equation (2.54),

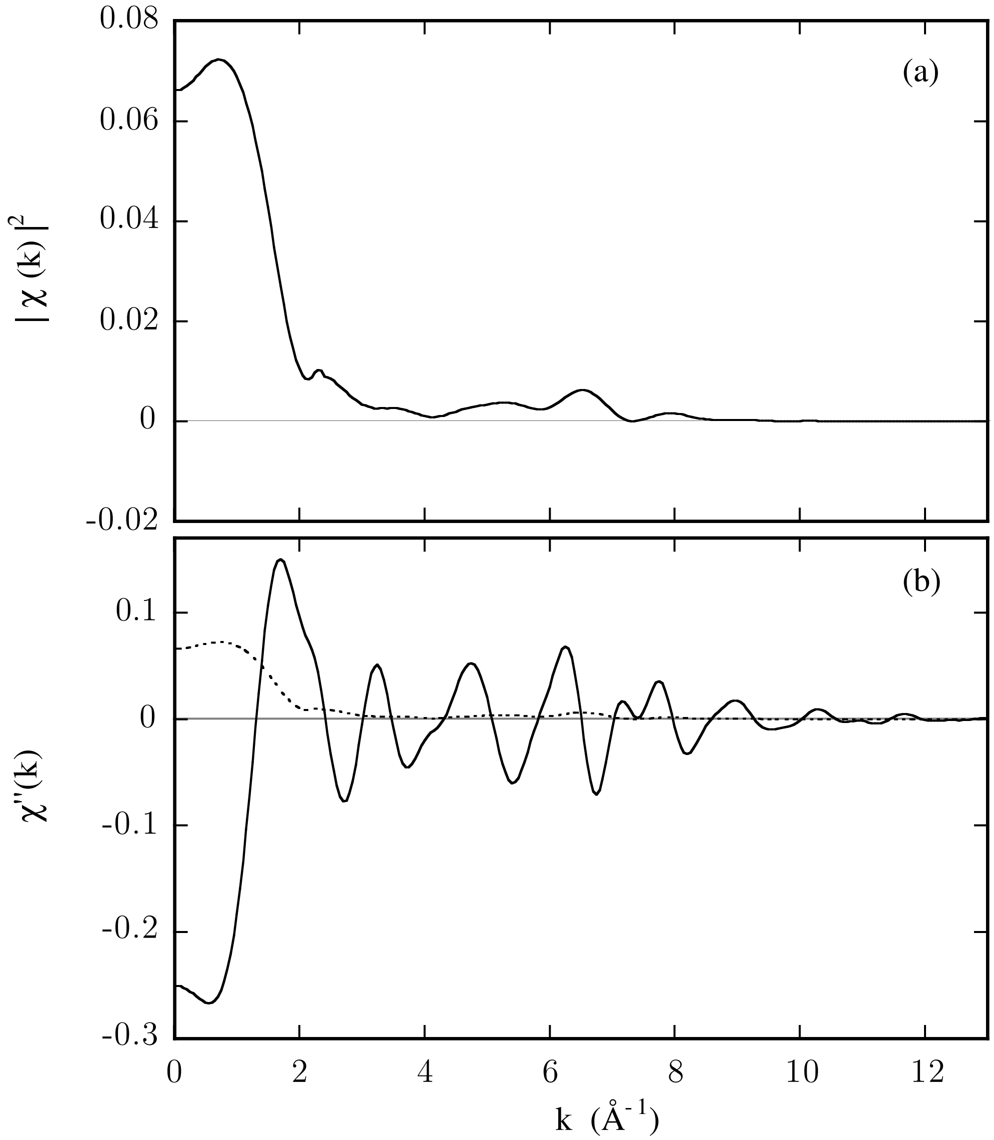

Figure 5.13: The relative size of $|\chi(k)|^2$ compared to $\chi''(k)$ calculated by FEFF. (a) Expanded view of $|\chi(k)|^2$. (b) Overplot of $\chi''(k)$ (solid line) and $|\chi(k)|^2$ (dashed line) for visual comparison. For $k > 3.5$, there is very little structure in $|\chi(k)|^2$. The size is further diminished by the leading coefficient $|\alpha| f_0''/|F_\mathrm{s}| \sim 0.6$ for Cu.

Table 5.4: Table of FEFFIT fitting results for the Spline-isolated function $\overline{\chi}(k)$ and the iterative Kramers-Krönig isolated function $\chi'(k)$.

	S_0^2	Θ_D	E_0	α
$\overline{\chi}(k)$	1.309±0.07	284±7	3.3 ±0.5	0.000607±0.0012
$\chi'(k)$	1.295±0.19	254±15	0.29±1.2	0.000015±0.004

we can rewrite Equation (5.19) using the identities $\cos a \cos b + \sin a \sin b = 2\cos(a+b)$ and $\cos a = \sin(a - \frac{\pi}{2})$ to obtain

$$\begin{aligned}
\overline{\chi} &= \alpha \sum_{\text{path } i} \left[\frac{N_i f_i(k)}{kR_i^2} (\cos \Phi_\mathrm{s} \cos(kR_i + \delta_i) + \sin \Phi_\mathrm{s} \sin(kR_i + \delta_i)) \right] \\
&= \alpha \sum_{\text{path } i} \left[\frac{2N_i f_i(k)}{kR_i^2} \sin(kR_i + \delta_i + (\Phi_\mathrm{s} - \frac{\pi}{2})). \right] \qquad (5.21)
\end{aligned}$$

The coefficient of $\overline{\chi}$ and the additional phase shift in the argument of the fine structure are both functions of $\mathbf{Q}$ and E, since the smooth function F_s contains ΔF. Letting $\beta = \Phi_\mathrm{s} - \frac{\pi}{2}$, and converting the argument using Equation (5.2), the explicit $\mathbf{Q}$ and E dependence of $\overline{\chi}$ is

$$\overline{\chi}(\mathbf{Q}, k) = \alpha(\mathbf{Q}, k) \sum_{\text{path } i} [A_i(k) \sin(kR_i + \delta_i + \beta(\mathbf{Q}, k)),] \qquad (5.22)$$

The two functions $\chi'(k)$ and $\overline{\chi}(k)$ are overplotted in Figure 5.14(a), and their R-space transforms are overplotted in Figure 5.14(b). Results of a FEFFIT fit to the first shell $R = 1.6$ Å to $R = 2.75$ Å, and $k = 1.5$ Å -1 to $k = 12$ Å^{-1}, for $\chi'(k)$ and $\overline{\chi}(k)$ are shown in Figures 5.15(a) and 5.15(b), respectively. The resulting structural parameters are compared in Table 5.4.

5.5 *Comments on the iterative Kramers-Krönig technique*

The iterative Kramers-Krönig algorithm is only applicable to materials for which the subset of resonant sites projected onto the direction of the momentum transfer has a center of symmetry. Then the sum $\sum_r e^{i\mathbf{Q}\cdot\mathbf{R}_r}$ is purely real and there are no cross-terms of the form $f'(E)f''(E)$. This was discussed in Section 3.3, but the point cannot be overemphasized. When the iterative Kramers-Krönig method cannot be applied, an alternative approach is to model the whole DAFS intensity signal. This entails modeling the amplitude using whatever tools are available to calculate *a priori*

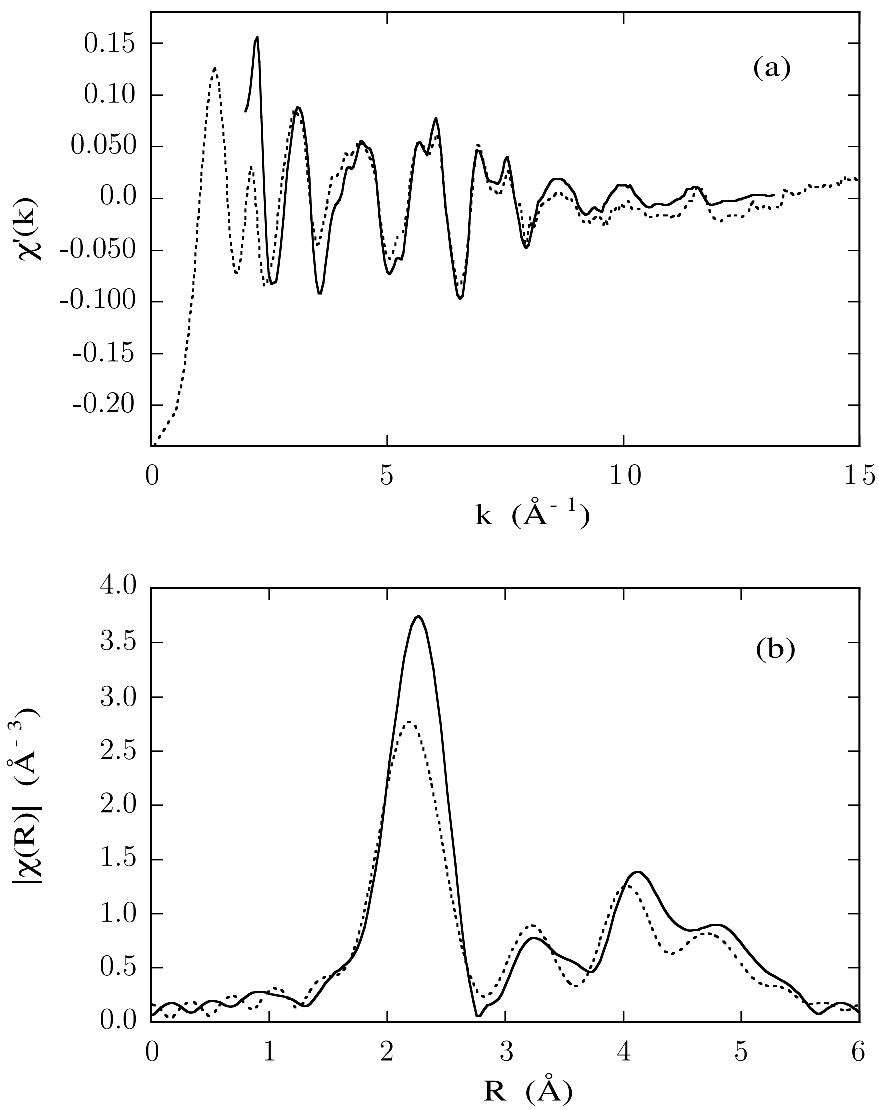

Figure 5.14: Comparison between the spline and KKFIT fine-structure functions. Overplots of $\overline{\chi}(k)$ (solid line) and $\chi'(k)$ (dashed line) in (a) k-space and (b) R-space.

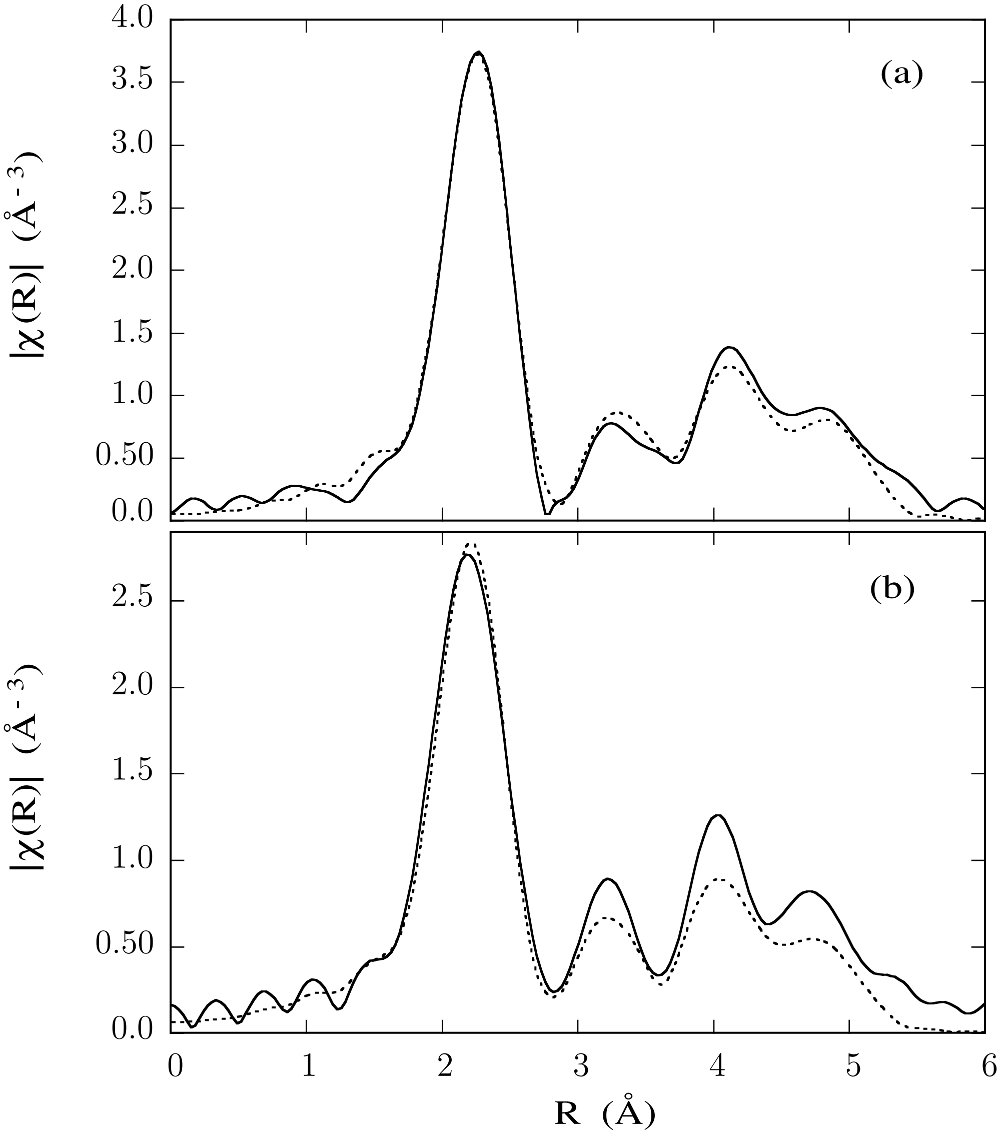

Figure 5.15: FEFFIT fits to spline and KKFIT fine-structure. The results of the fit are shown in Table 5.4.

$\Delta f(E)$ and the fine structure. A whole signal fit avoids the iterative Kramers-Krönig algorithm, and thus can be applied to the more general non-centrosymmetric crystal, but it only provides site-specific features that are calculated by the fine-structure modeling program.

In the first stage of KKFIT the smooth structure factor model does not take into account the fine structure, which is distributed with a large moment about the best fit to the data. This makes it difficult to define a "goodness of fit" parameter in KKFIT. One possible solution is to minimize not to a bare-atom $\Delta f_a(E)$, but to a calculated $\Delta f_{\mathrm{w}}(E)$ based on FEFF for the fine-structure combined with either Cromer-Liberman or a differential Kramers-Krönig calculation on the FEFF embedded atom $\mu_0(E)$ to obtain a $\Delta f_a(E)$. At the very least, starting with an initial guess that includes the fine structure will improve the starting position in parameter space.

One unfortunate feature of the iterative method is that it *always* generates a fit that goes through the data points, including the noise, and manages to do so with a surprising variety of conjugate pairs of functions. In the best of all possible worlds there is a unique pair of functions that fit the data, and these are the real and imaginary parts of the true scattering amplitude. In reality, the pair of analytic $\chi(k)$ functions that best fits the measured DAFS depends on the the quality of the data, on the theoretical functions used for $\Delta f_a(E)$ and on how the data is processed before the analysis. Since the KKFIT 'model' is a projection of the data onto the complex plane, noise in the data is also projected into the real and imaginary parts of $\chi(E)$ and since the model intensity can overplot even the noise exactly, a fit can only be considered bad when $\chi(k)$ lacks physical meaning. Earlier versions of KKFIT minimized the functional

$$g(E, \mathbf{a}) = I(\mathbf{Q}, E) - I_{\mathrm{model}}(\mathbf{Q}, E, \mathbf{p}). \tag{5.23}$$

Frequently the functions $I(\mathbf{Q}, E)$ and $I_{\mathrm{model}}(\mathbf{Q}, E, \mathbf{p})$ would be indistinguishable, but comparison between the real and imaginary parts of $f_{\mathrm{w}}(E)$ and $f_a(E)$ was very poor. My solution was to change the minimization to the more complicated functional of Equation (5.9). This could be refined to included both the real and imaginary parts of $f_a(E)$ or, better yet, to base the minimization on the information content of the resulting fine structure function, the way that AUTOBK now does for XAFS. There are so many questions to address about the reliability of the iterative Kramers-Krönig algorithm that I have devoted all of Chapter 7 to this topic.

Chapter 6

DAFS ANALYSIS OF $YBa_2Cu_3O_{6.8}$

The local goal of this chapter is to show how the site-specific resonance response functions from the two inequivalent Cu sites in $YBa_2Cu_3O_{6.8}$ are isolated using DAFS. The larger goal is to demonstrate a general method for isolating site-specific response functions from complex materials. The approach I have adopted takes the Kramers-Krönig extracted $\chi_{\mathrm{w}}(\mathbf{Q},k)$ functions, which are linear combinations of the fine structure functions from the individual resonant sites and fits them *en masse*, using FEFFIT, in the extended energy region. The mixing coefficients that determine the amount of $\chi_{\mathrm{Cu(1)}}(k)$ and $\chi_{\mathrm{Cu(2)}}(k)$ in each $\chi_{\mathrm{w}}(\mathbf{Q},k)$ are adjusted using a single kinematic structure factor model for all of the data sets with $\mathbf{Q}$ as the independent variable. This allows the coefficients $W_{j,\mathbf{Q}}$, which contain crystallographic information about the sub-lattice of resonant sites, to be refined from the DAFS fine structure using existing XAFS analysis tools. Once a complete set of coefficients is determined, the original response functions $\chi_{\mathrm{w}}(\mathbf{Q},k)$, $\tilde{\chi}_{\mathrm{w}}(\mathbf{Q},R)$, $\mu_{\mathrm{w}}(\mathbf{Q},E)$, *etc.*.., are combined to obtain their site-separated parts. This amounts to solving the original mixed data for the individual site response functions by inverting the matrix of mixing coefficients.

I have relied on results from crystallographic studies to generate working models for both the diffraction intensities and the fine structure. Using this knowledge about the average arrangement of the atoms in the unit cell, and the output of the KKFIT, I am able to isolate the near-threshold resonance structure from the individual sites. There are two other approaches to analyzing DAFS that I am aware of, not counting for small differences in the structure factor model[1] The first approach, applicable in the case of n inequivalent sites, is to treat the χ_{w} at each point in energy as a linear sum of a set of n unknown functions mixed according to the long-range positions of

---

[1] The parameterized structure factor in Equation (5.7), which was normalized to the total non-resonant scattered intensity $|F_0|^2$, could also have been normalized to $\mathrm{Re}[F_0]$ or $\mathrm{Im}[F_0]$ [13, 17]. I prefer the symmetry in the form of Equation (5.7) which does not give precedence to $f'(E)$ over $f''(E)$, and so can be easily modified to accommodate weak or forbidden reflections without changing the program source code.

resonant sites in the unit cell. This is equivalent to my approach in that it assumes no *a priori* understanding of the local structure, needing only the long-range order of the sublattice of resonant atoms, to build a model for the linear combination, and centrosymmetry of the resonant sites parallel to $\mathbf{Q}$, required for the iterative Kramers-Krönig analysis. The second approach is to model the DAFS intensity according to a combined model for both the crystallographic *carrier* signal and the Fourier content of the fine structure. This avoids the iterative Kramers-Krönig algorithm, and thus can be applied to the more general non-centrosymmetric crystal, but it cannot provide the site-specific XANES. Any of these methods might be preferred under different circumstances and depending on the taste of the researcher.

The methods described in this chapter are applicable to the general case of N inequivalent sites in the unit cell provided an least N *non-degenerate* reflections are accessible such that the matrix of mixing coefficients has an inverse. Collecting data at a larger number of reflections than the minimum number required for inversion will add overspecification to the solution and improve the certainty of the coefficients. For the general inversion problem, crystal symmetry and the geometry of the experiment need careful consideration. The $\chi(k)$ functions themselves have a strong dependence on the direction of the polarization vectors of the incident and outgoing photons, as discussed in Section 2.3.3. The polarization dependence of the individual photoelectron scattering path contributions to the fine structure goes as the product of the angle cosines between the incident photon polarization direction $\hat{\mathbf{e}}$ and the first leg of the path and between the outgoing photon polarization direction $\hat{\mathbf{e}}'$ and the last leg of the path. While this special polarization dependence can certainly be included path-by-path in the *ab initio* fine structure calculations, if the $\chi(k)$ functions from the individual sites are not the same at each reflection, linear inversion cannot be applied to the $\chi_{\mathrm{w}}(\mathbf{Q}k)$ functions. This problem is circumvented by choosing the axis of rotation of the crystal to be parallel to the polarization direction of the incident x-rays. In general, because of the increased number of unknown variables, the simplest polarization dependence is preferred unless the cross-terms yield some new or interesting bit of information about the material.

In order to satisfy both the polarization and the non-degeneracy requirements, the Fourier components of the density of the resonant atoms projected onto the plane perpendicular to $\hat{\mathbf{e}}$ must be separable. If the requirement for non-degeneracy can only be met by a subset of the atoms, then only a subset of the resonant sites are separable in that plane. As before, application of the iterative Kramers-Krönig algorithm adds the requirement that there be a center of symmetry for the projected density of resonant atoms in the direction of $\mathbf{Q}$. For the example of $YBa_2Cu_3O_{6.8}$ presented here, the two Cu sites are well separated in the projection along the c-axis so that the site-separated response functions are obtained using only the (00ℓ) Bragg reflections. In the $(h00)$ or $(0k0)$ directions, the projected density of Cu(1) and Cu(2) collapses. The solution to determining site-specific c polarized $\chi(k)$ functions is to choose directions that span the three-dimensional space but do *not* lie in the a-b plane. The resulting fine structure mixes c polarized $\chi(k)$ with some a-b polarized $\chi(k)$ (for the a-b twinned crystal) which can then be separated out based on the results from the (00ℓ) DAFS.

6.1 Information content of DAFS data

The structure factor model Equation (5.7) used in KKFIT requires only that the sublattice of resonant sites have a center of symmetry parallel to $\mathbf{Q}$, and no other information about the detailed structure of the unit cell. If the unit cell is not known then some trial and error is needed to put the phase argument Φ_0 in the correct quadrant but, in principle, nothing else is required for extracting the real and imaginary parts of $\chi_{\rm w}(k)$. Using results from information theory as applied to XAFS [21, 69], if the number of relevant independent data points in a fit to the DAFS $\chi''(k)$ from one site over some R-range is N, then the number of data points measured across M reflections is $M \times N$. The real and imaginary parts of $\chi_{\rm w}(k)$ are linear sums of one unknown $\chi(k)$ function for each class of site when $\mathbf{Q}$ confined to a plane perpendicular to the incident photon polarization vector. The mixing coefficients depend on $\mathbf{Q}$ but they do not depend on E so the number of unknown parameters in the same collection of M data sets is equal $J \times N + J \times M$ for the J-site problem. In terms of the number of data points versus the number of unknowns, the problem quickly becomes overspecified when J is small. This suggests that it should be possible to isolate the individual site $\chi(k)$ functions from fairly complex material knowing only that there is a center of symmetry for the sublattice of resonant atoms and nothing else about the unit cell structure. This is not the approach I have adopted for the analysis presented in this dissertation, but it was suggested to me by one interested reader [70] and so I present it here for the consideration of others.

6.2 *Separation of the Cu-site $\chi(k)$ functions in* $YBa_2Cu_3O_{6.8}$

The first step in setting up the site separation analysis is familiarity with the material to be analyzed. I approach this from the point of view that crystallography will generally give you all the information you could possibly want about a material provided the long-range order in a diffracting material persists at short-range. When there is only one class of resonant site present, the long-range *versus* short-range questions can be studied using XAFS. When there are multiple resonant sites, such as the case in $YBa_2Cu_3O_{7-\delta}$, or for an inhomogeneous alloy, the XAFS signal is more difficult to study. Polarized XAFS has had some success separating the individual site signals in $YBa_2Cu_3O_7$ [76, 77], which has low symmetry, but the best results to date have required isomorphous substitution for one of the copper atoms. The DAFS results are unambiguous for $YBa_2Cu_3O_{7-\delta}$ and DAFS is the only solution when the symmetry is high.

Several geometrical factors affect the analysis of a complex crystal, both in the structure factor intensities and in the fine structure. In this section I will start with a description of the known structure of the material, and then discuss the particulars of our experiment and the fine structure model. The advantage of working with $YBa_2Cu_3O_{7-\delta}$ is that there is a wealth of literature on this material to draw from which allows quantitative cross-checking of all the analysis results. There should be no surprises in the final outcome of the structural analysis, and the shiny prize at the end is the fully site-separated XANES for the two Cu sites.

6.2.1 *The unit cell*

Figure 6.1(a) shows the structure of $YBa_2Cu_3O_7$. This is an orthorhombic unit cell, $a \neq b \neq c$, which is usually described as an oxygen deficient perovskite [71–73]. The basic perovskite unit, shown in Figure 6.1(b) for comparison, is comprised of two inequivalent metal ions and three oxygens. In the center of the unit sits a single ion that is surrounded by a cage made of the second metal at the corners and oxygens along the edges. Each of the metal ions at the corners of the cage is coordinated by six oxygen neighbors forming an octahedron. In $YBa_2Cu_3O_7$, the central ions in the perovskite boxes are Y and Ba, stacked in trilayers with the sequence BaYBaBaYBa, tripling the size of the unit cell in the stacking direction (c-axis). The sides of the boxes surrounding the Y ions are completely depleted of oxygen in the a-b plane. This

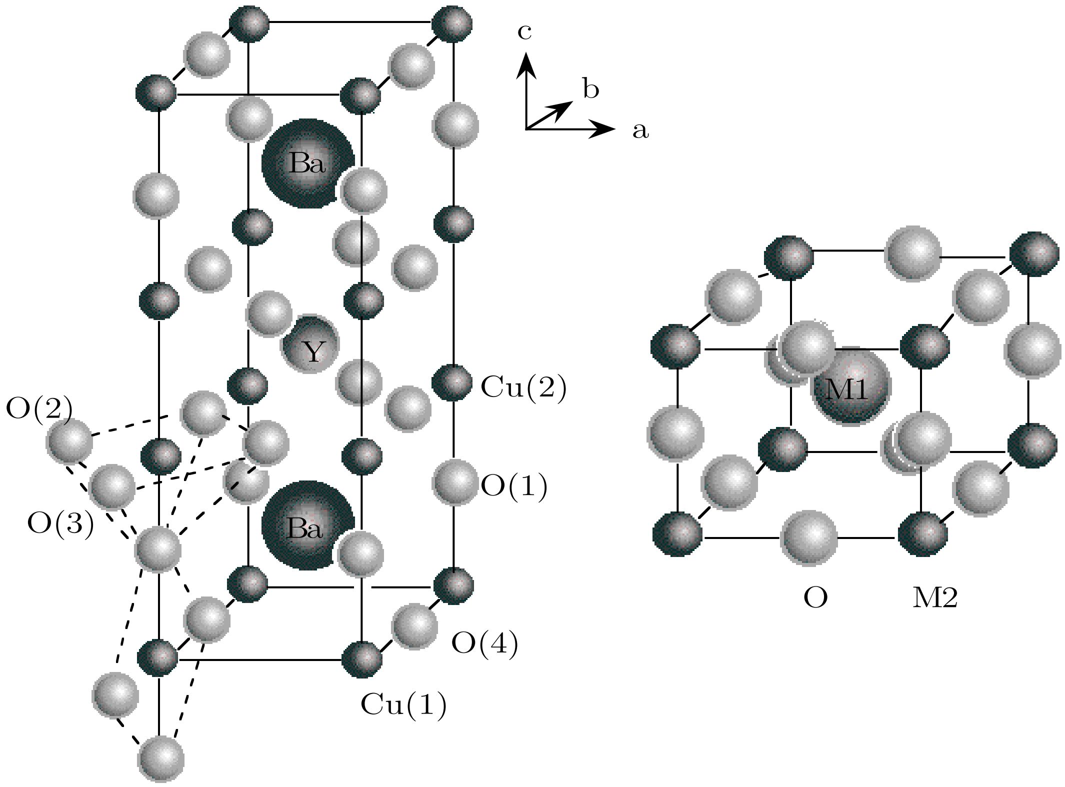

(a) (b)

Figure 6.1: (a) The unit cell for $YBa_2Cu_3O_7$ is comprised of three perovskite-like units with Ba in the central positions of two units and Y in the center of the third. (b) The arrangement of atoms in a general perovskite unit cell, $M1M2O_3$, where M1 and M2 are metal ions. The oxygens around the M2 ions form an octahedral shell. In $YBa_2Cu_3O_7$ this octahedron is missing a vertex, as can be seen in the dashed outline of the pyramid surrounding Cu(2) in (a). The oxygens around the Cu(1) site in $YBa_2Cu_3O_7$ are fully depleted along the a axis, and form chains of square-coordinated Cu-O parallel to b. One *link* in the chain is indicated by the dashed lines surrounding Cu(1) in (a).

has the effect of truncating one apex of the oxygen octahedra surrounding the Cu ions on the corners. The base of the resulting CuO_5 pyramid is buckled with the oxygens shifted towards the depleted region. There are four inequivalent oxygen sites and two inequivalent Cu sites in $YBa_2Cu_3O_7$. The apex of the CuO_5 pyramid is labeled O(1) and the base is formed by O(2) and O(3) along the a and b directions, respectively. The copper in the pyramid is labeled Cu(2). The Cu ion shared by adjacent Ba layers is labeled Cu(1) and is surrounded by only four oxygen neighbors. The oxygens that would lie along the a axis from Cu(1) are completely depleted. The oxygens along the b axis are labeled O(4) and form long flat chains of square coordinated O-Cu-O in this direction. These chains share the apical O(1) atoms with the pyramids, and one link in the chain is indicated in Figure 6.1(a) by dashed lines. When $YBa_2Cu_3O_7$ is depleted to form $YBa_2Cu_3O_{7-\delta}$, the depletion happens only at the O(4) site, gradually deteriorating the O-Cu-O chains. When depletion is complete, at $YBa_2Cu_3O_6$, the unit cell is tetragonal ($a = b \neq c$) and is not superconducting.

6.2.2 Experiment

The sample used in this study was a thin film of $YBa_2Cu_3O_{7-\delta}$ deposited by pulsed laser ablation on a 1 cm $\times$ 1 cm MgO (001) substrate [75]. The integrated intensities of 10 of the specular reflections were first measured on a rotating anode using Cu K-α radiation to determine the c lattice parameter. The rotating anode source provides an accurate determination of the photon energy, though the same results should obtain from any fixed-energy slice through the $\mathbf{Q}$-dependent DAFS data. The intensities were fit to a kinematic structure factor model with Debye-Waller factors taken from the literature [76]. Only the c lattice parameter and the positions of the Cu(2) atoms along the $\hat{\mathbf{z}}$ direction were refined from the data. The rotating anode data and fit are shown in Figure 6.2.

The oxygen depletion δ was estimated by the dependence of the c lattice parameter on δ from the literature [79, 80]. Taking c as a linear function of δ in Table II of [80] gives $c = 11.665 + 0.15933\delta$, or $\delta = 0.168$, $a = 3.83$ Å, and $b = 3.89$ Å, while the same procedure using Table II of [79] gives $c = 11.654 + 0.10248\delta$, or $\delta = 0.361$ Å, $a = 3.82$ Å, and $b = 3.88$ Å. The numbers for the oxygen depletion are very different, but the values for the a and b lattice parameters agree well enough for use as input to FEFF in the initial guess to the crystal structure. The measurements in [79] were taken at 5°K and our measurements were made at ambient temperatures. Reference [80] does not quote a temperature, but the measurements seem to have been made at liquid nitrogen ($\sim 77°$ K). The value of $\delta = 0.168$ is more consistent with a superconducting sample [73].

The DAFS data was collected at NSLS beamline X23A-2 using the three circle goniometer described in Section 4.2.1. All of the measurements were made in the vertical scattering plane so that the polarization vector was confined to the a-b plane, and there was no polarization correction to the diffracted intensity. Eight of the (00ℓ)

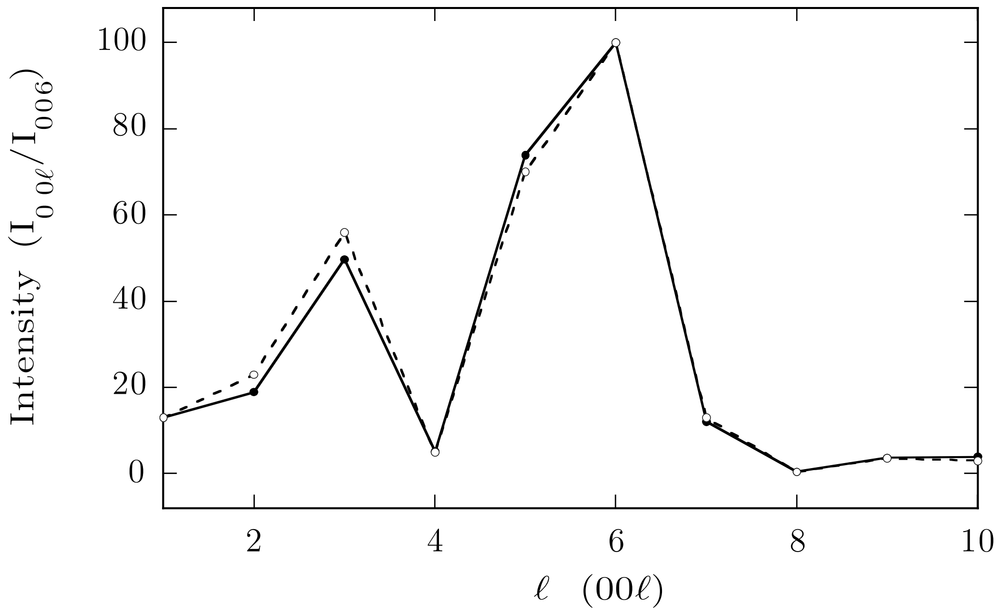

Figure 6.2: Structure factor fit to the specular Bragg intensities of $YBa_2Cu_3O_x$, measured on a rotating anode source ($\lambda = 1.5405$ Å). The best fit value (open circles) to the data (solid circles) for the c lattice parameter was 11.619 Å, consistent with an oxygen depletion of $\delta = 0.168$ [80]. The triple-perovskite unit cell is noticeable in the overall shape of the specular reflectivity. The dominant (003) and (006) reflections here correspond approximately to the (001) and (002) reflections in normal perovskite.

reflections were measured, $\ell = 1, 2, 3, 4, 5, 7, 9, 11$. Scattering was done in the vertical geometry so that the polarization of the incident and outgoing diffracted photons was confined to the a-b plane, making the polarization sense the same for all of the reflections. The density of the Cu sites in the unit cell projected onto the c axis has Cu(1) located at $z = 0$ and two Cu(2) sites located at $z = 0.3565c = 4.1422$ Å and $z = (1 - 0.3565)c = 7.4768$ Å, at equal distances from either end of the cell.

6.3 Analysis of $YBa_2Cu_3O_{6.8}$ *DAFS*

First, the $\Delta f_{\mathrm{w}}(\mathbf{Q}, E)$ and $\chi_{\mathrm{w}}(\mathbf{Q}, E)$ functions were solved from the measured intensity using KKFIT, as in Chapter 5. KKFIT takes an atom list as input which starts the initial parameters close to their expected values. For the $YBa_2Cu_3O_{6.8}$ fitting, FEFF was used to generate a mock-up of the fine structure using the first 25 significant scattering paths as a better initial guess than the Cromer-Liberman functions. This allowed the minimization to include the fine-structure in the minimization region. Consequently, one of the first steps in applying KKFIT to $YBa_2Cu_3O_{6.8}$ was to calculate $\chi'(E)$ and $\chi''(E)$. The input files used are given in Appendix B, and some features fo the fine-structure are addressed here.

6.3.1 The local environment of Cu(1) and Cu(2)

The direction of the incident and scattered photon polarization determines which scattering paths contribute to the total fine structure. Since these measurements were made with polarization vector in the *a*-*b* plane, the dominant part of the fine-structure signal is from the nearest-neighbor oxygen atoms lying in that plane. Figure 6.3 shows

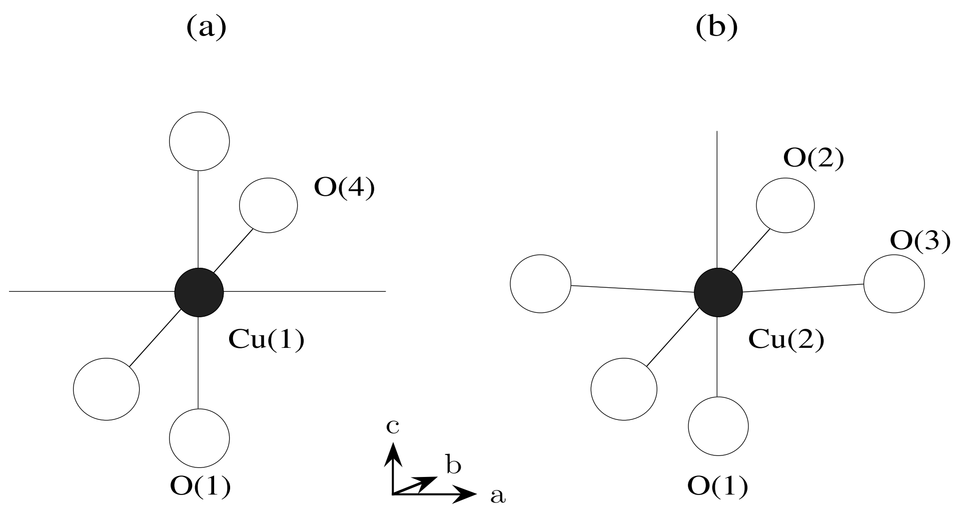

Figure 6.3: The local environment of (a) Cu(1) and (b) Cu(2) in $YBa_2Cu_3O_7$. For the (00ℓ) reflections in the vertical scattering plane, the DAFS fine structure is only sensitive to the oxygen atoms lying in th *a*-*b* plane. The Cu(1) site has two O(4) neighbors. The O(4) oxygens are depleted as $\delta \rightarrow 1$ in $YBa_2Cu_3O_{7-\delta}$. The Cu(2) site has four oxygen neighbors that sit slightly out of the plane, closer to the depleted region along the c axis.

the local environments of Cu(1), with the two neighboring O(4) oxygens in the plane, and Cu(2) with four oxygens, shifted slightly out of the plane. The O(4) neighbors of Cu(1) are preferentially depleted sites as $\delta \rightarrow 1$ in $YBa_2Cu_3O_{7-\delta}$. Recent improvements to FEFF make it possible to specify the polarization. For the a-b twinned crystal, the fine structure is a sum of a- and b-polarized fine-structure. The averaged path files can be tricked out of FEFF by calculating the path contributions for circularly polarized photons[2] spin-aligned along the c-axis. This is done by setting the FEFF input cards `ellipticity 1 0 0 1`, for circular polarization, and `polarization 1 1 0`, for a-b averaging. This input argument gives

$$\hat{\mathbf{e}} \cdot \hat{\mathbf{R}} = \frac{1}{\sqrt{2}}(\hat{\mathbf{x}} + i\hat{\mathbf{y}}) \cdot \hat{\mathbf{R}} \tag{6.1}$$

in the scattering amplitude and, consequently the same result in the squared magnitude

$$|\hat{\mathbf{e}} \cdot \hat{\mathbf{R}}|^2 = \frac{1}{2}\left(\hat{\mathbf{x}} \cdot \hat{\mathbf{R}}\right)^2 + \frac{1}{2}\left(\hat{\mathbf{y}} \cdot \hat{\mathbf{R}}\right)^2 \tag{6.2}$$

as $\hat{\epsilon}$ in the a-b plane of a twinned orthorhombic crystal.

6.4 *Simultaneous fitting of DAFS $\chi_{\mathrm{w}}(\mathbf{Q}, E)$ using* FEFFIT

Each of the DAFS $\chi_{\mathrm{w}}(\mathbf{Q}, E)$ functions is a linear combination of the $\chi(E)$ functions from the inequivalent sites, provided the photon polarization direction is held constant in the experiment. The individual site functions are combined according to the kinematic structure factor Equation 3.31 for the sublattice of resonant sites, which depends on the positions of the resonant atoms in the unit cell. The mixing coefficients for the two sites for the $\mathrm{YBa_2Cu_3O_x}$ (00ℓ) reflections depend on the positions and x-ray Debye-Waller factors for the resonant atoms and on the magnitude of $\mathbf{Q}$. They are given by

$$W_{\mathrm{Cu(1)}} = \frac{e^{-M_{\mathrm{Cu(1)}}}}{e^{-M_{\mathrm{Cu(1)}}} + 2e^{-M_{\mathrm{Cu(2)}}}\cos(Qz)} \tag{6.3}$$

and

$$W_{\mathrm{Cu(2)}} = \frac{2e^{-M_{\mathrm{Cu(2)}}}\cos(Qz)}{e^{-M_{\mathrm{Cu(1)}}} + 2e^{-M_{\mathrm{Cu(2)}}}\cos(Qz)} \tag{6.4}$$

according to Equation (3.38). For the (00ℓ) direction, using the relations $Q_z = 2\pi\ell/c$ and $M = B(sin\theta/\lambda)^2$, the only parameter that is different for each $\chi_{\mathrm{w}}(\mathbf{Q}, E)$ is ℓ. The

---

[2] For materials that do not exhibit magnetic circular dichroism.

structure and disorder parameters z and B_j are the same for every $\chi_{\rm w}(\mathbf{Q},E)$. This can written as a set of constraints using FEFFIT's user-defined Math Expressions. A simultaneous fit to a collection of $\chi_{\rm w}(\mathbf{Q},E)$ with constraints on the structural parameters will result in a set of mixing coefficients that is consistent with all of the data.

The $W_{j,\mathbf{Q}}$ are determined by the structure factor for the resonant atoms, including the diffraction Debye-Waller factors for each site. This suggests that there is some possibility of obtaining long-range order information about the sublattice of resonant sites by fitting the DAFS in the extended energy region. Unfortunately, because the DAFS $\chi_{\rm w}(\mathbf{Q},E)$ functions are normalized to the single-atom response in the iterative Kramers-Krönig analysis method, e^{-M} appears in both the numerator and denominator. When M is the same for all of the resonant sites, then the dependence of the mixing coefficients on the diffraction Debye-Waller factors disappears entirely. When there are different M_j for each of the sites, their individual effect on the coefficients is diminished from what it would be in a standard refinement of the diffraction peak intensities. The robustness of the diffraction Debye-Waller factors in the refinement of the $W_{j,\mathbf{Q}}$ could probably be improved by increasing the range number of points measured in reciprocal space or by fitting to $\beta\chi_{\rm w}$, but then the problem retains the structure factor due to all of the off-resonant sites from $|F_0|^2$, which needs to be included in the model as part of the amplitude at each reflection, reducing the effectiveness of the FEFFIT fit to the $\chi_{\rm w}$ as a linear sum. The focus of the work presented here is on obtaining a consistent set of coefficients for a group of DAFS $\chi_{\rm w}(\mathbf{Q},k)$, and on the resulting site-separated functions determined by pairwise inversion from the original data. I have included M_j as a fitting parameter in the FEFFIT model, but even in the reliability tests using FEFFIT generated mock-up data the results were not satisfying.

Using the structural parameters determined by the rotating anode data, an *ab initio* calculation of the XAFS from the two Cu sites in $YBa_2Cu_3O_{6.8}$ using FEFF 6.10 was used as grist for FEFFIT. This gave good values for the $W_{\rm site}$, treating the Debye-Waller factors as part of the mixing amplitude. These numbers can then be used in the full $f''_{\rm w}$ to separate the f''_{site} functions, including the near edge features and the edge position, by combining the $f''_{\rm w}$ functions in pairs with the FEFFIT determined coefficients. We have assumed nothing more than self-consistency through the series of (00ℓ) reflections.

Table 6.1: The important paths from FEFF 6.10 for $YBa_2Cu_3O_{6.8}$ at $293°K$. The polarization conditions `POLARIZED 0 0 1` and `ELLIPTICITY 1 0 0 1` were used in FEFF to simulated a polarization vector lying in the fully twinned *a*-*b* plane. $R_{\rm eff}$ are the half-path distances, N_{degen} accounts for the path degeneracy, and $A_{\rm cw}$ are the Zabinsky curved-wave importance factors, which are useful for eliminating scattering paths with negligible contributions to the fine structure. Paths are listed in order of amplitude, with a cutoff of $A_{\rm cw} > 12$.

scattering paths originating at Cu(1)

Path	$A_{\rm cw}$	N_{degen}	N_{scatt}	R_{eff}(Å)	Comments
2	100.00	2	2	1.9395	O(4) single scattering
12	50.97	4	3	3.8790	Cu(1)⇒O(4) focusing
4,5	48.99	4	2	3.4947	Ba single scattering
15	35.63	2	4	3.8970	O(4)⇒Cu(1) double focusing
27	28.25	8	3	4.4377	O(1)⇒O(4) triangle
23	21.71	4	2	4.2317	O(1) single scattering, $\hat{a}$
24	21.12	4	2	4.2814	O(1) single scattering, $\hat{b}$
9	19.16	2	2	3.2400	Cu(1) single scattering, $\hat{a}$
10	18.48	2	2	3.8790	Cu(1) single scattering, $\hat{b}$
11	15.39	2	3	3.8790	O(4)⇒Cu(1)⇒O(4) focusing

scattering paths originating at Cu(2)

Path	$A_{\rm cw}$	N_{degen}	N_{scatt}	R_{eff}(Å)	Comments
1	100.00	2	2	1.9285	O(2) single scattering
2	96.80	2	2	1.9557	O(3) single scattering
21	45.03	4	3	3.8405	O(2)⇒Cu(2) focusing, $\hat{a}$
27	43.15	4	3	3.8952	O(3)⇒Cu(2) focusing, $\hat{b}$
9,10	29.19	2	2	3.3682	Ba single scattering
4,5	28.05	2	2	3.1988	Y single scattering
24	26.58	2	4	3.8569	O(2)⇒Cu(2) double focusing, $\hat{a}$
30	25.28	2	4	3.9115	O(3)⇒Cu(2) double focusing, $\hat{b}$
19	19.53	2	2	3.8240	Cu(2) single scattering, $\hat{a}$
25	18.84	2	2	3.8790	Cu(2) single scattering, $\hat{b}$
20	15.32	2	3	3.8405	O(2)⇒O(2) focusing, $\hat{a}$
26	14.53	2	3	3.8952	O(3)⇒O(3) focusing, $\hat{b}$

Table 6.2: The relative amounts of Cu(1) and Cu(2) fine structure in some of the specular (00ℓ) Bragg reflections in $YBa_2Cu_3O_{6.8}$. The mixing coefficients depend on the structure factor for the sublattice of Cu sites and on the projection of the Cu Debye-Waller factors along the $\hat{c}$-axis.

	diffraction $W_j(\mathbf{Q}$ (calc.)			FEFFIT $W_j(\mathbf{Q}$s (fit)		
$(hk\ell)$	$W_{\mathrm{Cu}(1)}$	$W_{\mathrm{Cu}(2)}$	ratio	$W_{\mathrm{Cu}(1)}$	$W_{\mathrm{Cu}(2)}$	ratio
(001)	-4.1440	5.1440	-0.8056	-4.1119	5.1119	-0.8044
(002)	1.8579	-0.8579	-2.1656	—	—	—
(003)	0.3545	0.6455	0.5492	0.3514	0.64863	0.5417
(004)	-1.2455	2.2455	-0.5547	-1.1804	2.1804	-0.5414
(005)	0.7087	0.2913	2.4332	—	—	—
(007)	-0.9507	1.9507	-0.4874	-0.8265	1.8265	-0.4525
(009)	0.6501	0.3499	1.8579	—	—	—
(0011)	0.3474	0.6526	0.5324	—	—	—

Table 6.2 gives the relative amounts of the contribution from the Cu sites. If Cu(1) is chosen to be at the origin of coordinates within the unit cell, then the two Cu(2) sites are located symmetrically above and below the origin along the z-axis.

The curious case of $YBa_2Cu_3O_x$ *(002)*

One of the most dramatic differences between DAFS $\chi(\mathbf{Q}, E)$ and XAFS $\chi(E)$ functions is illustrated by the R-space transform of the $YBa_2Cu_3O_x$ (002) DAFS, shown in Figure 6.4. Notice that in the DAFS, the first shell contribution to the fine structure is almost entirely absent! This happens because of the special combination of the mixing coefficients for the (002) and the number of oxygen neighbors in the a-b plane for the two sites. In the vertical scattering geometry, the (00ℓ) Cu K-shell DAFS is dominated by the backscattering contribution from the oxygen neighbors in the a-b plane. The polarization of the incident x-rays is perpendicular to c, so there is no first-shell contribution from the oxygens above and below the Cu sites on the c-axis, even though these sites are closer. Summing over the first shell contributions, the

Table 6.3: Values of the fitting parameters from Equation (5.7) returned by KKFIT for the fits shown in Figure (6.9) through (6.16).

$(hk\ell)$	amplitude	Φ_0	β	δE_0	a_6	a_7
(001)	0.637100	0.329901	-0.020778	-0.547585	-0.119017	0.000032
(002)	0.575857	-0.370397	0.029384	-0.624415	-0.031108	0.000195
(003)	0.100532	-0.343200	0.082314	2.592777	0.011636	0.000039
(004)	0.196669	-0.005317	-0.031737	0.665380	-0.017590	0.000057
(005)	0.288974	3.029820	0.012077	-0.624415	-0.042157	0.000083
(007)	0.539834	-0.093349	-0.015735	0.059215	-0.041401	0.000154
(009)	0.101666	-0.196547	0.063501	5.491169	-0.068812	0.000051
(0011)	0.349241	2.998886	0.035052	-1.790790	-0.016932	0.000126

product of W_j and the path degeneracy[3] is

$$2(1-\delta)W_{(1)} + 4W_{(2)} = 3.716(1-\delta) - 3.432. \tag{6.5}$$

As $YBa_2Cu_3O_7 \rightarrow YBa_2Cu_3O_6$, the amplitude of the first shell contribution varies from 0.284 down to -3.432. This suggests that the (002) DAFS should be very sensitive to oxygen depletion. There are also differences in the Ba and Y backscattering, but these differences are far less dramatic than the effect in the oxygen shell. The ratio of (002) DAFS:XAFS in $YBa_2Cu_3O_7$ is $8:16$ for barium and $-6.8:8$ for yttrium, compared to the ratio of $0.284:10$ for oxygen. The absence of a first shell makes it difficult to fit the extended (002) DAFS—impossible if only the first shell is fit in R-space. FEFFIT has a tendency to walk E_0 very far out of the way to get a match. On the other hand, you can experimentally isolate the higher order shells. This may prove to be a very interesting experimental method: to look for reflections in complex materials that preferentially eliminate certain whole shells of neighbors. Maybe you can get the depletion number δ by looking at how *gone* the first shell is in R-space. This qualifies as gee whiz physics at the very least.

[3] I am assuming that the backscattering functions to all these neighbors is the same, which is not strictly true of $YBa_2Cu_3O_{7-\delta}$ where $a \neq b$, but this is a good approximation for evaluating the size of the effect.

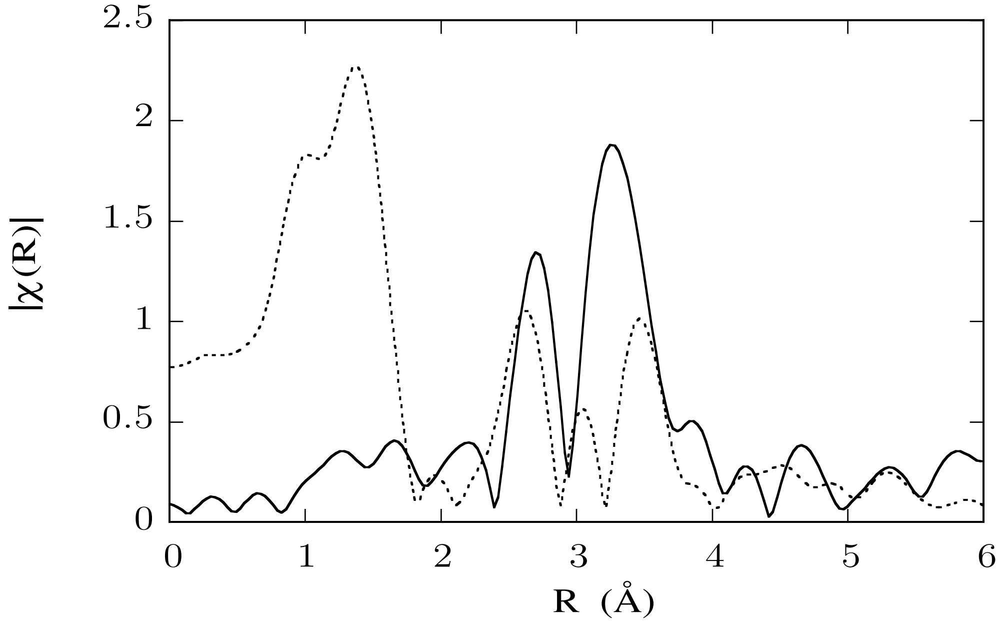

Figure 6.4: The R-space transform $\tilde{\chi}_{\mathrm{w}}(R)$ of (002) DAFS (solid line) compared to the XAFS $\tilde{\chi}(R)$ (dashed line) for the same material. The absence of a first shell signal in $\tilde{\chi}_{\mathrm{w}}(R)$ is due to a fortuitous combination of the (002) mixing coefficients, the number of oxygen neighbors in the *a*-*b* plane, and the total number of Cu(1) and Cu(2) sites.

6.4.1 Site Separated $YBa_2Cu_3O_{6.8}$ *XANES*

The most interesting application of the iterative Kramers-Krönig method is the complete isolation of the site-specific near-edge resonance features in multiple site materials. The near-edge structure can provide useful information about charge state and bonding [78] of the individual sites, and an experimental determination of these features is especially useful in those cases where they cannot always calculated from theory. In the extended region, where the fine-structure can be modeled more easily, site-separation of the response functions is not necessary for obtaining useful structural information.

6.5 Gallery of $YBa_2Cu_3O_{6.8}$ *DAFS results*

It is often useful and instructive to look at the various parts of the response function. I have therefore appended the data and fits from several stages of the $YBa_2Cu_3O_{6.8}$ analysis. The gallery begins with the site-separated response functions $f'(E)$ $f''(E)$

in the near-edge and extended regions. Then follows all eight of the $f'_{\mathrm{w}}(\mathbf{Q}, E)$ functions extracted from measured data using KKFIT using mocked-up data generated by FEFF and FEFFIT as the initial guess and for the Levenberg-Marquardt minimization of the functional in Equation (5.7). These are arguably too repetitive to be of any real use, but I have included them because they helped me appreciate the dramatic differences that occur in the DAFS response functions. Table 6.3 gives the final value for the fitting parameters returned by KKFIT for all eight reflections. Following the $f'(E)$ functions are the R-space plots of a constrained FEFFIT fit to four of (00ℓ) reflections. These fits determine the mixing coefficients in Table 6.2 which were in turn used to separate $f'(E)$ $f''(E)$ shown at the beginning of the gallery.

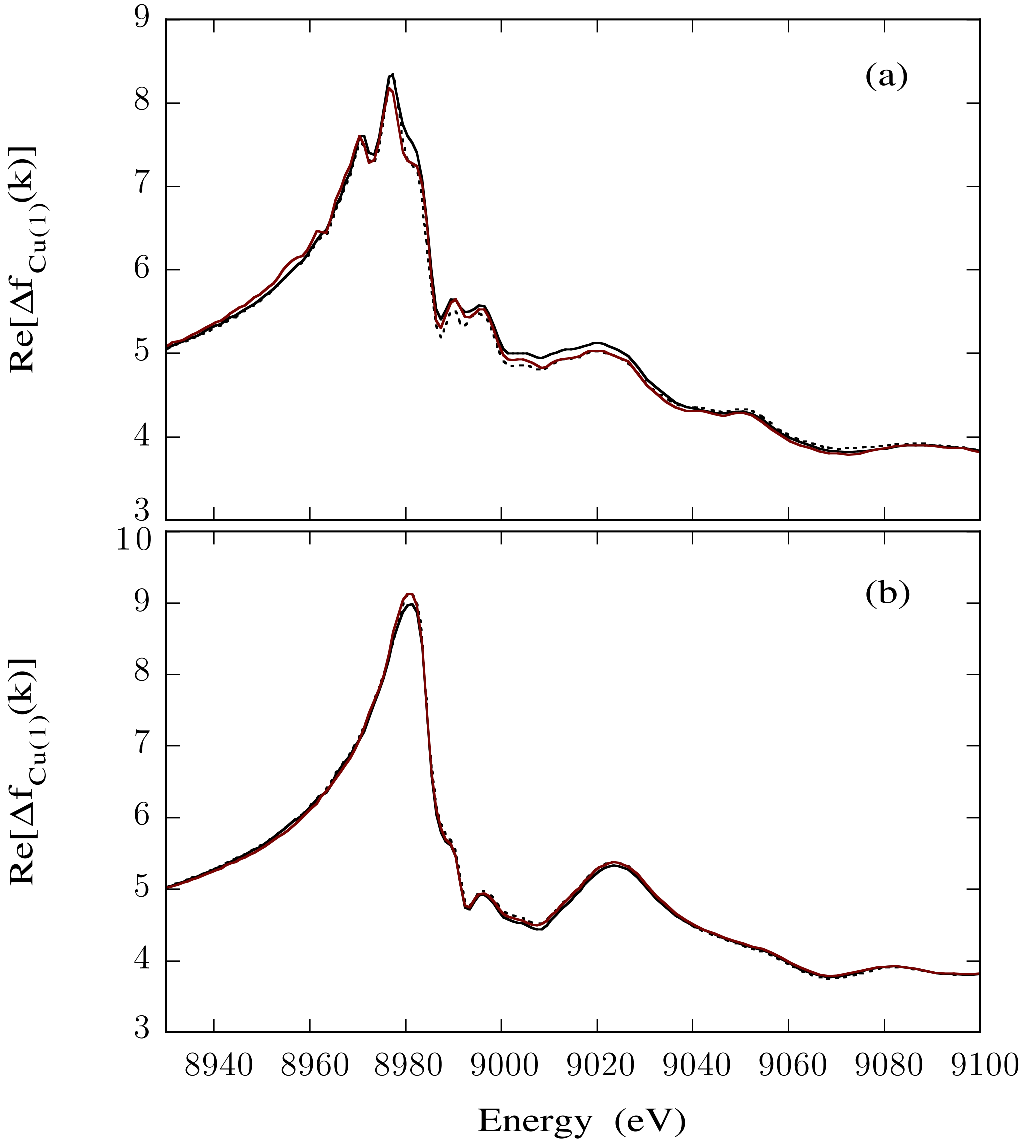

Figure 6.5: Site-separated $YBa_2Cu_3O_{6.8}$ $f'(E)$ in the near threshold region for (a) Cu(1) and (b) Cu(2).

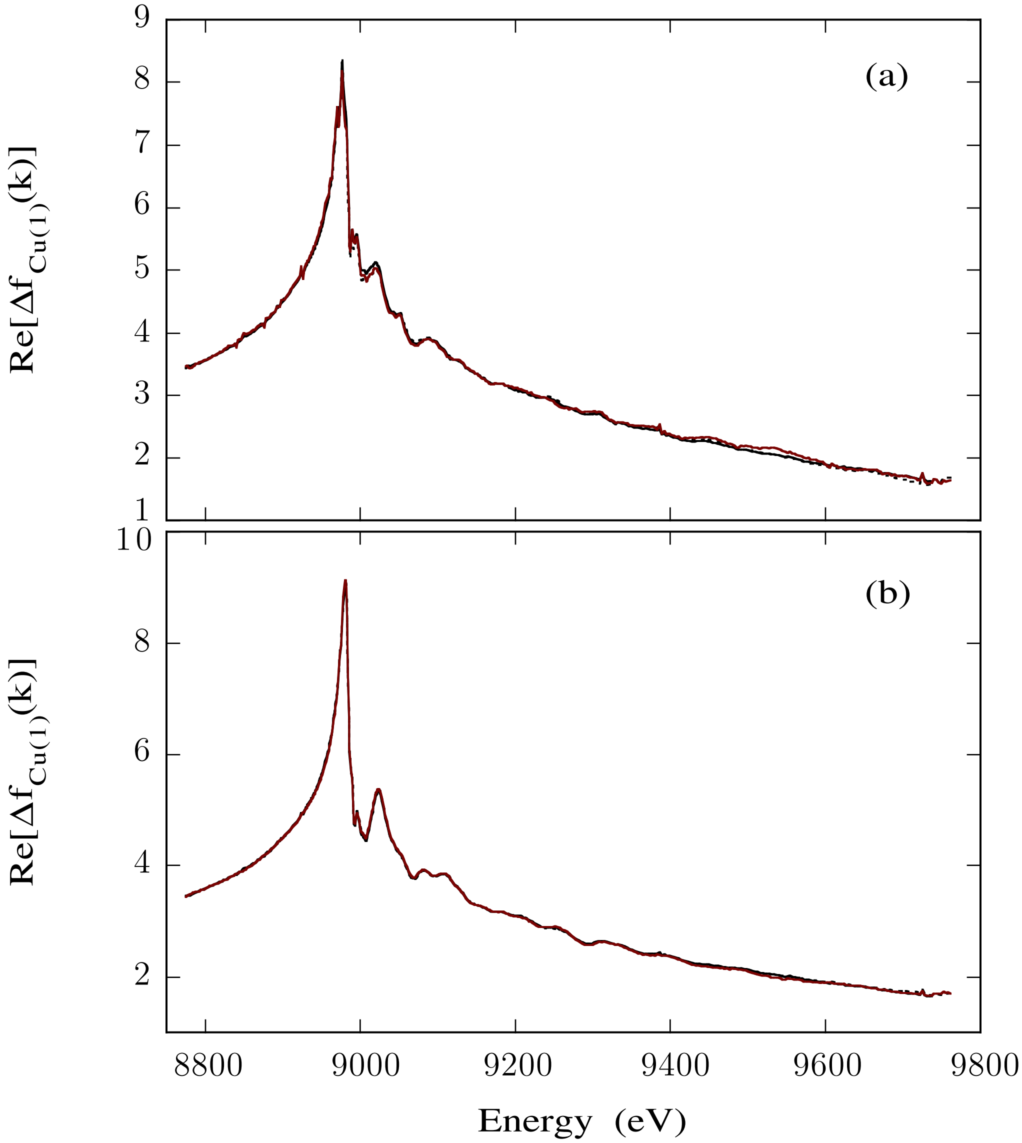

Figure 6.6: Site-separated $YBa_2Cu_3O_{6.8}$ $f'(E)$ functions in the extended energy region (a) Cu(1) and (b) Cu(2).

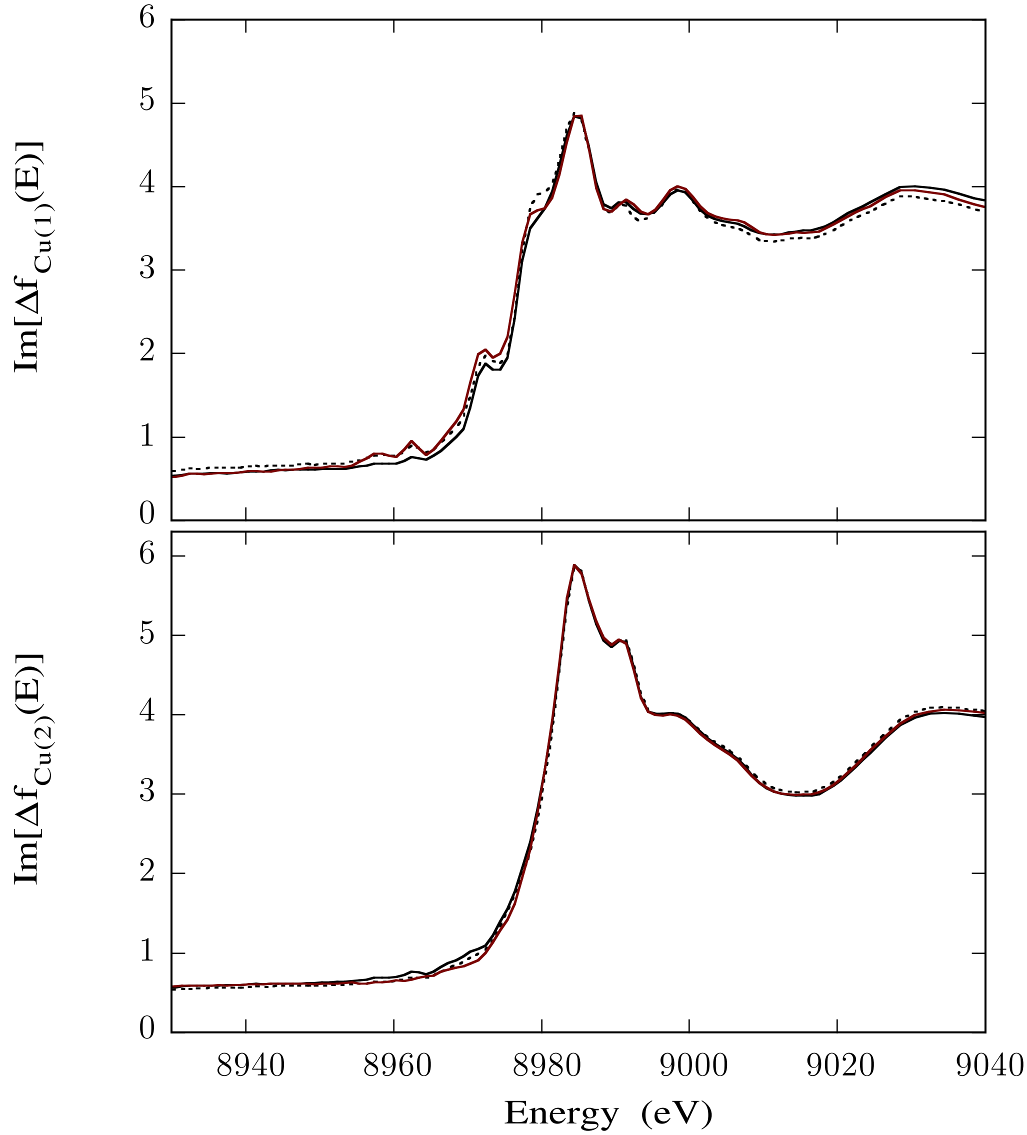

Figure 6.7: Site-separated $YBa_2Cu_3O_{6.8}$ $f''(E)$ in the near threshold region for (a) Cu(1) and (b) Cu(2).

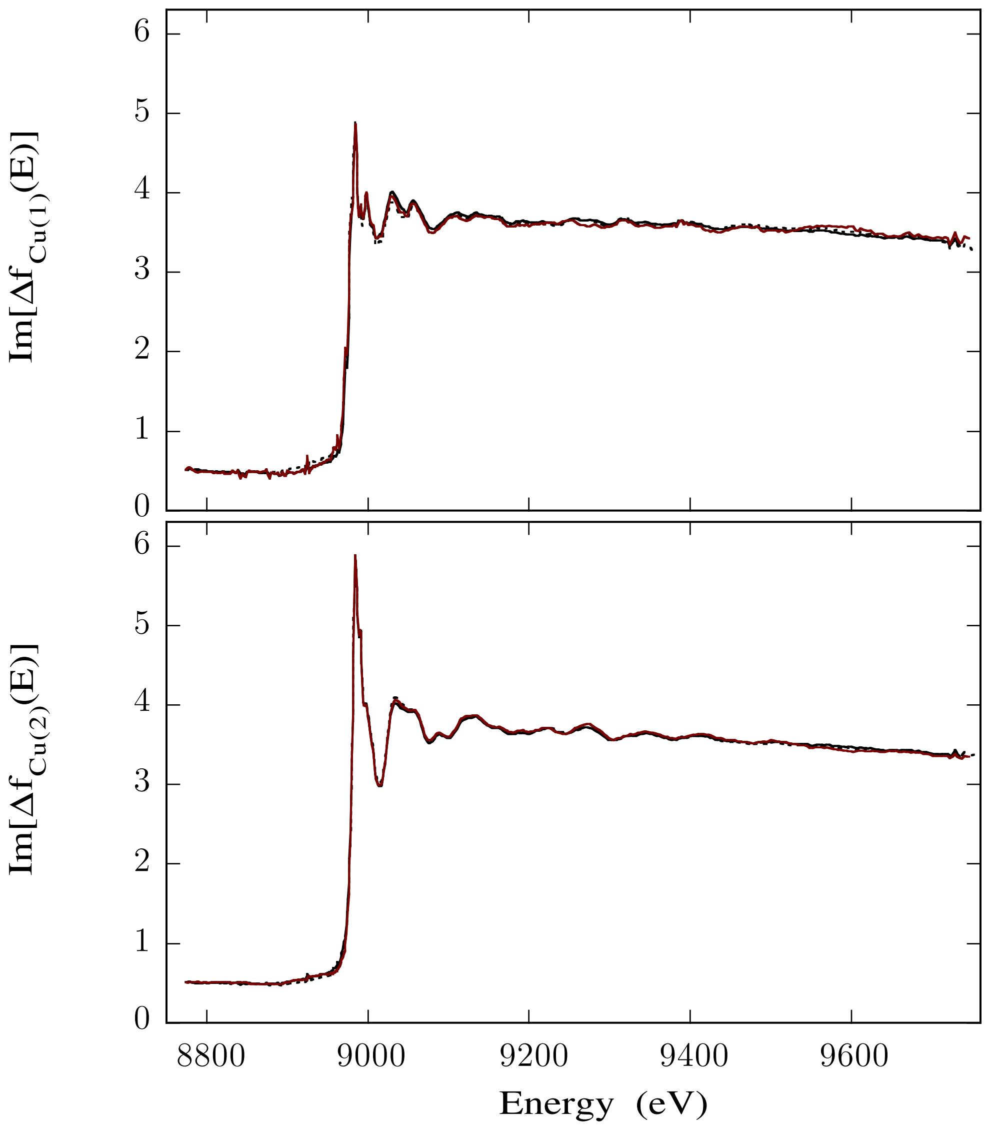

Figure 6.8: The results of the (a) Cu(1) and (b) Cu(2).

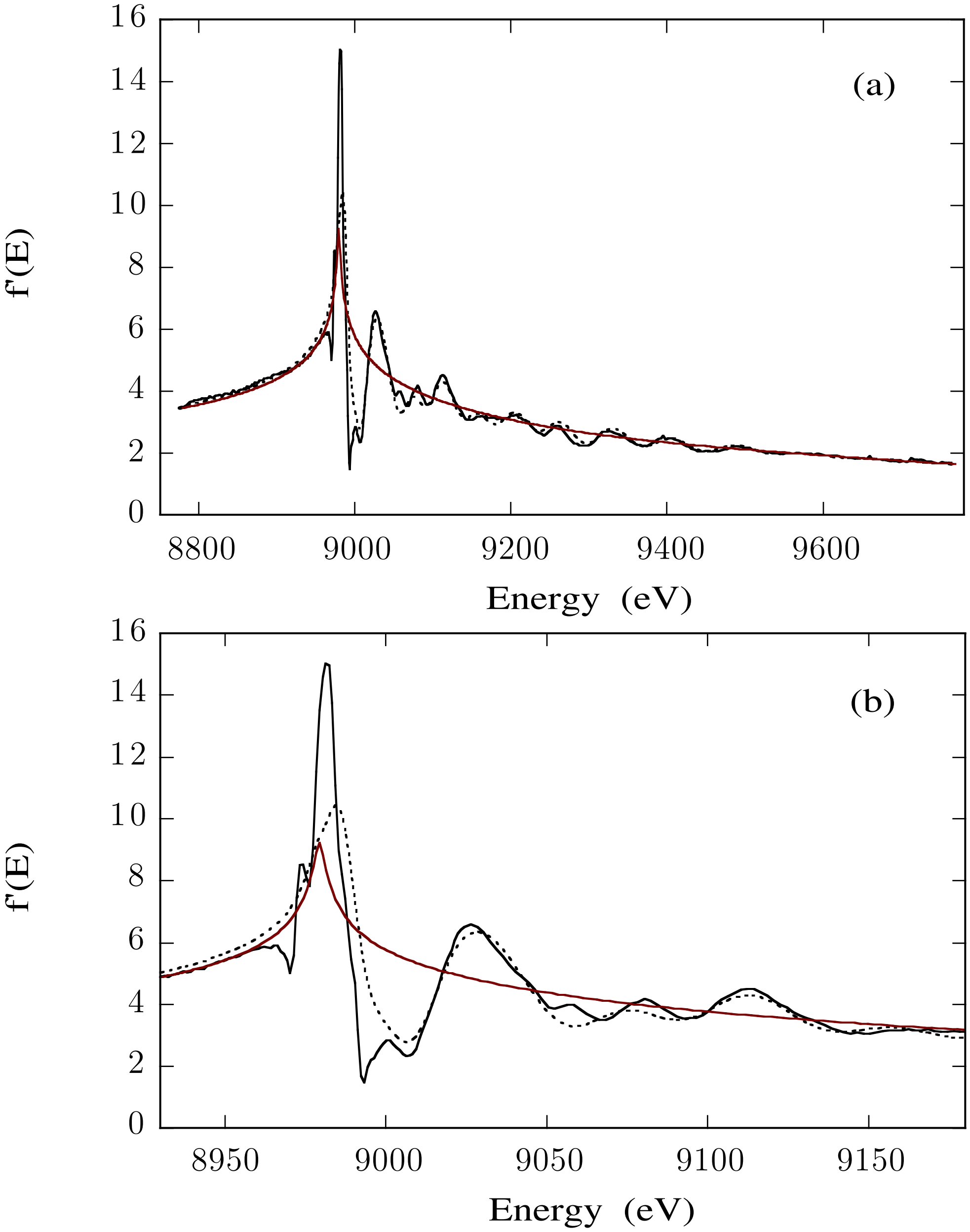

Figure 6.9: The results of KKFIT on $YBa_2Cu_3O_{6.8}$ (001) DAFS data. (a) The $f'(E)$ (solid line) solved from $YBa_2Cu_3O_{6.8}$ DAFS data by KKFIT and the initial guess (dashed line) used in the minimization as calculated by FEFF and FEFFIT. The tabulated theoretical bare-atom response from Sasaki (solid line) is shown for comparison. (b) An expanded view of the near-threshold region.

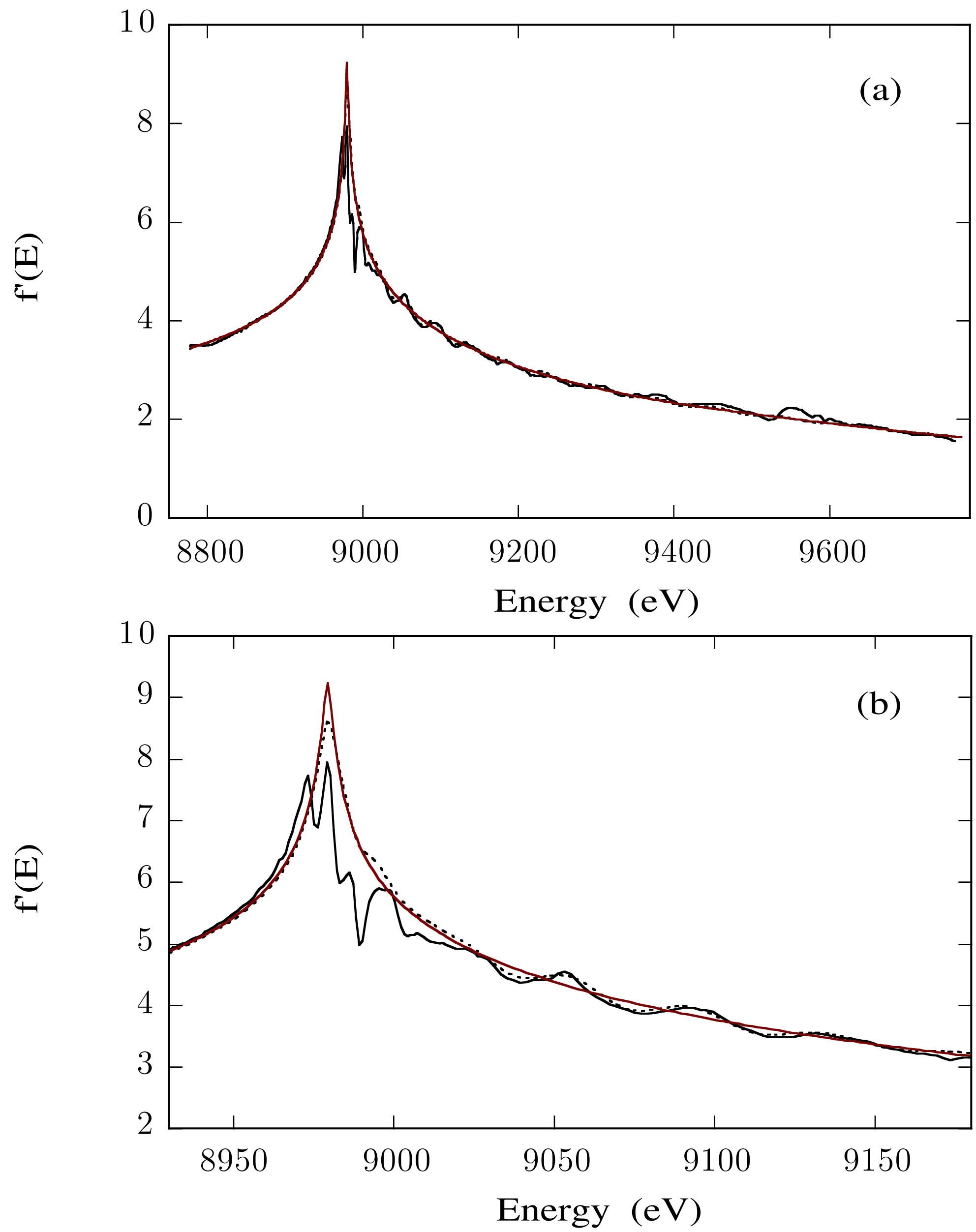

Figure 6.10: The results of KKFIT on $YBa_2Cu_3O_{6.8}$ (002) DAFS data. (a) The $f'(E)$ (solid line) solved from $YBa_2Cu_3O_{6.8}$ DAFS data by KKFIT and the initial guess (dashed line) used in the minimization as calculated by FEFF and FEFFIT. The tabulated theoretical bare-atom response from Sasaki (solid line) is shown for comparison. (b) An expanded view of the near-threshold region.

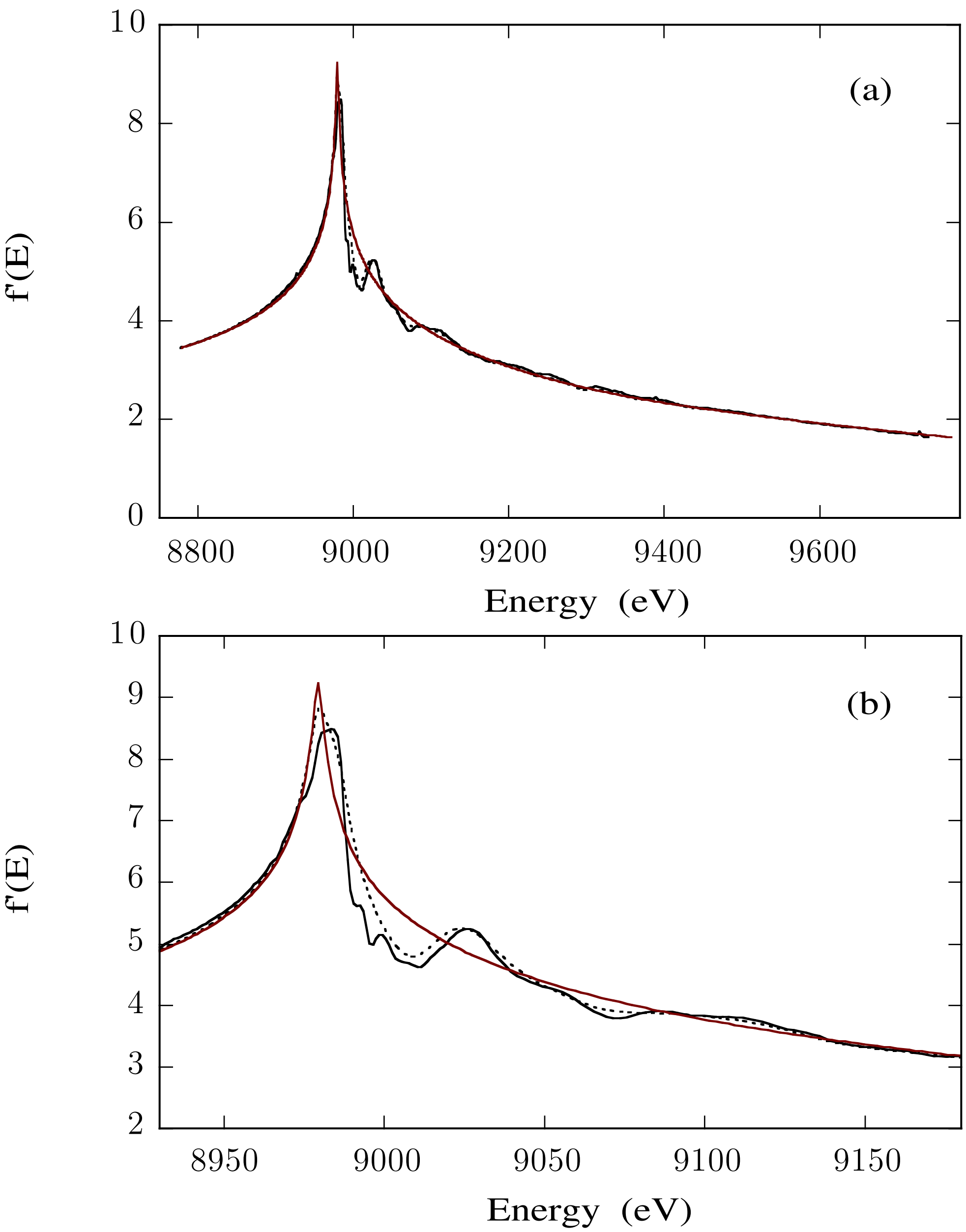

Figure 6.11: The results of KKFIT on $YBa_2Cu_3O_{6.8}$ (003) DAFS data. (a) The $f'(E)$ (solid line) solved from $YBa_2Cu_3O_{6.8}$ DAFS data by KKFIT and the initial guess (dashed line) used in the minimization as calculated by FEFF and FEFFIT. The tabulated theoretical bare-atom response from Sasaki (solid line) is shown for comparison. (b) An expanded view of the near-threshold region.

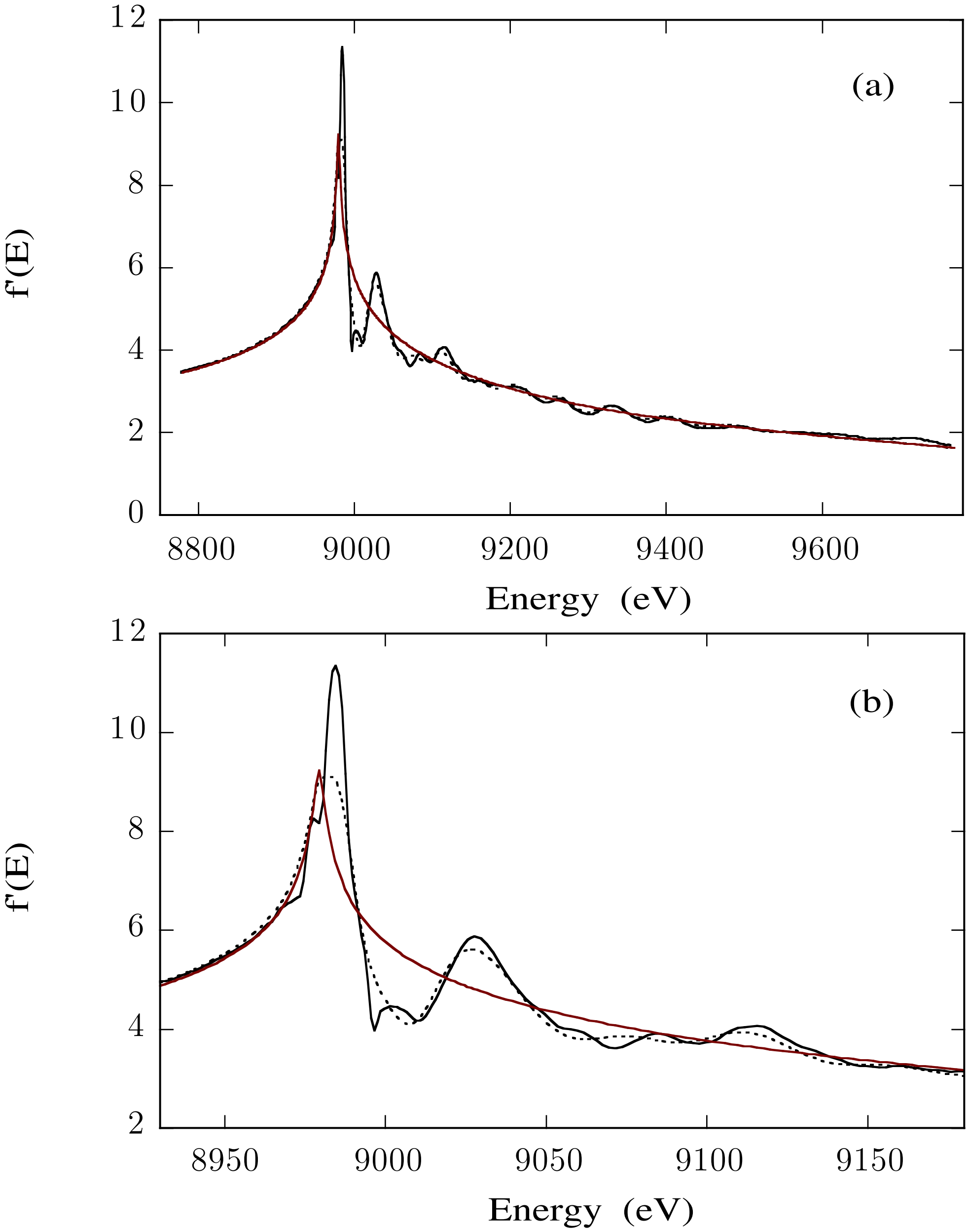

Figure 6.12: The results of KKFIT on $YBa_2Cu_3O_{6.8}$ (004) DAFS data. (a) The $f'(E)$ (solid line) solved from $YBa_2Cu_3O_{6.8}$ DAFS data by KKFIT and the initial guess (dashed line) used in the minimization as calculated by FEFF and FEFFIT. The tabulated theoretical bare-atom response from Sasaki (solid line) is shown for comparison. (b) An expanded view of the near-threshold region.

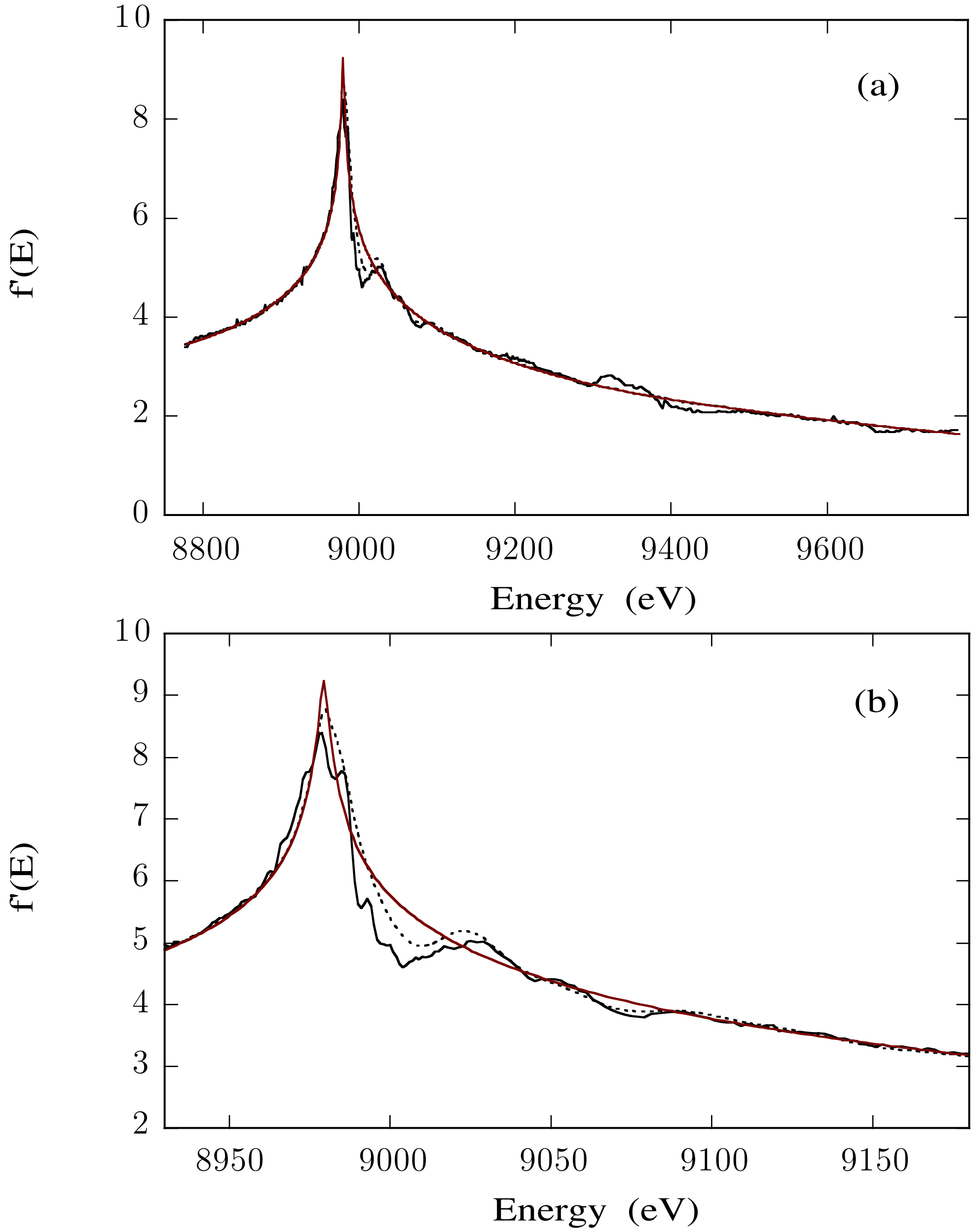

Figure 6.13: The results of KKFIT on $YBa_2Cu_3O_{6.8}$ (005) DAFS data. (a) The $f'(E)$ (solid line) solved from $YBa_2Cu_3O_{6.8}$ DAFS data by KKFIT and the initial guess (dashed line) used in the minimization as calculated by FEFF and FEFFIT. The tabulated theoretical bare-atom response from Sasaki (solid line) is shown for comparison. (b) An expanded view of the near-threshold region.

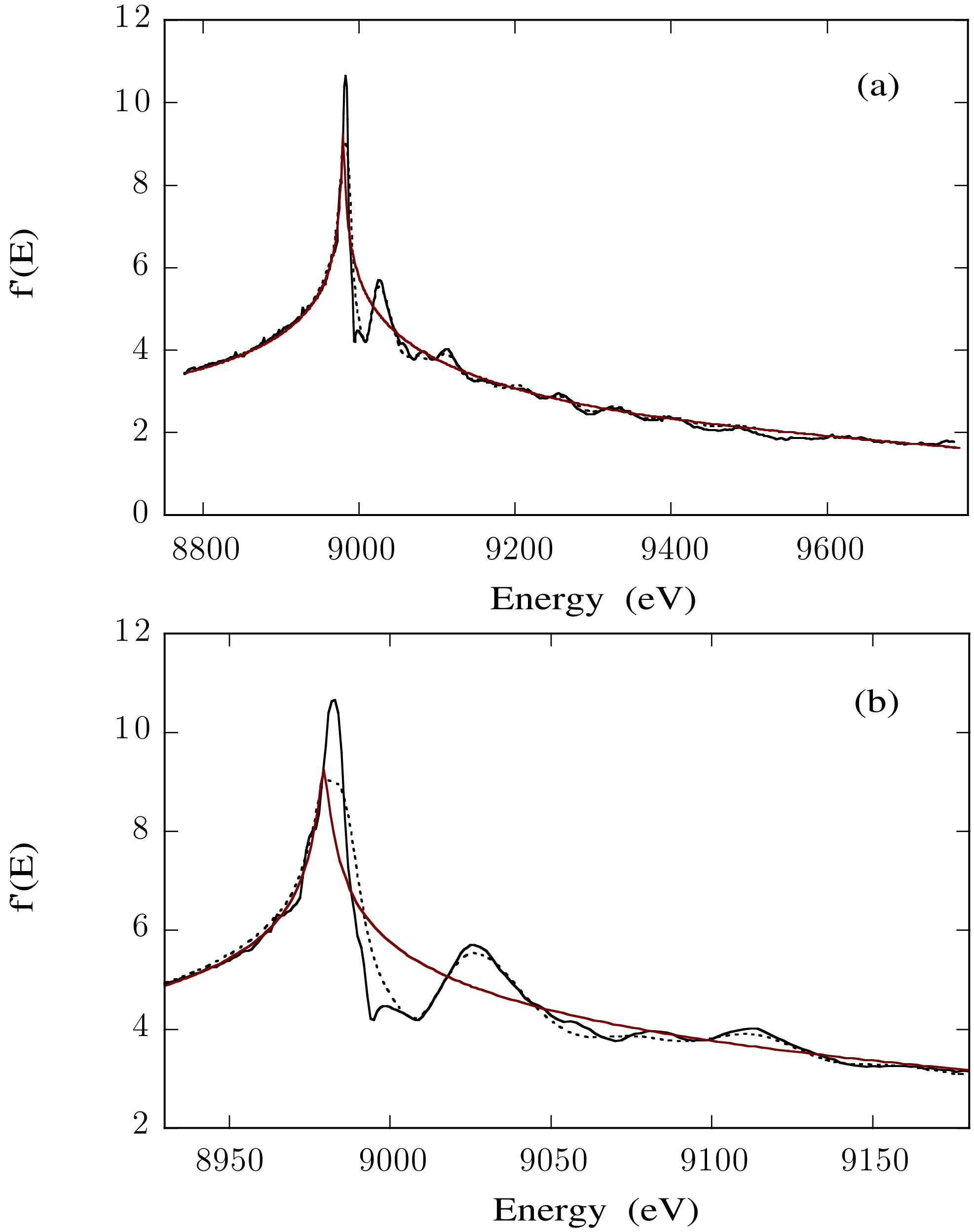

Figure 6.14: The results of KKFIT on $YBa_2Cu_3O_{6.8}$ (007) DAFS data. (a) The $f'(E)$ (solid line) solved from $YBa_2Cu_3O_{6.8}$ DAFS data by KKFIT and the initial guess (dashed line) used in the minimization as calculated by FEFF and FEFFIT. The tabulated theoretical bare-atom response from Sasaki (solid line) is shown for comparison. (b) An expanded view of the near-threshold region.

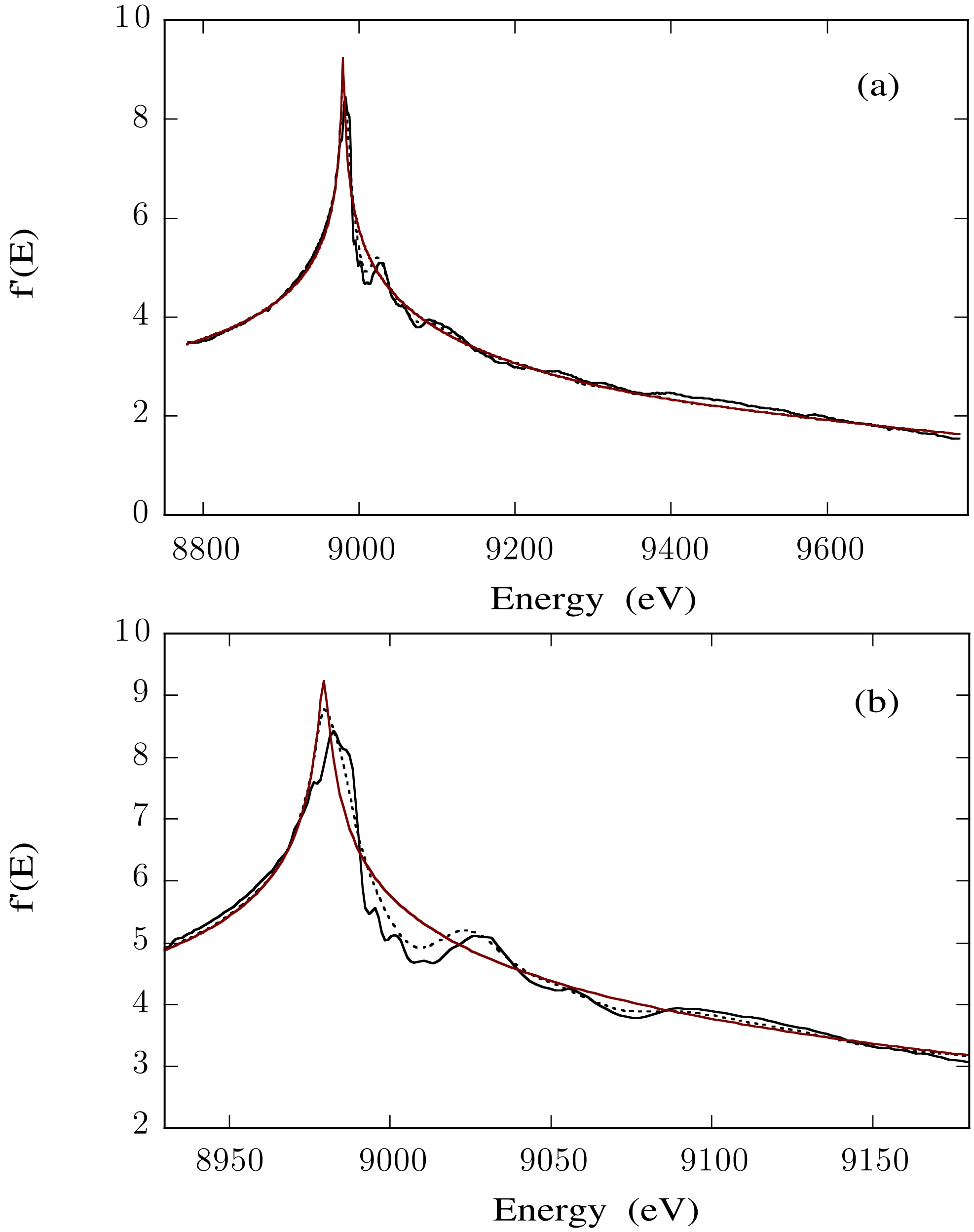

Figure 6.15: The results of KKFIT on $YBa_2Cu_3O_{6.8}$ (009) DAFS data. (a) The $f'(E)$ (solid line) solved from $YBa_2Cu_3O_{6.8}$ DAFS data by KKFIT and the initial guess (dashed line) used in the minimization as calculated by FEFF and FEFFIT. The tabulated theoretical bare-atom response from Sasaki (solid line) is shown for comparison. (b) An expanded view of the near-threshold region.

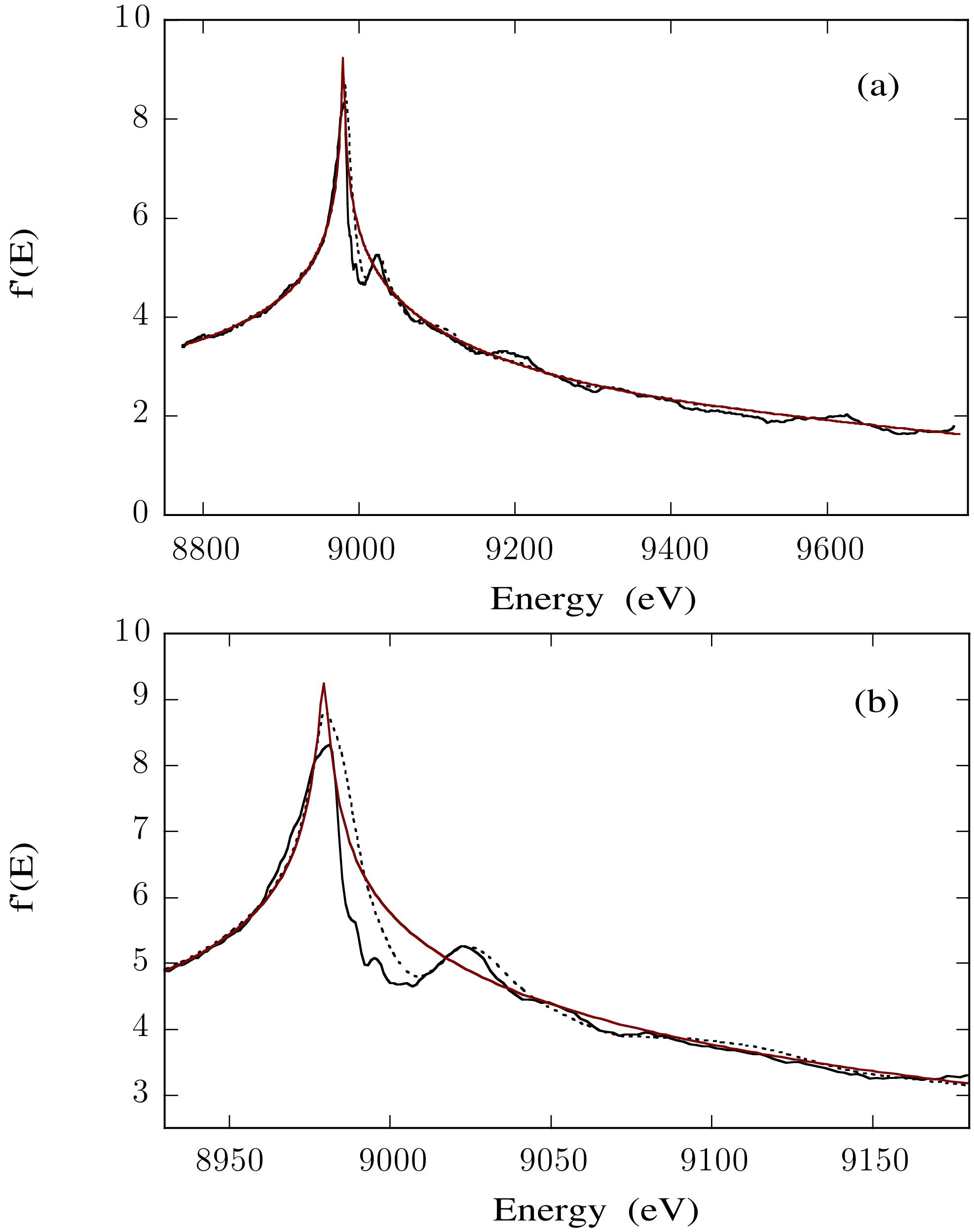

Figure 6.16: The results of KKFIT on $YBa_2Cu_3O_{6.8}$ (0011) DAFS data. (a) The $f'(E)$ (solid line) solved from $YBa_2Cu_3O_{6.8}$ DAFS data by KKFIT and the initial guess (dashed line) used in the minimization as calculated by FEFF and FEFFIT. The tabulated theoretical bare-atom response from Sasaki (solid line) is shown for comparison. (b) An expanded view of the near-threshold region.

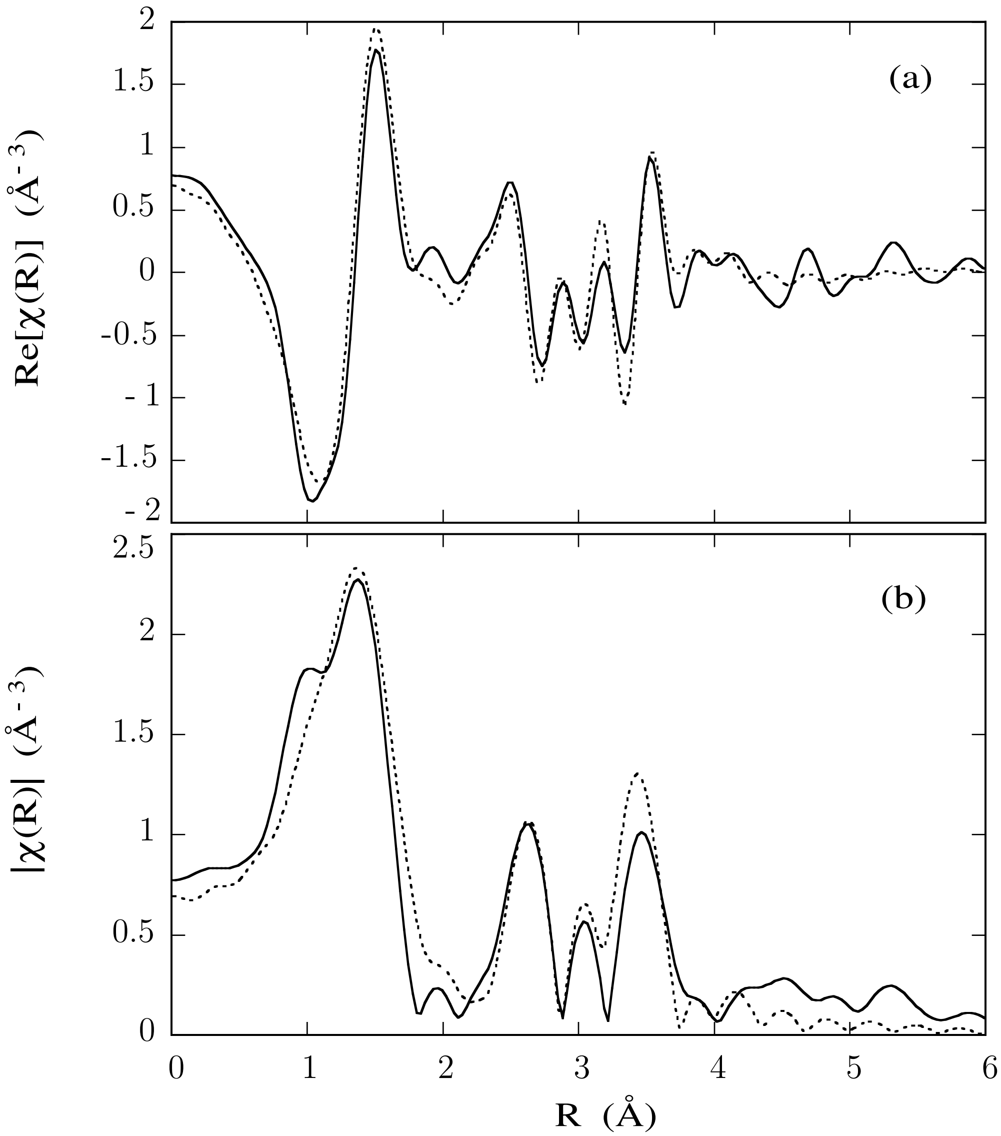

Figure 6.17: The results of the constrained FEFFIT fit to $YBa_2Cu_3O_{6.8}$ (001) DAFS $\chi''(k)$. (a) The real part of the Fourier transform of the data (solid line) overplotted with the FEFFIT best fit (dashed line). (b) The magnitudes of the functions shown in (a).

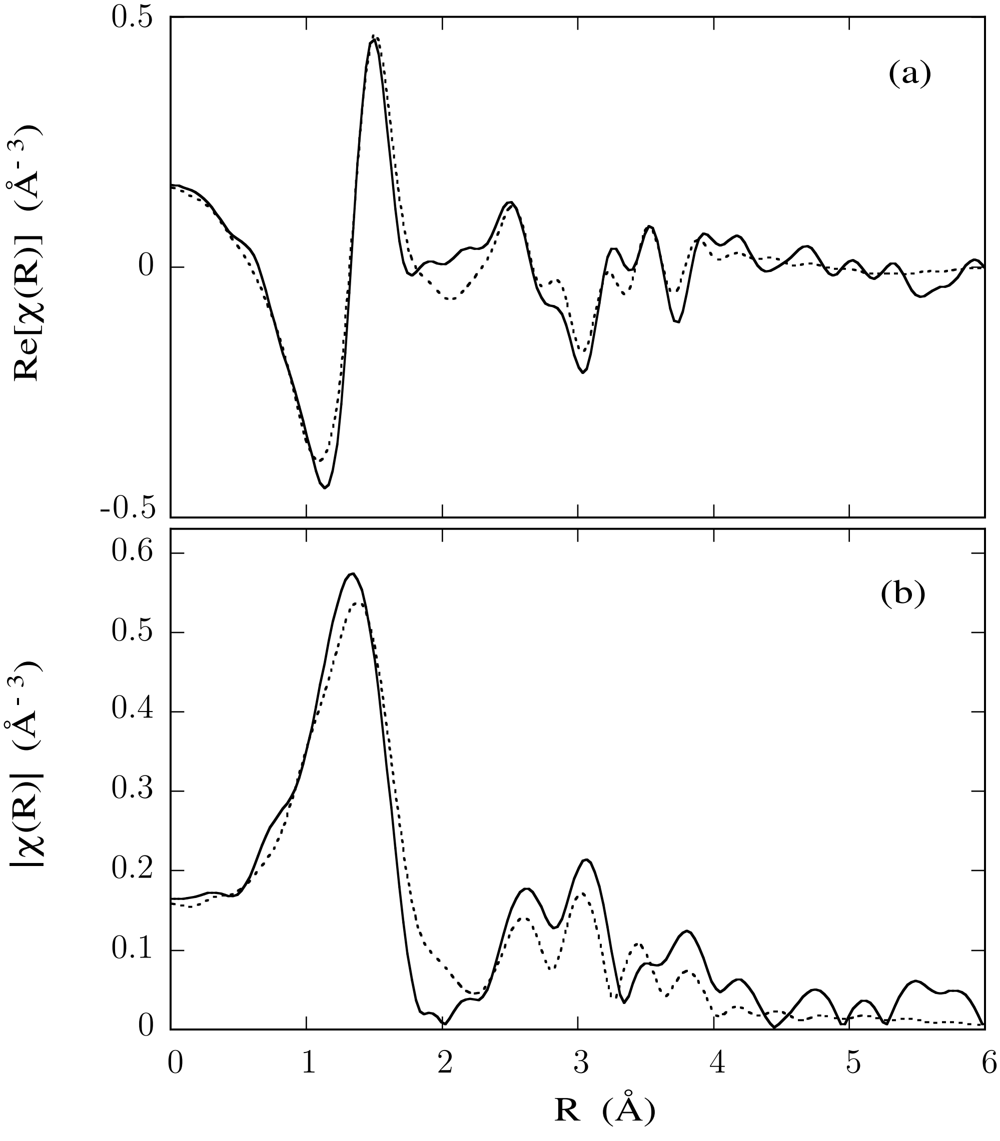

Figure 6.18: The results of the constrained FEFFIT fit to $YBa_2Cu_3O_{6.8}$ (003) DAFS $\chi''(k)$. (a) The real part of the Fourier transform of the data (solid line) overplotted with the FEFFIT best fit (dashed line). (b) The magnitudes of the functions shown in (a).

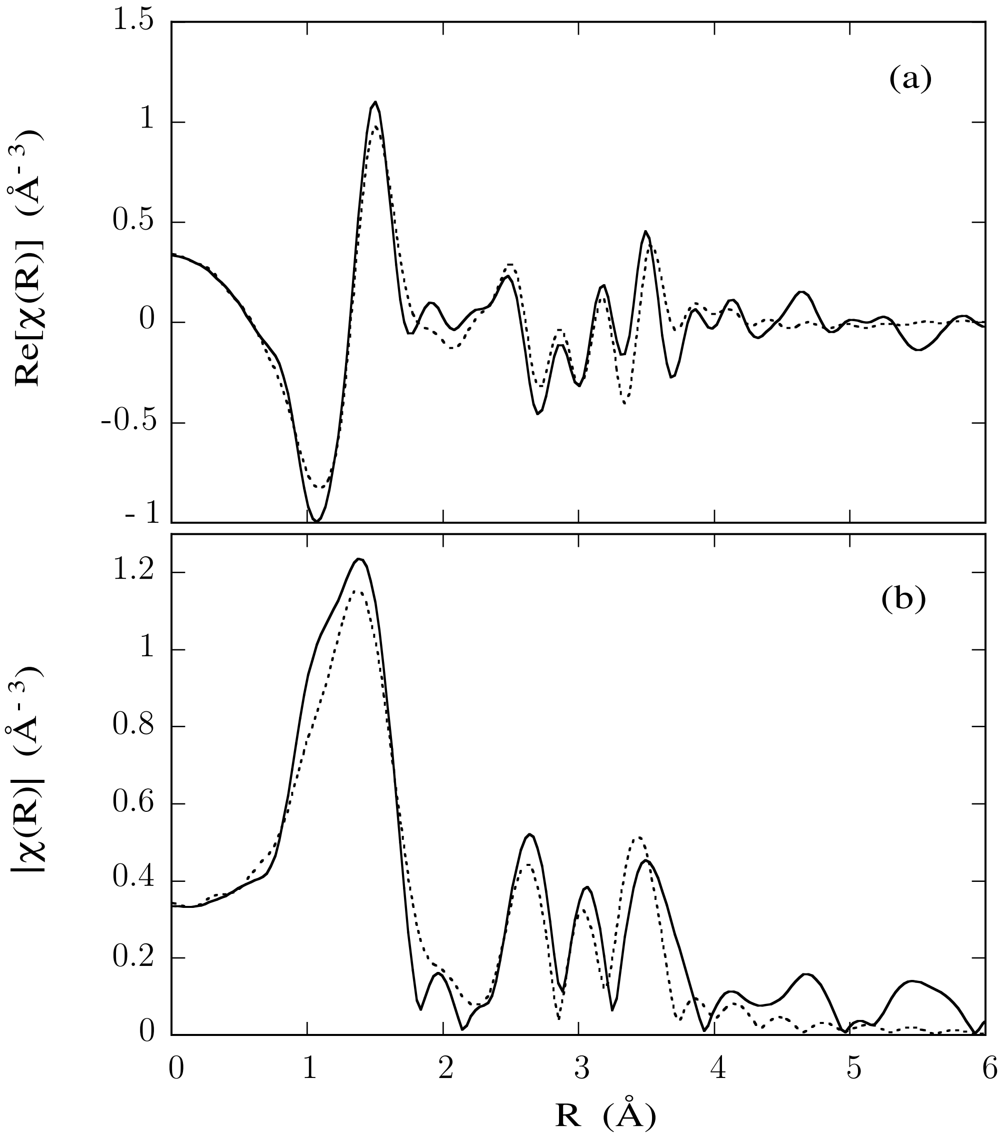

Figure 6.19: The results of the constrained FEFFIT fit to $YBa_2Cu_3O_{6.8}$ (004) DAFS $\chi''(k)$. (a) The real part of the Fourier transform of the data (solid line) overplotted with the FEFFIT best fit (dashed line). (b) The magnitudes of the functions shown in (a).

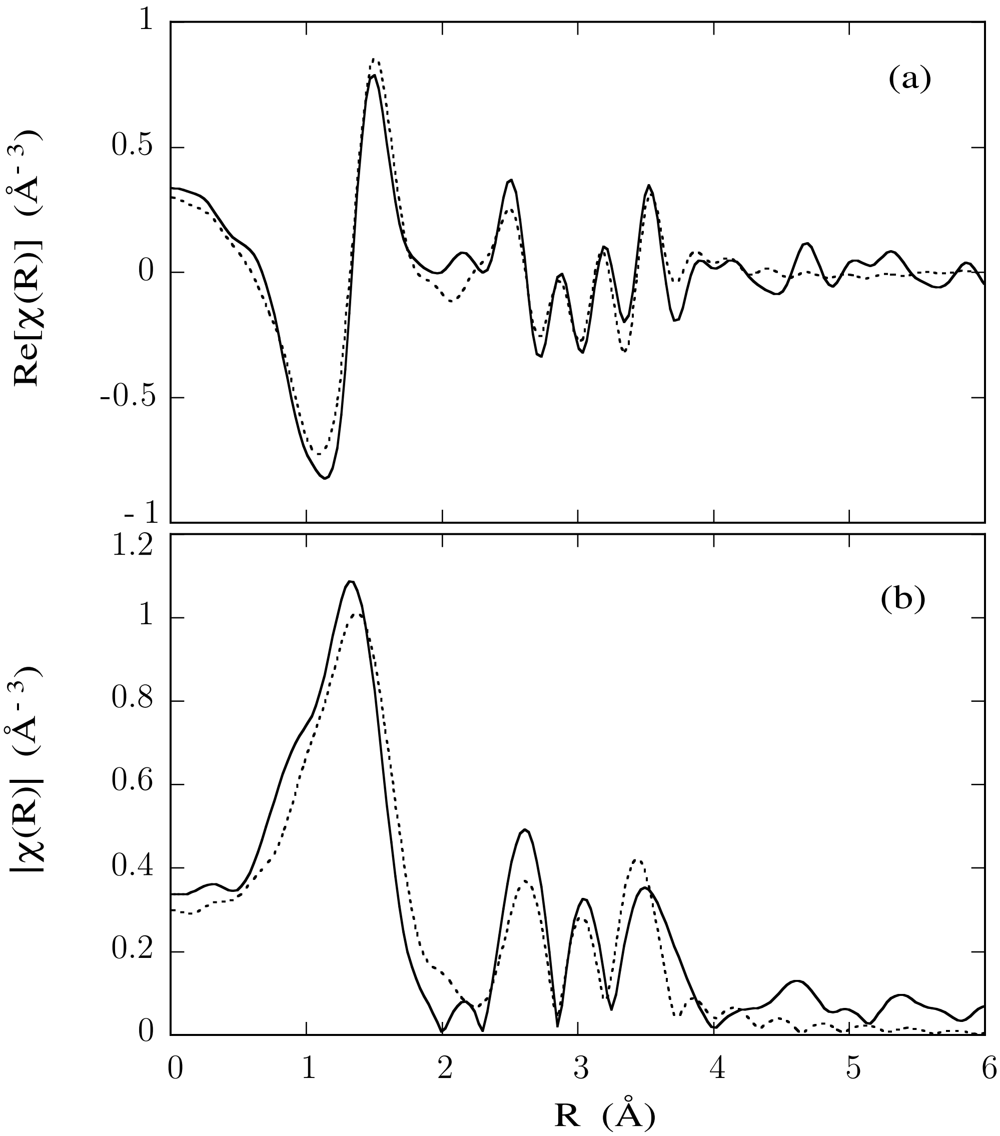

Figure 6.20: The results of the constrained FEFFIT fit to $YBa_2Cu_3O_{6.8}$ (007) DAFS $\chi''(k)$. (a) The real part of the Fourier transform of the data (solid line) overplotted with the FEFFIT best fit (dashed line). (b) The magnitudes of the functions shown in (a).

Chapter 7

RELIABILITY OF THE ITERATIVE KRAMERS-KRÖNIG ALGORITHM

This chapter contains the results of several computer experiments that were performed to test the reliability of the iterative Kramers-Krönig algorithm for isolating response function amplitudes from DAFS intensity data. There are two aspects of the analysis that I felt were most important to check: the accuracy of the XANES features returned by KKFIT and the integrity of the structural parameters, as determined by FEFFIT on the KKFIT output. Each computer experiment is presented with both a qualitative and a quantitative check: the XANES features are compared qualitatively by overplotting the KKFIT output with the original test functions; the structural parameters, as determined by FEFFIT, are compared quantitatively with the original input values. Along with the basic self-check of the iterative algorithm, I have also included a few examples of effects drawn from experimental considerations: the effects on the structural parameters of fitting the background with an incorrect self-absorption correction; the effects of energy broadening due to instrument resolution; and the effects of statistical noise in the intensity measurements.

All of the KKFIT reliability tests were done using mocked-up DAFS data in order to compare the output of the iterative algorithm with a known input. The fine structure for individual photoelectron backscattering paths was calculated by FEFF and combined using FEFFIT. The cusp and step functions were taken from tables of Cromer-Liberman calculations [63]. The procedure for generating the test functions is described in Section 7.2. A summary of the steps is also presented as a list of instructions, including the FEFF and FEFFIT input files, in Appendix B for convenient reference.

7.1 Kramers-Krönig integral calculations

At the heart of the iterative analysis method described in Chapter 5 is a fast and accurate method for calculating the differential Kramers-Krönig transform. The computation time is reduced by calculating the differential Kramers-Krönig transform from Section 1.2.1, which is based on the identities

$$\begin{aligned} f'(E) &= \frac{2}{\pi}\mathrm{P}\left(\int_0^\infty \frac{E' f_a''(E')}{E'^2 - E^2}dE' + \int_{\Delta E}\frac{E'(f''(E') - f_a''(E'))}{E'^2 - E^2}dE'\right) \\ &= f_a'(E') + \frac{2}{\pi}\mathrm{P}\int_{\Delta E}\frac{E' f_0''(E')\chi''(E')}{E'^2 - E^2}dE' \end{aligned} \tag{7.1}$$

and

$$\begin{aligned} f''(E) &= -\frac{2E}{\pi}\mathrm{P}\left(\int_0^\infty \frac{f_a'(E')}{E'^2 - E^2}dE' + \int_{\Delta E}\frac{(f'(E') - f_a'(E'))}{E'^2 - E^2}dE'\right) \\ &= f_a''(E') - \frac{2E}{\pi}\mathrm{P}\int_{\Delta E}\frac{f_0''(E')\chi'(E')}{E'^2 - E^2}dE'. \end{aligned} \tag{7.2}$$

with the subscript ΔE indicating that the integral is calculated only over the energy range where the fine structure is non-zero. The differential algorithm requires a pair of functions $f_a'(E)$ and $f_a''(E)$ that are conjugate to each other under the Kramers-Krönig transform and that strictly band-limit the fine structure $f(E') - f_a(E')$.

Algorithms for calculating the Kramers-Krönig dispersion integrals fall into two categories: 1) Summation algorithms calculate the Reimann integral, differing only in how they exclude the pole at $E = E_0$; and 2) Time domain algorithms are based on the symmetry properties of the Fourier transform. These algorithms exploit the crossing symmetry of the response function in the frequency domain and causality in the time domain to calculate the Krämers-Krönig transform using allied fast Fourier transforms (FFT-KK). Dispersion relations are widely used in reflectivity studies [82] and there are several published papers on computational methods [83–87]. I found the reviews by Ohta and Ishida [85] and by Bertie and Zhang [86] to be the most helpful in choosing the algorithms for KKFIT. Three summation algorithms and two FFT-KK algorithms were tested on two functions: a half-triangle ramp and a Lorentzian lineshape, and the results of the numerical integration were compared to the closed-form analytic transforms [87]. I observed little difference in the accuracy of the summation algorithms but Maclaurin's formula, described in Section 7.1.1 below, was considerable faster, in agreement with the conclusions of [85]. The time-domain algorithms were found to be equally reliable, but the enlarged energy range required for proper symmetrization of $f'(E)$ about $E = 0$ for realistic x-ray absorption energies, combined with the zero-padding required for the FFT, was found to make the calculation times and array sizes prohibitively large for normal analysis needs.

I have encoded the FFT-KK algorithm with proper symmetrization of the input functions as an option in KKFIT, but without absolute reference to zero energy.

The two algorithms coded into KKFIT, Maclaurin's formula and the FFT-KK, are described below, along with simple demonstrations of their accuracy using closed form test functions. Both procedures require that the values of the spectrum be given on a uniform mesh such that

$$\epsilon = E_{i+1} - E_i; \qquad i = 1, 2, \ldots, N-1, \tag{7.3}$$

and that the spectrum is zero at all energies outside of this range. In real DAFS experiments, the energy steps between data points are usually varied during the scan in order to optimize scanning time, with smaller energy steps taken in the near-edge region and larger steps taken far from the edge where the fine structure is small and varying more slowly. KKFIT recasts the input data onto a uniform 1 eV energy net by cubic spline interpolation for calculation of the transforms [88]; the output functions are returned at the original experimental energy values in the same manner.

7.1.1 Maclaurin's formula

Maclaurin's formula calculates the finite sum by taking every other data point in the finite approximation of Equation (7.2), for example

$$f_0''(E_j)\chi''(E_j) = \frac{2E}{\pi} \times 2\epsilon \times \sum_i \frac{f_0''(E_i)\chi'(E_i)}{E_i^2 - E_j^2}, \tag{7.4}$$

such that when j is *even*, the sum is taken over the *odd* values of i and likewise when j is *odd*, the sum is taken over the *even* values of i. This is a very simple algorithm that requires no special treatment of the pole. There is only a single logical check at each value of j, and then the even or odd sum is calculated. The number of calculations is thus reduced from the usual N^2 for the Kramers-Krönig transform to $(N/2)^2$. The range does not need to be extended beyond the range of the physical data, so the calculation time turns out to be shorter than for the FFT. The results are quite good, as can be seen in Figure 7.1(a) and (b), for a half-triangular test

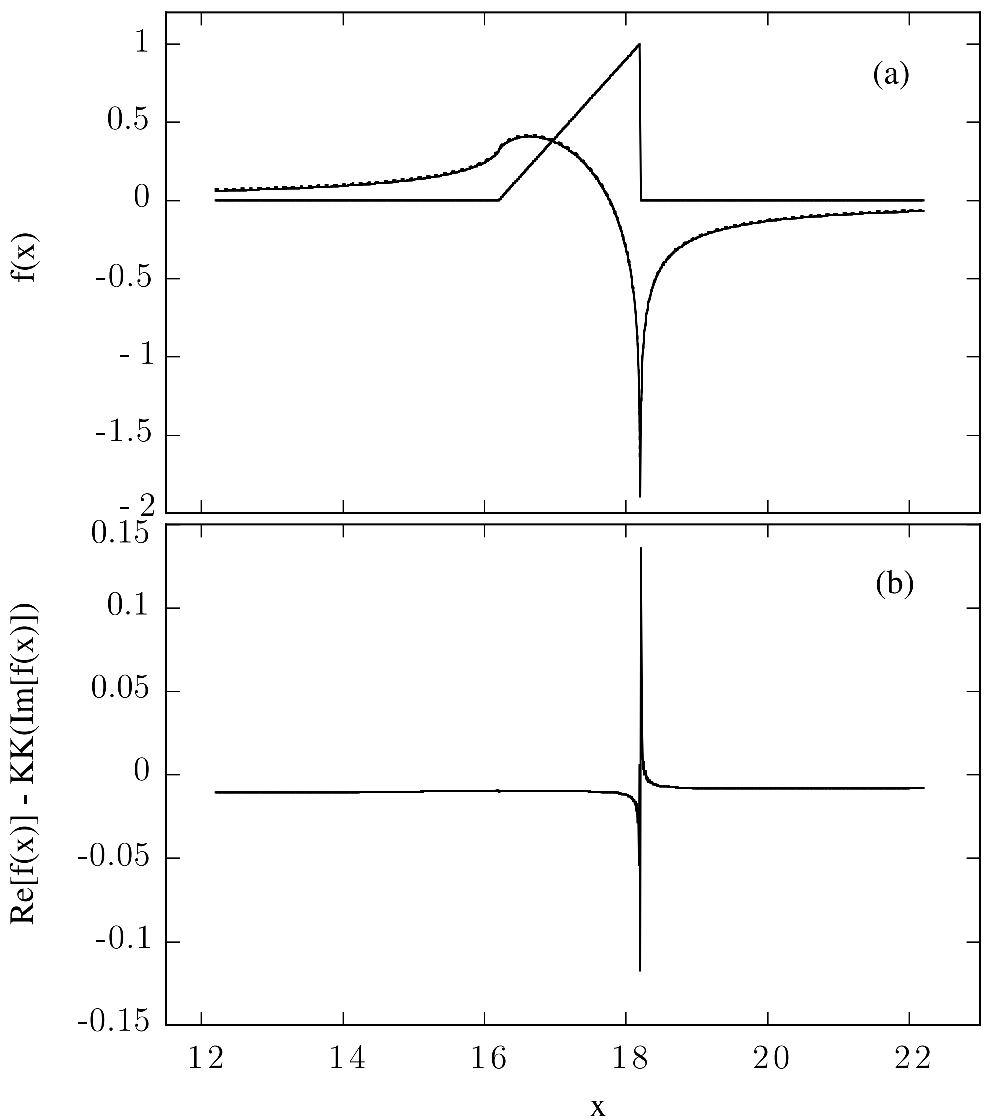

Figure 7.1: Application of the Maclaurin Kramers-Krönig algorithm to half-triangular test function with the quasi-discontinuous step split by a single data point. (a) The original function and the closed-form analytical transform (solid lines) are overplotted with the numerical transform (dashed line). (b) The difference between the closed-form and numerical transforms.

function[1] with quasi-discontinuous step For $\omega > 0$,

$$g'(\omega) = \begin{cases} \frac{1}{2}(\omega - \omega_0 + 1) & |\omega - \omega_0| < 1; \\ \frac{1}{2} & |\omega - \omega_0| = 1; \\ 0 & otherwise \end{cases} \tag{7.5}$$

and its conjugate

$$g''(\omega) = \frac{1}{\pi}\left(1 + \frac{\omega - \omega_0 + 1}{2}\left|\frac{(\omega - \omega_0) - 1}{(\omega - \omega_0) + 1}\right|\right) \tag{7.6}$$

with $g'(-\omega) = g'(\omega)$ and $g''(-\omega) = -g''(\omega)$. The difference between the analytical transform and the numerical calculation is expanded in Figure 7.2(b) to show the effects of the discontinuity at the step. Oscillation about the true conjugate function in the vicinity of the sharp discontinuity is due to the even/odd nature of the sum. The measured DAFS data and the mocked-up test functions used in this chapter do not have any discontinuities and this problem does not appear in the KKFIT results of Chapters 5 and 6, nor is it a problem in this chapter where the test functions are carefully constructed to be smooth, continuous functions of k and E.

7.1.2 FFT-KK

The FFT-KK algorithm is based on causality of the response functions. The time dependent response is assumed to be purely real and zero for all negative times. Since the Fourier transform of a purely real function in the time domain maps to a symmetric real part and an antisymmetric imaginary part in the conjugate frequency domain, the real and imaginary parts of $f(\hbar\omega)$ must be equal in magnitude and opposite in parity to get cancellation of $f(t)$ for all $t < 0$.

The computation comprises five steps: (anti)symmetric loading of the initial function, transforming into the time domain, multiplying by $\Theta(t)$, backtransforming into the frequency domain and unpacking the conjugate function. The starting function, $\mathrm{Re}[f(\hbar\omega)]$ or $\mathrm{Im}[f(\hbar\omega)]$ is loaded into an array and properly symmetrized about $E = 0$, symmetric for the real part or antisymmetric for the imaginary part. Since the FFT needs to be calculated on uniform steps, a large number of points is required to maintain a reasonably fine mesh size. If 1 eV steps are used around the transition

---

[1] A single data point has been added to the original function from Weinstein [87], Table 1, function 3 to split the difference at the step and ease the discontinuity.

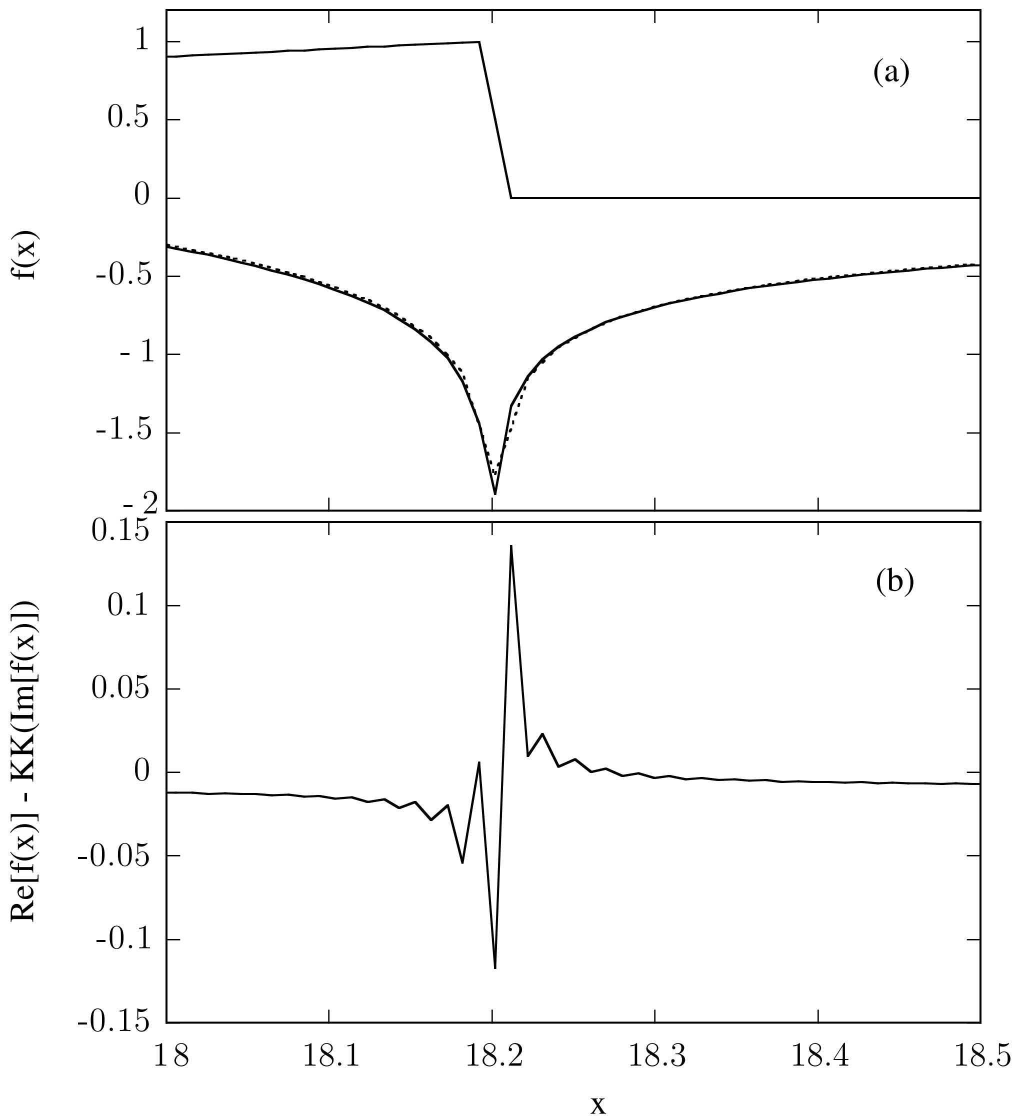

Figure 7.2: A close-up view of the functions from Figure 7.1. (a) The original function and the closed-form analytical transform (solid lines) overplotted with the numerical transform (dashed line). (b) The difference between the closed-form and numerical transforms. The effects of the even-odd alternation in the numerical sum show up as oscillation about the closed-form function. This effect is not present in functions that lack the discontinuity.

energy for Cu, which is at 8980 eV, and a 1000 eV data range. Then a minimum of $20,000$ points are needed just to load the real part, twice this if a complex transform is used. In addition, the FFT generally required padding by zeros to avoid aliasing [89]. The known symmetry properties can be used to reduce the calculation to only the real part of the transform. I have chosen to ignore the absolute phase problem and to symmetrize the frequency dependent input functions about the first energy point only. The first transform is a reverse transform into the time domain. KKFIT uses a Danielson-Lanczos algorithm, which requires that the array dimension be 2^N, and the result of the inverse transform are normalized to 2^{N-1}. The time domain functions is multiplied by

$$\Theta(t) = \begin{cases} 0, & t < 0; \\ \frac{1}{2}, & t = 0; \\ 1, & t > 0 \end{cases} \tag{7.7}$$

in the real channel, and zeroed in the imaginary channel. Finally the forward transform is taken back into the energy domain, giving $\frac{1}{2}f'(\hbar\omega)$ in the real channel and $\frac{1}{2}f''(\hbar\omega)$ in the imaginary channel. The results of the FFT-KK on the half-triangle test function are shown in Figure 7.3. When the $E = 0$ requirement is relaxed, the computation time is shorter than the Maclaurin algorithm, but the results show a slight sloping background compared to the closed-form of test function, as can be seen in Figure 7.3(b). The sign of the background slope changes depending on the loading parity, and so it can be reduced by performing the FFT-KK twice, once with symmetric loading and once with antisymmetric loading of the input function, and then taking the average of the two transforms.

7.2 *Model DAFS* $\chi(k)$ *calculated by* FEFF *and* FEFFIT

In order to test the reliability of KKFIT on DAFS data, known input functions are required. A convenient way to combine the FEFF output into a test function is to use FEFFIT and a simple model for the crystal. Using FEFFIT to generate $\chi(k)$ allows some control over the structural parameters parameters which can be checked quantitatively against the KKFIT results. The output of FEFF includes both the amplitude and the phase of $\chi(k)$, and so it can be used directly to mock-up DAFS fine structure using

$$\chi'(k) + i\chi''(k) = \texttt{mag}[\texttt{feff}] \times (\cos(\texttt{phase}[\texttt{feff}]) + i\sin(\texttt{phase}[\texttt{feff}])) \tag{7.8}$$

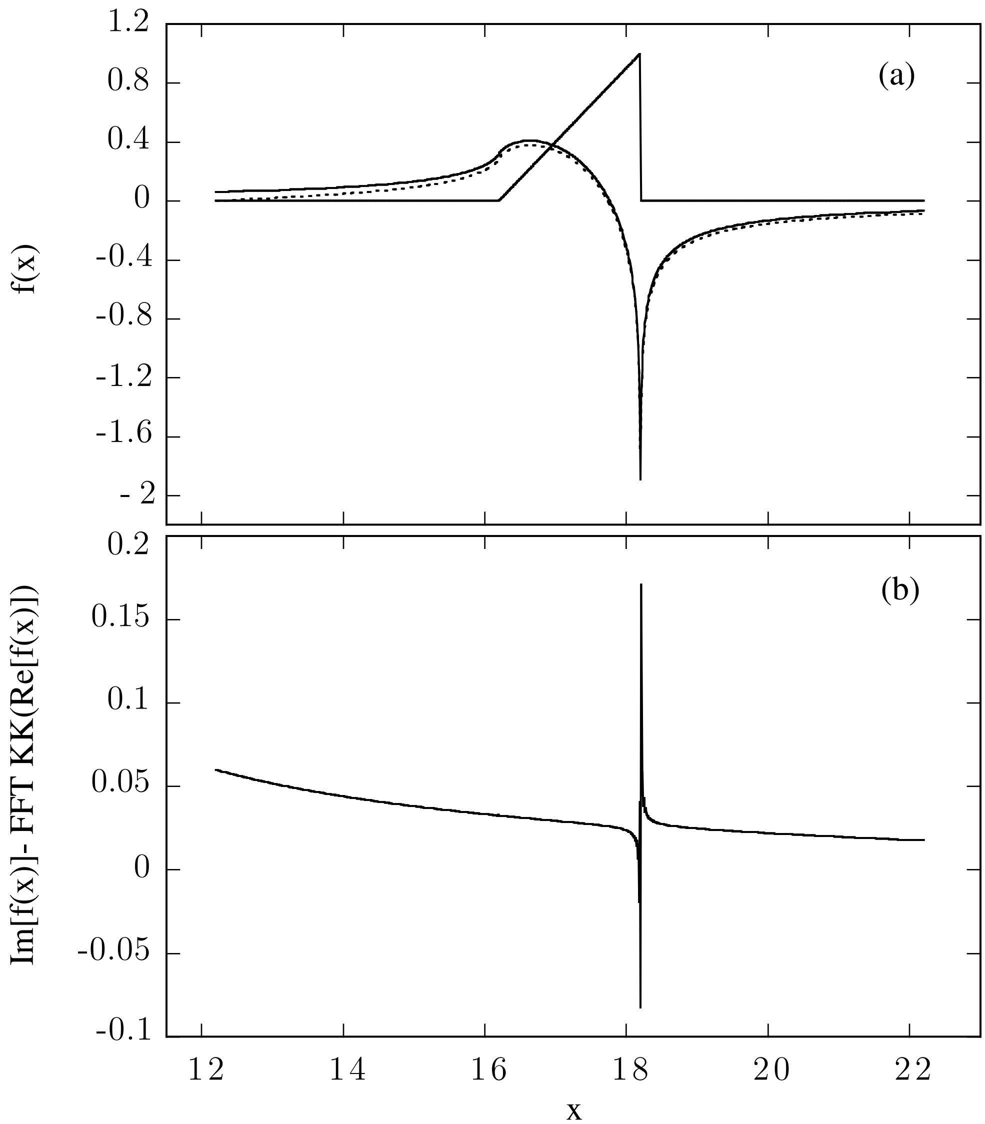

Figure 7.3: Application of the FFT-KK to a half-triangular test function. The quasi-discontinuous step in the input function is split by a single data point. (a) The original function and the closed-form analytical transform (solid lines) is overplotted with the numerical transform (dashed line). (b) The difference between the closed-form and numerical transforms. The sloping background is typical of the FFT-KK

where mag[feff] and phase[feff] are the third and fourth columns, respectively, of the individual feffnnnn.dat path files.

7.2.1 Using FEFFIT *to mock up DAFS data*

The complex $\chi(k)$ function for f.c.c. Cu metal was generated by running FEFFIT[2] on the input file makeCu.inp shown in Figure B.1. The broad R- and k-ranges of the Fourier transform eliminate any windowing of the data and the keyword **kfull** directs FEFFIT to add together the feffnnnn.dat files in k space with no intermediate transform or backfiltering. A Debye model [51] was used for the bond length disorder, with Θ_{Debye} set to 315°K. The amplitude reduction factor was set to $S_0^2 = 0.89$, consistent with values for Cu metal found in the literature [21]. The ordinate k was converted to E using

$$E = \frac{(\hbar k)^2}{2m_e} + E_0, \tag{7.9}$$

with $E_0 = 8980$ and the path parameter e0 set to zero. The average lattice parameter of Cu 3.6148 Å was taken from Cullity [115] and the model included a linear expansion coefficient α related to the effective path length R_{eff} of each scattering path by $R_{\text{fit}} = (1+\alpha)R_{\text{eff}}$. A value of $\alpha = 0.0035023$ was chosen based on an early fit to the Cu XAFS data, making the path length to the first shell $d_0 = 2.5650$ Å.

Self-conjugation of the fine structure

The $\chi'(k)$ and $\chi''(k)$ functions generated by FEFFIT are not a true conjugate pair. They can be made manifestly invariant under the Kramers-Krönig transform by calculating the transform of one or the other of the functions $f''_{\text{K}}\chi'(E)$ or $f''_{\text{K}}\chi''(E)$, where f''_{K} is the K-shell step function from a parameterization of $f''(E)$. Figures 7.4(a) and (b) show the real and imaginary parts, respectively, of $f''_{\text{K}}\chi(E)$ before and after this operation. First the product $f''_{\text{K}}\chi''(E)$ was calculated using the FEFFIT output

---

[2] For historical reasons, the complex $\chi(k)$ output of FEFFIT is rotated by $-\pi/2$ and some processing of the data is required before it can be used in the scattering amplitude. The column labels of the five column output file are

```
k  real(chi(k))   imag(chi(k))  ampl(chi(k))  phase(chi(k))
```

but the meaning of the columns, in terms of the output from FEFF, is:

```
k  imag(chi(k))  -real(chi(k))  ampl(chi(k))  phase(chi(k))-π/2
```

My solution is to delete the column imag(chi(k)), to relabel the column real(chi(k)) to read

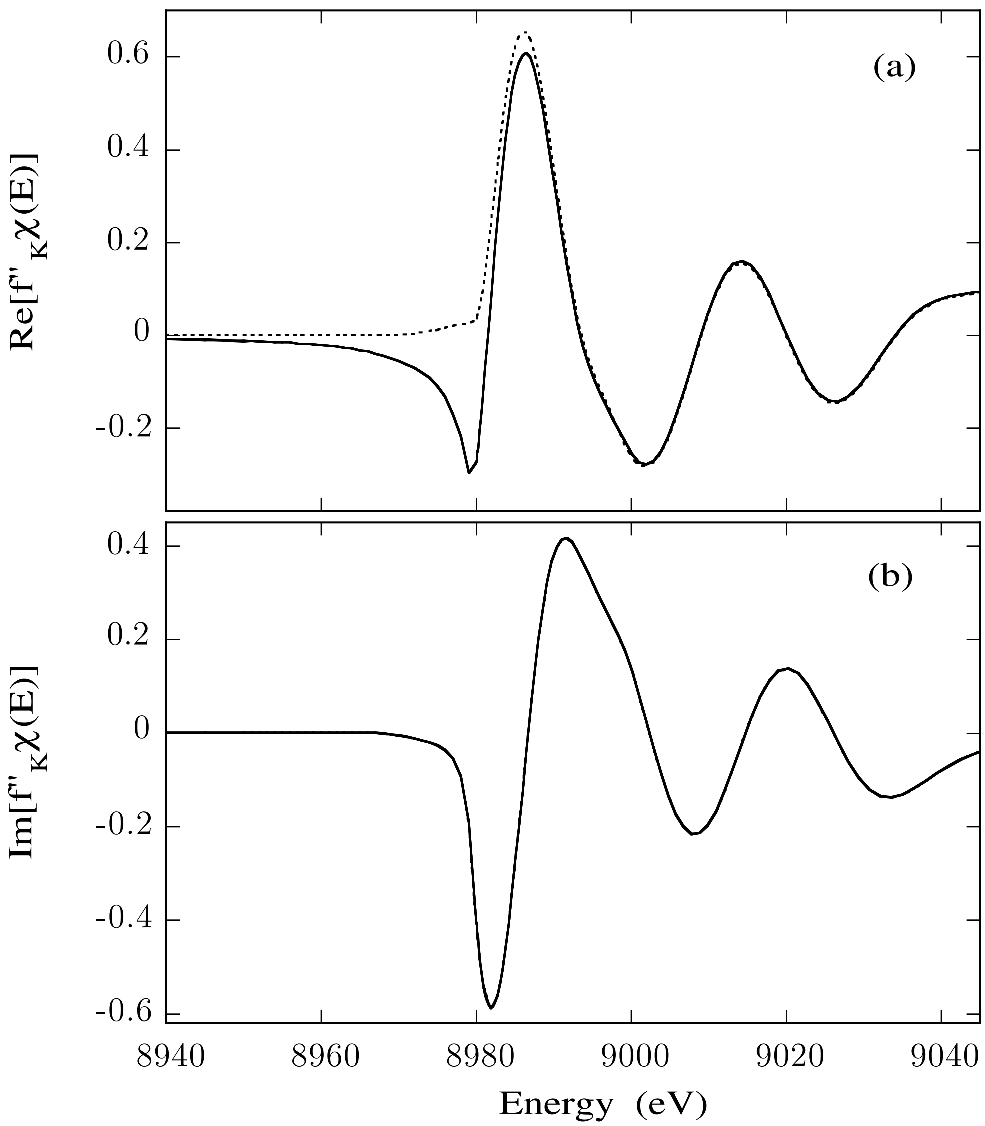

Figure 7.4: The near edge features of the (a) $f''_{\mathrm{K}}\chi'(E)$ and (b) $f''_{\mathrm{K}}\chi''(E)$ pair obtained by Kramers-Krönig transform of FEFFIT generated functions. The individual $\chi_{\mathrm{path}}(k)$ functions output by FEFF are combined using FEFFIT to obtain a complex $\chi(k)$ with known structural parameters. The functions generated by FEFFIT in this way are not a true Kramers-Krönig conjugate pair. They can be made self-conjugate by calculating the transform of the real or imaginary part of $f''_0\chi(E)$. The dashed lines show the original functions and the solid lines are an overplot of three successive iterations of the integral transform. The original $\mathrm{Im}[f''_0\chi(E)]$ is indistinguishable from subsequent iterations—convergence is immediate.

and convolved with a 2 eV Lorentzian lineshape to approximate core hole lifetime broadening [81]. $f''_{\mathrm{K}}\chi'(E)$ was calculated by Kramers-Krönig transform, and the self-conjugate functions were checked for stability by transforming and backtransforming four times. All four iterations are overplotted in Figure 7.4. The resulting pair of functions is invariant under the Kramers-Krönig algorithm , and so they should be returned exactly by KKFIT if the analysis methods are sound. Figure 7.5 shows the analytic test function that was the starting place for all of the computer experiments described below.

7.2.2 Self-fit to model data

The analytic functions for the self-test were normalized according to

$$\chi(E) = \frac{f''_{\mathrm{K}}(E)\chi(E)}{\Delta f''_{\mathrm{K}}(E = E_0)} \tag{7.10}$$

where $\Delta f''_{\mathrm{K}}(E = E_0)$ is the step height. This is the same as the normalization in KKFIT. The values of the fitting parameters are tabulated in the first data column of Table 7.1. Figure 7.6(a) shows the R-space FEFFIT self-fit to the real part of the test function. Four path parameters were allowed to vary: the overall amplitude, S_0^2; the position of the absorption edge ΔE_0; ΔR_{path}, using a linear expansion coefficient α with $\Delta R_{\mathrm{path}} = \alpha R_{\mathrm{eff}}$, to account for any changes in the lattice parameter caused by the Kramers-Krönig transform; and the XAFS Debye-Waller factor σ^2. The analytic $\chi'(k)$ was fit using the same input file as $\chi''(k)$ by adding a constant phase $\Delta\delta_{\mathrm{path}} = \pi/2$ to each path. Figure 7.6(b) shows an overplot of the R-space transforms of the original FEFFIT function and the real and imaginary parts of the *self-conjugated* analytic test function. The analytic test functions have slightly lower amplitude than the original FEFFIT output function. The difference is observed in both the real and imaginary channels, which are indistinguishable in the R-space magnitudes. The imaginary part of the test functions is identical to the FEFFIT output except for convolution with a Lorentzian and a factor of E_0/E due to the normalization. Multiplying the test functions by E_0/E was found to have not effect on the fitting parameters, so the drop in S_0^2 is attributed purely to the convolution.

`chi(k)`, and to add $\pi/2$ to `phase(chi(k))`. This results in a four column file that has the same order and meaning as the standard `chi.dat` output from FEFF 6.10.

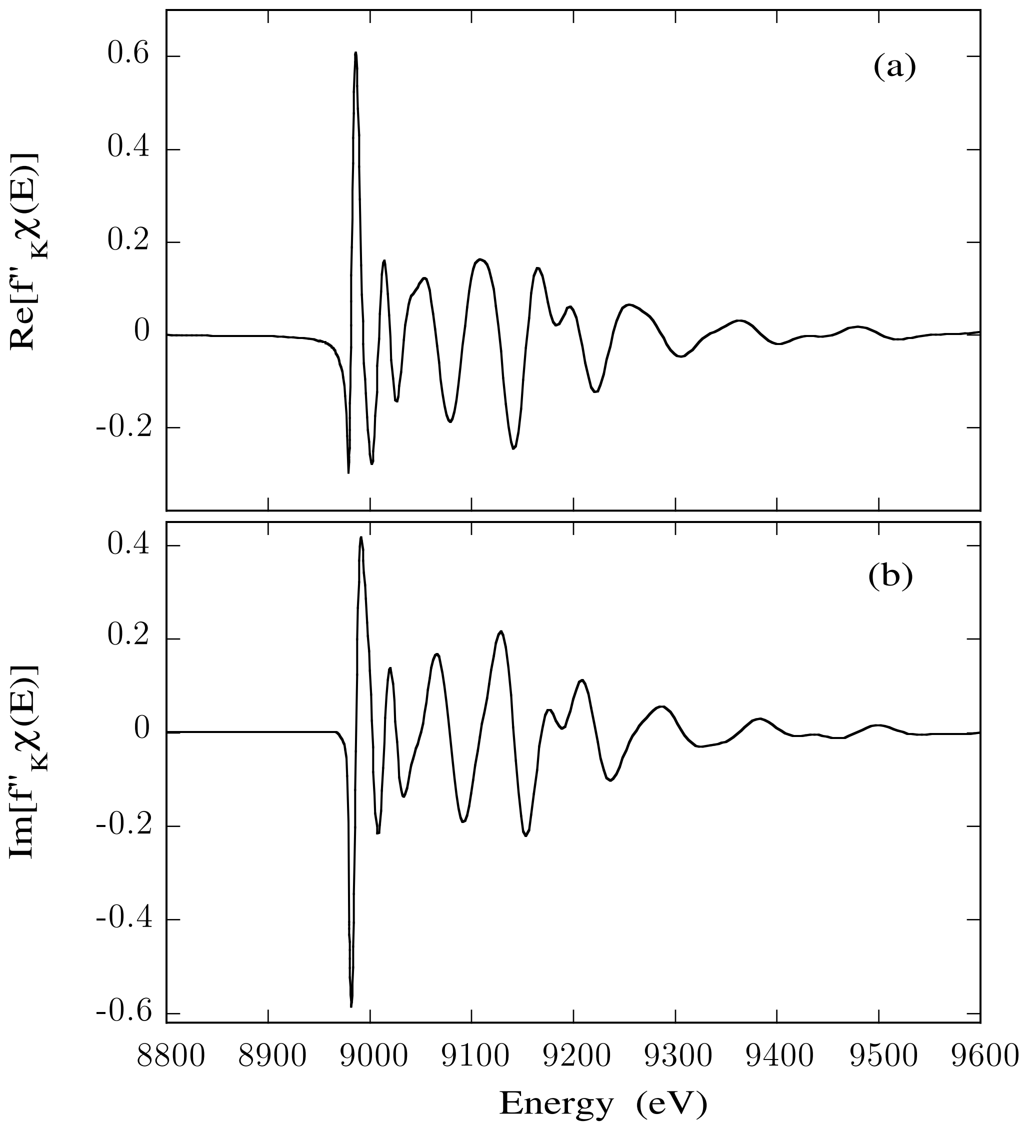

Figure 7.5: The complex $f''_{\rm K}\chi(E)$ test functions used to mock up Cu metal K-shell DAFS data. (a) $f''_{\rm K}\chi'(E)$ and (b) $f''_{\rm K}\chi''(E)$. $\chi''(k)$ was generated by adding together the twelve FEFF path files listed in table 5.2 using FEFFIT with $S_0^2 = 0.89$, and a Debye model for the XAFS Debye-Waller factors with $\Theta_D = 315°$K. The output from FEFFIT was converted to $f''_{\rm K}\chi''(E)$ and convolved with a 2 eV Lorentzian to approximate core-hole lifetime broadening. The conjugate function $f''_{\rm K}\chi'(E)$ was determined by taking the Kramers-Krönig transform of $f''_{\rm K}\chi''(E)$.

Table 7.1: Comparison between initial values and model fitting parameters for the fits to mocked-up Cu $\chi'(E)$ shown in Figure 7.6. The first row shows the initial value used to generate the mocked-up $\chi''(k)$ data. The second row is the result of a self-fit to the FEFFIT generated $\chi'(k)$ function and the third and fourth columns are the results of a fit to the core-hole broadened *analytic* $\chi(k)$ function shown in Figure 7.5(a). Four path parameters were allowed to vary in the fit: S_0^2, Θ_D, α and ΔE_0. The last column shows the resulting near-neighbor path length based on the best-fit value of α. Notice that S_0^2 for the test functions is systematically low due to convolution with a 2 eV Lorentzian that was done before calculating the conjugate. Uncertainties are those given by FEFFIT, and all of the structural parameters other than S_0^2 agree with the input values used to generate the data.

path parameters					
	S_0^2	$\Theta_\mathrm{D}(K)$	α	ΔE_0 (eV)	d_0 (Å)
Input parameters used to generate test functions (no uncertainty)					
$\chi''(k)$	0.890±0.00	315.0±0.0	0.0035±0.0000	0.00 ±0.00	2.5650±0.0000
FEFFIT *self-test results (uncertainties could not be estimated)*					
$\chi''(k)$	0.890±x.x	315.0±x.x	0.0035±x.x	0.00 ±x.x	2.5650±x.x
FEFFIT *fits to analytic* $\chi(k)$ *test functions*					
$\chi'(k)$	0.836±0.013	313.5±2.5	0.0033±0.0003	-0.002±0.15	2.5645±0.0008
$\chi''(k)$	0.838±0.010	313.3±1.9	0.0033±0.0003	-0.020±0.12	2.5644±0.0008

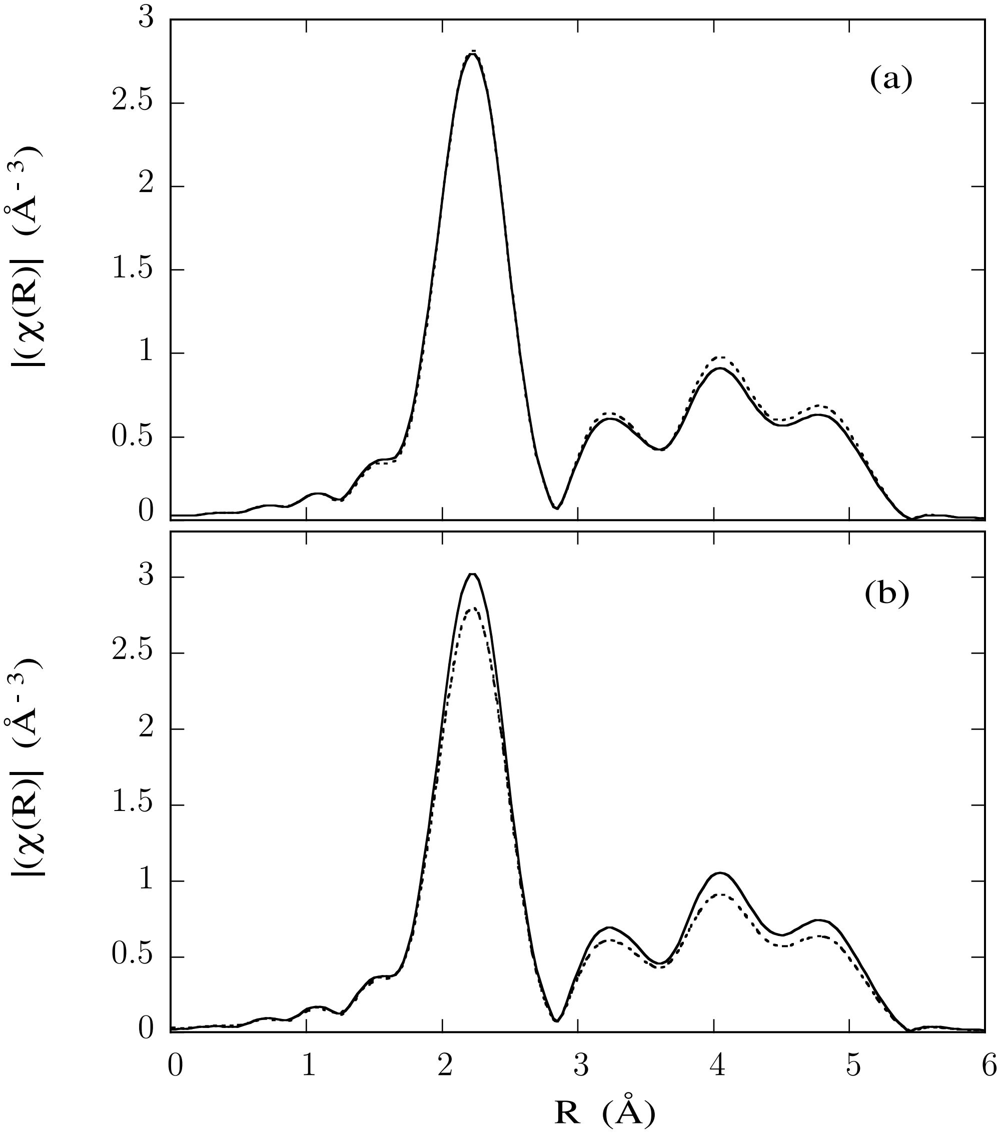

Figure 7.6: FEFFIT fit of the analytic test functions using twelve FEFF scattering paths and four variable path parameters. Fit results are given in Table 7.1 (a) An example, the worst of the three fits. $\tilde{\chi}'(R)$ from the test function (solid line) and the FEFFIT fit (dashed line). (b) The Fourier transform magnitudes of the initial FEFFIT $\chi''(R)$ (solid line), and the real and imaginary parts of the analytic test function from Figure 7.5(a) (dashed and dot-dashed lines); the R-space transform magnitudes of the real and imaginary parts of the test functions are indistinguishable.

7.3 KKFIT on mocked-up Cu DAFS

Mocked-up DAFS intensities for Cu (111) and Cu (222) were calculated according to the kinematic structure factor of Equation 3.29. Tabulated values of $f'(E)$ and $f''(E)$ were tested for invariance under the Kramers-Krönig transform by calculating the integrals over the entire range of available theoretical data[3].

The output from KKFIT is compared with the original $f'(E)$ and $f''(E)$ functions in Figure 7.7. Overall, the shape of the functions in the near-edge region is well-reproduced and the agreement in the extended region is excellent. The difference functions $\chi'(k)$ and $\chi''(k)$ are shown in Figure 7.8. The KKFIT normalized $\chi(k)$ functions tend to have a slowly varying background component that is not present when XAFS data is normalized using AUTOBK (see Section 5.2.3). This was removed by allowing FEFFIT to minimize the low-R part of $\tilde{\chi}(R)$ below $R = 1.5$ Å. To make a better comparison between the self-fit and the fit to the KKFIT results, the same background removal was also applied to the control self-fit in each test. From Figures 7.7 and 7.8, it is clear that $f'(E)$ and $f''(E)$ are reliably returned by KKFIT, but that $\chi'(k)$ and $\chi''(k)$ depend on the shape of the atomic response functions $f'_a(E)$ and $f''_a(E)$ in the near-edge region. For k larger than about 0.5, which is arguably as low as the reliable region for any XAFS $\chi(k)$ functions, KKFIT returns the input functions satisfactorily. The FEFFIT results in Table 7.2 show that all of the structural information is preserved in the KKFIT isolated and normalized complex $\chi(k)$ functions. It is interesting to note that the AUTOBK results, obtained by applying AUTOBK to the function $\mu(E) = \mathcal{C}f''(E)/E$ (see Appendix A give results that differ from the input values outside of the range of the uncertainty estimated by FEFFIT. It is not clear at this time what causes this difference.

7.4 The effects of common experimental errors

The following computer experiments were undertaken first to provide some insight into the differences between the Cu metal XAFS and DAFS presented in Chapter 5,

---

[3] The Sasaki tables are provided on a fine 1 eV net around the Cu K-shell E_0, but are limited in range to 4200 eV up to 123,000 eV. I extended this range using values from Chantler [64], which were provided to me on a 30 eV net near the edge, to fill in at the low energy range down to 6 eV, and the high energy range up to 194,000 eV. Calculating the integral over this range, to transform $f''(E)$ into $f'(E)$ at 1200 points, takes approximately eight hours to run on my Macintosh IIci.

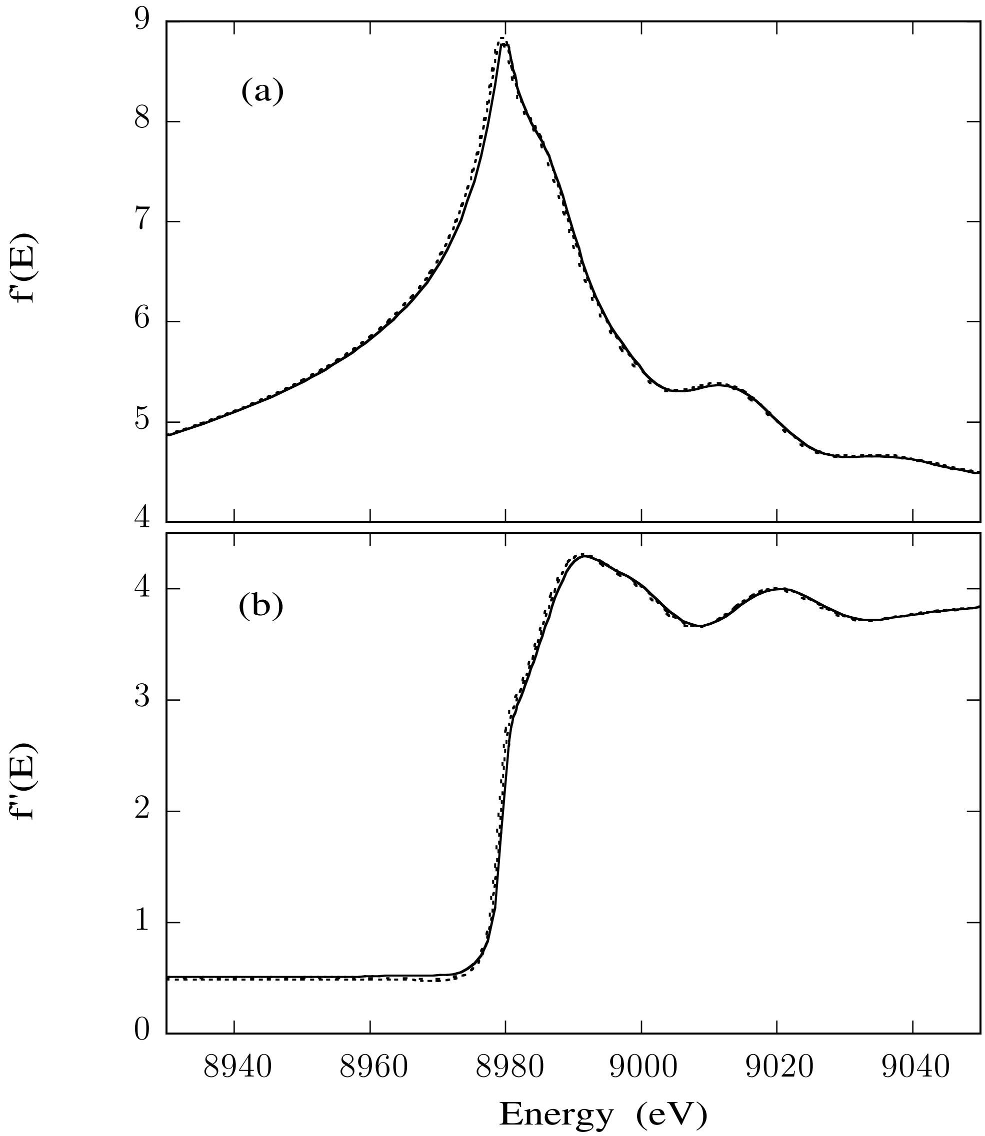

Figure 7.7: Self-test of KKFIT on mocked-up Cu DAFS: $f'(E)$ and $f''(E)$ The resulting (a) $f'(E)$ and (b) $f''(E)$ obtained by KKFIT using Maclaurin's formula for the integral transform. The near-edge region was reliably returned by the iterative algorithm. Three curves are shown in each frame: the original functions (solid line) and the KKFIT output for mocked-up Cu (111) DAFS (short dash line) and Cu (222) DAFS (long dash line).

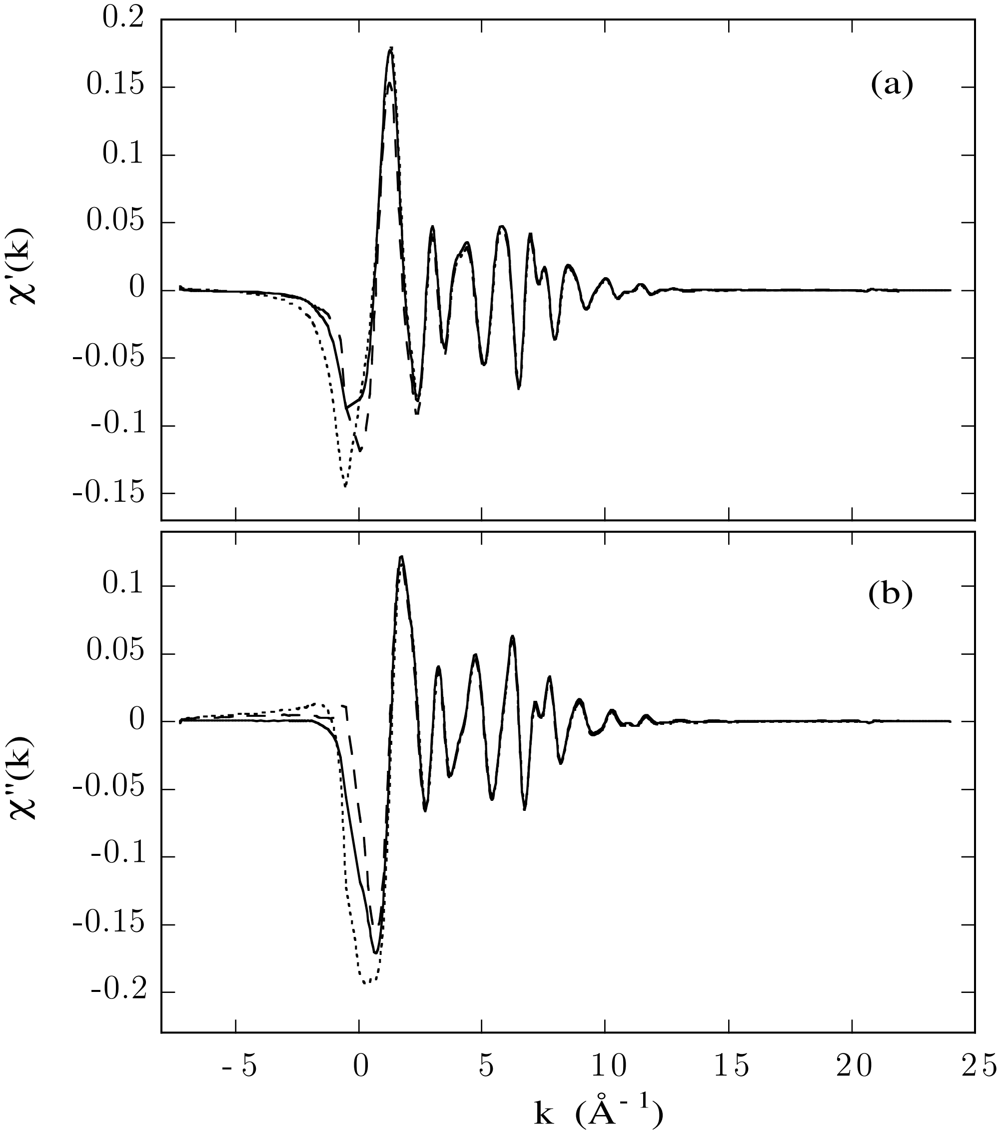

Figure 7.8: Self-test of KKFIT on mocked-up Cu DAFS: $\chi'(k)$ and $\chi''(k)$. The resulting (a) $\chi'(k)$ and (b) $\chi''(k)$ output from KKFIT using Maclaurin's formula for the integral transform. Three curves are shown in each frame: the original functions (solid line) and the KKFIT output for mocked-up Cu (111) DAFS (short dash line) and Cu (222) DAFS (long dash line). The differences for $k < 0$ are due to errors in subtracting off $f_a(E)$; $f'(E)$ and $f''(E)$ are reliably determined by KKFIT, as shown in Figure 7.7.

Table 7.2: The effect of KKFIT on structural parameters. KKFIT was used to isolate $\chi'(k)$, $\chi''(k)$ and $\mu(E)$ from mocked-up Cu (111) and Cu (222) DAFS data. A $\chi''(k)$ isolated by AUTOBK from the KKFIT $\mu(E)$ was analyzed along with the direct output $\chi'(k)$ and $\chi''(k)$. The fit used twelve paths and four variable parameters: S_0^2, Θ_D, α and ΔE_0. The nearest neighbor path distance is also given in this table using $d_0 \rightarrow d_0(1+\alpha)$. Uncertainties are those given by FEFFIT. Notice that the AUTOBK isolation and normalization results in significantly different values for S_0^2 and α from the original functions as compared to the KKFIT output. Correlations between the FEFFIT path parameters, which are determined by the off-diagonal elements of the Jacobian matrix in the Levenberg-Marquardt minimization [59, 88], are strongest between S_0^2 and Θ_D (anticorrelated ~ -0.93) and between α and ΔE_0 (correlated ~ 0.91).

	path parameters				
	S_0^2	$\Theta_{\rm D}(K)$	α	ΔE_0 (eV)	d_0 (Å)
FEFFIT *fits to analytic $\chi(k)$ test functions (control)*					
$\chi'(k)$	0.836±0.013	313.5±2.5	0.0033±0.0003	-0.002±0.15	2.5645±0.0008
$\chi''(k)$	0.838±0.010	313.3±1.9	0.0033±0.0003	-0.020±0.12	2.5644±0.0008
FEFFIT *fits to* KKFIT *output of mocked-up Cu (111) DAFS from test functions*					
$\chi'_{111}(k)$	0.820±0.016	310.0±3.1	0.0034±0.0005	0.345±0.18	2.5648±0.0013
$\chi''_{111}(k)$	0.819±0.013	310.3±2.4	0.0032±0.0004	0.268±0.15	2.5643±0.0010
$\mu_{111}(E)$	0.860±0.017	304.2±2.9	0.0073±0.0005	-0.680±0.18	2.5747±0.0013
FEFFIT *fits to* KKFIT *output of mocked-up Cu (222) DAFS from test functions*					
$\chi'_{222}(k)$	0.833±0.013	309.9±2.4	0.0033±0.0004	-0.365±0.15	2.5645±0.0010
$\chi''_{222}(k)$	0.838±0.013	308.9±2.4	0.0033±0.0004	-0.392±0.14	2.5643±0.0010
$\mu_{222}(E)$	0.884±0.017	302.2±3.0	0.0074±0.0005	-1.315±0.19	2.5750±0.0013

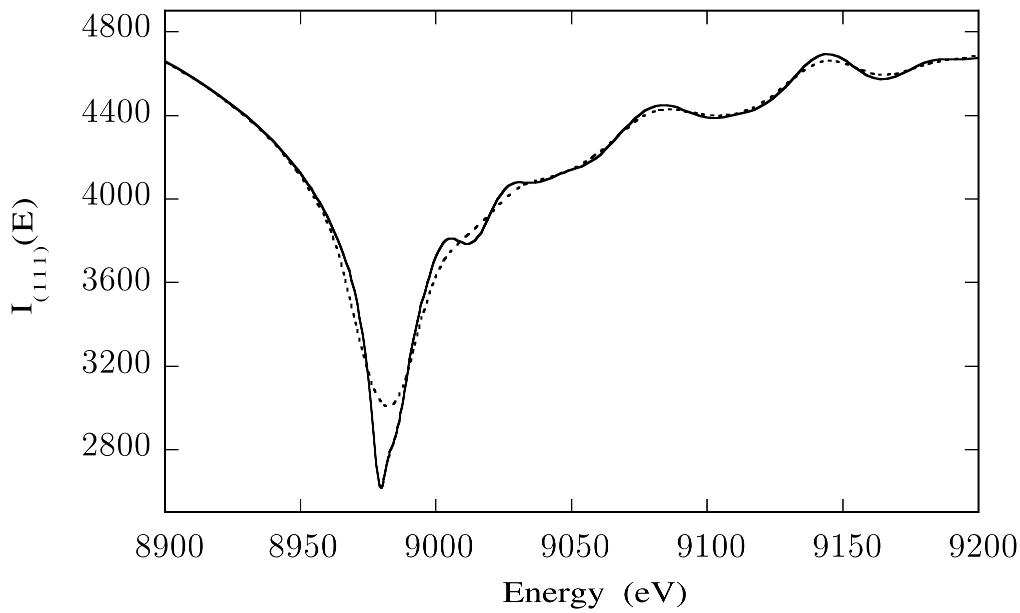

Figure 7.9: An example of the mock-up data used to test the effects of instrument broadening on DAFS structural parameters. Cu (111) DAFS intensity convolved with a Gaussian lineshape, 1 eV (solid line) and 10 eV (dashed line).

and second to quantitatively explore the reliability of KKFIT against some typical experimental problems.

7.4.1 Instrument broadening

This test was run to determine the effect that instrument broadening would have on the structural information in DAFS data. Mocked-up Cu (111) and (222) data was generated and the intensity was convolved with a Gaussian lineshape to approximate the instrument broadening of the data. The linewidth varied from 1 eV up to 10 eV in 1 eV steps. Figure 7.9 shows an example of the input data used for this test. Figure 7.10 shows the $\chi'(k)$ output of KKFIT for the Cu (111) mocked-up DAFS at all ten values of the resolution and Figure 7.11 shows the FEFFIT results for the path parameters S_0^2 and Θ_D. The results of fitting all of the $\chi'(k)$ function in Figure 7.10 are tabulated in Table 7.3. The strongest effects are on S_0^2 and Θ_D, which are highly anticorrelated, and on d_0, which appears to decrease as the instrument broadening increases. The effects on ΔE_0 are smaller than its uncertainty, as determined by FEFFIT.

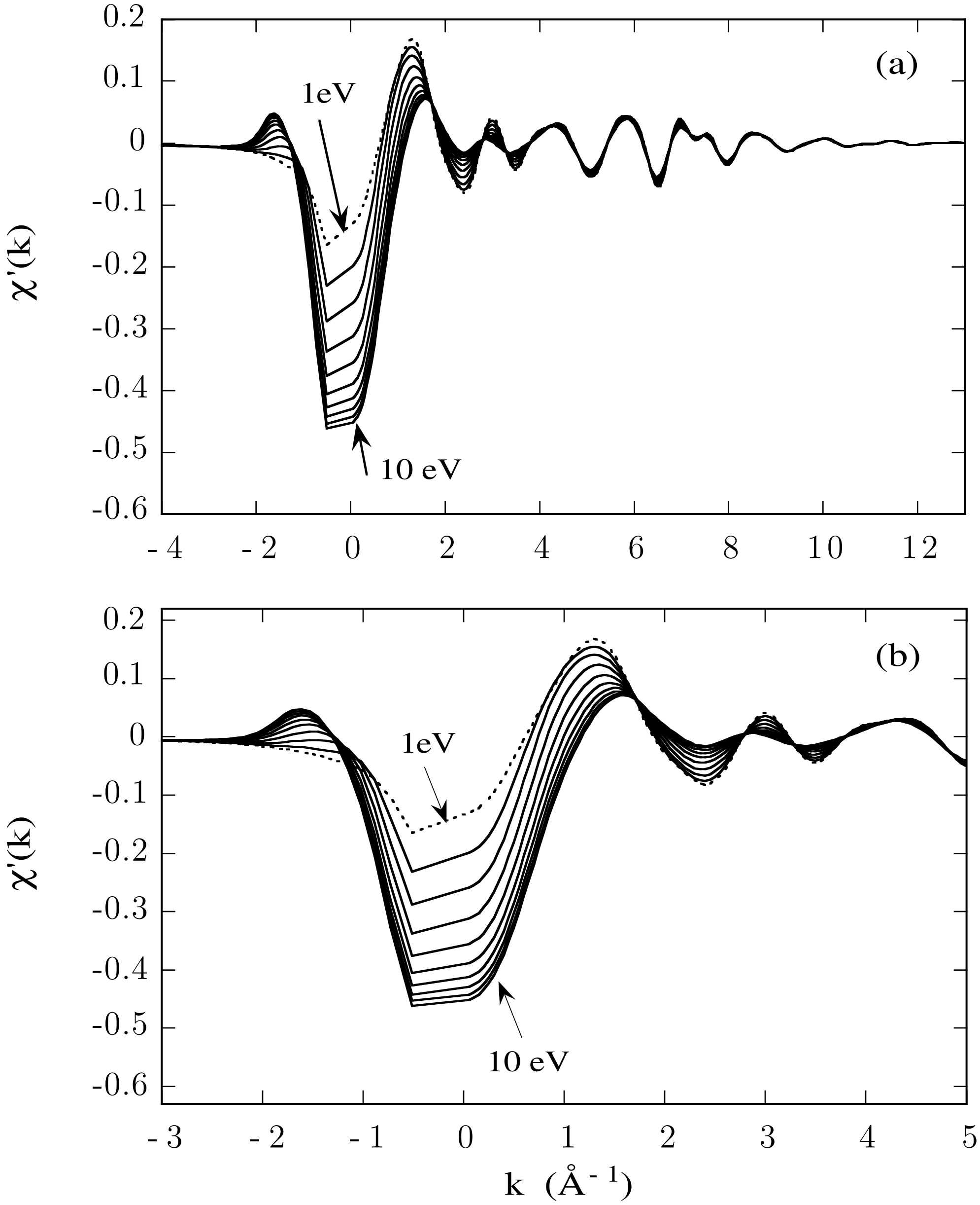

Figure 7.10: The effects of instrument broadening on the $\chi'(k)$ output of KKFIT. Cu (111) DAFS intensity convolved with a Gaussian lineshape 1 eV through 10 eV in 1 eV steps. The resulting $\chi'(k)$ is shown both (a) in the extended region and (b) in the near-edge region, for comparison.

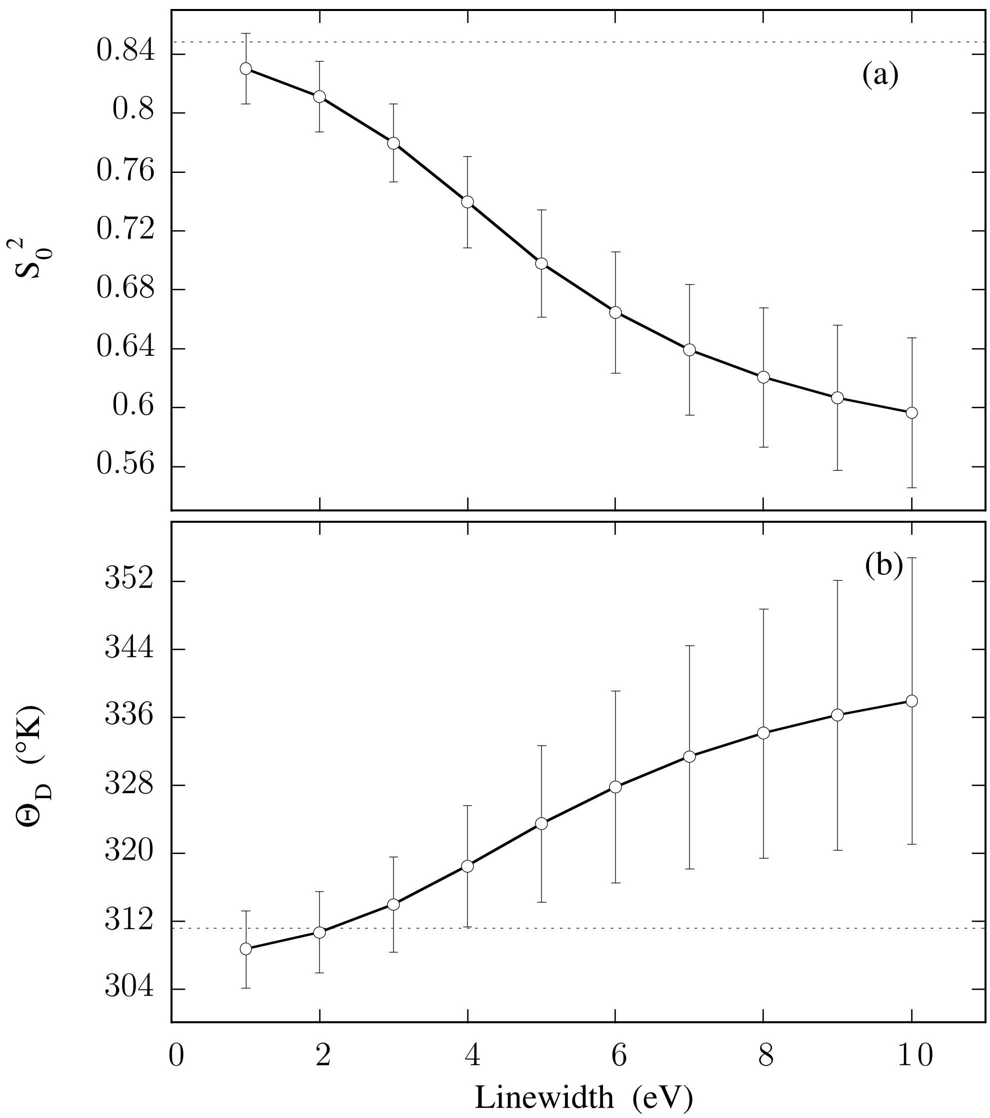

Figure 7.11: The effects of instrument broadening on S_0^2 and Θ_D. FEFFIT analysis of Cu (111) DAFS $\chi'(k)$ from KKFIT of mocked-up data convolved with a Gaussian lineshape 1 eV through 10 eV in 1 eV steps. The horizontal dashed lines indicate the original values of the parameters of FEFFIT analysis of the self-conjugate $\chi(k)$ test functions before the mock-up, convolution and KKFIT steps.

Table 7.3: Instrument broadening effects: results of FEFFIT analysis of $\chi'(k)$ functions obtained by KKFIT using a Gaussian instrument convolved on mocked-up DAFS data with 2000 Å film thickness. Linewidths from 1 eV through 10 eV in 1 eV steps for Cu (111) and Cu (222). The strongest effects are observed S_0^2 and Θ_D, which are strongly anticorrelated (~ -0.93), and on the first shell distance d_0 which decreases as the instrument broadening increases. The effect seen in ΔE_0 is smaller than than the uncertainty, as determined by FEFFIT.

path parameters					
linewidth	S_0^2	$\Theta_\mathrm{D}(K)$	α	ΔE_0 (eV)	d_0 (Å)
FEFFIT *fits to analytic* $\chi(k)$ *test functions (control)*					
$\chi'(k)$	0.849±0.026	311.1±5.0	0.0036±0.0008	0.094±0.31	2.5652±0.0020
$\chi''(k)$	0.852±0.026	310.2±5.0	0.0038±0.0008	0.187±0.31	2.5658±0.0020
FEFFIT *fits to* $\chi'(k)$ *from* KKFIT *of mocked-up Cu (111) DAFS*					
1 eV	0.833±0.027	308.2±5.0	0.0037±0.0008	0.231±0.31	2.5655±0.0020
2 eV	0.813±0.027	310.3±5.4	0.0035±0.0008	0.146±0.33	2.5650±0.0020
3 eV	0.780±0.030	314.0±6.5	0.0032±0.0011	-0.003±0.46	2.5642±0.0028
4 eV	0.738±0.034	318.8±7.9	0.0027±0.0011	-0.165±0.47	2.5630±0.0028
5 eV	0.695±0.038	324.3±9.9	0.0021±0.0014	0.409±0.56	2.5615±0.0036
6 eV	0.660±0.042	329.2± 11	0.0016±0.0016	0.641±0.65	2.5600±0.0041
7 eV	0.634±0.044	333.2± 13	0.0011±0.0017	0.833±0.71	2.5588±0.0044
8 eV	0.615±0.046	336.3± 15	0.0008±0.0018	0.977±0.77	2.5580±0.0046
9 eV	0.600±0.035	338.7± 16	0.0005±0.0019	-1.097±0.81	2.5573±0.0049
10 eV	0.648±0.048	340.6± 16	0.0002±0.0020	-1.204±0.84	2.5566±0.0051

7.4.2 Incorrect film thickness in the absorption correction

The film thickness is not a reliable adjustable fitting parameter in KKFIT, as discussed in Section 5.2.3, but it can be varied by hand. The following computer experiment was done to explore the effects of setting the film thickness incorrectly in KKFIT. Mocked-up Cu DAFS intensity data was made following the recipe in Appendix B with input values of the film thickness ranging from 1000 Å to 3500 Å in 500 Å increments. The real and imaginary parts of $\chi(k)$ were isolated from the mocked-up data using KKFIT with the film thickness in the fit fixed at 2000 Å. The DANES features for Cu (111) and Cu (222) are shown in Figures 7.12 and 7.13 respectively; the $\chi(k)$ functions for Cu (111) are shown in Figure 7.14. The twelve $\chi'(k)$ functions were analyzed using FEFFIT and the results are shown in Table 7.4. The fits were done over the first three paths of the original twelve so that the path parameter `delr` could be allowed to vary individually for each path without exceeding the number of independent data points in each set. The original analytic input functions were analyzed in the same manner for comparison. The effects of an incorrect absorption correction on the path parameters are also shown graphically versus film thickness, with uncertainties determined by FEFFIT: Figure 7.15(a) for S_0^2; Figure 7.15(b) for Θ_D; Figure 7.16(a) for E_0; and Figure 7.16(b) for the nearest neighbor distance d_0. It is interesting to note that the Cu (111) and Cu (222) results for both S_0^2 and Θ_D cross over each other at the correct value of t. This suggests that it may be possible to determine the film thickness to within a few hundred Å if no more accurate means is readily available, or as a check against the KKFIT results.

7.4.3 Poisson distributed random noise

Noise was added to the mocked-up data using a random Poisson deviate distributed about the calculated intensity. The intensities were normalized to 10^5 up to 10^9 counts at the first energy value to set the scale of the signal-to-noise. By comparison, the experimental Cu (111) and Cu (222) DAFS in Chapter 5 counts were $\sim 3.3 \times 10^8$ diffracted photon counts at each energy value (Section 5.1). Figure 7.17 shows the output of KKFIT on the noisy mocked-up data, and Figure 7.18 shows the Fourier transforms and FEFFIT fits for the 10^6 and 10^5 data sets where the signal-to-noise ratio is the poorest. Table 7.5 summarizes the FEFFIT fits the toe KKFIT $\chi(k)$ from the mocked up Cu (111) and Cu (222) DAFS with noise.

The Fourier components of the fine structure are robust under the influence of

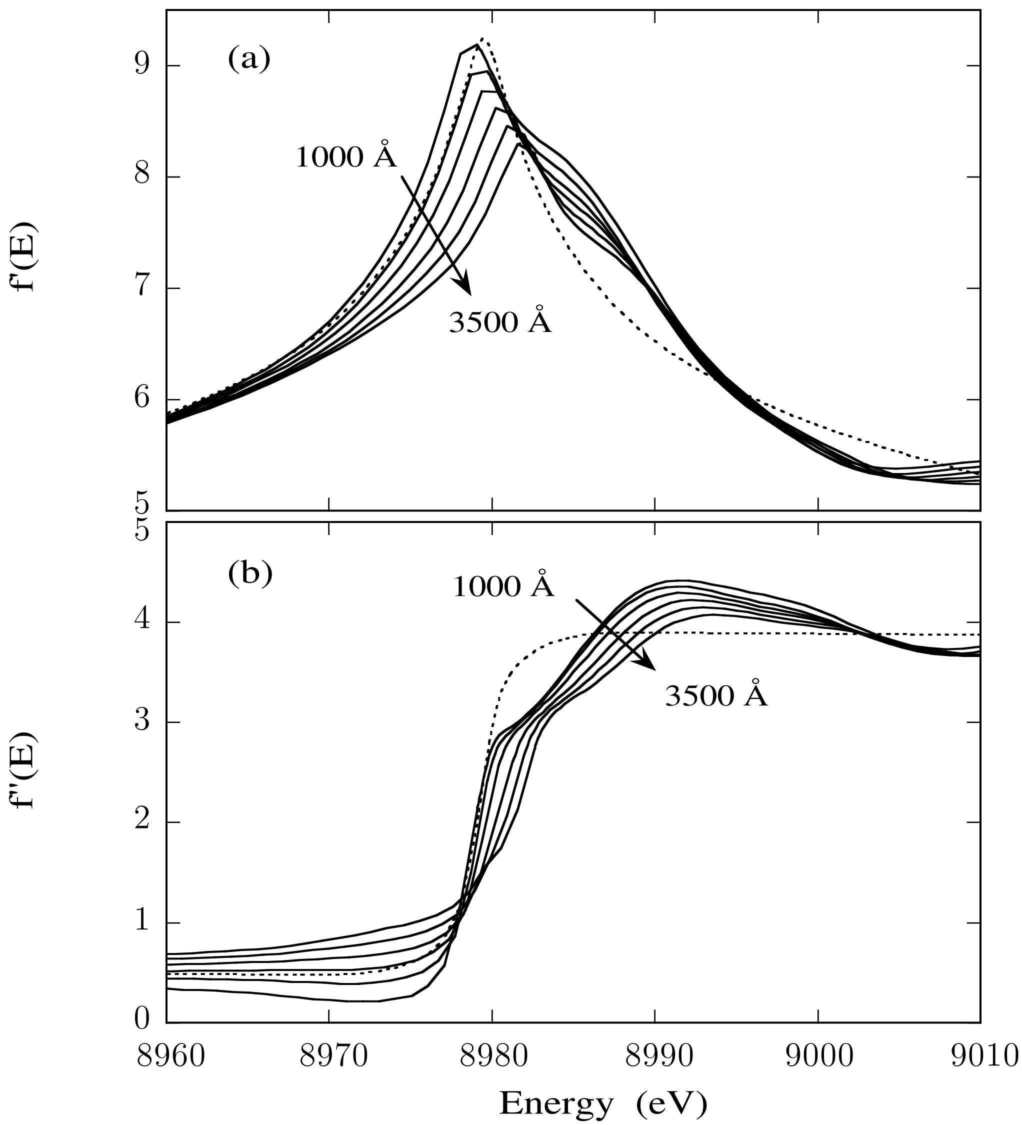

Figure 7.12: Film thickness effect on Cu (111) $f'(E)$ and $f''(E)$. The (a) $f'(E)$ and (b) $f''(E)$ output of KKFIT on mocked-up Cu (111) DAFS and using Maclaurin's formula for the integral transform. DAFS data with film thicknesses from 1000 Å to 3500 Å was mocked-up and fit by KKFIT with a fixed 2000 Å film thickness in the absorption correction to examine the effect of an incorrect self-absorption correction on the DAFS data. The effective film thickness $t/\sin\theta_{\text{in}}$ is larger for the (111) reflection than for the (222), so the effect is larger.

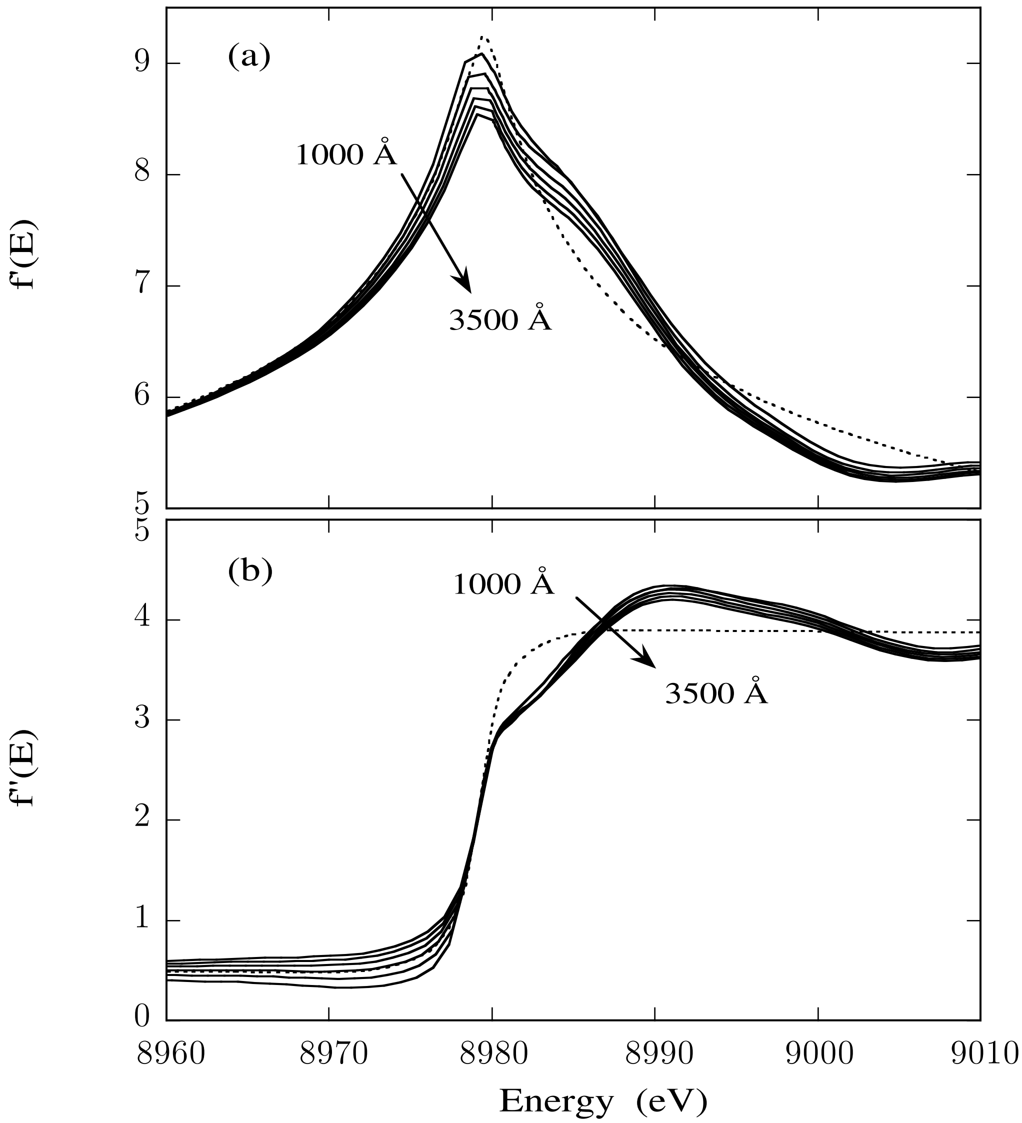

Figure 7.13: Film thickness effect t on Cu (222) $f'(E)$ and $f''(E)$. The (a) $f'(E)$ and (b) $f''(E)$ output of KKFIT on mocked-up Cu (222) DAFS and using Maclaurin's formula for the integral transform. DAFS data with film thicknesses from 1000 Å to 3500 Å was mocked-up and fit by KKFIT with a fixed 2000 Å film thickness in the absorption correction to examine the effect of an incorrect self-absorption correction on the DAFS data. The effective film thickness $t/\sin\theta_{\rm in}$ is smaller for the (222) reflection than for the (111), so the effect is smaller.

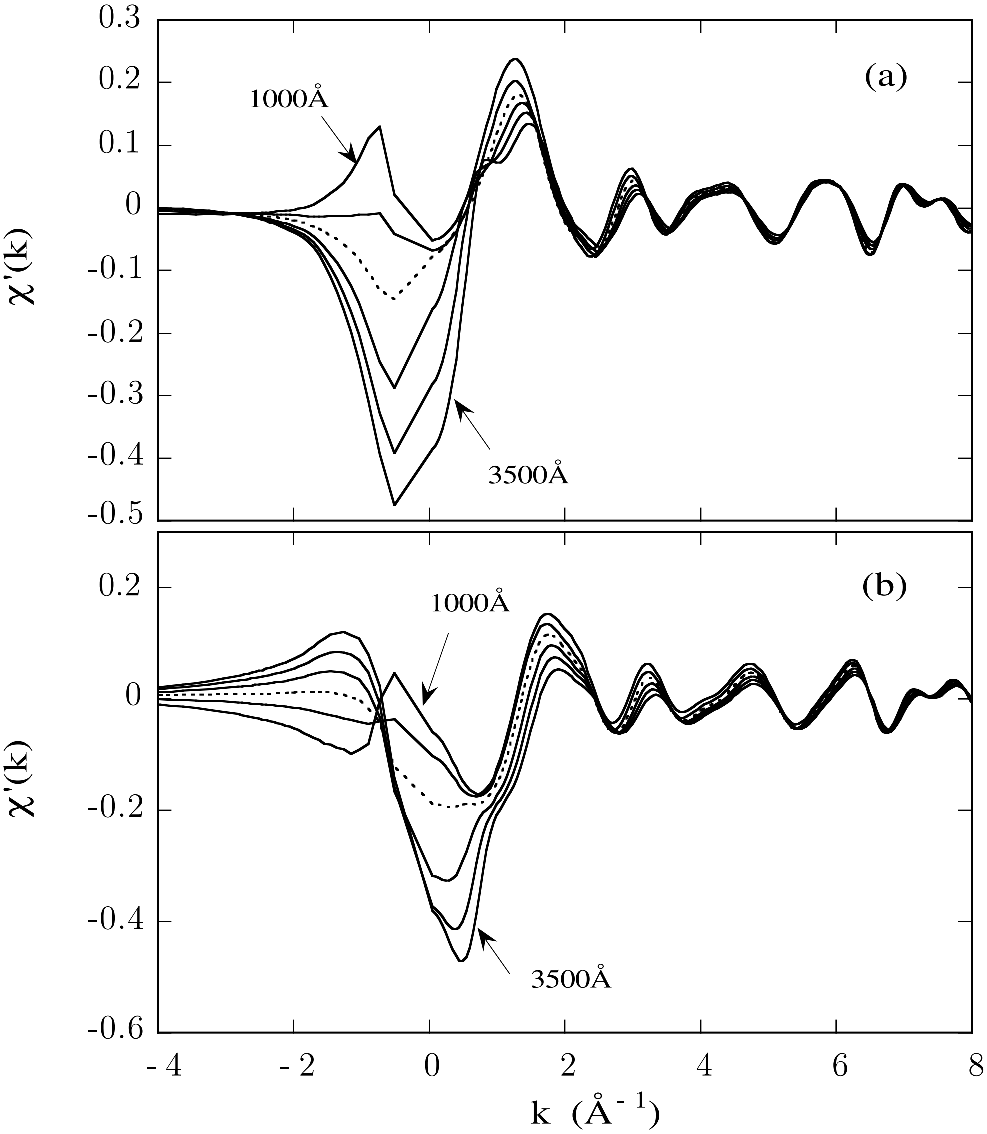

Figure 7.14: Film thickness effect on Cu (111) $\chi'(k)$ and $\chi''(k)$. The resulting (a) $\chi'(k)$ and (b) $\chi''(k)$ output from KKFIT using Maclaurin's formula for the integral transform. DAFS data with film thicknesses from 1000 Å to 3500 Å was mocked-up and fit by KKFIT with a fixed 2000 Å film thickness in the absorption correction to examine the effect of an incorrect self-absorption correction on the DAFS data. The dashed-line curves in (a) and (b) are for the 2000 Å film thickness in the fit, which is equivalent to a self-test of the mocked-up data.

Table 7.4: Film thickness effects: results of FEFFIT analysis of $\chi'(k)$ functions obtained by KKFIT using a fixed value for the film thickness of 2000 Å in the fits to mocked-up DAFS data generated with film thicknesses ranging from 1000 Å to 3500 Å in 500 Å steps. The effective film thicknesses are $t \sim 3.7\ t_0$ for Cu (111) DAFS and $t \sim 1.8\ t_0$ for Cu (222) DAFS.

	path parameters				
thickness	S_0^2	$\Theta_{\rm D}(K)$	α	ΔE_0 (eV)	d_0 (Å)
FEFFIT *fits to analytic $\chi(k)$ test functions (control)*					
$\chi'(k)$	0.836±0.013	313.5±2.5	0.0033±0.0003	-0.002±0.15	2.5645±0.0008
$\chi''(k)$	0.838±0.010	313.3±1.9	0.0033±0.0003	-0.020±0.12	2.5644±0.0008
FEFFIT *fits to $\chi'(k)$ from* KKFIT *of mocked-up Cu (111) DAFS*					
1000 Å	0.900±0.033	299.4±5.4	0.0049±0.0009	0.259±0.35	2.5684±0.0023
1500 Å	0.872±0.029	303.6±5.0	0.0043±0.0008	0.148±0.32	2.5669±0.0021
2000 Å	0.833±0.028	307.6±5.2	0.0038±0.0008	0.470±0.32	2.5658±0.0021
2500 Å	0.778±0.027	312.5±6.2	0.0035±0.0009	1.008±0.37	2.5649±0.0023
3000 Å	0.716±0.032	318.6±7.7	0.0031±0.0010	1.443±0.44	2.5639±0.0026
3500 Å	0.648±0.035	326.2±9.8	0.0026±0.0012	1.823±0.53	2.5627±0.0031
FEFFIT *fits to $\chi'(k)$ from* KKFIT *of mocked-up Cu (222) DAFS*					
1000 Å	0.836±0.029	306.4±5.4	0.0043±0.0009	-0.135±0.18	2.5670±0.0023
1500 Å	0.854±0.026	306.8±4.8	0.0039±0.0008	-0.258±0.15	2.5659±0.0021
2000 Å	0.847±0.024	307.5±4.5	0.0036±0.0007	-0.273±0.18	2.5652±0.0018
2500 Å	0.836±0.023	309.4±4.3	0.0033±0.0007	-0.263±0.18	2.5645±0.0018
3000 Å	0.825±0.021	311.4±4.1	0.0030±0.0006	-0.330±0.15	2.5637±0.0015
3500 Å	0.813±0.020	312.4±4.0	0.0028±0.0006	-0.382±0.18	2.5630±0.0015

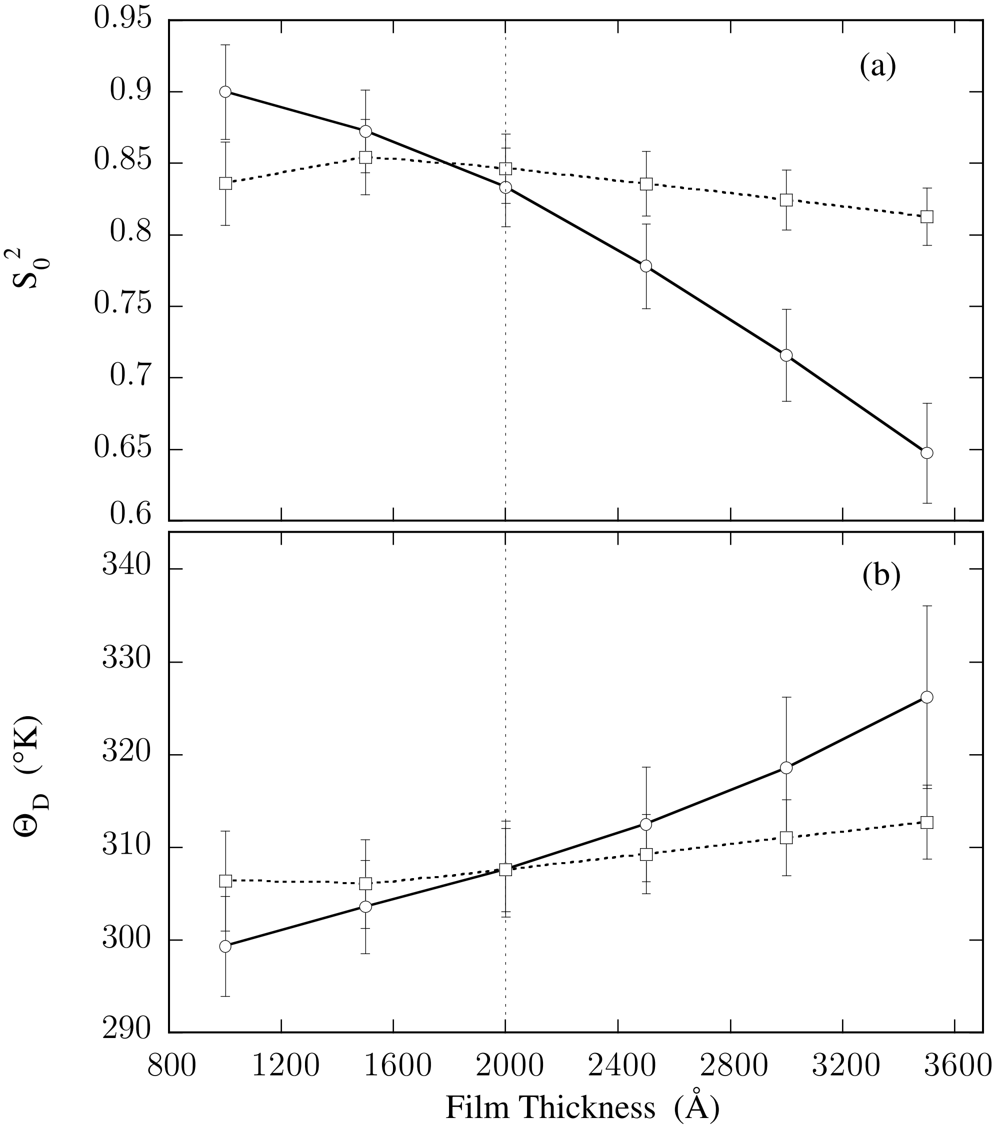

Figure 7.15: Film thickness effects: S_0^2 and Θ_D The effect of the absorption correction on (a) S_0^2 and (b) Θ_D for mocked-up Cu (111) (solid line) and Cu (222) (dashed line) DAFS are shown as a function of the film thickness. The KKFIT output was generated with t held fixed at 2000 Å, indicated by a vertical dashed line in both plots. The first shell was fit by FEFFIT using the first three paths in Table 5.2 and four variable path parameters. The results of the fits are shown in Table 7.4. The effective film thickness is smaller, $t \sim 1.8 t_0$, for the Cu (222) reflection compared to $t \sim 3.7 t_0$ for Cu (111), and even though the non-resonant Thomson scattering is also smaller for larger $\mathbf{Q}$, the effect of an incorrect film thickness in KKFIT is much smaller for Cu (222) than for Cu (111). S_0^2 and Θ_D are anticorrelated in FEFFIT by $\cos\theta \approx -0.93$.

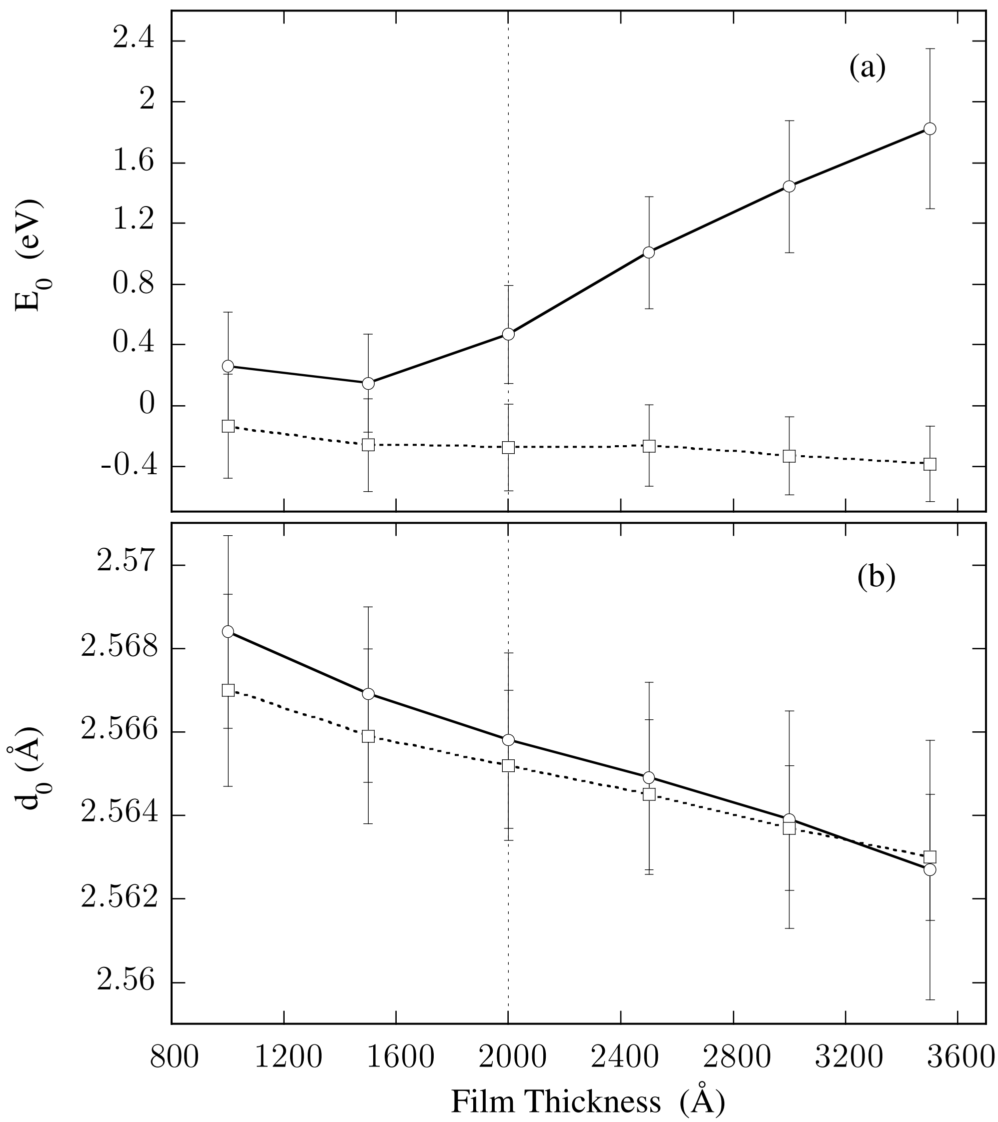

Figure 7.16: Film thickness effects: δE_0 and d_0. The effect of the absorption correction on (a) the edge shift δE_0 and (b) the first neighbor distance d_0 for Cu (111) (solid line) and Cu (222) (dashed line) are shown as a function of the film thickness for the mocked-up input data. The KKFIT output was generated with t held fixed at 2000 Å, indicated by a vertical dashed line in both plots. The first shell was fit by FEFFIT using the first three paths in Table 5.2 and four variable parameters. The results of the fits are shown in Table 7.4. The effects of an incorrect film thickness in KKFIT on these two variables is on the order of the uncertainty in their final values as determined by FEFFIT. δE_0 and d_0 are correlated in FEFFIT by $\cos\theta \approx 0.91$.

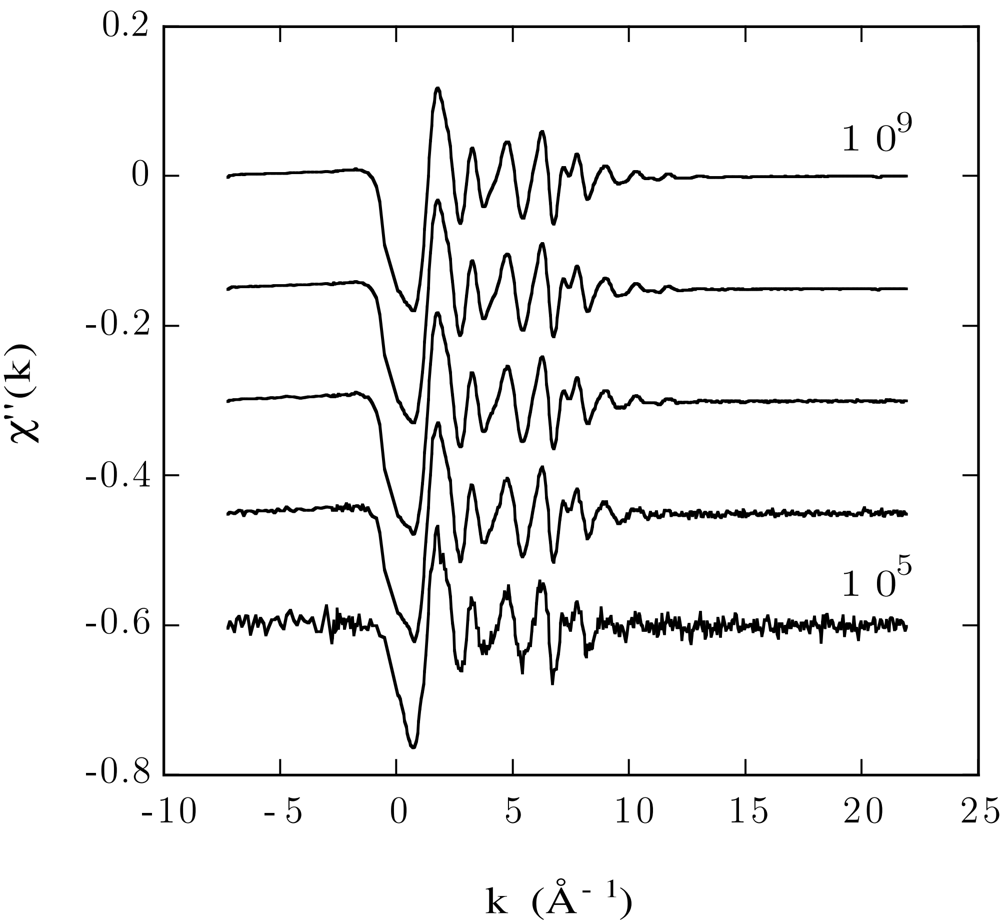

Figure 7.17: DAFS $\chi''(k)$ from KKFIT with Poisson distributed noise. Each successive data set has been shifted downward by 0.15 for easier comparison. The $\chi(k)$ from top to bottom are 10^9, 10^8,...,10^5 intensity of the mocked-up DAFS Cu (111) DAFS data before adding the Poisson distributed noise.

randomly distributed noise. From Table 7.5, it is apparent that only when the noise level is increased to the order of 10% of the fine structure does any change appear in the structural parameters. This suggests that reliable results might be obtained from DAFS experiments with lower integration times.

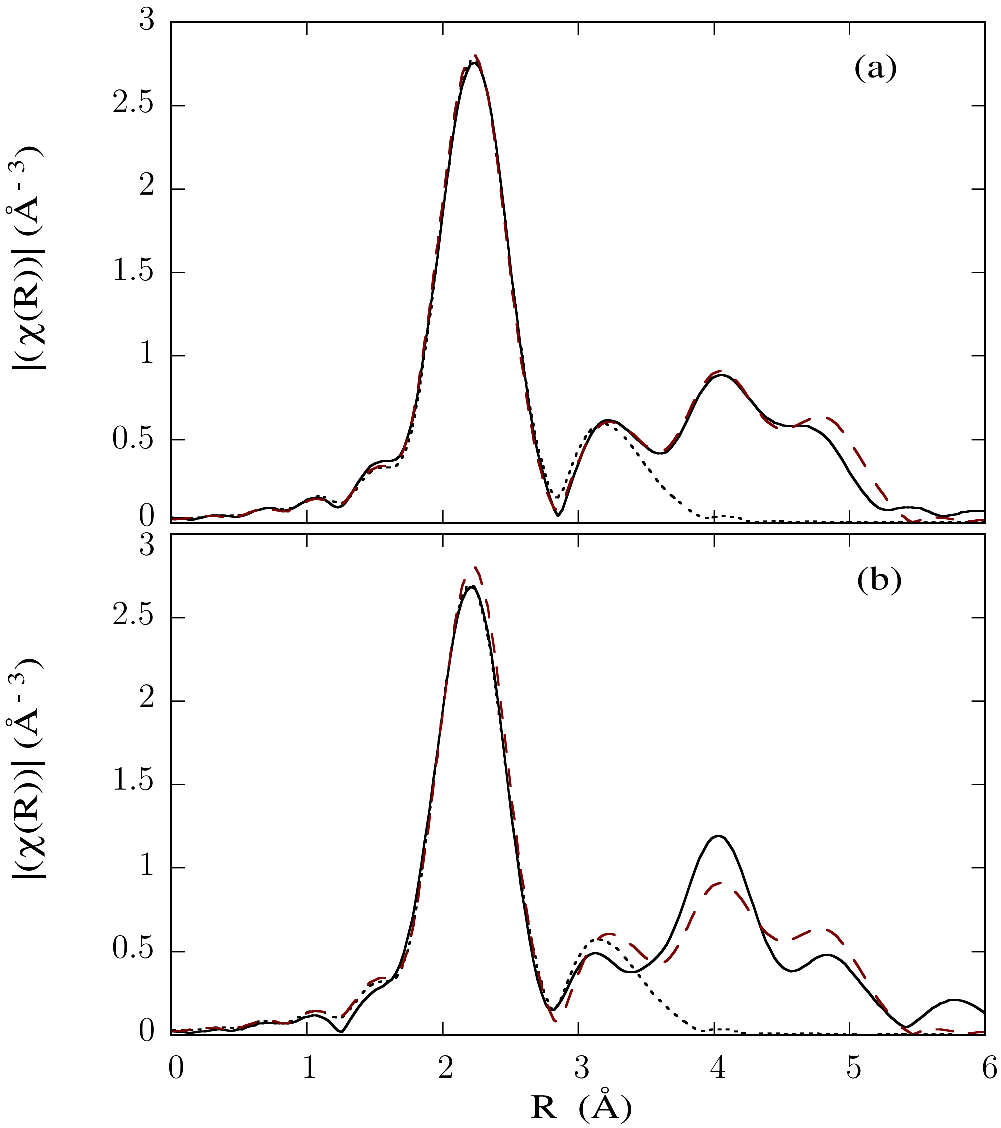

Figure 7.18: DAFS $|\tilde{\chi}(R)|$ from KKFIT with Poisson distributed noise. (a) with $I \sim 10^6$ and (b) $I \sim 10^5$. Overplots of the Fourier transforms of the KKFIT output (solid lines), FEFFIT fit (short-dash lines) and the noise-free functions (long-dash lines).

Table 7.5: Random noise effects: results of FEFFIT analysis of $\chi'(k)$ functions obtained by KKFIT using .

	path parameters				
thickness	S_0^2	$\Theta_{\mathrm{D}}(K)$	α	ΔE_0 (eV)	d_0 (Å)
FEFFIT *fits to analytic* $\chi(k)$ *test functions (control)*					
$\chi'(k)$	0.849±0.026	311.1± 5.0	0.0036±0.0008	0.095±0.31	2.5652±0.0021
$\chi''(k)$	0.852±0.026	310.5± 5.0	0.0038±0.0008	0.187±0.31	2.5658±0.0021
FEFFIT *fits to* $\chi'(k)$ *from* KKFIT *of mocked-up Cu (111) DAFS*					
10^9 Å	0.841±0.027	307.2± 4.9	0.0038±0.0008	0.284±0.31	2.5657±0.0021
10^8 Å	0.841±0.027	307.1± 5.0	0.0039±0.0008	0.303±0.31	2.5659±0.0021
10^7 Å	0.833±0.029	308.1± 5.4	0.0034±0.0008	0.114±0.34	2.5646±0.0021
10^6 Å	0.828±0.024	314.1± 4.8	0.0036±0.0007	0.646±0.28	2.5697±0.0018
10^5 Å	0.787±0.050	317.4±10.7	0.0038±0.0016	-0.677±0.64	2.5570±0.0041
FEFFIT *fits to* $\chi'(k)$ *from* KKFIT *of mocked-up Cu (222) DAFS*					
10^9 Å	0.849±0.025	307.1± 4.5	0.0037±0.0007	-0.152±0.29	2.5655±0.0018
10^8 Å	0.849±0.025	307.2± 4.6	0.0036±0.0007	-0.187±0.29	2.5653±0.0018
10^7 Å	0.857±0.024	305.5± 4.4	0.0041±0.0007	-0.060±0.28	2.5664±0.0018
10^6 Å	0.864±0.027	303.2± 4.8	0.0043±0.0008	0.467±0.31	2.5670±0.0021
10^5 Å	0.872±0.035	301.6± 6.1	0.0014±0.0010	-0.757±0.40	2.5597±0.0026

7.5 Embedded atom $f'(E)$ and $f''(E)$ calculated by FEFF

For forward modeling of the whole DAFS intensity, as well as for crystallographic and resonant magnetic scattering applications, it is useful to have complex resonant scattering amplitudes that include the embedded atom and fine-structure contributions $\Delta f_a(E)$. Cromer-Liberman calculations do not include the white line features of resonant scattering which can be on the order of ten times the step height in $f''(E)$ in the actinides [107]. The complete embedded atom $\Delta f_a(E)$, as well as the $\Delta f(E)$ with fine-structure, can be derived from the output of FEFF by applying the differential Kramers-Krönig transform. Figures 7.19(a) and 7.20(a) show $f'_a(E)$ calculated this way in the extended and near-edge regions respectively. First, the keyword `XANES` is used in a call to FEFF 6.10 to generate the embedded atom $\mu_0(E)$ for the single core level. In general, the FEFF calculation is reliable over a restricted energy range and tends to diverge for energies more than ≈ 600 eV above the edge. The divergence can be reduced some by decreasing the mesh size of the R-space steps used for calculating the phase shifts.

The $f''_a(E)$ shown in the bottom half of Figures 7.19 and 7.20 was calculated by FEFF using a mesh size of $\Delta R/R = 0.02$ for calculating the phases[4]. The output of FEFF is the functions $\mu_0(E)$, which is the absorption for the single deep core level, must be modified before $f'_a(E)$ can be calculated. After converting $\mu_0(E)$ to $f''_0(E)$ using the tables in Appendix A, the K-shell lineshape $f''_0(E)$ was adjusted to agree with Cromer-Liberman functions from tables [63]. First the L-shell contribution was removed from the tabulated $f''_a(E)$ by fitting to a functional form in the near-edge region and taking the difference: $f''_{0,\text{C.L.}} = f''_a(E) - f''_L(E)$, where the L-shell contribution is determined by a parameterized fit to $f''(E < E_0)$ after McMaster [62]

$$ln(f''(E)/E) = \sum_{i=1}^{3} a_i \left(ln(E)\right)^i . \tag{7.11}$$

The resulting scaled Cromer-Liberman K-shell $f''_{0,\text{C.L.}}(E)$ was then used to rescale the FEFF $f''_0(E)$ using two adjustable parameters

$$f''_0(E) = (a + bE) f''_{0,\text{C.L.}}(E). \tag{7.12}$$

After the FEFF K-shell contribution was scaled to agree with Cromer-Liberman far from the edge, the L-shell contribution was added and a differential Kramers-Krönig

[4] The default mesh size for FEFF XANES calculations is $\Delta R/R = 0.05$.

transform was calculated on the FEFF $f''_a(E)$ to obtain the real part $f'_a(E)$ shown in the top half of Figures 7.19 and 7.20.

This pair of functions differs from the tabulated functions only near the edge and they are invariant under Kramers-Krönig transform by construction. Since the embedded atom response depends on the local environment, separate calculations are needed for each inequivalent resonant site in the unit cell.

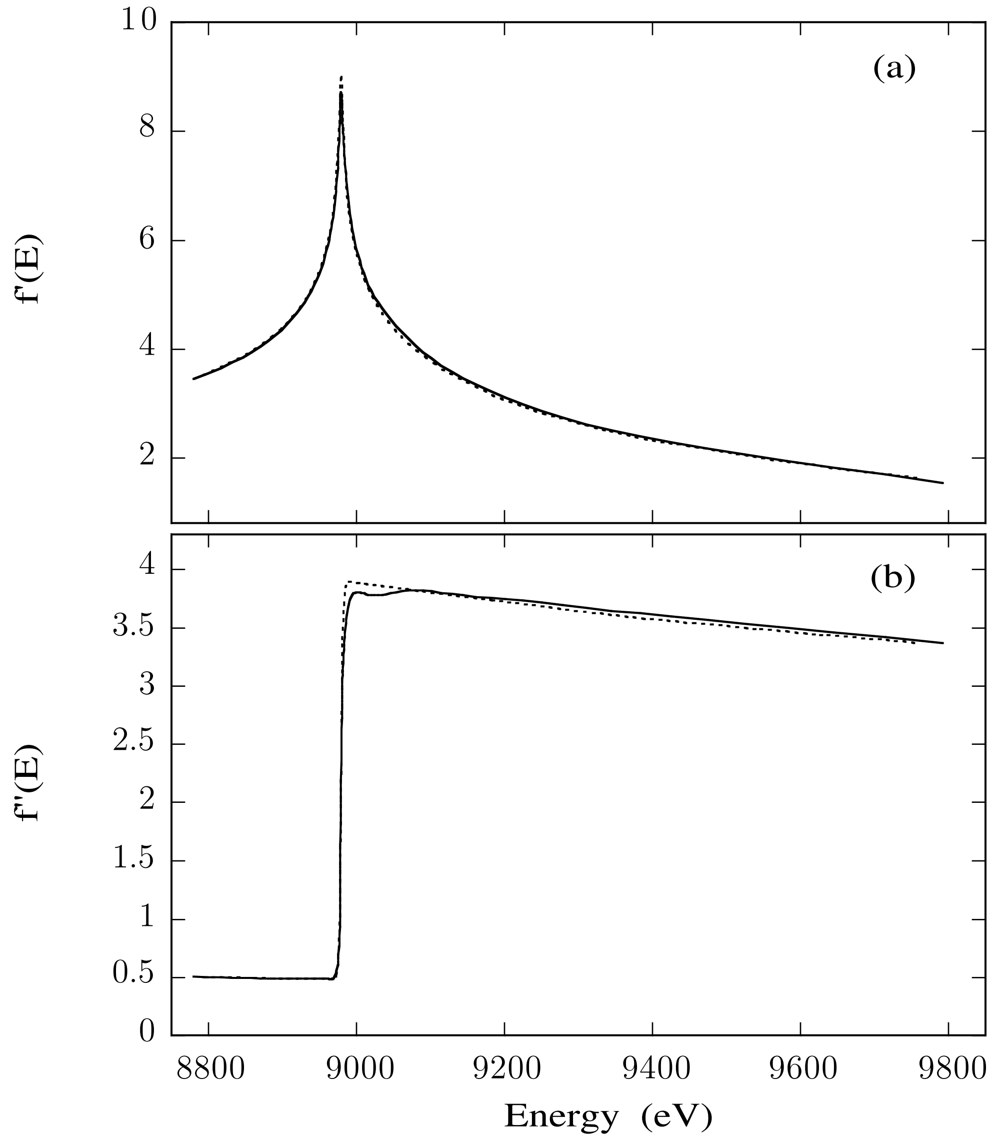

Figure 7.19: Embedded atom $f'(E)$ for Cu metal generated by differential Kramers-Krönig transform of FEFF $f''(E)$. (a) An overplot of the embedded atom $f'(E)$ (solid line) and the Cromer-Liberman $f_a'(E)$ convolved with a 2 eV Lorentzian (dashed line) used in the differential transform. (b) The embedded atom $f''(E)$ (solid line) generated by FEFF using the `xanes` input card. The slope and amplitude were scaled to give agreement with $f_a''(E)$ (dashed line) at the ends of the range. The scaling was allowed to make only the multiplicative linear correction, which is insufficient in freedom to match higher than the first derivative at the endpoints.

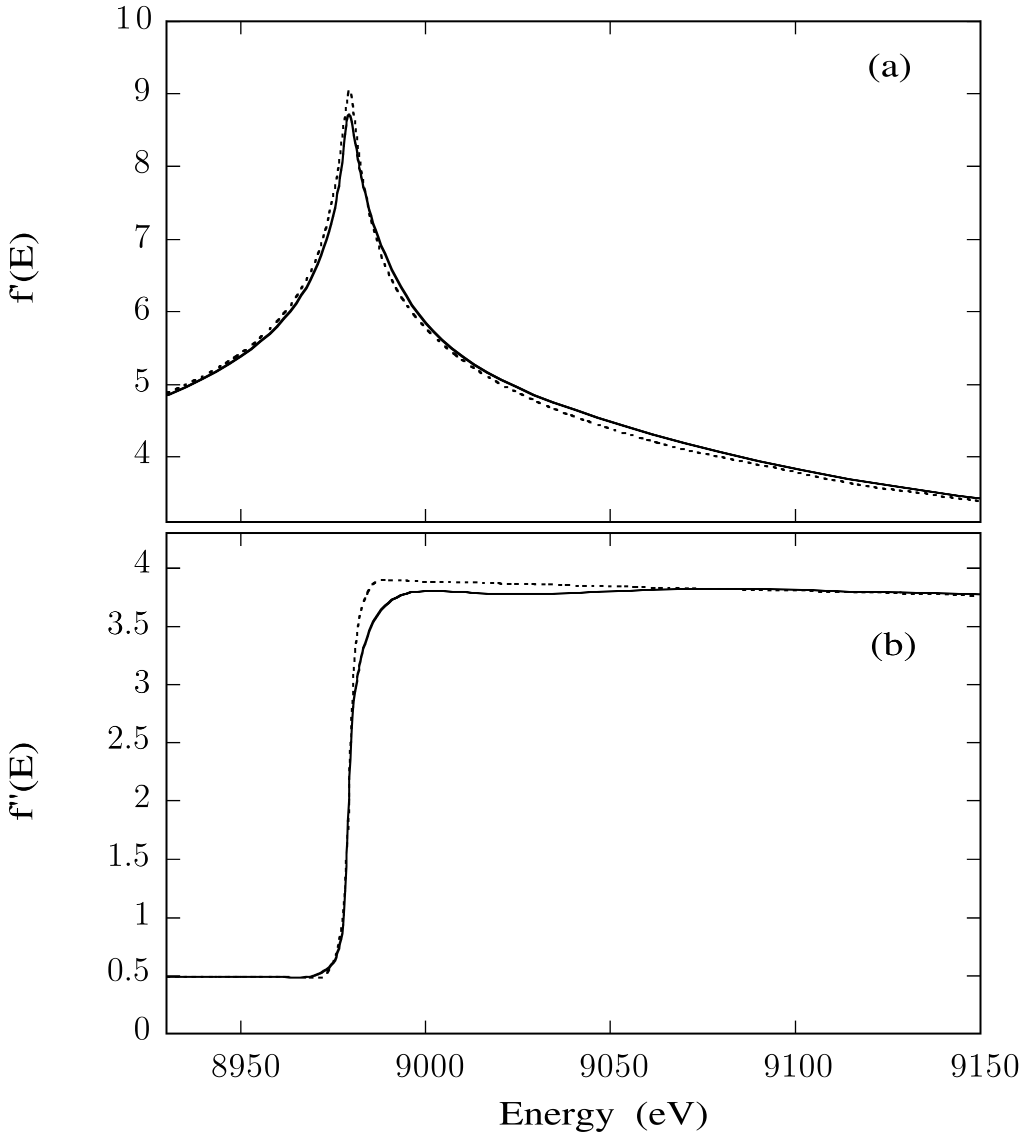

Figure 7.20: Near-edge region of the embedded atom $\Delta f(E)$ functions shown in Figure 7.19. (a) The embedded atom $f'(E)$ for Cu metal (solid line) determined by differential Kramers-Krönig transform and and the lifetime-broadened Cromer-Liberman $f'_a(E)$ (dashed line). (b) The embedded atom $f''(E)$ (solid line) generated by FEFF using the `xanes` input card and $f''_a(E)$ (dashed line).

Chapter 8

DISCUSSION

In this thesis, I have demonstrated that the iterative Kramers-Krönig algorithm, with a small modification to account for the anomalous scattering from the off-resonant atoms in the unit cell, is a reliable method for isolating the real and imaginary parts of the resonant scattering amplitude from DAFS intensity data. The reliability tests show that the analysis program KKFIT does not corrupt the structural information content of the resonance fine-structure. The most important application of KKFIT will be the determination of the site-specific resonant scattering amplitudes from complex materials, particularly in the near-edge region. This information cannot be obtained by any other method that I am aware of, making DAFS the unique solution to questions about the chemical and valence state of resonant atoms in a large class of technologically important materials.

The DAFS analysis methods described in this thesis are presented in a language and style directed towards the XAFS community, with the idea that workers already familiar with XAFS will immediately recognize the applicability of DAFS to familiar systems. This amounts to treating the crystallographic intensities that underlie the DAFS as background and, consequently, ignoring some of the important physics in favor of an increased subscription to the technique. Some of the most intriguing applications of DAFS are those which make use of all of the information contained in the DAFS signal, *i.e.*, the crystallographic information contained in the overall intensities measured as a function of of $\mathbf{Q}$, *and* the near neighbor and valence information contained in the resonance fine structure as a function of energy.

8.1 Co-Refinement of DAFS and XAFS Structural Information

My first attempt to bring diffraction and XAFS together using FEFFIT on a set of DAFS $\chi_{\mathrm{w}}(\mathbf{Q}, k)$ functions from different reflections, under constraints based on the partial structure factor, has shown that normalization to the single atom resonance response required by KKFIT dilutes the long-range structural information in the coefficients $W_{i,\mathbf{Q}}$. It appears that while KKFIT is clearly the correct method for producing site-separated XANES in complex materials, it is not the approach to take if correlation between long-rang and short-range structural parameters are sought. If there is a solution for parameter correlation, it will have to include a fit to the whole DAFS enchilada: resonant scattering *and* the overall intensity. This can be accomplished by modelling the scattering amplitude in a refinement of the structure factor including the resonant scattering and the fine-structure. Some work has already been started in this direction. A computer program WEFIT [98], based on FEFF and FEFFIT is being implemented in which the energy dependence of the DAFS intensity data is given equal footing with the $\mathbf{Q}$ dependence. The fine-structure fit will be performed in energy, instead of the usual R-space transform fitting for XAFS analysis, and will make use of FEFF calculations for the complex fine-structure and embedded-atom $f_0''(E)$.

Unfortunately, the polarization dependencies of the fine structure and the Thomson scattering work somewhat against each other. While this effect was conveniently exploited for simplifying the DAFS Debye-Waller factors in Section 3.2.1, it works against simple parameter coupling. Constraints between the bond lengths and the atomic positions are complicated because the fine structure is sensitive to bonds that are perpendicular to $\mathbf{k}$ and $\mathbf{k}'$. Since the Thomson scattering has the $\hat{\mathbf{e}} \cdot \hat{\mathbf{e}}'$ polarization dependence, the diffracted intensity is strongest when the scattering plane is perpendicular to the incident photon polarization direction. The effect is that the intensities of the reflections along one direction in reciprocal space, which are related to the long-range order, will couple to structural information in the energy dependent fine structure measured on reflections in the orthogonal direction. This is a four-dimensional problem. One additional advantage of WEFIT is that the polarization constraint required for linear decomposition of a collection of DAFS $f_{\mathrm{w}}(\mathbf{Q}, k)$ is relaxed. The path-by-path polarization can be calculated by FEFF even when $\hat{\mathbf{e}} \neq \hat{\mathbf{e}}'$, and this simply becomes part of the amplitude calculation.

8.2 A micro-survey of related work

8.2.1 Magnetic and quadrupole scattering

Resonant magnetic scattering [106, 107] is related to DAFS in that the scattering is measured in the near-edge region (white line), although these experiments measure the long-range magnetic order of the system and the measurements are taken at a single fixed energy. The energy range and materials that are accessible for resonant magnetic scattering are limited by the availability of suitable polarizing optics, but newer broad-band polarizing elements [108] may change the way in which these experiments are performed to include probing the density of final states as a function of energy. There have been beautiful resonance scattering experiments on α-hematite showing a 50-fold enhancement of a quadrupole feature [109], attributed to the crystal symmetry [110] since the Fe atoms site locally distorted oxygen octahedra. There are many materials of technological importance, $YBa_2Cu_3O_{6.8}$ for one, in which transition metal cations sit in a distorted oxygen shell. To my knowledge the enhancement seen for Fe in α-hematite has not been looked for at the K-edges of other transition metals in similar distorted environments.

8.2.2 Resonant Raman scattering

The similarities between the second-order terms in the elastic scattering matrix elements and the first-order absorption matrix elements are echoed in the inelastic scattering channel. These give rise to the x-ray resonant Raman effect, and there are two options for resonance arising from the energy denominator [111, 112]. However, these signals are extremely small. High resolution measurements of the x-ray fluorescence has already been used to improve the resolution of XAFS features smaller than the core-hole linewidth [113, 114]. If successful experiments can be done, in might be possible to measure near-edge features in the presence of lifetime broadening.

8.3 Causality, analyticity and dispersion

Analysis of DAFS data by a method that relies on the dispersion relations between the real and imaginary parts of Δf raises some deeper questions about the information content of the data. The cyclic connections between causality, analyticity and the dispersion relations make the validity of the Kramers-Krönig integrals equivalent to the statement that photon-atom scattering is strictly causal, *i.e.*, that there can be no scattering output before the input reaches the sample. Of course this is what everyone tends to believe, including this humble investigator, but I also agree with Charles Bennett's statement that "regardless of one's prejudices, the question of the possible existence of acausal physical phenomena should be answered on the basis of experimental data, not on the basis of epistemology" [22]. A natural question to ask about DAFS data is: if resonant x-ray scattering were not strictly causal, would there be an observable effect in the DAFS fine structure? Limits on the time scales we could measure for any such acausal *leakage* are set by the core hole lifetime (long time scales) and by the total extent in energy of the DAFS fine structure (short time scales). For example, if the Cu K-shell resonance is $\delta E \sim 2$ eV wide, then the longest time scale we could observe is on the order of $t_{max} \sim \hbar/(2\delta E) \sim 10^{-15}$ seconds, and if the maximum range over which the fine structure is distinguishable from the noise is $\Delta E \sim 800$ eV, then the shortest time scale is $t_{min} \sim \hbar/(\Delta E) \sim 10^{-18}$ seconds. For comparison, the time scale for Thomson scattering is $t_{Thom} \sim \hbar/E_0 \sim 10^{-19}$ for the Cu K-shell energy.

8.3.1 Types of acausality

Considering the properties of the Fourier transform [89], there are two types of acausal *leakage* that might be introduced into the response functions. The first type of leakage preserves crossing symmetry in $\Delta f(\omega = E/\hbar)$, changing only the amplitudes of the real and imaginary components. This corresponds to introducing a real negative-energy tail into the real, causal response function in the time domain $\Delta\tilde{f}(t)$. Using the fact that any function can be written as the sum of a symmetric function and an antisymmetric function and the symmetry properties of the Fourier transform, the symmetric part of the time-domain leakage function contributes to the real part of the frequency dependent response function while the antisymmetric part of the leakage appears in the imaginary part. This does not change the crossing symmetry of $\Delta f(E)$ but only causes a change the ratio of their amplitudes. The second type of leakage violates crossing symmetry by adding a small antisymmetric part to $f'(E)$ or a small symmetric part to $f''(E)$, or both. Again, considering the properties of the Fourier transform, the antisymmetric leakage in the real frequency response and symmetric leakage in the imaginary part of the frequency response both appear in the imaginary part of $\Delta\tilde{f}(t)$ in the time domain. Note that it is possible to violate crossing symmetry with a causal function.

8.3.2 The signature of acausality in resonant scattering

In principle, the signature of acausal behavior could be looked for experimentally. I have begun some computer experiments using mocked-up acausal DAFS data, generated by introducing an exponential *tail* into negative times at the intermediate step of the FFT-KK described in Section 7.1.2. The time-domain Fourier transform of the real part of the response function is multiplied by a modified step function $\Theta(t,\tau)$ with negative time leakage of the form

$$\Theta(t,\tau) = \begin{cases} e^{t/\tau}, & t < 0; \\ \frac{1}{2}, & t = 0; \\ 1, & t > 0 \end{cases} \tag{8.1}$$

My computer experiments show, as expected, that when τ is small[1], on the order of $\hbar/E_0 \sim 10^{-18}$ seconds, there is no discernible difference between the causal and acausal $\Delta f(E)$. In the limiting case, as $\tau \to \infty$, the backtransform goes to $2\chi'(E)$ in the real channel and 0 in the imaginary channel. However, as τ approaches the core-hole lifetime of $\sim 10^{-15}$ seconds differences between the causal and acausal functions increase to the order of 20% of the causal amplitudes. Since the acausal leakage is changing away from the step at $t = 0$, the amplitude shift will be smaller for the more rapidly oscillating Fourier components in Energy space and largest for the slowly varying components in Energy space, with the observable low limit corresponding to the range of the data. Since DAFS fine structure is periodic in the photoelectron momentum, and since $\hbar k = \sqrt{2m(E-E_0)/\hbar^2}$, a single Fourier component of $\chi(k)$, which corresponds to a single distance in the material, is a *chirp* in the energy domain, *i.e.*, the wavelength of the fine structure of $\chi(E)$ changes continuously with the frequency, as shown in Figure 8.1. Each Fourier component of the chirp will be affected differently by the acausal leakage, and so the signature of the leakage is expected to appear on all length scales in R-space simultaneously, though the size of difference may be too small to measure.

Aside from questions about the meaning of the results of such an investigation, the behavior of DAFS within the context of acausal resonant diffraction at the very least offers a new viewpoint from which to examine the properties of the dispersion relations themselves and perhaps gain new insight into their nature. I have not included the results of these experiments as the study is still very much a work-in-progress. The cyclic connection between causality, analyticity, and the dispersion relations for physical response functions is a convoluted trinity that has sent far

[1] I have chosen an exponential leakage function somewhat arbitrarily; it is also interesting to consider the signature of the *form* of the leakage, *e.g.*, how does Gaussian or algebraic acausality differ from an exponential acausality?

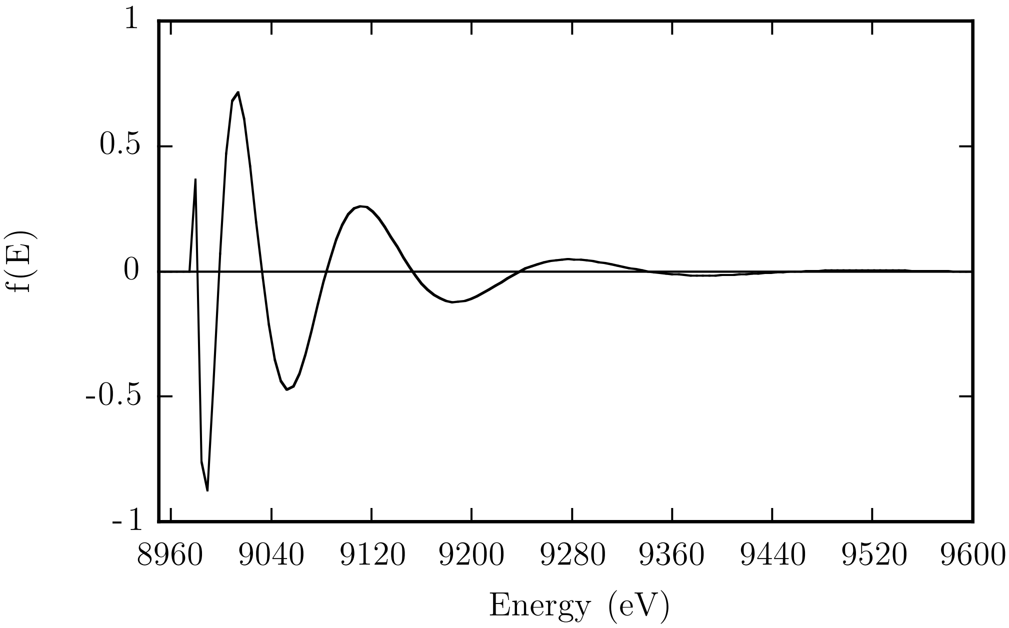

Figure 8.1: A single Fourier component of $\tilde{\chi}(R)$, corresponding to one distance in the solid, is periodic in the conjugate photoelectron momentum $\hbar k$. Since $k \propto \sqrt{E - E_0}$, the periodic function in k-space is a *chirp* in E-space, *i.e.*, the wavelength of the fine structure of $\chi(E)$ changes continuously with the frequency.

greater minds than my own reeling in confusion. Of the many treatments of this topic I have read, the ones I found to be the most helpful were [90–93], as well as an interesting anecdotal reference to the origins of complex analysis in Bell's chapter on Gauss [94].

8.4 Directional polarization effects in DAFS

Apparently when $\hat{\mathbf{e}} \neq \hat{\mathbf{e}}'$, certain types of triangular paths can have a dependence on the direction the path is traversed. Consider the case of an equilateral triangle and scattering with $\hat{\mathbf{e}}' \cdot \hat{\mathbf{e}} = \cos(\frac{\pi}{6})$, as shown in Figure 8.2. If the photoelectron scattering path is traversed clockwise, then the amplitude reduction due to polarization is $(\hat{\mathbf{e}} \cdot \hat{\mathbf{R}}_{01})(\hat{\mathbf{e}}' \cdot \hat{\mathbf{R}}_{20})$. On the other hand, if the path is traversed counterclockwise, then the amplitude reduction is $(\hat{\mathbf{e}} \cdot \hat{\mathbf{R}}_{20})(\hat{\mathbf{e}}' \cdot \hat{\mathbf{R}}_{01})$. The symmetry that should occur by considering both of the matrix elements for DAFS is broken by the size of the energy denominator for the antiresonant term. This is not an artifact of the path formalism. Considered from the point of view of classical resonant scattering, when the incoming photon polarization excites an electron, coupling is strongest if the bond direction to the neighbor is parallel to $\hat{\mathbf{e}}$. Likewise the outgoing photon will couple strongest with a bond that is parallel to its polarization vector. The signature of the directional

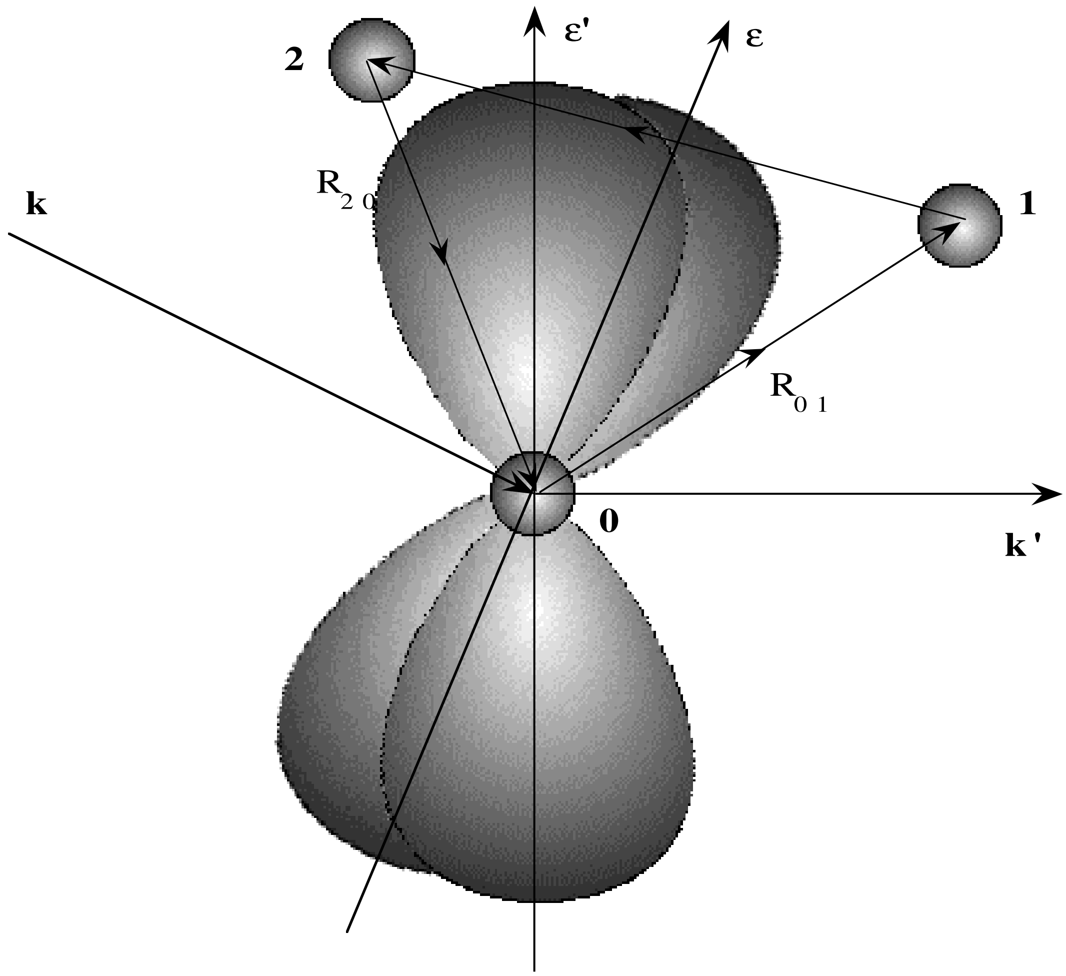

Figure 8.2: The polarization dependence of the contribution to the total DAFS $\chi(k)$ from a single triangular scattering path. For a K-shell resonance with $l = 0$, and if the incident photon is linearly polarized, the polarization dependence goes as $(\hat{\mathbf{e}} \cdot \hat{\mathbf{R}}_{01})(\hat{\mathbf{e}} \cdot \hat{\mathbf{R}}_{20})$. The polarization depends on the first and last legs of the scattering path. The Green's function also contains a term that will traverse this same path in the opposite direction. For DAFS, the polarization direction of the outgoing photon can be different from the polarization direction of the incident photon. For linear polarization the path-by-path polarization dependence of $l = 0$ DAFS is $(\hat{\mathbf{e}} \cdot \hat{\mathbf{R}}_{01})(\hat{\mathbf{e}}' \cdot \hat{\mathbf{R}}_{20})$. This can be different for clockwise and counterclockwise traversal of some triangular paths.

dependence would be a reduction of the contributions to the χ functions for this type of path, although the role of symmetry in the measured sum-over-paths still needs to be considered, and for high symmetry crystals these effects will cancel.

8.5 Energy dispersive DAFS experiments

All of these experiments described in this thesis were performed in the energy scanning mode, in which the incident monochromatic beam is scanned through the resonance, similar to the standard XAFS experiments. Recently experiments have been performed at the European Synchrotron Radiation Facility [99–101] and at Argonne National Laboratory [102] to measure DAFS in the dispersive energy mode. In these experiments the incident radiation is polychromatic and the sample itself serves as the dispersive element. There are still problems with instrument normalization in these experiments, and the energy resolution is limited by the crystalline quality of the sample, but the measurement times are much shorter than measurements in the fixed-energy mode, 2 minutes compared to 2 hours, and the sample orientation is fixed during the measurement. Counting time has not been a terrible problem with DAFS experiments so far. Our count rates for the Cu and $YBa_2Cu_3O_{6.8}$ experiments allowed a DAFS data set at one reflection to be collected in under four hours. But counting time will definitely be an issue for experiments that are already signal limited, such as circular magnetic dichroism [103] if that is expanded to the DAFS regime.

BIBLIOGRAPHY

[1] The earliest experimental report of diffraction fine structure that I am aware of is by Y. Cauchois, "Distribution spectrale obvservée dans une région d'absorption propre de divers cristaux," *Comptes Rendus de l'Academie des Sciences (Paris)* **242** (1956) pp. 100-102.

[2] Y. Cauchois and C. Bonnelle, "Distribution spectrale observée dans une région d'absorption propre du quartz," *ibid.* pp. 1596-1599.

[3] Y. Heno, "Essai d'interprétation théoretique de la diffusion anomale des rayons X par les cristaux," *ibid.* p. 1599-1602.

[4] T. Fukamachi, S. Hosoya, T. Kawamura and J. Hastings, *Journal of Applied Crystallography* **10** (1977) p. 321.

[5] G. Wendin, "Anomalous x-ray scattering," *Physica Scripta* **21** (1980) pp. 535-542.

[6] D.M. Barrus, R.L. Blake, A.J. Burek, K.C. Chambers, and L.E. Cox, "X-ray coefficient of reflection of acid pthalate crystals across the oxygen K-edge region," *Physical Review B* **22** (1980) pp. 4022-4037.

[7] D.H. Templeton, L.K. Templeton, D.C. Phillips and K.O. Hodson, "Anomalous scattering of x-rays by cesium and cobalt measured with synchrotron radiation," *Acta Crystallographica A* **36** (1980) pp. 436-442

[8] S.I. Salem and V.L. Hall, "Extended x-ray fine structure in crystalline copper," *Journal of Physics F* **10** (1980) pp. 1627-1629.

[9] V. Ponomarev and Y.A. Turutin, "Fine structure of Bragg reflection of x-rays near the far edge of the absorption band," *Soviet Physics. Technical Physics.* **29** (1984) pp. 232-234.

[10] I. Arčon, A. Kodre, D. Glavič and M. Hribar, "Extended fine structure of Bragg reflectivity of copper sulphate in the vicinity of copper K-edge," *Journal de Physique C (Paris)* **9** *Supplement n^{o}12* (1987) pp. 1105-1108.

[11] I. Arčon, A. Kodre and M. Hribar, "Bragg reflectivity extended fine structure of germanium crystals," in *X-Ray Absorption Fine Structure*, edited by S.S. Hasnain (Ellis Horwood, London, 1991) pp. 726-728.

[12] H. Stragier, J.O. Cross, J.J. Rehr, L.B. Sorensen, C.E. Bouldin and J.C. Woicik, "Diffraction anomalous fine structure: a new X-ray structural technique," *Physical Review Letters* **69** (1992) pp. 3064-3067.

[13] H.J. Stragier, *DAFS: A New X-Ray Structural Technique*, Ph.D. thesis, University of Washington (1993).

[14] Larry B. Sorensen, Julie O. Cross, M. Newville, B. Ravel, J.J. Rehr, H. Stragier, C.E. Bouldin and J.C. Woicik, "Diffraction anomalous fine structure: Unifying x-ray diffraction and x-ray absorption with DAFS," in *Resonant Anomalous X-Ray Scattering: Theory and Applications,* G. Materlik, C.J. Sparks and K. Fischer, editors (Elsevier Science B.V., 1994) pp. 389-420.

[15] C.E. Bouldin, J.C. Woicik, H. Stragier, J.O. Cross, J.J. Rehr and L.B. Sorensen, "Diffraction anomalous fine structure: XAFS with virtual photoelectrons," *Japanese Journal of Applied Physics* **32** Suppl. 32-2 (1993) p. 198.

[16] D.J. Tweet, K. Akimoto, I. Hirosawa, T. Tatsumi, H. Kimura, J. Mizuki, L.B. Sorensen, C.E. Bouldin and T. Matsushita, "Structural study of the Si/B($\sqrt{3} \times \sqrt{3}$)R30° Ge_xSi_{1-x}(111) interface by spatially selective diffraction anomalous fine structure (DAFS)," *Japanese Journal of Applied Physics* **32** Suppl. 32-2 (1993) p. 203.

[17] Ingrid J. Pickering, Michael Sansone, James Marsch, and Graham N. George, "Diffraction anomalous fine structure: a new technique for probing local atomic environment," *Journal of the American Chemical Society* **115** (1993) pp. 6302-6311.

[18] I.J. Pickering, M. Sansone, J.J. Marsch and G.N. George, "Site-specific x-ray absorption spectroscopy using DIFFRAXAFS," *Japanese Journal of Applied Physics* **32** Suppl. 32-2 (1993) p. 206.

[19] J.D. Jackson, *Classical Electrodynamics*, Second Edition (1975) chapter 7.

[20] L.K. Templeton and D.H. Templeton, "K-edge anomalous scattering in zinc tartrate hydrate," *Journal of Applied Crystallography* **21** (1988) pp. 558-561.

[21] M.G. Newville, *Local Thermodynamic Measurements of Dilute Binary Alloys Using XAFS*, Ph.D. thesis, University of Washington (1995), Chapter 4.

[22] Charles L. Bennett, "Evidence for microscopic causality violation," *Physical Review A* **35** (1987) pp. 2409-2419.

[23] J. Mustre de Leon, J.J. Rehr, and S.I. Zabinsky, "*Ab initio* curved-wave x-ray absorption fine structure," *Physical Review B* **44** (1991) pp. 4146-4145.

[24] Don T. Cromer and David Liberman, "Relativistic calculation of anomalous scattering factors for x-rays," *The Journal of Chemical Physics* **53** (1970) pp. 1891-1898.

[25] Brillouin attributes the original development of this model to Sommerfeld in reference [97].

[26] J.J. Sakurai, *Advanced Quantum Mechanics,* (Addison-Wesley Publishing Company, Inc., 1967) Chapter 2.

[27] In memory of Dr. P.C. Peters, r.i.p.

[28] M. Blume, "Magnetic effects in anomalous dispersion," in *Resonant Anomalous X-Ray Scattering: Theory and Applications,* G. Materlik, C.J. Sparks and K. Fischer, editors (Elsevier Science B.V., 1994) pp. 495-512.

[29] J.M. Tranquada, *X-Ray Absorption Studies of Solids at High Pressures*, Ph.D. thesis, University of Washington (1983).

[30] B.D. Hauser, *Study of Bond Angle Determination by XAFS Using the Separable Spherical Wave Approximation*, Ph.D. thesis, University of Washington (1990).

[31] S.I. Zabinsky, J.J. Rehr, A. Ankudinov, R.C. Albers, and M.J. Eller, "Multiple-scattering calculations of x-ray absorption spectra," *Physical Review B* **52** (1995) pp. 2995-3009.

[32] J. Mustre de Leon, *Curved Wave Calculations in X-Ray Spectroscopies, XAFS and Photoelectron Diffraction*, Ph.D. thesis, University of Washington (1995).

[33] S.I. Zabinsky, *Multiple Scattering Theory of XAFS*, Ph.D. thesis, University of Washington (1993).

[34] A. Ankudinov, Ph.D. thesis, University of Washington (after 1995).

[35] Information about FEFF may be found on the FEFF project home page at `http://krazy.phys.washington.edu/Feff/`.

[36] KKFIT was written in the Pascal programming language for a Macintosh IIci computer. It makes use of tabulated values of Δf_a from Sasaki [63], f_0 from Rez, *et. al*, [43] and theoretical calculations of $\chi(E)$ by FEFF [23]. KKFIT can be also used to generate mocked-up DAFS data. The author may be reached, after 15 April 1996, at: Naval Research Laboratory code 6680, 4555 Overlook Avenue S.E., Washington, D.C. 20375; (202) 767-3014.

[37] Gordon Baym, *Lectures on Quantum Mechanics*, (The Benjamin/Cummings Publishing Co., 1969).

[38] R.W. James, *The Optical Principles of the Diffraction of X-Rays*, (Oxbow Press, 1962), chapters II and III.

[39] H.K. Wagenfeld, "The angular dependence of x-ray dispersion corrections," *Journal of Physics B* **65** (1987) 437-441.

[40] For a review of anomalous scattering and references, see D.H. Templeton in *Handbook on Synchrotron Radiation*, edited by G. Brown and D.E. Moncton (Elsevier, Amsterdam, 1991) pp. 201-220.

[41] H.A. Kramers and W. Heisenberg, "Über die Streuung von Strahlung durch Atome," *Zeitschrift für Physik* **31** (1925) 681.

[42] I. Waller and D.R. Hartree, "On the intensity of total scattering of x-rays," *Proceedings of the Royal Society of London A* **124** (1929) pp. 119-142.

[43] D. Rez, P. Rez and I. Grant, "Dirac-Fock calculations of x-ray scattering factors and contributions to the mean inner potential for electron scattering," *Acta Crystallographica A* **50** (1994) pp. 481-497.

[44] B.E. Warren, *X-Ray Diffraction,* (Dover Publications, Inc., New York, 1990 reprint), appendix IV.

[45] S. Ramaseshan, T.G. Ramesh, and G.S. Ranganath, "A unified approach to the theory of anomalous scattering—some novel applications of the multiple-wavelength method," in *Anomalous Scattering*, S. Ramaseshan and S.C. Abrahams, editors (Munksgaard, 1975) pp. 139-161.

[46] R.H. Pratt, Lynn Kissel, and P.M. Bergstrom, Jr. "New relativistic S-matrix results for scattering — beyond the usual anomalous factors/beyond impulse approximation," in *Resonant Anomalous X-Ray Scattering: Theory and Applications,* G. Materlik, C.J. Sparks and K. Fischer, editors (Elsevier Science B.V., 1994) pp. 9-33.

[47] D.J. Tweet, *X-ray Determination of the Molecular Tilt and Layer Fluctuation Profiles of Freely Suspended Liquid Crystal Films*, Ph.D. thesis, University of Washington (1990), appendix E.

[48] R.W. James, *The Optical Principles of the Diffration of X-Rays*, (Oxbow Press, 1962), Chapter II, §2(d) and §2(f).

[49] M.G. Kendall, *The Advanced Theory of Statistics, Volume 1* (Charles Griffin & Co. Ltd., London, 1958).

[50] S. Dietrich and W. Fenzl, "Correlations in disordered crystals and diffuse scattering of x rays or neutrons," *Physical Review B* **39** (1989) pp. 8873-8899.

[51] E. Sevillano, H. Meuth, and J.J. Rehr, "Extended x-ray absorption fine structure Debye-Waller factors I. Monoatomic crystals," *Physical Review B* **20** (1979) pp. 4908-4911.

[52] C.G. Darwin, "The theory of x-ray reflexion," *Philosophical Magazine, Series 7* **27** (1914) pp. 315-333; "The theory of x-ray reflexion. Part II," *Philosophical Magazine, Series 7* **27** (1914) pp. 675-690.

[53] B.W. Batterman and H. Cole, "Dynamical diffraction of x rays by perfect crystals," *Reviews of Modern Physics* **36** (1964) pp. 681-717.

[54] Philip. R. Bevington, *Data Reduction and Error Analysis for the Physical Sciences,* (McGraw-Hill Book Company, 1969).

[55] J.A. Golovchenko, R.A. Levesque, and P.L. Cowan, "X-ray monochromator system for use with synchrotron radiation sources," *Reviews of Scientific Instruments* **52** (1981) pp. 509-516.

[56] The X23A-2 monochromator energy correction software was written by K.H. Kim.

[57] W. Bambynek, B. Craseman, R.W. Fink, H.U. Freund, H. Mark, C.D. Swift, R.E. Price, and P.V. Rao, "X-Ray fluorescence yields, Auger, and Coster-Kronig transition probabilities," *Reviews of Modern Chemistry* **44** (1972) pp. 716-813.

[58] Information about the UWXAFS 3.0 package, (including AUTOBK, FEFFIT and ATOMS) and the UWXAFS project may be currently be obtained through the world wide web site at `http://krazy.phys.washington.edu/`. Those interested in acquiring the UWXAFS 3.0 codes are directed to contact Professor E.A. Stern at the University of Washington.

[59] M.G. Newville, "FEFFIT: Using FEFF to model XAFS in R-space," unpublished (1994). This documentation is part of the UWXAFS 3.0 package [58].

[60] The AUTOBK documentation is part of the UWXAFS 3.0 package package [58].

[61] T.M. Hayes and J.B. Boyce, "Extended x-ray absorption fine structure spectroscopy," *Solid State Physics: Advances in Research and Applications*, H. Ehrenreich, F. Seitz and D. Turnbull, eds., vol. 37 (1982) p. 173.

[62] W.H. McMaster, N. Kerr-Del Grande, J.H. Mallett, and J.H. Hubbell, *Compilation of x-ray cross-sections. Lawrence Radiation Laboratory Report UCRL-50174* (National Bureau of Standards, VA, 1969).

[63] S. Sasaki, *Numerical Tables of Anomalous Scattering Factors Calculated by the Cromer and Liberman's Method*, KEK Report 88-14 (National Laboratory for High Energy Physics, 1989).

[64] C.T. Chantler, "Towards improved form factor tables," in *Resonant Anomalous X-Ray Scattering: Theory and Applications,* G. Materlik, C.J. Sparks and K. Fischer, editors (Elsevier Science B.V., 1994) pp. 61-78.

[65] S. Brennan and P.L. Cowan, "A suite of programs for calculating x-ray absorption, reflection, and diffraction performance for a variety of materials at arbitrary wavelengths," in *Reviews of Scientific Instrumentation* **63** (1992) pp. 850-853. These codes are available via anonymous ftp at `chevax.slac.stanford.edu` in the directory `[bren.absorption]`, as of 1995.

[66] The Henke tables are available at the world wide web site `http://xray.uu.se/hypertext/henke.html`, as of summer 1995. There is also a link to this site via the "X-Ray WWW Server" at `http://xray.uu.se/`, which is a generally useful place to look for x-ray lore and culture.

[67] D. Yee and collaborators provided this sample.

[68] G. Dräger and W. Czolbe, in *Resonant Anomalous X-Ray Scattering: Theory and Applications,* G. Materlik, C.J. Sparks and K. Fischer, editors (Elsevier Science B.V., 1994) pp. 99-102.

[69] E.A. Stern, "Number of relevant independent points in x-ray-absorption fine-structure spectra," *Physical Review B* **48** (1993) pp. 9825-9827.

[70] Yizhak Yakoby, personal communication.

[71] T. Siegrist, S.A. Sunshine, D.W. Murphy, R.J. Cava and S.M.Zahurak, "Crystal structure of the high-T_c superconductor $Ba_2YCu_3O_{9-\delta}$," *Physical Review B* **35** (1987) 7137-7139.

[72] M.A. Beno, L. Soderholm, D.W. Capone II, D.G. Hinks, J.D. Jorgensen, I.K. Schuller, C.U. Segre, K. Zhang, and J.D. Grace, "Structure of the single-phase high-temperature superconductor $YBa_2Cu_3O_{7-\delta}$," *Applied Physics Letters* **51** (1987) pp. 57-59.

[73] M. Marezio, "Oxygen Stoichiometry in High-T_c Superconductors," *Acta Crystallographica A* **47** (1991) 640-654.

[74] D. Haskel, personal communication.

[75] Sample provided by the Naval Research Laboratory.

[76] C.Y. Yang, S.M. Heald, J.M. Tranquada, A.R. Moodenbaugh, and Youwen Xu, "Lattice vibrational stucies of superconducting $YBa_2Cu_3O_7$ by polarized extended x-ray-absorption fine-structure measurements," *Physical Review B* **38** (1988) pp. 6568-6574.

[77] J. Guo, D.E. Ellis, E.E. Alp and G.L. Goodman, "Polarized copper K-edge x-ray-absorption spectra in $YBa_2Cu_3O_{7-y}$," *Physical Review B* **42** (1990) pp. 251-256.

[78] L. Soderholm and G.L. Goodman, "Use of x-ray absorption spectroscopy in electronic structure studies of high-T_c superconducting oxides," *Journal of the Optical Society of America B* **6** (1989) pp. 483-489.

[79] R.J. Cava, A.W. Hewat, E.A. Hewat, B. Batlogg, M. Marezio, K.M. Rabe, J.J. Krajewski, W.F. Peck Jr. and L.W. Rupp Jr., "Structural Anomalies, Oxygen Ordering and Superconductivity in Oxygen Deficient $Ba_2YCu_3O_x$, *Physica C* **165** (1990) pp. 419-433

[80] J.D. Jorgensen, B.W. Veal, A.P. Paulikas, L.J. Nowicki, G.W. Crabtree, H. Claus, and W.K. Kwok, "Structural Properties of Oxygen-Deficient $YBa_2Cu_3O_x$," *Physical Review B* **41** (1990) pp. 1863-1877.

[81] Olavi Keski-Rahkonen and Manfred O. Krause, "Total and Partial Atomic-Level Widths," *Atomic Data and Nuclear Data Tables* **14** (1974) pp. 139-146.

[82] P. Drier, P. Rabe, W. Malzfeldt and W. Niemann, "Anomalous x-ray scattering factors calculated from experimental absorption spectra," *Journal of Physics C: Solid State Physics* **17** (1984) pp. 3123-3136.

[83] C.W. Peterson and B.W. Knight, "Causality calculations in the time domain: An efficient alternative to the Kramers-Krönig method," *Journal of the Optical Society of America* **63** (1973) pp. 1238-1242.

[84] D.W. Johnson, "A Fourier series method for numerical Kramers-Krönig analysis," *Journal of Physics A* **8** (1975) pp. 490-495.

[85] K. Ohta and H. Ishida, "Comparision among several numerical integration methods for Kramers-Krönig transformation," *Applied Spectroscopy* **42** (1988) 952.

[86] John E. Bertie and Shuliang L. Zhang, "Infrared intensities of liquids. IX. The Kramers-Krönig transform, and its approximation by the finite Hilbert transform via fast Fourier transforms," *Canadian Journal of Chemistry* **70** (1992) pp. 520-531.

[87] F.C. Weinstein, J.D. Dow, and B.Y. Lao, "Optical respnse of semiconductors in electric fields: excitonic effects," *Physical Review B* **4** (1971) pp. 3502-3517. *n.b.* There is an error in the third function in Table 1,*i.e.*, the function labelled Figure 4(c) in column one. The analytic transform is a function of $\omega - \omega_0$, not $\omega + \omega_0$, so the plus sign in the numerator of the coefficient of $\ln|\ldots|$ must be replaced with a minus sign or the function will blow up.

[88] W.H. Press, B.P. Flannery, S.A. Teukolsky, and W.T. Vetterling, *Numerical Recipes in Pascal* (Cambridge University Press, 1989).

[89] Oran E. Brigham, *The Fast Fourier Transform*, (Prentice-Hall, 1974).

[90] James D. Bjorken and Sidney D. Drell, *Relativistic quantum fields,* (New York, McGraw-Hill, 1965), §18.1.

[91] J.D. Jackson, "Introduction ot dispersion relation techniques," in *Dispersion Relations*, G.R. Screaton, ed. (Oliver and Boyd, 1960) §1.

[92] Jan Hilgevoord, *Dispersion Relations and Causal Description*, (North Holland, 1962).

[93] Paul Forman, "Weimar culture, causality and quantum theory, 1918-1927: adaptation by german physicists and mathematicians to a hostile intellectual environment," *Historical Studies in the Physical Sciences* **3** (1971) pp. 1-115.

[94] Eric Temple Bell, *Men of Mathematics*, (New York, Simon and Schuster, 1937).

[95] George Arfken, *Mathematical Methods for Physicists*, Third Edition (Academic Press, 1985), §7.3

[96] Philip M. Morse and Herman Feschbach, *Mathematical Methods in Physics*, (McGraw-Hill Book Company, Inc., 1953) §4.2.

[97] Léon Brillouin, *Wave Propagation in Periodic Structures: Electric Filters and Crystal Lattices*, (Dover Publications, Inc., 1953) pp. 1-25.

[98] M.G. Newville, J.O. Cross, B. Ravel, C.E. Bouldin, and Y. Yacoby, unpublished.

[99] J.L. Hodeau, J. Vacinova, P. Wolfers, Y. Garreau, A. Fontaine, M. Hagelstein, E. Elkaim, J.P. Lauriat, A. Collomb, and J. Muller, "Site selectivity of DAFS analysis on hexaferrite at Fe K edge by using both monochromatic optics and energy dispersive optics," *Nuclear Instruments and Methods in Physics Research B* **97** (1995) pp. 115-118.

[100] J. Vacinova, J.L. Hodeau, P. Wolfers, E. Elkaim, J.P. Lauriat, Bouchet-Fabre-B. Chamberland-B-L , "Anomalous scattering and DAFS measurements of small single crystal of barium platinum oxide," *Nuclear Instruments and Methods in Physics Research B* **97** (1995) pp. 102-106.

[101] J.L. Hodeau, J. Vacinova, V. Garreau, A. Fontaine, M. Hagelstein, E. Elkaim, J.P. Lauriat, A. Prat, P. Wolfers, "Diffraction anomalous fine structure measurements by using an energy/angular "dispersive diffraction" experimental setup," *Review of Scientific Instruments* **66** (1995) pp. 1499-1501.

[102] P.L. Lee, M.A. Beno, G.S. Knapp, G. Jennings, "Continuous energy diffraction spectroscopy: a new d-space matching technique for energy dispersive synchrotron radiation diffraction." *Review of Scientific Instruments* **65** (1994) pp. 2206-2209.

[103] G. Shütz, M. Knülle, and H. Ebert, "X-Ray magnetic circular dichroism and its relation to local magnetic structures," in *Resonant Anomalous X-Ray Scattering: Theory and Applications,* G. Materlik, C.J. Sparks and K. Fischer, editors (Elsevier Science B.V., 1994) pp. 535-555.

[104] H. Renevier, J. Weigelt, S. Andrieu, R. Frahm, D. Raoux, "A diffraction anomalous fine structure (DAFS) study of Ir(100)/Fe superlattices," *Physica B* **208-209** (1995) pp. 217-219.

[105] D.C. Meyer, K. Richter, P. Paufler, H.G. Krane, "DAFS experiments for the determination of ordering on different (111) planes in epitaxial GaInP/GaAs layers," *Crystal Research and Technology* **29** (1994) pp. K66-70.

[106] D.B. Pengra, N.B. Thoft, M. Wulff, R.Feidenhans'l, and J. Bohr, "Resonance-enhanced magnetic x-ray diffraction from a rare-earth alloy," *Journal of Physics: Condensed Matter* **6** (1994) pp. 2409-2422.

[107] G. Helgesen, J.P. Hill, T.R. Thurston, D. Gibbs, "X-ray-scattering study of higher harmonic satellites near the antiferromagnetic phase transitions in rare-earth metals," *Physical Review B* **52** (1995) pp. 9446-9454.

[108] J.O. Cross, "Synthetic wide band-pass x-ray polarizers," in press.

[109] K.D. Finkelstein, M. Hamrick and Q. Shen, "Resonant x-ray diffraction and polarization analysis at the iron K-edge," in *Resonant Anomalous X-Ray Scattering: Theory and Applications,* G. Materlik, C.J. Sparks and K. Fischer, editors (Elsevier Science B.V., 1994) pp. 91-97.

[110] P. Carra and B.T. Thole, "Anisotropic x-ray anomalous diffraction and forbidden reflections," *Reviews of Modern Physics* **66** (1994) pp. 1509-1515.

[111] T. Kazuyuki and Y.Udagawa, "Novel approach for structure analysis by x-ray Raman scattering," *Physical Review B* **36** (1987) pp. 9410-9412.

[112] Y. Udagawa, H. Hisashi, T. Kazuyuki, and T. Mizushima, "X-Ray resonant Raman spectra of several copper compounds," *Journal of the Physical Society of Japan* **63** (1994) pp. 1713-1720.

[113] K. Hämäläinen, D.P. Siddons, J.B. Hastings, and L.E. Berman, "Elimination of the inner-shell lifetime broadening in x-ray-absorption spectroscopy," *Physical Review Letters* **67** (1991) pp. 2850-2853.

[114] P. Carra, M. Fabrizio, and B.T. Thole, "High resolution x-ray resonant Raman scattering," *Physical Review Letters* **74** (1995) pp. 3700-3703.

[115] B.D. Cullity, *Elements of X-Ray Diffraction, Second Edition* (Addison-Wesley, 1978).

[116] *International Tables for X-Ray Crystallography, Volume 3* (Kynoch Press, for the International Union of Crystallography, 1962) pp. 46-56.

[117] *CRC Handbook of Chemistry and Physics,* 62nd *edition* (CRC Press, Inc., 1982).

Appendix A

CONVERSION FACTORS

The mass absorption coefficient $\mu(E)$ is related to $f''(E)$ through a series of equations that takes me about an hour to rediscover every time I need to use them. This simple conversion is complicated by some confusion in the literature over a factor of 8π. While my intelligent readers might consider this appendix little more than a gratuitous exercise in dimensional analysis, I have judged it fit to include here from a very practical standpoint: these formulas come from one of the most dog-eared pages of my notebooks. The following trail of equations leads to a table of conversion factors that will transform f'' data, such as from the tables in reference [63], into μ/ρ data, such as that found in Appendix 8 of reference [115].

In the forward scattering direction, the imaginary part of the resonance correction to the Thomson scattering cross-section $f''(E)$ is related to the total absorption cross-section $\sigma_{tot}(E)$ by the optical theorem:

$$f''(\mathbf{Q}=0,E) = \frac{E}{2hcr_e}\sigma_{tot}(E), \tag{A.1}$$

where f'' is given in electron units, σ_{tot} is given in barns/atom, h is Planck's constant, c is the speed of light, and r_e is the classical electron radius given in units such that the units of $(hc)/r_e$ are the same as the energy E in the numerator. The mass absorption coefficient, $\mu(E)$, is usually wanted in units of cm^{-1} for calculating the absorption correction to the Bragg intensities. The cross-section for interaction within a material also naturally depends on the area density that is presented to the incident x-ray beam, which will change along with the contents and the configuration of the unit cell. For this reason, it is most useful to have a table of $\mu(E)/\rho$, where ρ is the partial mass density of the atoms within the unit cell in grams/cm^3. The conversion factor between σ, given in barns/atom, and μ/ρ, given in cm^2/gram, is

$$\frac{\mu(E)}{\rho} = \sigma(E)\left(\frac{10^{-24}cm^2}{barn}\right)\left(\frac{N_\mathrm{A}}{\mathrm{W}}\right) = (0.6022)\frac{\sigma(E)}{\mathrm{W}}. \tag{A.2}$$

W is the atomic weight in grams/mole, and $N_\mathrm{A} = 6.022045\times10^{23}$ mole^{-1} is Avagadro's number. Combining Equation (A.1) and Equation (A.2) gives the most convenient working equation for conversion between $f'' \equiv f''(\mathbf{Q}=0,E)$ and $\mu(E)$

$$\frac{\mu(E)}{\rho} = \frac{f''}{WE} 4.208 \times 10^{7} = \frac{f''}{E}\mathcal{C}_{\mathrm{w}} \tag{A.3}$$

where E is in eV, $\mu(E)/\rho$ is in gm/cm^2, W is in gm/mole, and f'' is in electron units. This is as far as the calculation can go without specific information about the contents of the unit cell. The total absorption coefficient for the material is summed over all of the atoms. In a crystalline material, this is equivalent to a sum over the contents of the unit cell. If there are N different species of atom in the unit cell, and N_j of the j^{th} species then

$$\begin{aligned} \mu_{\mathrm{tot}}(E) &= \frac{1}{E}\sum_{j=1}^{N} \rho_j f_j'' \mathcal{C}_{\mathrm{w_j}} \\ &= \frac{4.208 \times 10^{7}}{EVN_{\mathrm{A}}} \sum_{j=1}^{N} N_j f_j''. \end{aligned} \tag{A.4}$$

Programs for calculating the smooth part of $f''(\mathbf{Q}=0,E)$, based on Cromer-Liberman [24], are available electronically [65], as are tabulated values of these calculations [63, 66]. An abbreviated table of the conversion factors, $\mathcal{C}_W = 4.208 \times 10^7/W$, along with densities of some pure materials, is given below for convenience. In order to apply standard XAFS analysis techniques to the f' obtained from diffraction, the $\mathbf{Q}$ dependence of $f''(\mathbf{Q} \neq 0, E)$ is ignored and Equation (A.3) or Equation (A.4) is used to convert to $\mu(E)$.

Table A.1: Conversion factors between $f''(E)$, given in electron units, and $\mu(E)$, given in $\mathrm{gm/cm^2}$, for use in Equation (A.3). Only a few materials are tabulated here, but these should serve well in most applications and provide a comparison check for other calculations. Values for the densities at room temperature are from *International Tables for X-Ray Crystallography* [116] and atomic weights are from *CRC Handbook of Chemistry and Physics* [117].

Element	Density ($\mathrm{gm/cm^3}$)	$\mathcal{C}_W$ ($\times 10^5$)
Ti	4.508	8.745
Cr	7.194	8.093
Mn	7.473	7.569
Fe	7.873	7.535
Ni	8.907	7.167
Cu	8.933	6.622
Zn	7.134	6.439
Ga	5.908	6.034
Ge	5.324	5.797
As	5.776	5.617
Y	4.475	4.733
Nb	8.578	4.529
Mo	10.222	4.386
Ag	10.500	3.901
Cd	8.647	3.743
In	7.290	3.665
Sn	7.285	3.545
Sb	6.692	3.456
Ba	3.594	3.064
Au	19.281	2.134
Pb	11.343	2.031
Bi	9.803	2.014

Appendix B

CALCULATING DAFS WITH FEFF AND FEFFIT

This Appendix describes the steps that were taken to generate the mocked-up Cu DAFS data used in Chapter 7 for testing the reliability of the iterative Kramers-Krönig analysis algorithm. Input files for generating mocked-up $YBa_2Cu_3O_{7-\delta}$ DAFS are also described. The $YBa_2Cu_3O_{7-\delta}$ *ab initio* DAFS was used to test KKFIT on the more complex unit cell, with a large off-resonance anomalous scattering amplitude, and to check the *en masse* FEFFIT fitting to χ_{w} used in Chapter 6 to determine the DAFS mixing coefficients. The $YBa_2Cu_3O_{7-\delta}$ computer experiments were not included in this dissertation since the methods follow closely those described in Chapter 7 for Cu data, but the $YBa_2Cu_3O_{7-\delta}$ input files sufficiently complicated that the reader may find it useful to see them written out explicitly and to use them for reference.

All of the fine structure calculations were done by FEFF 6.10 [35] using the `XANES` card to generate embedded atom $\mu_0(E)$ functions for the Cu K-shell. In general, the FEFF calculation is reliable over a restricted energy range and tends to diverge for energies more than ≈ 600 eV above the edge. The divergence can alleviated somewhat by reducing the R-space step size used for calculating the phase shifts. The $f''_a(E)$ shown in Figs.7.19(b) and 7.20(b) were calculated with $\Delta R/R = 0.02$ set by the keyword `RGRID = 0.02` (the default is $\Delta R/R = 0.05$). For $YBa_2Cu_3O_{7-\delta}$, the polarization dependence of the fine structure for $YBa_2Cu_3O_{6.8}$ was calculated using a trick [74]. Setting `ellipticity 1 0 0 1`, for circular polarization, and `polarization 1 1 0` gives

$$\hat{\mathbf{e}} \cdot \hat{\mathbf{R}} = \frac{1}{\sqrt{2}}(\hat{\mathbf{x}} + i\hat{\mathbf{y}}) \cdot \hat{\mathbf{R}} \tag{B.1}$$

in the amplitude, and consequently the same result in the squared magnitude

$$|\hat{\mathbf{e}} \cdot \hat{\mathbf{R}}|^2 = \frac{1}{2}\left(\hat{\mathbf{x}} \cdot \hat{\mathbf{R}}\right)^2 + \frac{1}{2}\left(\hat{\mathbf{y}} \cdot \hat{\mathbf{R}}\right)^2 \tag{B.2}$$

as $\hat{\epsilon}$ in the a-b plane of a twinned orthorhombic crystal.

The complex $\chi_{\text{path}}(k)$ files were added together by FEFFIT [59], which allows additional physical structural information to be included in the calculation. A Debye model was used for the bond-length disorders in Cu, with $\Theta_{\text{Debye}} = 315$; an Einstein model was used for the bond-length disorders in $YBa_2Cu_3O_{7-\delta}$ with $\Theta_{\text{E}} = \hbar\omega_{\text{E}}/k_{\text{B}}$ from Haskel [74] and Tranquada [76], as seen in the $YBa_2Cu_3O_{7-\delta}$ `model.inp` file in Figure D.2. A fixed value of 0.89 was used for the multiple-electron attenuation factor in all cases. The steps taken to generate the mocked-up DAFS data are enumerated here:

i. Run ATOMS to generate the `feff.inp` file of atom positions in the cluster of size R_{max} centered at the excited atom. For a multiple resonant site material, ATOMS must be run once for each inequivalent site. ATOMS will also give the McMaster correction to use in FEFFIT.

ii. Run FEFF to generate the backscattering from the individual paths. For multiple resonant sites, FEFF must be run once for each site.

iii. Run FEFFIT on a subset of the individual path contributions. Check the values of $A_{\text{c.w.}}$ and R_{eff} in the third and fifth columns, respectively, of the `list.dat` file output by FEFFand use these to choose the important paths. Since the output of FEFFIT is not strictly analytic, FEFFIT must be run once per inequivalent site generate $\chi(k)$ functions that can be self-conjugated (see Section 7.2.1). The individual photoelectron backscattering path contributions are summed according to a physical model for the bond length disorders, multiple-electron attenuation, edge shift, and shifts in the path lengths. Figure B.1 below is an input file for Cu metal; Figures B.2 through B.4 are input files for the two Cu sites in $YBa_2Cu_3O_{6.8}$.

iv. The output from FEFFIT needs to be explicitly integrated using the Kramers-Krönig dispersion relations to obtain a true conjugate pair. Working with either $\chi'(k)$ or $\chi''(k)$, convert the abscissa from k to E, and calculate the conjugate using the differential integral of Equations (1.9) and (1.10). The data first also needs to be extended into the region $E < E_0$, and convolved with the core-hole lineshape before autoconjugation. I pour the data between the real and imaginary spaces three times (six calculations of the integrals) in insure convergence.

v. The smooth part of the resonant scattering can be taken from tabulated values or you can use the embedded atom $\mu(E)$ generated by FEFF 6.10 using the `XANES` input card. If the tabulated values are used, these need to be convolved with a Lorentzian lineshape to account for the core-hole lifetime broadening. Tabulated values of lifetimes are available in [81]. If the FEFF 6.10 output is used, the function $f''(E)$ is generated by first scaling $\mu(E)$ to the Cromer-Liberman $f''_a(E)$ lineshape, and then adding on the off-resonance shell contributions (L-shell contribution in the case of Cu K-shell resonance). The conjugate embedded-atom $f'(E)$ is generated by a differential Kramers-Krönig transform.

vi. Sum together the real and imaginary parts using the structure factor sum of Eq. (3.10) with $f(E) = f_0(Q) + \Delta f_a(E) + f''_{\text{shell}}\chi(E)$, Debye-Waller factors M and atomic positions R. Take the squared magnitude to get the intensity.

vii. Multiply the intensity by the absorption correction. The fine structure contribution to the absorption correction can be taken from simultaneously measured XAFS, or in the case of a mono-site problem, it can be co-refined with the fine structure in the scattering channel using the relationship between $f''(E)$ and $\mu(e)$.

```
%-----------------------------------------------------------
 %-------- FEFFIT fft range parameter, etc.  ---------
    rmin     = 0.00       rmax        = 10.0  % r fitting range
    kmin     = 0.00       kmax        = 20.0  % k fitting range
    dk       = 0.0        kweight     = 0
 %-------- file i/o directions ----------------------
    out      =  ffCu.dat
    formout  =  ascii
    kspout   =  true
    kfull    =  true
    allout   =  false
    nofit    =  true
 %-------- define variables and set Values-----------
    set      temp         =  293
    set      theta_debye  =  315      % Debye temperature for Cu
    set      sigma_mcm    =  0.00052  % McMaster correcton from ATOMS
    set      so2          =  0.89     % amplitude
    set      e0           =  0.00     % e0 offset
    set      phase        =  0.00     % constant phase shift
    set      alpha        =  0.0035   % thermal expansion coefficient
 %-------- path files from FEFFXX6.10 ---------------
    e0       0   e0
    delR     0   alpha*reff
    s02      0   s02
    sigma2   0   debye(temp,Debye_Temp) + sigma_mcm
    dphase   0   phase
    path     1   ../feff/feff0001.dat
    path     2   ../feff/feff0002.dat
    path     3   ../feff/feff0003.dat
    etc...
    path     11  ../feff/feff0011.dat
    path     12  ../feff/feff0013.dat
%-----------------------------------------------------------
```

Figure B.1: The `feffit.inp` file for generating a $\chi(k)$ function to mock up Cu DAFS data.

```
%------------------------------------------------------------
 %-------- FEFFIT fft range parameter, etc.  ---------
    rmin     = 0.00   rmax     = 10.0  % r fitting range
    kmin     = 0.00   kmax     = 20.0  % k fitting range
    dk       = 0.0    kweight  = 0
 %-------- file i/o directions ----------------------
    out      =  feffCu1.dat
    formout  =  ascii
    kspout   =  true
    kfull    =  true
    allout   =  false
    nofit    =  true
 %-------- define variables and set Values-----------
    set      temp     =  293
    set      so2      =  0.89   % amplitude
    set      e0Cu1    =  0.00   % e0 offset
    set      delta    =  0.168  % O(4) site depletion
    set      ampCu1   =  so2    % Cu(1) amplitude
    set      Theta01  =  561    % einstein temp for Cu-O
    set      ThetaBa  =  225    % einstein temp for Cu-Ba
    set      ThetaCu  =  225    % einstein temp for Cu-Cu
 %-------- path files from FEFFXX6.10 ---------------
    e0       0   EoCu1
 % FEFF PATH 0002.dat
 % Cu(1)->O(4)->Cu(1), along b-axis to O-Cu-O chain oxygen
 % Single scattering path, first shell
    path     11   ../feff/polarized/cu1/feff0002.dat
    s02      11   ampCu1*(1-delta) %scatters once from depleted site
    sigma2   11   eins(temp,Theta01)
%------------------------------------------------------------
```

Figure B.2: The first part of the `feffit.inp` file for generating the Cu(1) $\chi(k)$ function to be used for mocked-up $YBa_2Cu_3O_{6.8}$ DAFS. Values for the Einstein temperatures are from Haskel [74] and Tranquada [76].

```
% -----------------------------------------------------------
 %-------- path files from FEFFXX6.10 ---------------
 % FEFF PATH 0012.dat
 % Cu(1)->Cu(1)->O(4)->Cu(1), along b-axis
 % Single focusing path
    path    12   ../feff/polarized/cu1/feff0012.dat
    s02     12   ampCu1*(1-delta) %scatters once from depleted site
    sigma2  12   eins(temp,ThetaO1)
 % FEFF PATH 0004.dat
 % Cu(1)->Ba->Cu(1), down to center of perovskite unit
 % Single scattering
    path    13   ../feff/polarized/cu1/feff0004.dat
    s02     13   ampCu1
    sigma2  13   eins(temp,ThetaBa)
 % FEFF PATH 0005.dat
 % Cu(1)->Ba->Cu(1), up to center of perovskite unit
 % Single scattering
    path    14   ../feff/polarized/cu1/feff0005.dat
    s02     14   ampCu1
    sigma2  14   eins(temp,ThetaBa)
 % FEFF PATH 0015.dat
 % Cu(1)->O(4)->Cu(1)->O(4)->Cu(1)
 % double focusing
    path    15   ../feff/polarized/cu1/feff0015.dat
    s02     15   ampCu1*(1-delta) %scatters twice from same depleted site
    sigma2  15   eins(temp,ThetaO1)
 % FEFF PATH 0027.dat
 % Cu(1)->O(1)->O(4)->Cu(1)
 % Triangular path
    path    16   ../feff/polarized/cu1/feff0027.dat
    s02     16   ampCu1*(1-delta) %scatters once from depleted site
    sigma2  16   eins(temp,ThetaO1)
%------------------------------------------------------------
```

Figure B.3: The second part of the `feffit.inp` file for generating the Cu(1) $\chi(k)$ function to be used for mocked-up $YBa_2Cu_3O_{6.8}$ DAFS.

```
%-----------------------------------------------------------
 %------- path files from FEFFXX6.10 ---------------
 % FEFF PATH 0023.dat
 % Cu(1)->O(1)->Cu(1)
 % Diagonal single-scattering to O(1) site along a-axis
    path    17   ../feff/polarized/cu1/feff0023.dat
    s02     17   ampCu1
    sigma2  17   eins(temp,ThetaO1)
 % FEFF PATH 0024.dat
 % Cu(1)->O(1)->Cu(1)
 % Diagonal single-scattering to O(1) site along b-axis
    path    18   ../feff/polarized/cu1/feff0024.dat
    s02     18   ampCu1
    sigma2  18   eins(temp,ThetaO1)
 % FEFF PATH 0009.dat
 % Cu(1)->Cu(1)->Cu(1)
 % Single-scattering to Cu(1) site along a-axis
    path    19   ../feff/polarized/cu1/feff0009.dat
    s02     19   ampCu1
    sigma2  19   eins(temp,ThetaCu)
 % FEFF PATH 0010.dat
 % Cu(1)->Cu(1)->Cu(1)
 % Single-scattering to Cu(1) site along b-axis
    path    20   ../feff/polarized/cu1/feff0010.dat
    s02     20   ampCu1
    sigma2  20   eins(temp,ThetaCu)
 % FEFF PATH 0011.dat
 % Cu(1)->O(4)->O(4)->Cu(1)
 % Double focusing off two adjacent O(4) sites
    path    21   ../feff/polarized/cu1/feff0011.dat
    s02     21   ampCu1*(1-delta)*(1-delta) % assume uncorrelated
    sigma2  21   eins(temp,ThetaO1)
%-----------------------------------------------------------
```

Figure B.4: The third part of the `feffit.inp` file for generating the Cu(1) $\chi(k)$ function to be used for mocked-up $YBa_2Cu_3O_{6.8}$ DAFS.

```
%------------------------------------------------------------
 %-------- FEFFIT fft range parameter, etc.  ---------
    rmin     = 0.00   rmax      = 10.0  % r fitting range
    kmin     = 0.00   kmax      = 20.0  % k fitting range
    dk       = 0.0    kweight   = 0
 %-------- file i/o directions ----------------------
    out      =  feffCu2.dat
    formout  =  ascii
    kspout   =  true
    kfull    =  true
    allout   =  false
    nofit    =  true
 %-------- define variables and set Values-----------
    set      temp     =  293
    set      so2      =  0.89   % amplitude
    set      e0Cu2    =  0.80   % Cu(2) has higher O coordination than Cu(1)
    set      delta    =  0.168  % O(4) site depletion
    set      ampCu1   =  so2    % Cu(1) amplitude
    set      Theta0   =  561    % einstein temp for Cu-O
    set      ThetaBa  =  225    % einstein temp for Cu-Ba
    set      ThetaY   =  248    % einstein temp for Cu-Y
    set      ThetaCu  =  225    % einstein temp for Cu-Cu
 %-------- path files from FEFFXX6.10 ---------------
    e0       0   EoCu2
    s02      0    ampCu2 % no depleted sites around Cu(2)
 % FEFF PATH 0001.dat
 % Cu(2)->O(2)->Cu(2), square pyramid oxygen, a axis
 % Single scattering, first shell oxygen
    path     21   ../feff/polarized/cu1/feff0001.dat
    sigma2   21   eins(temp,Theta0)
%------------------------------------------------------------
```

Figure B.5: The first part of the `feffit.inp` file for generating the Cu(2) $\chi(k)$ function to be used for mocked-up $YBa_2Cu_3O_{7-\delta}$ DAFS.

```
%------------------------------------------------------------
 %-------- path files from FEFFXX6.10 ---------------
 % FEFF PATH 0002.dat
 %Cu(2)->O(3)->Cu(2), square pyramid oxygen, b axis
 % Single scattering, first shell
    path    22   ../feff/polarized/cu2/feff0002.dat
    sigma2  22   eins(temp,ThetaO)
 % FEFF PATH 0021.dat
 % Cu(2)->O(2)->Cu(2)->Cu(2); single focusing path along a-axis
    path    23   ../feff/polarized/cu2/feff0021.dat
    sigma2  23   eins(temp,ThetaO)
 % FEFF PATH 0027.dat
 % Cu(2)->O(2)->Cu(2)->Cu(2); single focusing path along a-axis
    path    24   ../feff/polarized/cu2/feff0027.dat
    sigma2  24   eins(temp,ThetaO)
 % FEFF PATH 0009.dat
 % Cu(2)->Ba->Cu(2); single scattering
    path    25   ../feff/polarized/cu2/feff0009.dat
    sigma2  25   eins(temp,ThetaBa)
 % FEFF PATH 0010.dat
 % Cu(2)->Ba->Cu(2); single scattering
    path    26   ../feff/polarized/cu2/feff0010.dat
    sigma2  26   eins(temp,ThetaBa)
 % FEFF PATH 0004.dat
 % Cu(2)->Y->Cu(2); single scattering
    path    27   ../feff/polarized/cu2/feff0004.dat
    sigma2  27   eins(temp,ThetaY)
 % FEFF PATH 0005.dat
 % Cu(2)->Y->Cu(2); single scattering
    path    28   ../feff/polarized/cu2/feff0005.dat
    sigma2  28   eins(temp,ThetaY)
%------------------------------------------------------------
```

Figure B.6: The second part of the `feffit.inp` file for generating the Cu(2) $\chi(k)$ function to be used for mocked-up $YBa_2Cu_3O_{7-\delta}$ DAFS

```
%------------------------------------------------------------
 %-------- path files from FEFFXX6.10 ---------------
 % FEFF PATH 0024.dat
 % Cu(2)->O(2)->Cu(2)->O(2)->Cu(2), along the a-axis
 % double focusing
    path    29   ../feff/polarized/cu2/feff0024.dat
    sigma2  29   eins(temp,ThetaO)
 % FEFF PATH 0030.dat
 % Cu(2)->O(3)->Cu(2)->O(3)->Cu(2) along the b-axis; double focusing
    path    30   ../feff/polarized/cu2/feff0030.dat
    sigma2  30   eins(temp,ThetaO)
 % FEFF PATH 0019.dat
 % Cu(2)->Cu(2)->Cu(2) along the a-axis; single scattering
    path    31   ../feff/polarized/cu2/feff0019.dat
    sigma2  31   eins(temp,ThetaBa)
 % FEFF PATH 0025.dat
 % Cu(2)->Cu(2)->Cu(2) along the b-axis; single scattering
    path    32   ../feff/polarized/cu2/feff0025.dat
    sigma2  32   eins(temp,ThetaBa)
 % FEFF PATH 0020.dat
 % Cu(2)->O(2)->O(3)->Cu(2) along the a-axis; double focusing
    path    33   ../feff/polarized/cu2/feff0020.dat
    sigma2  33   eins(temp,ThetaO)
 % FEFF PATH 0026.dat
 % Cu(2)->O(3)->O(3)->Cu(2) along the a-axis; focusing
    path    34   ../feff/polarized/cu2/feff0026.dat
    sigma2  34   eins(temp,ThetaO)
%------------------------------------------------------------
```

Figure B.7: The third part of the `feffit.inp` file for generating the Cu(2) $\chi(k)$ function to be used for mocked-up $YBa_2Cu_3O_{7-\delta}$ DAFS

Appendix C

FEFFIT INPUT FILE FOR CU XAFS AND DAFS

The non-structural background left in $\chi(k)$ by KKFIT can be can be corrected for by using the background removal feature of FEFFIT. This gives a visually pleasing result, as illustrated in Figure 5.8, but does not change any of the structural information. To use this feature, FEFFIT needs to be run twice. The first call, with the background fitting feature turned on, will generate k-space and R-space background files consistent with low R minimization of $\tilde{\chi}(R)$. The second call, with the background feature turned off and the files generated on the first pass named as the background source files, will subtracted off the background signal generated by first call and fit to this new background-subtracted function. Both calls to FEFFIT use the twelve paths enumerated in Table 5.2.

```
% ---------------------------------------------
title    =  Fit the XAFS chi.dat file with background fitting
data     =  ../ChisKKff/Cu111R21k.chi
out      =  Cu111R21w.dat
bkg      =  true
  include "ppCu12.inp"
% ---------------------------------------------

% ---------------------------------------------
title    =  Fit the XAFS chi.dat file with background subtraction
data     =  ../ChisKKff/Cu111R21k.chi
out      =  Cu111R21wb.dat
bkg      =  false
bkgfile  =  Cu111R21wk.bkg
  include "ppCu12.inp"
% ---------------------------------------------
```

Figure C.1: The FEFFIT input files for Cu metal with background correction. The upper part of this figure is the first call to FEFFIT. The instruction `bkg = true` generates a background spline that minimizes the signal in the low R region. The background spline is stored in an external ASCII file. The lower part of this figure is the second call to FEFFIT. The background determined by the first call is subtracted off of the data before fitting.

Appendix D

FEFFIT INPUT FOR CONSTRAINED DAFS FITTING

This appendix contains the input files to FEFFIT for fitting the fine structure from the (00ℓ) DAFS $\chi''_{\mathbf{w}}(\mathbf{Q}, E)$ functions, subject to constraints between the structural parameters in the fine structure and the structure factor coefficients for the two inequivalent Cu sites.

```
% ---------------------------------------------
   % feffit input for ybco
   % calls the files that contain the constraint model
   % and a file that contains the list of dafs data sets
   % sfmodel.inp  defines the variables and the functional
   %              constraints between them
   % list.inp     lists all of the data files to be fit, with
   %              definitions of any local variables that are
   %              specific to the data set (i.e., momentum transfer)
  include "sfmodel.inp"
  include "list.inp"
% ---------------------------------------------
```

Figure D.1: The `feffit.inp` for simultaneous fitting of multiple DAFS data sets from $YBa_2Cu_3O_{6.8}$ at the (00ℓ) Bragg reflections. This short input file calls two other files that contain the constraint model and the data files. The individual path files are given in Appendix B.

The methods, as well as the FEFFIT input files, presented in this appendix should be readily applicable to other systems. For an example of a complex set of constraints on temperature dependent XAFS data, see Appendix A of [21].

The steps for preparing the input k-space χ'' functions were presented in section 5.2.1. Following the example in Appendix A of [21], we create a general input file that links to the model and to the $\chi''_{\mathbf{w}}(\mathbf{Q}, E)$ data files, shown in figure D.1. The `model.inp` file in Figure D.2 defines and initializes a generalized set of variables for the individual path contributions to the fine structure from each the two inequivalent Cu sites and for the mixing ratio of Cu(1) and Cu(2) fine structure in terms of crystallographic parameters. Each data set is allowed to have its own E_0 to account for slipping of the edge position in the iterative Kramers-Krönig algorithm. Figure D.3 shows part of the `list.inp` called by `model.inp`. This file identifies the file names of the input files for each reflection and assigns a local value to the Miller indices. Each item in the list includes a separate call the file `paths.dat` where the FEFF path files and Fourier transform parameters are defined anew for each data set. The `paths.dat` for this fit contains both Cu(1) and Cu(2) paths as well as a header that redefines the Fourier transform parameters at each call. For a complete list of the paths for $YBa_2Cu_3O_{7-\delta}$ with the x-ray polarization vector confined to the *a*-*b* plane, see Figures B.2 through B.7.

```
% -----------------------------------------------
   % list file for simultaneous fitting of YBa_2Cu_30_7-dela
   title  = (00L)DAFS --> KK --> f'' norm'd chi(k)
   guess  so2       =  0.88
   guess  e0_001    =  0.00
   guess  e0_002    =  0.00
   guess  e0_003    =  0.00
   guess  e0Cu1     =  0.00
   guess  deltaEo   =  0.80     %   higher O coordination on Cu(2)
   set    temp      =  293
   % XAFS Debye-Waller factors
   set    ThetaO    =  561      %  Haskel
   set    ThetaBa   =  225      %  Tranquada
   set    ThetaY    =  248      %  Tranquada
   % Crystallographic Debye-Waller factors
   set    BCu1      =  0.53     %  Jorgensen
   set    BCu2      =  0.24     %  Jorgensen
% -----------------------------------------------
   % this is the crystallographic part
   set    c         =  11.6916  %  Cross, rotating anode data
   set    Q         =  2*Pi*L/c
   set    zCu2      =  0.3565   %  Tranquada
   set    R         =  zCu2*c
   set    alphaCu1  =  exp(-1*abs(BCu1)*((Q/(4*Pi))^2))
   set    alphaCu2  =  2*cos(Q*R)*exp(-1*abs(BCu2)*((Q/(4*Pi))^2))
   set    alpha     =  alphaCu1 + alphaCu2
   % coefficients for Cu(1) and Cu(2) fine structure
   set    ampCu1    =  so2*alphaCu1/alpha
   set    ampCu2    =  so2*alphaCu2/alpha
% -----------------------------------------------
```

Figure D.2: The `model.inp` file for simultaneously fitting multiple DAFS data sets of $YBa_2Cu_3O_{7-\delta}$ at different Bragg reflections. The oxygen depletion is accounted for in the accompanying `path.dat` file at the end of Appendix B.

```
% -----------------------------------------------
   list the individual DAFS chi(k) data sets and load the path
   % parameters from paths.inp.  The local variables L and e0_00L
   % are redefined for each data set.
   title    = (001) Bragg reflection from YBa_2Cu_30_7-dela
   data     = ../../chidata/KKchi/001k.chi
   out      = Lfit_ff001.dat
   local    L      =  1
   local    EoCu1  =  e0_001
   bkgfile  = Lfit_ff001k.bkg
   include "paths.inp"
   next data set  %   incoming...
   title    = (002) Bragg reflection from YBa_2Cu_30_7-dela
   data     = ../../chidata/KKchi/002k.chi
   out      = Lfit_ff002.dat
   local    L      =  2
   local    EoCu1  =  e0_002
   bkgfile  = Lfit_ff002k.bkg
   include "paths.inp"
   next data set  %   incoming...
   title    = (003) Bragg reflection from YBa_2Cu_30_7-dela
   data     = ../../chidata/KKchi/003k.chi
   out      = Lfit_ff003.dat
   local    L      =  3
   local    EoCu1  =  e0_003
   bkgfile  = Lfit_ff003k.bkg
   include "paths.inp"
% -----------------------------------------------
```

Figure D.3: Part of a `list.inp` for simultaneously fitting of multiple DAFS data sets from $YBa_2Cu_3O_{6.8}$ at different Bragg reflections. The accompanying `paths.dat` file is given in Appendix B.

VITA

Julie Olmsted Cross was born in Redwood City, California on February 1, 1958 to Jane Henderson Gill and Geoffrey Coburn Cross. She graduated from the experimental School Within a School (SWAS) at Sir Francis Drake High School in San Anselmo, California in 1976. She moved to Portland, Oregon, in 1979 to attend Reed College and received her B.A. in 1984 with the thesis titled *Classification of Some New Liquid Crystal Forming Materials*. She moved to Seattle in 1986 to begin graduate studies at the University of Washington. Julie takes her bourbon neat and has been known to outdrink men up to twice her weight and half her age: a skill she claims to have inherited, along with her sense of humor, from her grandmother Charlotte Olmsted Kursh.